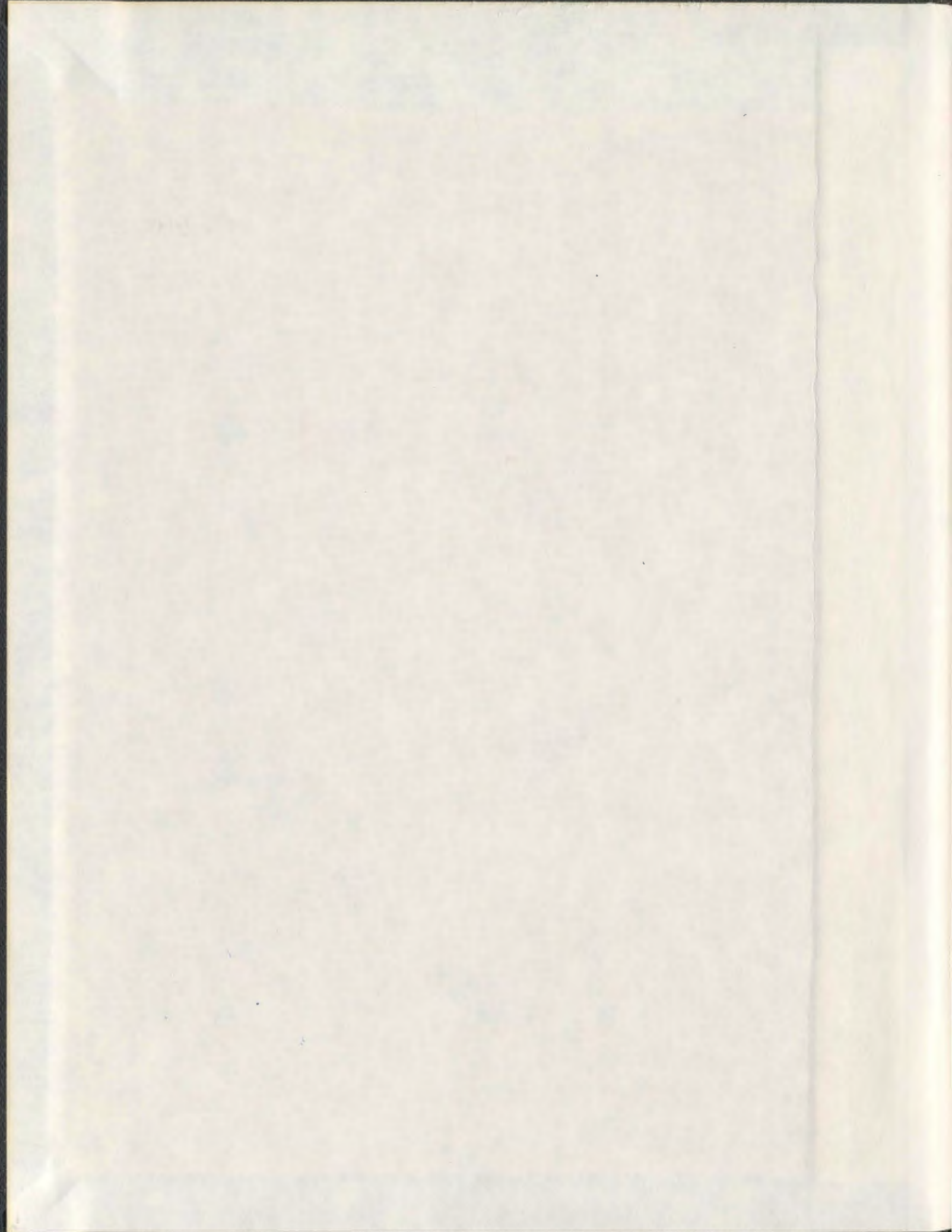
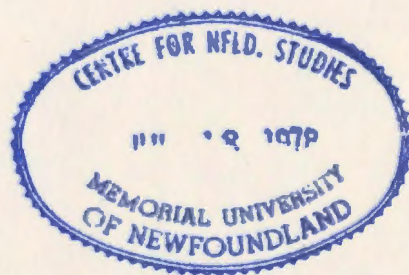


STRUCTURES AND INTERACTIONS OF LUNG  
SURFACTANT PROTEIN B (SP-B) PEPTIDES

MUZADDID SARKER



001311



# **Structures and Interactions of Lung Surfactant Protein B (SP-B) Peptides**

By

**Muzaddid Sarker**

A thesis submitted in conformity with the requirements  
for the Degree of Doctor of Philosophy

Department of Physics and Physical Oceanography  
Memorial University of Newfoundland  
St. John's, Newfoundland, Canada.

© July 2010 by Muzaddid Sarker

# Abstract

Lung surfactant is a complex mixture of lipids and proteins that enables normal breathing by reducing the surface tension at the alveolar air-water interface, and additionally provides the first line of defense against inhaled microbes in the lungs. Surfactant protein B (SP-B) is an indispensable component of lung surfactant system and absolutely essential for the survival of mammals. SP-B is thought to function by facilitating large-scale rearrangements of lipid structures at various stages of the breathing cycle. However, neither the structural mechanisms for this ability nor the physiological ramifications of the lipid rearrangements are yet understood, in part because a high-resolution structure of SP-B has not been determined. As is generally the case for membrane and other lipid-associated hydrophobic proteins, the production of an SP-B sample for structural studies has been very challenging and unsuccessful to date. Interestingly, synthetic fragments of SP-B retain substantial biological activity when compared to the full-length protein. This Ph.D. research has applied solution nuclear magnetic resonance (NMR) methods to three SP-B-based peptides to reveal at least some of the critical structural features and lipid/protein interactions that presumably underlie the functional mechanisms of SP-B in physiological conditions.

The high-resolution structure of Mini-B, an N-terminal – C-terminal construct of SP-B that exhibits even better performance than the full-length protein in rat models, is determined in the presence of surfactant lipid-mimetic sodiumdodecylsulfate (SDS) micelles. Mini-B consists of two  $\alpha$ -helices with a projecting tryptophan anchor and displays a strikingly amphipathic surface. The structure of Mini-B appears very well-suited for making strong interactions with surfactant phospholipid analogues. Indeed, Mini-B binds both anionic and zwitterionic micelles composed of SDS, dodecylphosphocholine (DPC), lysomyristoylphosphatidylcholine (LMPC), lysomyristoylphosphatidylglycerol (LMPG) and mixed LMPC/LMPG, and induces substantial rearrangements of the micelle structures. To prepare a foundation for directly probing the interaction between Mini-B and surfactant protein A (SP-A), the conformation and lipid interactions of SP-A are investigated separately in the presence of micelles composed from the same model surfactant lipids. SP-A also binds

both zwitterionic and anionic micelles. Surprisingly, in the presence of micelles, SP-A exists predominantly as smaller oligomers, in sharp contrast to the octadecamers observed when in an aqueous environment, and the form in which SP-A has long been presumed to function. Mini-B appears to interact with SP-A in all micelle systems, although the interaction is indirect and the degree of the interaction is dependent on the type of detergent/lipid headgroup. Next investigated are the changes to SP-B's structure and lipid interactions brought about by tryptophan oxidation, a modification which is thought to be a major contributor to acute respiratory distress syndrome (ARDS). Replacement of tryptophan by one of its oxidized forms, kynurenine, substantially disrupts the helical structure of SP-B<sub>8-25</sub>, an N-terminal fragment of SP-B, and also affects its interactions with the micelles. Lastly, as a step towards the determination of the structure of full-length SP-B, the overall conformation of Maxi-B<sub>CT</sub>, the C-terminal half of SP-B, has been investigated in the organic solvent hexafluoroisopropanol (HFIP) and SDS micelles.

SP-B is indispensable for life, but the molecular basis for its activity is not yet understood. The findings of this Ph.D. research contribute to the ongoing endeavor in characterizing SP-B's structure-function relationships and its mechanisms of lipid/protein interactions that are crucial for lung surfactant function. This work also provides a strong foundation for future studies on the conformation and interactions of full-length SP-B.

# Acknowledgements

## Dr. Valerie Booth

Dr. Michael R. Morrow

Dr. Kaushik Nag

Dr. Alan J. Waring

Donna Jackman

Jennifer Rendell

June Stewart

Dr. Jolanta Lagowski

Mark McDonald

Raymond Bishop

Dr. Kevin M.W. Keough

Dr. David H. Heeley

Dr. Anand Yethiraj

Dr. Michael Hayley

Dr. Tsan-Chin Yang

Dr. Sarah Bourbigot

Dr. Celine Schneider

Suliman Barhoum

Swomitra Palit

Booth Lab

Department of Physics and Physical Oceanography

Department of Biochemistry

CREAIT Network (C-CART)

School of Graduate Studies

Office of the Dean of Science

& Graduate Students' Union

of

Memorial University of Newfoundland (MUN)

Canadian Institutes of Health Research (CIHR)

& National Institutes of Health (NIH)

# Contents

<b>Abstract</b> .....	ii
<b>Acknowledgements</b> .....	iv
<b>List of Tables</b> .....	viii
<b>List of Figures</b> .....	ix
<b>List of Abbreviations</b> .....	xiii
<b>Chapter 1 : Introduction</b> .....	1
1.1 Respiratory System and Lung Surfactant .....	2
1.2 Synthesis and Composition of Lung Surfactant .....	4
1.3 Lung Surfactant Activity, Disorder and Treatment .....	6
1.4 Roles of Surfactant Lipids .....	8
1.5 Roles of Surfactant Proteins .....	10
1.6 Properties and Function of SP-B .....	13
1.7 Activities and Structures of SP-B Fragments .....	16
1.8 Outline and Objectives of Present Work .....	18
<b>Chapter 2 : Protein NMR Methods</b> .....	20
2.1 Protein Structure .....	21
2.2 Methods for Protein Structure Determination .....	23
2.3 Basic Principles of NMR .....	24
2.4 Basic NMR Parameters .....	28
2.4.1 Relaxation Times ( $T_1$ and $T_2$ ) .....	28
2.4.2 Chemical Shift ( $\delta$ ) .....	30
2.4.3 Linewidth ( $\Delta\nu_{1/2}$ ) .....	31
2.4.4 Scalar Coupling ( $J$ ) .....	32
2.4.5 Nuclear Overhauser Effect (NOE) .....	33
2.5 Protein NMR Experiments .....	33
2.6 Protein Structure Calculation .....	39
2.7 Strategies for Studying SP-B Peptides .....	40
<b>Chapter 3 : Structure of Mini-B, an N-Terminal – C-Terminal Construct of SP-B,     in Detergent Micelles</b> .....	43
3.1 Overview .....	44
3.2 Materials and Methods .....	46
3.2.1 Peptide Synthesis and Purification .....	46
3.2.2 Sample Preparation .....	47
3.2.3 NMR Data Collection .....	47
3.2.4 Data Processing and Structure Calculation .....	48
3.3 Results .....	49
3.4 Discussion .....	54

<b>Chapter 4 : Mini-B in Model Surfactant Lipids: Conformations and Interactions .....</b>	<b>60</b>
4.1 Overview .....	61
4.2 Materials and Methods .....	63
4.2.1 Peptide Synthesis and Purification .....	63
4.2.2 Sample Preparation .....	63
4.2.3 NMR Data Collection and Processing .....	64
4.3 Results .....	65
4.3.1 Mini-B in SDS Micelles .....	65
4.3.2 Mini-B in DPC Micelles .....	70
4.3.3 Mini-B in LMPC Micelles .....	74
4.3.4 Mini-B in LMPG Micelles .....	78
4.3.5 Mini-B in Mixed LMPC/LMPG Micelles .....	82
4.4 Discussion .....	86
<b>Chapter 5 : SP-A in Model Surfactant Lipids: Conformations and Interactions .....</b>	<b>93</b>
5.1 Overview .....	94
5.2 Materials and Methods .....	95
5.2.1 Protein Isolation and Purification .....	95
5.2.2 Sample Preparation .....	96
5.2.3 NMR Data Collection and Processing .....	97
5.3 Results .....	98
5.3.1 SP-A alone in Aqueous Solution .....	98
5.3.2 SP-A in SDS Micelles .....	101
5.3.3 SP-A in DPC Micelles .....	104
5.3.4 SP-A in LMPC Micelles .....	107
5.3.5 SP-A in LMPG Micelles .....	110
5.3.6 SP-A in Mixed LMPC/LMPG Micelles .....	113
5.4 Discussion .....	116
<b>Chapter 6 : Interaction between Mini-B and SP-A in Model Surfactant Lipids .....</b>	<b>125</b>
6.1 Overview .....	126
6.2 Materials and Methods .....	127
6.2.1 Protein Preparation .....	127
6.2.2 Sample Preparation .....	127
6.2.3 NMR Data Collection and Processing .....	128
6.3 Results .....	129
6.3.1 Mini-B and SP-A in SDS Micelles .....	129
6.3.2 Mini-B and SP-A in DPC Micelles .....	137
6.3.3 Mini-B and SP-A in LMPC Micelles .....	145
6.3.4 Mini-B and SP-A in LMPG Micelles .....	150
6.3.5 Mini-B and SP-A in Mixed LMPC/LMPG Micelles .....	155
6.4 Discussion .....	160

<b>Chapter 7 : Modifications to SP-B<sub>8-25</sub> Structure and Lipid Interactions upon Tryptophan Oxidation</b> .....	166
7.1 Overview .....	167
7.2 Materials and Methods .....	168
7.2.1 Peptide Synthesis and Purification .....	168
7.2.2 Sample Preparation .....	169
7.2.3 NMR Data Collection and Processing .....	169
7.2.4 CD Data Collection and Processing .....	171
7.3 Results .....	172
7.3.1 NMR Spectra of SP-B <sub>8-25</sub> in SDS .....	172
7.3.2 CD Spectra of SP-B <sub>8-25</sub> in SDS .....	176
7.3.3 NMR Spectra of SP-B <sub>8-25</sub> in DPC .....	177
7.3.4 CD Spectra of SP-B <sub>8-25</sub> in DPC .....	181
7.3.5 NMR Spectra of SP-B <sub>8-25</sub> in HFIP (40%) .....	182
7.3.6 CD Spectra of SP-B <sub>8-25</sub> in HFIP (40%) .....	185
7.3.7 NMR Spectra of SP-B <sub>8-25</sub> in Water .....	186
7.3.8 CD Spectra of SP-B <sub>8-25</sub> in Water .....	189
7.4 Discussion .....	190
<b>Chapter 8 : Conformation of Maxi-B<sub>CT</sub>, the C-Terminal Half of SP-B</b> .....	196
8.1 Overview .....	197
8.2 Materials and Methods .....	198
8.2.1 Peptide Synthesis and Purification .....	198
8.2.2 Sample Preparation .....	199
8.2.3 NMR Data Collection and Processing .....	199
8.2.4 CD Data Collection and Processing .....	200
8.3 Results .....	201
8.3.1 NMR Spectra of Maxi-B <sub>CT</sub> in HFIP (40%) .....	201
8.3.2 NMR Spectra of Maxi-B <sub>CT</sub> in SDS .....	205
8.3.3 CD Spectra of Maxi-B <sub>CT</sub> in HFIP (40%) and SDS .....	209
8.4 Discussion .....	210
<b>Chapter 9 : Conclusion</b> .....	214
9.1 Summary and Remarks .....	215
9.2 Future Work .....	218
<b>References</b> .....	221

## List of Tables

<b>Table 1.1 :</b> The composition of adult human lung surfactant .....	6
<b>Table 1.2 :</b> Amino acid sequence of human surfactant protein B .....	13
<b>Table 1.3 :</b> Amino acid sequence of Saposin family proteins .....	15
<b>Table 2.1 :</b> Properties of nuclei commonly used in bio-NMR .....	27
<b>Table 3.1 :</b> Mini-B Structural Restraints .....	48
<b>Table 5.1 :</b> Estimates of rotational correlation times, proton linewidths and relative signal intensities for SP-A oligomers at 37 °C .....	119
<b>Table 5.2 :</b> Molecular masses of SP-A species, calculated using the experimentally determined translational diffusion coefficients, and their matching oligomeric states .....	121
<b>Table 6.1 :</b> Translational diffusion coefficients and the corresponding hydrodynamic diameters of pure SDS micelles and protein/SDS complexes .....	136
<b>Table 6.2 :</b> Translational diffusion coefficients and the corresponding hydrodynamic diameters of pure DPC micelles and protein/DPC complexes .....	144
<b>Table 6.3 :</b> Translational diffusion coefficients and the corresponding hydrodynamic diameters of pure LMPC micelles and protein/LMPC complexes .....	149
<b>Table 6.4 :</b> Translational diffusion coefficients and the corresponding hydrodynamic diameters of pure LMPG micelles and protein/LMPG complexes .....	154
<b>Table 6.5 :</b> Translational diffusion coefficients and the corresponding hydrodynamic diameters of pure LMPC/LMPG micelles and protein/LMPC/LMPG complexes .....	159

## List of Figures

<b>Figure 1.1 :</b>	A schematic representation of the human respiratory system .....	3
<b>Figure 1.2 :</b>	A model for the life cycle of lung surfactant .....	5
<b>Figure 1.3 :</b>	Chemical structures of major lung surfactant lipids .....	9
<b>Figure 1.4 :</b>	Structural models for lung surfactant proteins .....	12
<b>Figure 1.5 :</b>	Topology of SP-B predicted based on the known structures of Saposin family proteins .....	15
<b>Figure 1.6 :</b>	Respiratory function related responses from rats subjected to removal of lung surfactant by <i>in vivo</i> lavage and then exogenously administered with synthetic surfactants .....	17
<b>Figure 1.7 :</b>	Ensembles of the high-resolution structures of the terminal fragments of SP-B determined by solution NMR .....	18
<b>Figure 2.1 :</b>	Chemical structure of a protein .....	21
<b>Figure 2.2 :</b>	Four levels of protein structure, from primary to quaternary .....	22
<b>Figure 2.3 :</b>	Energy levels of a spin 1/2 nucleus in an external magnetic field .....	25
<b>Figure 2.4 :</b>	Steps of a simple one-pulse 1D NMR experiment .....	28
<b>Figure 2.5 :</b>	Basic NMR spectral parameters .....	31
<b>Figure 2.6 :</b>	Schematic representation of the 1D $^1\text{H}$ NMR spectrum of a protein .....	34
<b>Figure 2.7 :</b>	Schematic representation of the 2D $^{15}\text{N}$ - $^1\text{H}$ HSQC spectra of a protein .....	35
<b>Figure 2.8 :</b>	Schematic representations of the 2D homonuclear TOCSY and NOESY spectra of a protein .....	36
<b>Figure 2.9 :</b>	Translational diffusion coefficient obtained from the DOSY data .....	38
<b>Figure 2.10 :</b>	Schematic representation of a micelle-protein complex .....	41
<b>Figure 2.11 :</b>	Chemical structures of the single acyl chain analogs of the most abundant lung surfactant phospholipids and the organic solvent HFIP .....	42
<b>Figure 3.1 :</b>	Topology of SP-B and Mini-B predicted on the basis of the known structures of other Saposin proteins .....	45
<b>Figure 3.2 :</b>	2D $^{15}\text{N}$ - $^1\text{H}$ HSQC spectra of Mini-B in SDS at different concentrations .....	50
<b>Figure 3.3 :</b>	Portions of 2D $^1\text{H}$ - $^1\text{H}$ NOESY spectra of Mini-B in SDS micelles .....	51
<b>Figure 3.4 :</b>	Secondary structure indicators for Mini-B in SDS micelles .....	52
<b>Figure 3.5 :</b>	High resolution structure of Mini-B in SDS micelles .....	53
<b>Figure 3.6 :</b>	Electrostatic potential surface of Mini-B and the corresponding segments of NK-lysin and Saposin C .....	56
<b>Figure 3.7 :</b>	Overlay of the backbone structures of Mini-B and other Saposin family proteins .....	58

<b>Figure 4.1 :</b>	Chemical structures of the micelle-forming detergent mimetics and phospholipid analogues of DPPC and POPG .....	62
<b>Figure 4.2 :</b>	1D $^1\text{H}$ spectra of Mini-B <sub>OX</sub> and Mini-B <sub>RED</sub> in SDS .....	67
<b>Figure 4.3 :</b>	2D $^{15}\text{N}$ - $^1\text{H}$ HSQC spectra of Mini-B <sub>OX</sub> and Mini-B <sub>RED</sub> in SDS .....	68
<b>Figure 4.4 :</b>	SDS micelles and Mini-B <sub>OX</sub> /SDS complex sizes as indicated by translational diffusion .....	69
<b>Figure 4.5 :</b>	1D $^1\text{H}$ spectra of Mini-B <sub>OX</sub> and Mini-B <sub>RED</sub> in DPC .....	71
<b>Figure 4.6 :</b>	2D $^{15}\text{N}$ - $^1\text{H}$ HSQC spectra of Mini-B <sub>OX</sub> and Mini-B <sub>RED</sub> in DPC .....	72
<b>Figure 4.7 :</b>	DPC micelles and Mini-B <sub>OX</sub> /DPC complex sizes as indicated by translational diffusion .....	73
<b>Figure 4.8 :</b>	1D $^1\text{H}$ spectra of Mini-B <sub>OX</sub> in LMPC .....	75
<b>Figure 4.9 :</b>	2D $^{15}\text{N}$ - $^1\text{H}$ HSQC spectra of Mini-B <sub>OX</sub> in LMPC .....	76
<b>Figure 4.10 :</b>	LMPC micelles and Mini-B <sub>OX</sub> /LMPC complex sizes as indicated by translational diffusion .....	77
<b>Figure 4.11 :</b>	1D $^1\text{H}$ spectra of Mini-B <sub>OX</sub> in LMPG .....	79
<b>Figure 4.12 :</b>	2D $^{15}\text{N}$ - $^1\text{H}$ HSQC spectra of Mini-B <sub>OX</sub> in LMPG .....	80
<b>Figure 4.13 :</b>	LMPG micelles and Mini-B <sub>OX</sub> /LMPG complex sizes as indicated by translational diffusion .....	81
<b>Figure 4.14 :</b>	1D $^1\text{H}$ spectra of Mini-B <sub>OX</sub> in LMPC/LMPG .....	83
<b>Figure 4.15 :</b>	2D $^{15}\text{N}$ - $^1\text{H}$ HSQC spectra of Mini-B <sub>OX</sub> in LMPC/LMPG .....	84
<b>Figure 4.16 :</b>	LMPC/LMPG mixed micelles and Mini-B <sub>OX</sub> /LMPC/LMPG complex sizes as indicated by translational diffusion .....	85
<b>Figure 5.1 :</b>	A model of SP-A monomer, trimer and octadecamer .....	94
<b>Figure 5.2 :</b>	1D $^1\text{H}$ spectrum of SP-A in 90% H <sub>2</sub> O and 10% D <sub>2</sub> O .....	99
<b>Figure 5.3 :</b>	Size of SP-A as indicated by translational diffusion .....	100
<b>Figure 5.4 :</b>	1D $^1\text{H}$ spectra of SP-A alone and SP-A in SDS .....	102
<b>Figure 5.5 :</b>	SDS micelles and SP-A/SDS complex sizes as indicated by translational diffusion .....	103
<b>Figure 5.6 :</b>	1D $^1\text{H}$ spectra of SP-A in DPC .....	105
<b>Figure 5.7 :</b>	DPC micelles and SP-A/DPC complex sizes as indicated by translational diffusion .....	106
<b>Figure 5.8 :</b>	1D $^1\text{H}$ spectra of SP-A in LMPC .....	108
<b>Figure 5.9 :</b>	LMPC micelles and SP-A/LMPC complex sizes as indicated by translational diffusion .....	109
<b>Figure 5.10 :</b>	1D $^1\text{H}$ spectra of SP-A in LMPG .....	111
<b>Figure 5.11 :</b>	LMPG micelles and SP-A/LMPG complex sizes as indicated by translational diffusion .....	112
<b>Figure 5.12 :</b>	1D $^1\text{H}$ spectra of SP-A in LMPC/LMPG .....	114

<b>Figure 5.13 :</b>	LMPC/LMPG mixed micelles and SP-A/LMPC/LMPG complex sizes as indicated by translational diffusion .....	115
<b>Figure 5.14 :</b>	Overlay of the HN (6-9 ppm) regions of 1D <sup>1</sup> H spectra of SP-A in different environments .....	120
<b>Figure 6.1 :</b>	1D <sup>1</sup> H spectra of Mini-B <sub>OX</sub> , SP-A and Mini-B <sub>OX</sub> + SP-A in SDS .....	131
<b>Figure 6.2 :</b>	1D <sup>1</sup> H spectra of Mini-B <sub>RED</sub> , SP-A and Mini-B <sub>RED</sub> + SP-A in SDS .....	132
<b>Figure 6.3 :</b>	2D <sup>15</sup> N- <sup>1</sup> H HSQC spectra of Mini-B <sub>OX</sub> and Mini-B <sub>OX</sub> + SP-A in SDS .....	133
<b>Figure 6.4 :</b>	2D <sup>15</sup> N- <sup>1</sup> H HSQC spectra of Mini-B <sub>RED</sub> and Mini-B <sub>RED</sub> + SP-A in SDS ...	134
<b>Figure 6.5 :</b>	Translational diffusion measurements of Mini-B <sub>OX</sub> and SP-A in SDS .....	135
<b>Figure 6.6 :</b>	Bar graphs representing the apparent hydrodynamic diameters of pure SDS micelles and protein/SDS complexes .....	136
<b>Figure 6.7 :</b>	1D <sup>1</sup> H spectra of Mini-B <sub>OX</sub> , SP-A and Mini-B <sub>OX</sub> + SP-A in DPC .....	139
<b>Figure 6.8 :</b>	1D <sup>1</sup> H spectra of Mini-B <sub>RED</sub> , SP-A and Mini-B <sub>RED</sub> + SP-A in DPC .....	140
<b>Figure 6.9 :</b>	2D <sup>15</sup> N- <sup>1</sup> H HSQC spectra of Mini-B <sub>OX</sub> and Mini-B <sub>OX</sub> + SP-A in DPC .....	141
<b>Figure 6.10 :</b>	2D <sup>15</sup> N- <sup>1</sup> H HSQC spectra of Mini-B <sub>RED</sub> and Mini-B <sub>RED</sub> + SP-A in DPC ...	142
<b>Figure 6.11 :</b>	Translational diffusion measurements of Mini-B <sub>OX</sub> and SP-A in DPC .....	143
<b>Figure 6.12 :</b>	Bar graphs representing the apparent hydrodynamic diameters of pure DPC micelles and protein/DPC complexes .....	144
<b>Figure 6.13 :</b>	1D <sup>1</sup> H spectra of Mini-B <sub>OX</sub> , SP-A and Mini-B <sub>OX</sub> + SP-A in LMPC .....	146
<b>Figure 6.14 :</b>	2D <sup>15</sup> N- <sup>1</sup> H HSQC spectra of Mini-B <sub>OX</sub> and Mini-B <sub>OX</sub> + SP-A in LMPC ...	147
<b>Figure 6.15 :</b>	Translational diffusion measurements of Mini-B <sub>OX</sub> and SP-A in LMPC ...	148
<b>Figure 6.16 :</b>	Bar graphs representing the apparent hydrodynamic diameters of pure LMPC micelles and protein/LMPC complexes .....	149
<b>Figure 6.17 :</b>	1D <sup>1</sup> H spectra of Mini-B <sub>OX</sub> , SP-A and Mini-B <sub>OX</sub> + SP-A in LMPG .....	151
<b>Figure 6.18 :</b>	2D <sup>15</sup> N- <sup>1</sup> H HSQC spectra of Mini-B <sub>OX</sub> and Mini-B <sub>OX</sub> + SP-A in LMPG ...	152
<b>Figure 6.19 :</b>	Translational diffusion measurements of Mini-B <sub>OX</sub> and SP-A in LMPG ...	153
<b>Figure 6.20 :</b>	Bar graphs representing the apparent hydrodynamic diameters of pure LMPG micelles and protein/LMPG complexes .....	154
<b>Figure 6.21 :</b>	1D <sup>1</sup> H spectra of Mini-B <sub>OX</sub> , SP-A and Mini-B <sub>OX</sub> + SP-A in LMPC/LMPG .....	156
<b>Figure 6.22 :</b>	2D <sup>15</sup> N- <sup>1</sup> H HSQC spectra of Mini-B <sub>OX</sub> and Mini-B <sub>OX</sub> + SP-A in LMPC/LMPG .....	157
<b>Figure 6.23 :</b>	Translational diffusion measurements of Mini-B <sub>OX</sub> and SP-A in LMPC/LMPG .....	158
<b>Figure 6.24 :</b>	Bar graphs representing the apparent hydrodynamic diameters of pure LMPC/LMPG micelles and protein/LMPC/LMPG complexes .....	159
<b>Figure 7.1 :</b>	Chemical structures of tryptophan and kynurenine .....	168
<b>Figure 7.2 :</b>	1D <sup>1</sup> H spectra of SP-B <sub>8-25</sub> (Wild-Type) and SP-B <sub>8-25</sub> (Trp9Kyn) in SDS ...	173

<b>Figure 7.3 :</b>	HN-HN regions of 2D $^1\text{H}$ - $^1\text{H}$ NOESY spectra of SP-B <sub>8-25</sub> (Wild-Type) and SP-B <sub>8-25</sub> (Trp9Kyn) in SDS .....	174
<b>Figure 7.4 :</b>	SP-B <sub>8-25</sub> /SDS complex sizes as indicated by translational diffusion .....	175
<b>Figure 7.5 :</b>	Far-UV CD spectra of SP-B <sub>8-25</sub> (Wild-Type) and SP-B <sub>8-25</sub> (Trp9Kyn) in SDS .....	176
<b>Figure 7.6 :</b>	1D $^1\text{H}$ spectra of SP-B <sub>8-25</sub> (Wild-Type) and SP-B <sub>8-25</sub> (Trp9Kyn) in DPC ...	178
<b>Figure 7.7 :</b>	HN-HN regions of 2D $^1\text{H}$ - $^1\text{H}$ NOESY spectra of SP-B <sub>8-25</sub> (Wild-Type) and 1 mM SP-B <sub>8-25</sub> (Trp9Kyn) in DPC .....	179
<b>Figure 7.8 :</b>	SP-B <sub>8-25</sub> /DPC complex sizes as indicated by translational diffusion .....	180
<b>Figure 7.9 :</b>	Far-UV CD spectra of SP-B <sub>8-25</sub> (Wild-Type) and SP-B <sub>8-25</sub> (Trp9Kyn) in DPC .....	181
<b>Figure 7.10 :</b>	1D $^1\text{H}$ spectra of SP-B <sub>8-25</sub> (Wild-Type) and SP-B <sub>8-25</sub> (Trp9Kyn) in 40% HFIP (plus 50% H <sub>2</sub> O and 10% D <sub>2</sub> O) .....	183
<b>Figure 7.11 :</b>	HN-HN regions of 2D $^1\text{H}$ - $^1\text{H}$ NOESY spectra of SP-B <sub>8-25</sub> (Wild-Type) and SP-B <sub>8-25</sub> (Trp9Kyn) in 40% HFIP (plus 50% H <sub>2</sub> O and 10% D <sub>2</sub> O) .....	184
<b>Figure 7.12 :</b>	Far-UV CD spectra of SP-B <sub>8-25</sub> (Wild-Type) and SP-B <sub>8-25</sub> (Trp9Kyn) in 40% HFIP (plus 50% H <sub>2</sub> O and 10% D <sub>2</sub> O) .....	185
<b>Figure 7.13 :</b>	1D $^1\text{H}$ spectra of SP-B <sub>8-25</sub> (Wild-Type) and SP-B <sub>8-25</sub> (Trp9Kyn) in water (90% H <sub>2</sub> O and 10% D <sub>2</sub> O) .....	187
<b>Figure 7.14 :</b>	HN-HN regions of 2D $^1\text{H}$ - $^1\text{H}$ NOESY spectra of SP-B <sub>8-25</sub> (Wild-Type) and SP-B <sub>8-25</sub> (Trp9Kyn) in water (90% H <sub>2</sub> O and 10% D <sub>2</sub> O) .....	188
<b>Figure 7.15 :</b>	Far-UV CD spectra of SP-B <sub>8-25</sub> (Wild-Type) and SP-B <sub>8-25</sub> (Trp9Kyn) in water (90% H <sub>2</sub> O and 10% D <sub>2</sub> O) .....	189
<b>Figure 7.16 :</b>	Topology and structure of SP-B <sub>8-25</sub> (Wild-Type) based on the structure of Mini-B in SDS .....	191
<b>Figure 8.1 :</b>	Topology of SP-B, Maxi-B, truncated Maxi-B (Maxi-B <sub>TR</sub> ) and Maxi-B <sub>CT</sub> , based on known Saposin protein structures .....	197
<b>Figure 8.2 :</b>	1D $^1\text{H}$ spectra of Maxi-B <sub>CT</sub> and Mini-B <sub>RED</sub> in 40% HFIP (plus 50% H <sub>2</sub> O and 10% D <sub>2</sub> O) .....	203
<b>Figure 8.3 :</b>	HA-HN regions of 2D $^1\text{H}$ - $^1\text{H}$ TOCSY spectra of Maxi-B <sub>CT</sub> and Mini-B <sub>RED</sub> in 40% HFIP .....	204
<b>Figure 8.4 :</b>	HN-HN regions of 2D $^1\text{H}$ - $^1\text{H}$ NOESY spectra of Maxi-B <sub>CT</sub> and Mini-B <sub>RED</sub> in 40% HFIP .....	204
<b>Figure 8.5 :</b>	1D $^1\text{H}$ spectra of Maxi-B <sub>CT</sub> and Mini-B <sub>OX</sub> in SDS .....	207
<b>Figure 8.6 :</b>	HA-HN regions of 2D $^1\text{H}$ - $^1\text{H}$ TOCSY spectra of Maxi-B <sub>CT</sub> and Mini-B <sub>OX</sub> in SDS .....	208
<b>Figure 8.7 :</b>	HN-HN regions of 2D $^1\text{H}$ - $^1\text{H}$ NOESY spectra of Maxi-B <sub>CT</sub> and Mini-B <sub>OX</sub> in SDS .....	208
<b>Figure 8.8 :</b>	Far-UV CD spectra of Maxi-B <sub>CT</sub> in 40% HFIP and in SDS .....	209

## List of Abbreviations

ALI	: acute lung injury
ARDS	: acute respiratory distress syndrome
CD	: circular dichroism
CMC	: critical micelle concentration
CRD	: carbohydrate recognition domain
CSI	: chemical shift index
DOSY	: diffusion-ordered spectroscopy
DOPC	: dioleoylphosphatidylcholine
DPC	: dodecylphosphocholine
DPPC	: dipalmitoylphosphatidylcholine
DSS	: sodium 2,2-dimethyl-2-silapentane-5-sulfonate
FID	: free induction decay
FTIR	: Fourier transform infrared
HFIP	: hexafluoroisopropanol
HPLC	: high performance liquid chromatography
HSQC	: heteronuclear single quantum correlation
LB	: lamellar bodies
LMPC	: lysomyristoylphosphatidylcholine
LMPG	: lysomyristoylphosphatidylglycerol
LS	: lung surfactant
MALDI-TOF	: matrix-assisted laser desorption/ionization - time-of-flight
MD	: molecular dynamics
NMR	: nuclear magnetic resonance
NOE	: nuclear Overhauser effect (or enhancement)
NOESY	: nuclear Overhauser effect spectroscopy
NRDS	: neonatal respiratory distress syndrome
PAGE	: polyacrylamide gel electrophoresis
PC	: phosphatidylcholine

PE	: phosphatidylethanolamine
PFG	: pulsed field gradient
PI	: phosphatidylinositol
PG	: phosphatidylglycerol
POPC	: palmitoyloleoylphosphatidylcholine
POPE	: palmitoyloleoylphosphatidylethanolamine
POPG	: palmitoyloleoylphosphatidylglycerol
POPS	: palmitoyloleoylphosphatidylserine
ppm	: parts per million
PS	: phosphatidylserine
RF	: radiofrequency
SDS	: sodiumdodecylsulfate
SM	: sphingomyelin
S/N	: signal to noise
SP-A	: surfactant protein A
SP-B	: surfactant protein B
SP-C	: surfactant protein C
SP-D	: surfactant protein D
TM	: tubular myelin
TMS	: tetramethylsilane
TOCSY	: total correlation spectroscopy
RDS	: respiratory distress syndrome
Re-LPS	: rough lipopolysaccharide
ROS	: reactive oxygen species
TEM	: transmission electron microscopy

*Chapter 1*

**Introduction**

## 1.1 Respiratory System and Lung Surfactant

It is essential for almost all multicellular living organisms to inhale oxygen from the external environment in order to perform various physiological functions and to exhale carbon dioxide produced in the internal metabolic reactions from the body. For humans and all air-breathing vertebrates, the blood transports both of these gases and the exchange takes place in the lungs. This lung function is accomplished through airways ending in tiny air sacs known as alveoli (Figure 1.1). Adult human lungs contain approximately 2400 km of airways and 300 to 500 million alveoli, covering a total surface area of about 70 m<sup>2</sup> [1]. In the lungs, the air-filled alveoli are surrounded by blood-filled capillaries and the barrier in between is extremely thin. Molecules of oxygen and carbon dioxide are passively exchanged by diffusion between the air and the blood. Because of an incessant direct exposure to the external gaseous environment, the inner surface of the alveoli is coated by an approximately 0.2 μm thick water layer to prevent it from dehydration [2]. As a result, a surface tension is created at the air-water interface since the forces of attraction between water molecules are stronger than the forces between water and air.

The water-coated alveoli are roughly spherical in shape. The alveoli, and thereby the lung as a whole, inflate and deflate cyclically with inhalation and exhalation. Maintaining the alveolar structure throughout the cyclical changes in the lung volume is critical for normal respiration. The surface tension created at the air-water interface is largely governed by LaPlace's equation that relates the fluid pressure  $P$  inside a spherical vessel of radius  $R$  with the surface tension  $T$ ,

$$T = RP/2. \quad 1.1$$

Pure water has a surface tension of about 70 mN/m. Such a surface tension, unless countered, would promote lung collapse and increase the work required to re-inflate the lung at the end of an expiration [3]. However, the surface tension is indeed countered by a material called lung surfactant (also known as pulmonary surfactant) which enables normal breathing. Lung surfactant is a mixture of lipids and proteins that lines the air-water interface in alveoli. When lung surfactant is at thermodynamic equilibrium between the outer or water surface covering

monolayer and a bulk phase inside water, it decreases the surface tension to about 25 mN/m [4]. However, when the monolayer is compressed laterally, as at the end of expiration, it reduces the surface tension to near 0 mN/m [4]. This function of lung surfactant, termed “surface activity”, successfully prevents alveolar collapse during exhalation and also eases the work of breathing during subsequent inhalation.

In addition to reducing the surface tension and thereby enabling normal breathing, lung surfactant also provides the first line of defense and the innate immune response against inhaled pathogens, toxins and allergens [5]. This function of lung surfactant is also crucial since the respiratory system is continually exposed to toxic substances and infectious agents due to its direct contact with the external environment.

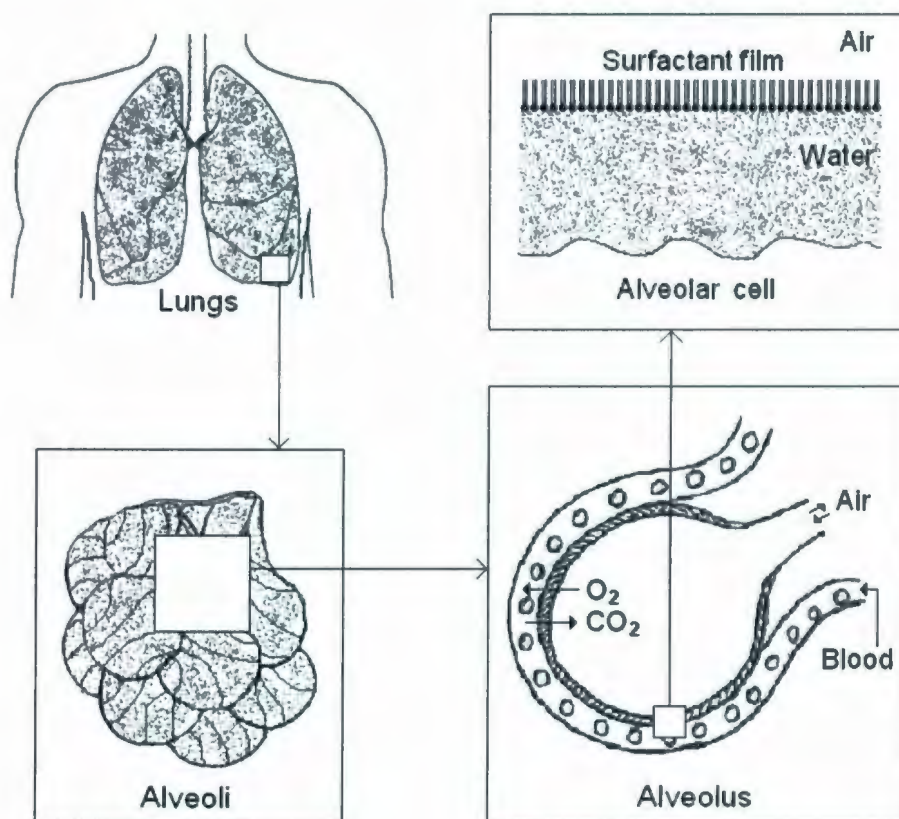


**Figure 1.1** : A schematic representation of the human respiratory system. The lungs are composed of millions of alveoli where the  $O_2/CO_2$  exchange takes place. The inner surface of the alveoli is coated by a water layer. Lung surfactant, a lipid-protein lining at the air-water interface, reduces the surface tension and enables normal breathing.

The initial discovery of lung surfactant was made by von Neergaard in the late 1920s [6]. However, the significance of his discovery was not understood at that time. In the mid 1950s, the observation of surfactant's ability to reduce the surface tension led to its rediscovery by Pattle [7] and Clements [8]. Since then, extensive research has been performed to unveil the molecular mechanisms that underlie its essential physiological functions. Although important advancements have been made over past decades, a complete structural description of the components and their interactions during the respiratory dynamics are still unavailable.

## **1.2 Synthesis and Composition of Lung Surfactant**

Lung surfactant is synthesized and secreted into the alveolar fluid by one of the two boundary-forming cells of the alveoli, known as Type II pneumocytes (Figure 1.2) [9]. These cells are cuboidal in shape and contain specialized secretory intermediaries known as the lamellar bodies (LB) [10]. LB is actually a storage form of the surfactant. It consists of a core composed of multilamellar membranes surrounded by another membrane [11]. Its secretion occurs in response to local biochemical factors [12], signals from the autonomic nervous system [13] and deep breathing [14] or stretch [15]. After reaching the extracellular aqueous environment, the LB contents become hydrated and can unravel into a highly ordered array of tubules with nearly rectangular cross section known as the tubular myelin (TM) [16]. The sidewalls of the TM are thought to be constructed from bilayers of surfactant phospholipids and their characteristic crosshatched structures are probably maintained through interactions with surfactant proteins [17]. Some models for surfactant formation suggest TM as the immediate precursor from which the surfactant components are released and finally form a surface active film at the alveolar air-water interface that is responsible for surface tension reduction [18, 19]. Electron microscopic images and surface activity studies suggest that the surface active film consists of multiple layers of phospholipids closely packed by the proteins [20, 21]. These multilayered structures act as a surface-associated reservoir of surfactant material and remain attached to the interface although the constituents are probably interchanged and recycled [22]. The final coating at the edge of the surface film, however, is

likely in the form of a lipid monolayer with the headgroups in contact with water and other polar molecules and the hydrocarbon acyl chains exposed into the air [22].

The composition of lung surfactant varies among different vertebrates and also throughout the physiological development of a particular species [23]. For adult humans, and most mammals, phospholipids make up the bulk of surfactant materials (~ 80% by weight), with the remaining being neutral lipids (~ 10% by weight) and proteins (~ 10%, by weight) [24]. Table 1.1 lists the components of adult human lung surfactant with percentages by weight [23-25].

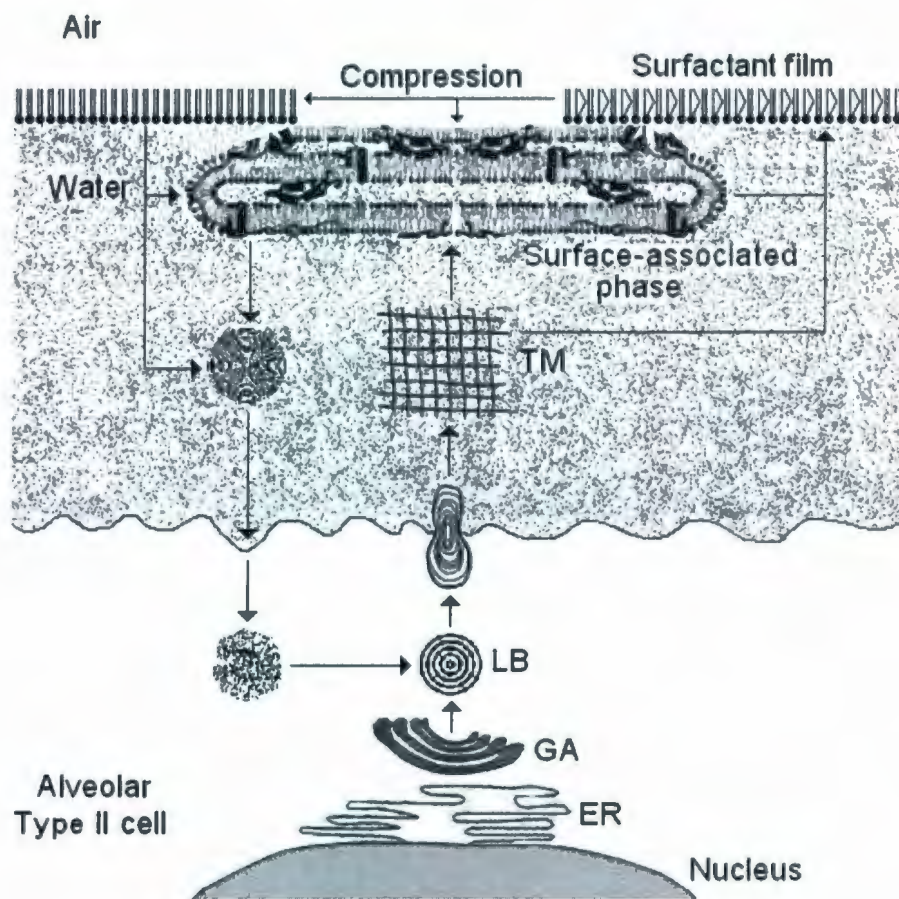


**Figure 1.2** : A model for the life cycle of lung surfactant [19, 22]. After being synthesized in the endoplasmic reticulum (ER), surfactant materials are transported to the golgi apparatus (GA) and then packed into the lamellar bodies (LB). The LB, being secreted then into the water layer, swells and unravels to form the tubular myelin (TM). From the TM, lipids and proteins are released to form the surface active film at the air-water interface.

**Table 1.1 :** The composition of adult human lung surfactant [23-25].

Category	Components with Percentages by Weight
Phospholipids (~ 80%)	<ol style="list-style-type: none"><li>1. Phosphatidylcholine (PC) ~ 70% ~ 35% dipalmitoylphosphatidylcholine (DPPC), ~ 15% other disaturated species, and ~ 20% unsaturated forms</li><li>2. Phosphatidylglycerol (PG) ~ 9%</li><li>3. Minor amount of Phosphatidylinositol (PI)</li><li>4. Minor amount of Phosphatidylethanolamine (PE)</li><li>5. Minor amount of Phosphatidylserine (PS)</li><li>6. Minor amount of Sphingomyelin (SM)</li></ol>
Neutral lipids (~ 10%)	<ol style="list-style-type: none"><li>1. Mostly Cholesterol ~ 10%</li><li>2. Minor amounts of mono, di and triglycerides</li><li>3. Minor amount of free fatty acids</li></ol>
Proteins (~ 10%)	<ol style="list-style-type: none"><li>1. Surfactant Protein A (SP-A) ~ 6%</li><li>2. Surfactant Protein B (SP-B) ~ 1.5%</li><li>3. Surfactant Protein C (SP-C) ~ 1.5%</li><li>4. Surfactant Protein D (SP-D) ~ 1%</li></ol>

### 1.3 Lung Surfactant Activity, Disorder and Treatment

An effective surfactant exhibits at least three critical properties. Firstly, it adsorbs quickly (within a few seconds) to the alveolar air-water interface [21]. This ensures that the materials reach the respiratory interface before a newborn completes the first inspiration. Secondly, attaining a thermal equilibrium after lining the interface, the surfactant brings down the surface tension close to 25 mN/m [26], which is further reduced to almost 0 mN/m during lung compression following an expiration [25]. This ensures that the alveolar collapse is avoided at the end of the expiration and that the subsequent lung expansion, following the next inspiration, can be performed with ease. Thirdly, during the re-expansion of the lung, the surfactant respreads back and covers the whole respiratory interface again [12]. This ensures that the surface film is protected from any rupture and is ready to repeat the cycle.

Since its rediscovery in the mid 1950s, lung surfactant has been subjected to various analytical and experimental techniques, but the molecular mechanisms underpinning its functions are not yet known in detail. There are a lot of unanswered questions regarding the structures, roles and mechanistic behaviors of the components at different stages of the breathing cycle. However, based on various biophysical studies, a few models have been proposed [12, 25, 27]. These models suggest that the phospholipids, due to their ability to form oriented interfacial monolayers, act as the principal surface active agents in the surfactant [27]. The proteins are primarily considered as modulating agents, evolved to optimize the surface activity of the phospholipids during the respiratory cycle and provide the innate immune response to microbes in the lungs [28, 29]. However, one of the proteins, namely surfactant protein B (SP-B), plays such crucial roles that lung surfactant loses its surface activity in the absence of SP-B and fails to function [30]. Thus SP-B is absolutely essential for the survival of mammals [31].

Deficiency or inactivation of lung surfactant leads to potentially fatal respiratory disorders such as neonatal respiratory distress syndrome (NRDS) in premature newborns [32] and acute respiratory distress syndrome (ARDS) in adults with acute injury or illness [33]. Development of lung surfactant replacement treatments in the early 1990s greatly improved the outlook for NRDS [34], but successful treatment of ARDS with endogenous surfactant has proved more challenging, probably because the conditions that lead to ARDS in the first place also lead to a rapid deactivation of the replacement surfactant [35]. Clinical trials have shown artificial surfactants to be much more effective if they include the proteins, SP-B in particular, as compared to protein-free preparations [36]. The requirement for SP-B's presence in effective surfactant replacement therapy is in keeping with the lethality of hereditary SP-B deficiency in humans [37] and knockout mice [38]. Improvement of surfactant replacement preparations, for example to avoid the use of animal derived surfactant and to improve its activity in the context of ARDS, is hampered by the lack of understanding of the structural features of surfactant proteins in detail that lead to their activities in the lungs.

## 1.4 Roles of Surfactant Lipids

Lung surfactant consists of a distinct set of phospholipids that is largely dissimilar to other membranous systems in most organisms. The importance of these phospholipids for the physiological function of lung surfactant has been recognized for many years [24]. The roles of the major phospholipid species belonging to the PC and PG categories (Figure 1.3) have been well-identified but those of the minor phospholipid species, such as PI, PE, PS and SM, are still far less characterized. For the most part, experimental focus has been on the surface activity properties of the surfactant lipids, i.e., the surface tension reduction, rapid adsorption and respreading characteristics. In addition to these essential functions, however, the lipid components may also play other important roles, such as controlling lung fluid balance and thereby preventing alveolar edema [39].

During expiration, the surfactant film at the air-water interface is compressed and the surface tension must be reduced to almost 0 mN/m in order to prevent alveolar collapse [8]. This means that the surfactant film sustains a surface pressure of about 70 mN/m at the interface. Previous biophysical studies on monolayers composed of the major surfactant phospholipids led to a general consensus that only a pure dipalmitoylphosphatidylcholine (DPPC) film is capable of withstanding such high pressures [40]. This is because the disaturated hydrocarbon acyl chains of DPPC can be packed tightly enough to sustain the highest pressure. However, this idea has undergone some revision recently following observations such as (1) the monolayers which include unsaturated lipids, such as palmitoyloleoylphosphatidylcholine (POPC), can also reduce the surface tension to very low values if they are compressed quickly enough [41, 42], (2) the collapse pressures of mixed monolayers, such as a monolayer of DPPC/DPPG (at a ratio of 80 : 20), are similar to that of pure DPPC [43], and (3) the liquid-expanded and tilted condensed monolayer phases coexist even at surface tensions approaching zero [44-47]. Thus a new school of thought, aimed at explaining how lung surfactant reaches near-zero surface tension without necessitating a pure DPPC monolayer formed by squeezing out other phospholipids, suggests that the mixture of DPPC and other phospholipids may take on a metastable super-compressed structure when they are compressed sufficiently rapidly at the alveolar air-water interface [41, 48].

Molecular dynamics (MD) simulations of several different phospholipid compositions, performed at the Booth lab, have found results consistent with this newer view [49]. Nevertheless, since DPPC is the most abundant surfactant phospholipid in most organisms (in humans, ~ 35% of the total weight), all working models consider at least a DPPC-enriched film as the critical surface tension reducing structure at the alveolar air-water interface [19, 22, 25, 27, 50]. Other phospholipid components are mainly attributed with modulating roles to facilitate DPPC's adsorption to the interface as well as its respreading in the successive respiratory cycles [24]. It has been shown that DPPC, by itself, adsorbs very slowly into the air-water interface, especially at temperatures below its gel-to-liquid crystalline phase transition temperature of 41 °C [51]. However, mixing with more fluid phospholipids, such as unsaturated PCs, PG and/or PI, improves the adsorption of DPPC by a large extent [24].

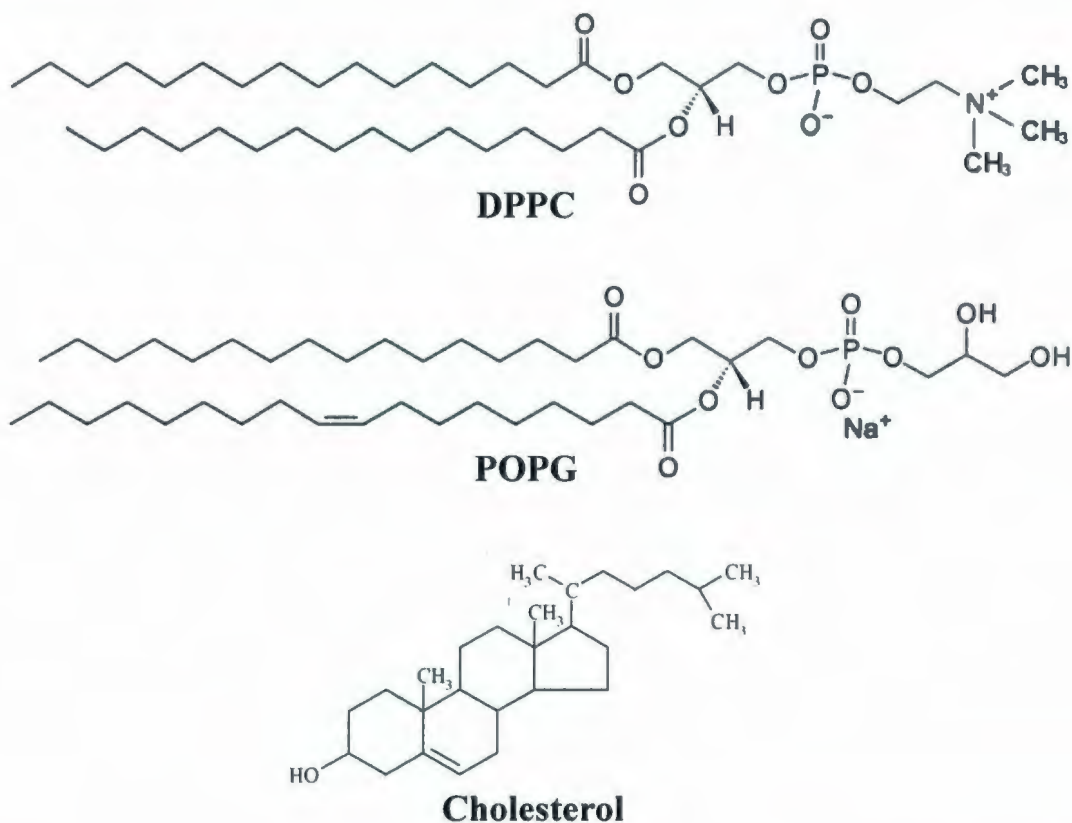


**Figure 1.3** : Chemical structures of major lung surfactant lipids. DPPC is the most abundant phospholipid with PC headgroup, POPG is the most abundant phospholipid with PG headgroup and Cholesterol is the main neutral lipid in human lung surfactant.

Other than the phospholipids, a considerable amount (~ 10% of the total weight) of cholesterol is also present in lung surfactant. The ability of cholesterol to alter many essential physical properties of membranous systems is well-established. Its involvement in lateral phase separation of native lung surfactant membrane at physiological temperatures has been reported [52]. However, no clear data are available to date to evaluate its actual roles in lung surfactant function.

It is to be noted that the lipids alone do not make a fully functional endogenous lung surfactant. The protein SP-B is indispensable for an effective lung surfactant. The other proteins are also important for its optimum performance, in terms of the surface activity as well as the host defense. However, the detailed mechanistic descriptions of the proteins' roles are not available till to date.

## 1.5 Roles of Surfactant Proteins

Lung surfactant consists of four proteins which are named as surfactant protein A (SP-A), surfactant protein B (SP-B), surfactant protein C (SP-C) and surfactant protein D (SP-D) according to their chronological order of discovery. In the native condition, SP-A is octadecameric consisting of six trimers [53], SP-B is dimeric [54], SP-C is monomeric [55], and SP-D is dodecameric consisting of four trimers [56]. SP-A is the most abundant protein of lung surfactant by weight (~ 6% of the total weight). Its main role is thought to be in defending the lungs against pathogens [5, 57]. Experiments showed that mice born without SP-A could breathe normally but were extremely prone to developing infections [58]. *In vitro* and *in vivo* studies suggest that SP-A also promotes the formation of tubular myelin, but this requires the protein SP-B and calcium too [59-61]. In addition, it has been observed that SP-A enhances adsorption of phospholipids along the air-water interface in a concerted action with SP-B [62, 63]. The protein SP-B is indispensable for life. It performs such crucial roles in surfactant function that its hereditary deficiency is lethal in humans [37] and in knockout mice [38]. Deactivation of SP-B by antibodies also causes respiratory distress

syndrome (RDS) in rabbit models [64]. Deficiency of the protein SP-C is not lethal at birth in knockout mice but they develop mild respiratory dysfunction later in life [65, 66]. Also, several cases have been described in which mutations of the SP-C gene are related to the occurrence of chronic familial respiratory diseases [67, 68]. The exact roles played by SP-B and SP-C in surfactant function and the mechanisms by which they act are not yet known. However, experiments showed that the presence of SP-B and SP-C provide necessary enhancement in adsorption of phospholipids at the alveolar air-water interface [69]. These proteins also appear to be important in preventing detachment of the folded structures from the water layer [70]. The other protein SP-D is not associated with the surface active lipid-protein complexes and is not considered to play any significant role in the biophysical mechanisms of lung surfactant at the air-water interface in alveoli [71]. Although it is evident that SP-D affects the lipid homeostasis *in vivo*, perhaps, like SP-A, its main role is to provide an immune response against microbes in the lungs [72].

Understanding the molecular basis of surfactant proteins' functions and obtaining the mechanistic descriptions of their interactions are hindered, in part, by the lack of knowledge of their high-resolution structures. To date, the only known full-length structure of a surfactant protein is that of SP-C determined using solution-state nuclear magnetic resonance (NMR) spectroscopy (PDB ID 1SPF) [55]. However, X-ray crystallographic structures of the carbohydrate recognition and neck domains, in both native and ligand-bound forms, of rat SP-A (PDB IDs 1R13 and 1R14) and human SP-D (PDB IDs 1B08 and 1PWB) have been determined [73-75]. Additionally, the structures of SP-B fragments containing the terminal regions have been determined in organic solvent and/or detergent micelles by NMR (PDB IDs 1KMR, 1RG3, 1RG4 and 2JOU) [76, 77]. Figure 1.4 shows the structural models for the native multimeric forms of SP-A, SP-B and SP-D constructed based on preliminary assumptions [56, 70] and the high-resolution structure of SP-C determined by NMR [55]. The high-resolution crystallographic structures of the trimeric carbohydrate recognition and neck domains of SP-A and SP-D [73, 74] are also shown.

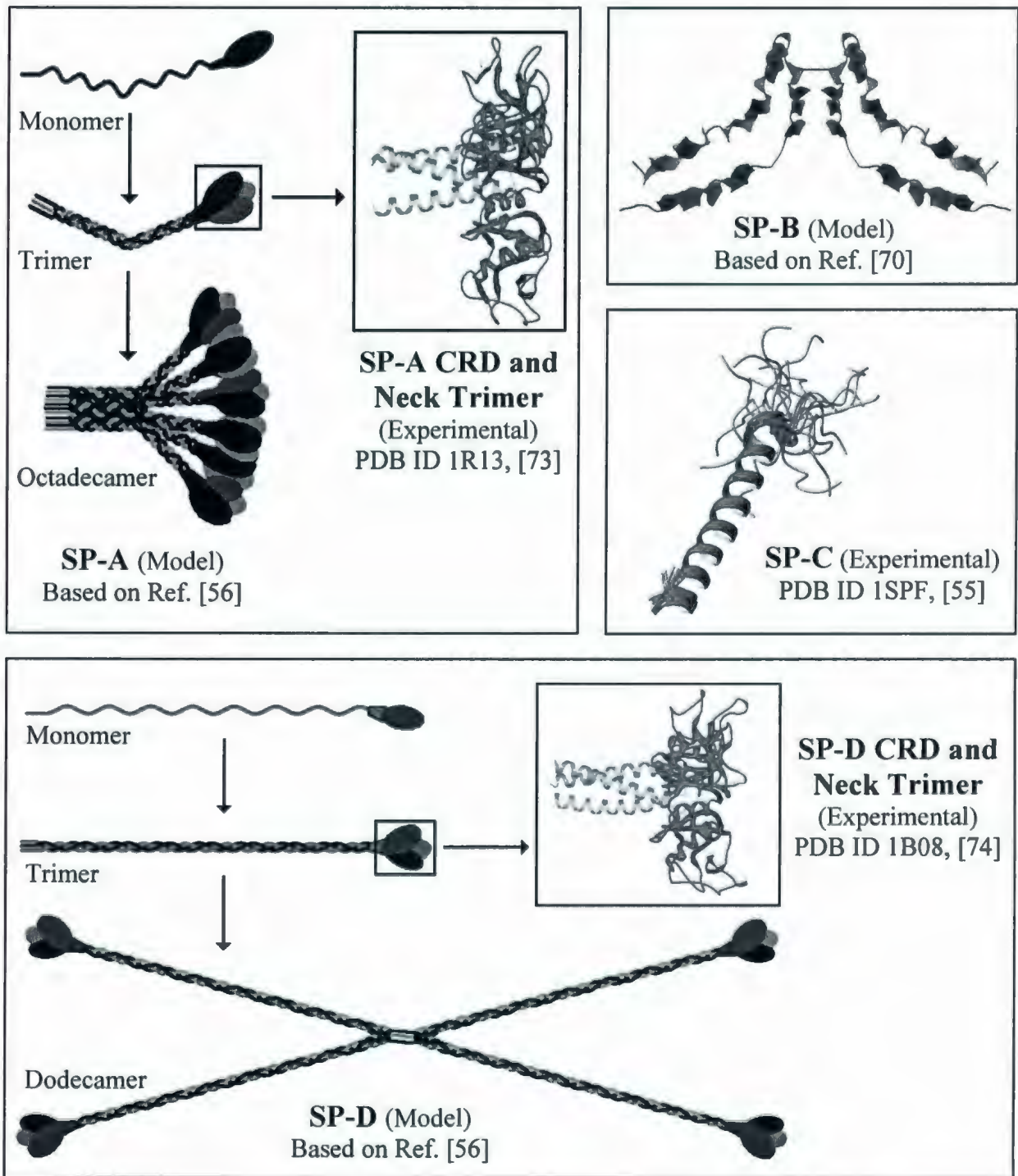


**Figure 1.4** : Structural models for lung surfactant proteins, based on Refs. [55, 56, 70]. Native SP-A, SP-B and SP-D are multimers while SP-C is a monomer. High-resolution X-ray crystallographic structures of the carbohydrate recognition and neck domains of SP-A and SP-D are shown enlarged [73, 74]. For SP-C, an ensemble of the 20 lowest energy structures, determined by solution NMR, is shown [55].

## 1.6 Properties and Function of SP-B

SP-B is considered the most important protein component of lung surfactant as it is essential for survival [37, 38, 78]. In mammals, native SP-B is composed of two covalently linked identical proteins (homodimer) [54]. Human SP-B monomer consists of 79 amino acids and weighs about 8.7 kDa [70]. However, the SP-B gene is first transcribed and translated into a significantly larger precursor consisting of 381 residues [79]. The mature form of SP-B consists of residues 201-279 of the precursor [80]. The flanking regions of the precursor are cleaved in at least two steps within type II alveolar cell compartments that lie between the trans-golgi and the lamellar body [81]. The amino acid sequence of mature human SP-B is shown in Table 1.2 [70].

**Table 1.2 :** Amino acid sequence of human surfactant protein B [70].

1-20	Phe-Pro-Ile-Pro-Leu-Pro-Tyr-Cys-Trp-Leu-Cys-Arg-Ala-Leu-Ile-Lys-Arg-Ile-Gln-Ala-
21-40	Met-Ile-Pro-Lys-Gly-Ala-Leu-Ala-Val-Ala-Val-Ala-Gln-Val-Cys-Arg-Val-Val-Pro-Leu-
41-60	Val-Ala-Gly-Gly-Ile-Cys-Gln-Cys-Leu-Ala-Glu-Arg-Tyr-Ser-Val-Ile-Leu-Leu-Asp-Thr-
61-79	Leu-Leu-Gly-Arg-Met-Leu-Pro-Gln-Leu-Val-Cys-Arg-Leu-Val-Leu-Arg-Cys-Ser-Met

Compared to water soluble proteins, SP-B consists of a high proportion (~ 52%) of nonpolar and hydrophobic amino acids, such as alanine, valine, leucine, isoleucine, methionine, phenylalanine and tryptophan. SP-B also exhibits a strong cationic profile as it contains nine positively charged (arginine & lysine) and two negatively charged (aspartic acid & glutamic acid) amino acids yielding a net charge of +7 at neutral pH. There are seven cysteines, six of which form three intra-molecular disulfide bridges and the remaining one forms an inter-molecular bond responsible for the dimerization.

Biophysical studies have presented a long list of SP-B activities including membrane binding, membrane lysis, membrane fusion, promotion of lipid adsorption to air-water surfaces, stabilization of monomolecular surface films and respreading of films from collapsed phases [82]. However, it is not clear which of these activities, if any, underlies SP-B's crucial contributions to surfactant function in the lungs. As SP-B is positively

charged at neutral pH, it seems likely that electrostatic interactions between SP-B and surfactant lipids with negatively charged headgroups contribute to its physiological function. Indeed, there are studies which have found that SP-B preferentially binds negatively charged phospholipids such as phosphatidylglycerol (PG) in surface monolayers of surfactant films [83, 84], as well as in multilamellar vesicles [85]. Some models aiming to explain the functional mechanism of SP-B suggest that upon compression, as would happen in lungs during the expiration, films composed of positively charged SP-B and negatively charged lipids may form buckled structures that remain attached to the monolayer [86]. During subsequent expansion of the film at a lower surface pressure, the buckled structures may rapidly be reincorporated into the film to re-form a flat monolayer [87, 88]. The most dramatic acceleration of the interfacial adsorption of phospholipids is also caused by SP-B [25]. Furthermore, SP-B, in addition to SP-A, is required for the formation of tubular myelin, an ordered array of phospholipid aggregates that is thought to be involved in transporting lipids from aqueous subphase to the surface-associated phase [59, 60]. All these observations suggest that SP-B's critical contributions to lung surfactant function are made via facilitating large-scale rearrangements of lipids and stabilizing complex structures required at various stages of the breathing cycle. Unfortunately, the molecular basis of SP-B's function in the lung is still far from being understood, in part because the three-dimensional structure of SP-B has not yet been determined.

SP-B belongs to the Saposin protein superfamily [Table 1.3], a unique family of small lipid-binding and membrane-perturbing proteins [54, 89, 90]. High-resolution structures are known for quite a few Saposin proteins such as Saposin A (PDB ID 2DOB) [91], Saposin B (PDB ID 1N69) [92], Saposin C (PDB ID 1SN6) [93], NK-Lysin (PDB ID 1NKL) [94], Amoebapore A (PDB ID 1OF9) [95] and the saposin-like Granulysin (PDB ID 1L9L) [96]. All these proteins display a predominantly  $\alpha$ -helical conformation, although the extent of the helices and the way the helices pack together vary from protein to protein. However, in all Saposins, three intra-protein disulfide bonds are formed by six conserved cysteines which define a characteristic fold that has been conserved for an estimated 300 million years [97]. Thus, SP-B is expected to possess four (or five)  $\alpha$ -helical regions connected by loops and

bundled by three disulfide bonds (Figure 1.5). The helical structure of native SP-B has been verified by circular dichroism (CD) and Fourier transform infrared (FTIR) spectroscopy in both lipid and organic solvent environments [98-100].

**Table 1.3** : Amino acid sequence of Saposin family proteins [70]. Mini-B and Maxi-B, shown at the bottom, are peptide fragments of SP-B.

Protein	Amino acid sequence
SapA	SLP- <b>C</b> DI <b>C</b> NDVVTAAGDMLKDNAT-EEEILVYLEKT <b>C</b> DWLPKPNMSAS <b>C</b> KEIVDSYLPVILDI IKGEMSRPGEV <b>C</b> SALN <b>L</b> CESLQ
SapB	GDV <b>C</b> QD <b>C</b> IQMVTDIQTAVRTNSTFVQALVEHVKEE <b>C</b> DRLG-PGMADI <b>C</b> KNYISQYSEIAIQMMH--MQPK <b>E</b> ICALVGF <b>C</b> D--E
SapC	SDVY <b>C</b> EV <b>C</b> EFLVKEVTKLIDNNKT-EKEILDAFDKM <b>C</b> SKLPKS-LSE <b>E</b> C <b>C</b> QEVVDTYGSSILSILLEEVS-PELV <b>C</b> SMLHL <b>C</b> SGT
SapD	DGG <b>F</b> CEV <b>C</b> CKKLVGYLDRNLEKNST-KQEILAALEK <b>G</b> C <b>S</b> FLPDP-YQ <b>K</b> Q <b>C</b> DQFVAEYEPVLEIEILVEVMD-PSFV <b>C</b> LKIGACPSAH
NKL	G-Y <b>F</b> CE <b>S</b> CRK <b>I</b> IQKLEDMVGPQPN-EDTVTQ <b>A</b> ASQV <b>C</b> DKL-K-ILRGL <b>C</b> KKIMRSFLRRISWDILT <b>G</b> K-KPQ <b>A</b> I <b>C</b> VDIK <b>I</b> CK-E
PFP	GEIL <b>C</b> N <b>L</b> C <b>T</b> GLINTLENLL <b>T</b> TK-G-ADK <b>V</b> KDYIS <b>S</b> L <b>C</b> NKA-SGF <b>I</b> AT <b>L</b> C <b>T</b> KVLD <b>F</b> GID <b>K</b> LI-QL <b>I</b> ED <b>K</b> VDANAL <b>C</b> AK <b>I</b> H <b>A</b> C
SP-B	FPIPL <b>P</b> Y <b>C</b> N <b>L</b> C <b>R</b> ALIKRIQAMIP <b>K</b> GA----LAVAVAQ <b>V</b> CRVVPLVA-GG <b>I</b> C <b>Q</b> CLAERYSVILLD <b>T</b> LLGR <b>M</b> L-PQ <b>L</b> V <b>C</b> R <b>L</b> V <b>L</b> R <b>C</b> S-M
Mini-B	----- <b>C</b> N <b>L</b> C <b>R</b> ALIKRIQAMIP <b>K</b> G-----GR <b>M</b> L-PQ <b>L</b> V <b>C</b> R <b>L</b> V <b>L</b> R <b>C</b> S--
Maxi-B	----- <b>C</b> N <b>L</b> C <b>R</b> ALIKRIQAMIP <b>K</b> GA----LAVAVAQ <b>V</b> CRVVPLVA-GG <b>I</b> C <b>Q</b> SLAARYSVILLD <b>T</b> LLGR <b>M</b> L-PQ <b>L</b> V <b>C</b> R <b>L</b> V <b>L</b> R <b>C</b> S--

S-S  
Bonds

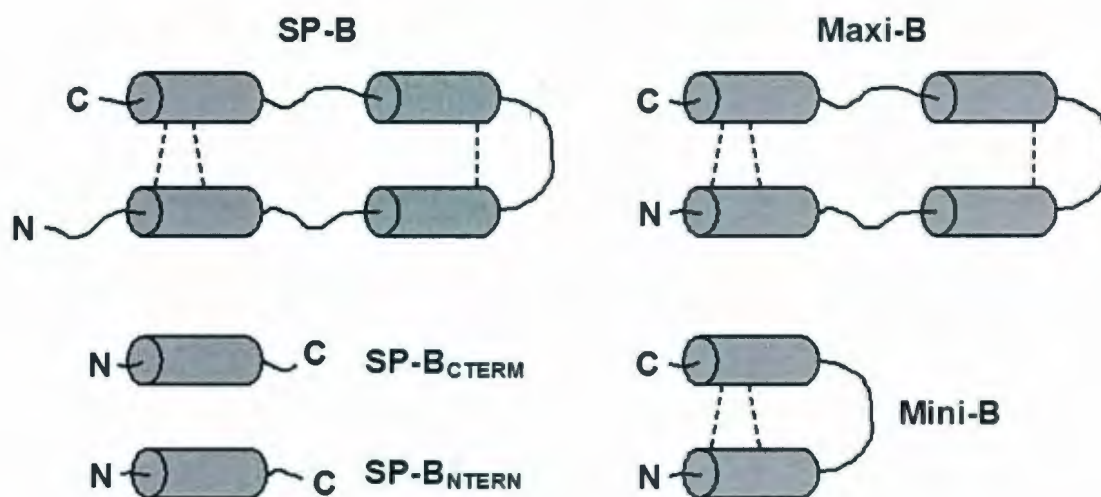


**Figure 1.5** : Topology of SP-B predicted based on the known structures of Saposin family proteins.  $\alpha$ -Helical regions are portrayed by cylinders and disulfide bonds connecting the helices are shown by dashed lines. Fragments covering the terminal helical regions that are known to exhibit some biological activity and a near-full proposed peptide are also shown.

## 1.7 Activities and Structures of SP-B Fragments

Fragments of SP-B containing individual helices or pairs of helices have been shown to retain significant biological activity when compared to the full-length protein (Figure 1.6). Surfactant preparations that include synthetic peptides representing either N- or C-terminal helical segments of SP-B enhance oxygenation and lung compliance in surfactant-deficient animal models [101, 102]. A 25-residue N-terminal segment of SP-B (SP-B<sub>1-25</sub>) facilitates dynamic respreading [103] and improves lung function in premature rabbits and lavaged rats [104]. Peptides based on the C-terminal domain also induce *in vitro* and *in vivo* surfactant activities that, at least partially, simulate those of the native protein [101, 105, 106]. The N-terminal half of SP-B consisting of residues 1-37 promotes rapid liposome fusion, while a shorter peptide containing residues 7-22 is sufficient for liposome lysis [107]. KL4 (a component of Surfaxin), a 21-residue peptide designed by use of the hydrophobic and hydrophilic repeats of SP-B<sub>57-63</sub> as a molecular template, has shown some promise as a bronchoalveolar lavage for improving lung function in meconium aspiration syndrome [108].

Mini-B is another synthetic construct that includes both N- and C-terminal predicted helical regions of SP-B. This 34-residue peptide consists of SP-B<sub>8-25</sub> and SP-B<sub>63-78</sub> covalently connected through the backbone [109]. Like the full-length protein, Mini-B possesses a net charge of +7. The proportion of hydrophobic amino acids is also similar, 44% in Mini-B as compared to 52% in SP-B. In addition, Mini-B possesses four of the six conserved cysteines that define the Saposin fold and thus, in its oxidized form, has two disulfide bridges linking the two helices. Surfactant deficient rats treated with synthetic surfactant preparations containing Mini-B attain oxygenation and lung compliance values as good as, or better than, those achieved in the presence of native SP-B [109] (Figure 1.6).

To date, structures of three peptide fragments representing SP-B's terminal regions have been determined at atomic resolution by solution NMR. The structure of an N-terminal peptide (SP-B<sub>11-25</sub>) was determined in methanol (PDB ID 1KMR) [76]. The structure of a C-terminal peptide (SP-B<sub>63-78</sub>) was determined in aqueous solution containing 40%

fluorinated alcohol hexafluoroisopropanol (HFIP) (PDB ID 1RG4) and in lipid-mimicking sodiumdodecylsulfate (SDS) micelles (PDB ID 1RG3) [77]. The structure of a reduced version of Mini-B, that lacks the two disulfide bonds between the helices, was determined in aqueous solution containing 40% HFIP (PDB ID 2JOU) during my M.Sc. work (Booth lab, Memorial University of Newfoundland) [110]. Figure 1.7 shows the high-resolution structures of these three SP-B-based peptides.

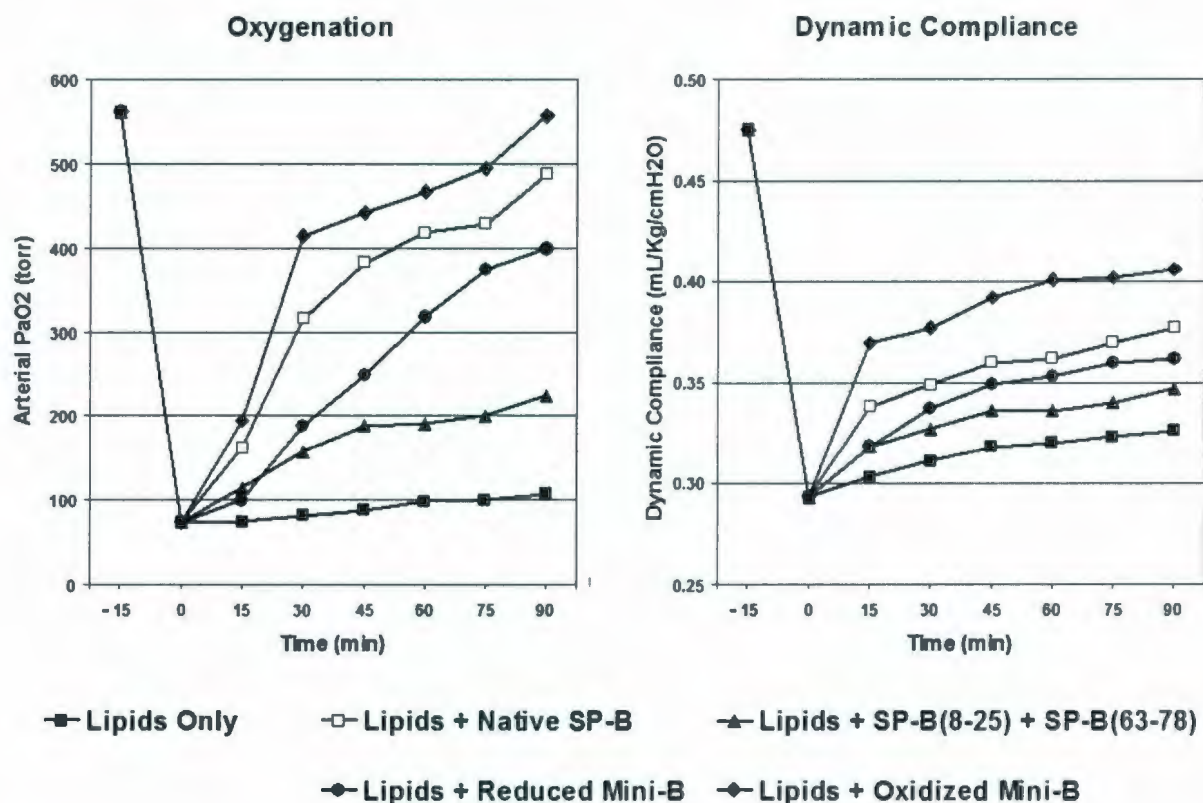


**Figure 1.6 :** Respiratory function related responses from rats subjected to removal of lung surfactant by *in vivo* lavage and then exogenously administered with synthetic surfactants prepared from lipids only and lipids plus native SP-B or Mini-B [109]. The lipid-based surfactant contained 35 mg of phospholipids (16 mg of DPPC, 10 mg of DOPC, 3 mg of POPG, 1 mg of POPE and 3 mg of POPS) and 2 mg of cholesterol in 1 mL of phosphate-buffered saline. The lipid-protein mixed surfactants contained an additional 0.1  $\mu\text{mol}$  of protein or peptide. Arterial partial pressure of oxygen ( $\text{PaO}_2$ ) and dynamic lung compliance (calculated by dividing tidal volume/kg body weight by changes in airway pressure) are shown as a function of time after surfactant instillation. The plots are prepared using the published data of Ref. [109].

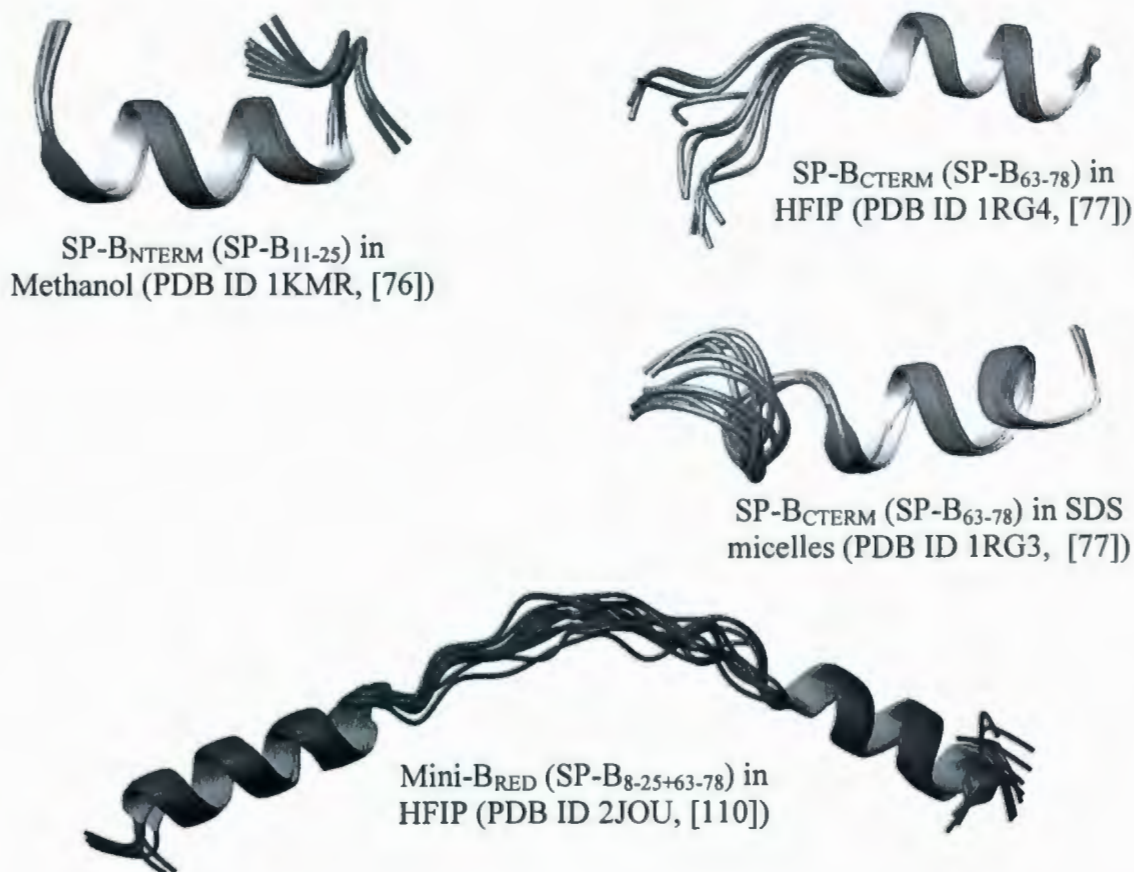


**Figure 1.7 :** Ensembles of the high-resolution structures (lowest energy 10 to 17) of the terminal fragments of SP-B determined by solution NMR. The fragments are SP-B<sub>NTERM</sub> (SP-B<sub>11-25</sub>) in methanol (17 structures, PDB ID 1KMR) [76], SP-B<sub>CTERM</sub> (SP-B<sub>63-78</sub>) in HFIP (10 structures, PDB ID 1RG4) [77], SP-B<sub>CTERM</sub> (SP-B<sub>63-78</sub>) in SDS micelles (10 structures, PDB ID 1RG3) [77] and reduced Mini-B (SP-B<sub>8-25 + 63-78</sub>) in HFIP (15 structures, PDB ID 2JOU) [110].

## 1.8 Outline and Objectives of Present Work

A protein's biological function comes about due to the organization of its amino acid chain into a specific well-folded three-dimensional structure. Knowledge of the high-resolution structure of SP-B is thus essential for understanding its function at the molecular and submolecular levels. However, the production of an SP-B sample to pursue the structural studies, either in the form of a crystal to perform X-ray crystallography or appropriately

labeled with  $^{13}\text{C}/^{15}\text{N}$  isotopes to perform solution NMR, has been very challenging and unsuccessful to date. For SP-B, solution NMR would be a suitable choice since using this method the protein can be studied in a physiologically relevant lipid-mimetic environment and its dynamics and interactions can also be probed. Unfortunately, attempts at recombinant expression of the full-length protein or chemical synthesis of a near-full protein have not succeeded yet, mainly due to its high degree of hydrophobicity and the presence of three intrachain disulfide bonds. Interestingly on the other hand, some of the successfully produced synthetic fragments of SP-B have shown substantial biological activity when compared to the full-length protein. Oxidized Mini-B tops this list and it likely encompasses the key functional regions of the full-length protein. The structure of reduced Mini-B was determined in 40% HFIP during my M.Sc. but the lack of disulfide bonds and the fluorinated organic solvent environment limit this structure's ability to explain SP-B's function in native lung conditions. Nevertheless, it was an important first step that aided in the structural studies of physiologically relevant oxidized Mini-B in a lipid-mimetic detergent micelle environment.

This Ph.D. research was conducted with Mini-B and two other SP-B-based peptides to reveal the key structural features that underlie the functional mechanisms of SP-B in physiological conditions. The research was performed using solution NMR spectroscopy. The entire work was divided into six specific projects and thereby the findings are reported in six separate chapters of this Thesis. The research objectives were to :

1. determine the high-resolution structure of oxidized Mini-B in SDS micelles,
2. investigate the conformation of Mini-B in the presence of lung phospholipid analogues and probe its interactions with the model surfactant lipids,
3. investigate the conformation of SP-A in the presence of lung phospholipid analogues and probe its interactions with the model surfactant lipids,
4. probe the interaction between Mini-B and SP-A, if any, in the presence of lung phospholipid analogues,
5. investigate the modifications to SP-B's structure and lipid interactions brought about by tryptophan oxidation, that is common in ARDS, using the N-terminal fragment SP-B<sub>8-25</sub>, and
6. investigate the conformation of the C-terminal half of SP-B.

*Chapter 2*  
**Protein NMR Methods**

## 2.1 Protein Structure

Proteins are molecular machines that perform numerous indispensable functions for life; enzymatic catalysis, immunity against pathogens, regulation of cellular conditions, information processing, transportation of cellular cargo, formation of body tissues and muscle movement are a few to name. Proteins are polymeric macromolecules composed of a long chain of chemical units called amino acids (also known as residues). While there are literally hundreds of amino acids known, only 20 are directly encoded by the universal genetic code and all of them are in the L isomeric form [111]. The backbone chemical structure,  $-N-C_{\alpha}(H)-C(O)-$ , is the same for all 20 amino acids (Figure 2.1 (A)). The third substituent of  $C_{\alpha}$ , an H, is also the same. However, the fourth substituent is represented by 20 different side chains (or R groups) and this is what distinguishes one amino acid from another. Individual atoms in an amino acid are referred to as  $H_N$ ,  $C_{\alpha}$ ,  $H_{\alpha}$ ,  $C_{\beta}$ ,  $H_{\beta}$ , etc. (Figure 2.1 (B)). In a full-length protein, the constituent amino acids are linked into a linear sequence through peptide bonds between the carboxyl C of one residue and the amino N of the next residue [111]. The first and the last residues in the chain are termed as the N- and C-terminal residues, respectively [111].

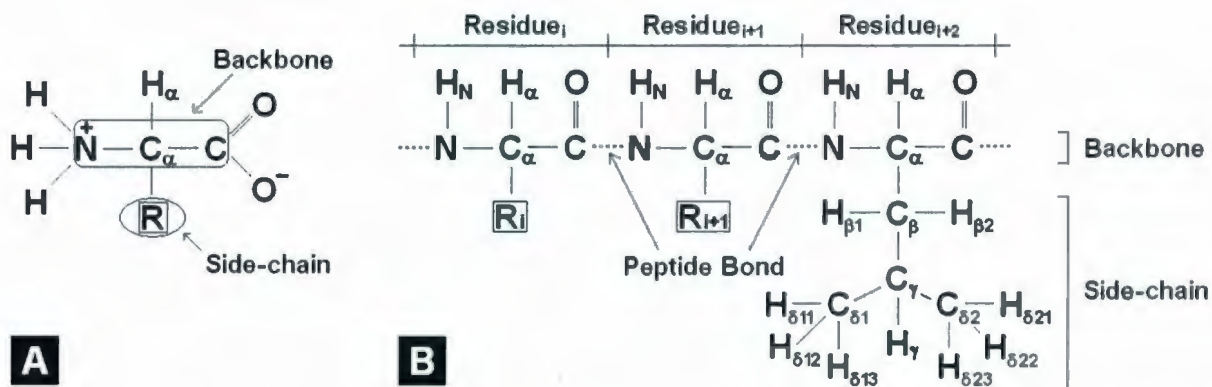


**Figure 2.1 :** Chemical structure of a protein. (A) A single amino acid. All 20 amino acids have the same backbone chemical structure ( $-N-C_{\alpha}-C-$ ) but different side-chains ( $R$ s). (B) Amino acids are connected by peptide bonds between  $C_i$  and  $N_{i+1}$  to form a full-length protein. A residue is shown with the names of the side-chain nuclei as an example.

Proteins do not have a uniform, standard structure, in part, because the 20 different amino acids from which they are made have widely varied chemical and physical properties. However, the function of any protein depends on how its linear chain of amino acids folds to assume a defined, three-dimensional (3D) structure. Like other polymeric biomolecules, proteins can be described in terms of levels of organization, in this case, their primary, secondary, tertiary and quaternary structures [112] (Figure 2.2). A protein's primary structure is the amino acid sequence of its polypeptide chain(s). Individual segments or regions of the chain may form local regular configurations, such as  $\alpha$ -helices and/or  $\beta$ -strands, that represent the protein's secondary structure. The tertiary structure refers to the overall 3D conformation of the entire chain formed by packing such regular structural elements. Many proteins are composed of two or more polypeptide chains, loosely referred to as subunits. The quaternary structure of a multi-chain protein represents the spatial arrangement of all folded subunits.

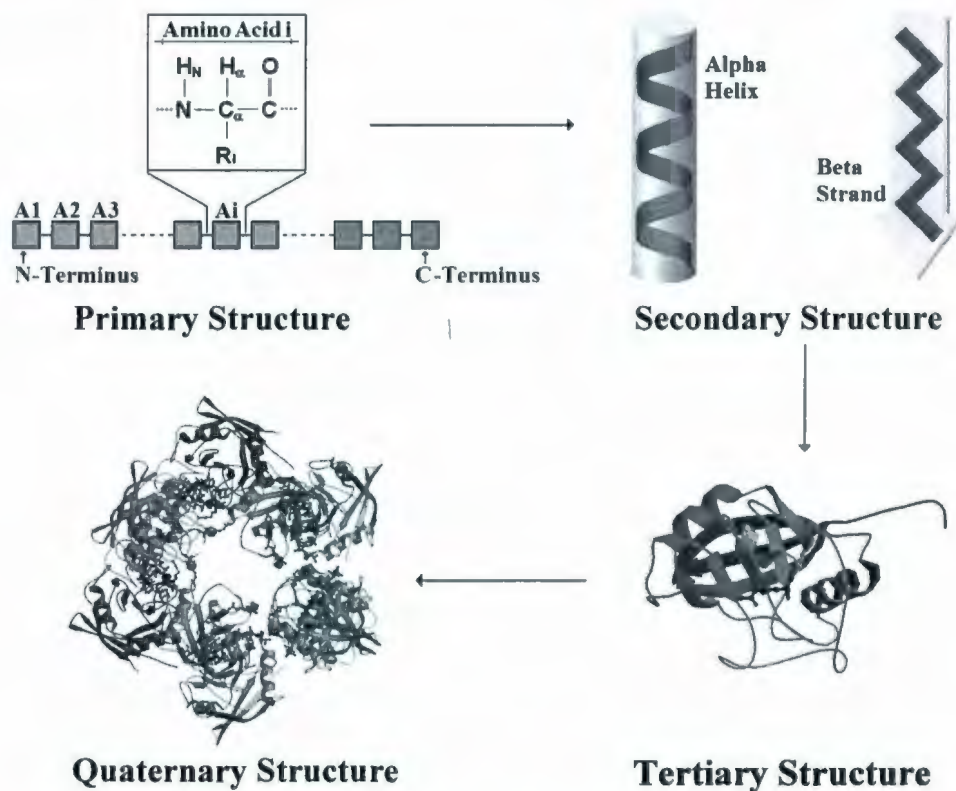


**Figure 2.2 :** Four levels of protein structure, from primary to quaternary. The figures used to demonstrate the tertiary and quaternary structures are taken from the Protein Data Bank (PDB) (PDB IDs 2X25 and 2X2C, respectively).

## 2.2 Methods for Protein Structure Determination

A key to deciphering the function of a given protein is to understand its structure, since it is the distinct structure that leads to the chemical and physical properties of the protein and, ultimately, its mechanism of action in a living organism [113]. To date, only two techniques are available for determining the structure of a protein at atomic resolution; X-ray crystallography and solution NMR spectroscopy [114].

X-ray crystallography requires the protein to be grown as a well-ordered crystal [115]. When the protein crystal is exposed to a collimated (parallel) beam of X-rays, the atoms scatter the X-rays and the resulting diffraction pattern is recorded. An electron density map is then generated from which the 3D image of the crystal structure is constructed by fitting the known sequence of the protein. This technique can calculate the atomic coordinates precisely. However, it only provides information about one of the low-energy conformations that the protein may adopt but nothing regarding the dynamics. Therefore, the crystal structure of a protein may sometime be misleading and may lack physiological relevance. Furthermore, for membrane and other lipid-associated hydrophobic proteins, it is very challenging to grow diffraction-quality crystals due to the problems caused by aggregation.

Solution NMR spectroscopy has only been developed as a technique for protein structure determination in the last three decades [116]. The first complete 3D structure solved using NMR was presented in 1986 [117]. The unique advantage of NMR spectroscopy over X-ray crystallography is that the protein structural studies can be performed in a physiologically relevant solution environment. The technique exploits the quantum mechanical property of any nuclei with nonzero spin, but predominantly works with spin 1/2 nuclei ( $^1\text{H}$ ,  $^{13}\text{C}$ ,  $^{15}\text{N}$ , etc.). The NMR phenomenon derives from the fact that the energy levels of nuclei with nonzero spin become unequal when the nuclei are placed in a magnetic field. The energy of the nuclei are then perturbed (i.e., moved between levels) by the application of radiofrequency (RF) pulses whose wavelength corresponds to the gap between the energy levels. High-resolution structural data are generated by manipulating the magnetization of the nuclei using scalar (through bond) and dipolar (through space) couplings by application of

appropriate pulse trains, delays and phase cyclings. The data contain information on inter-nuclear distances and backbone dihedral angles which are used to compute the structural model of the protein. However, the inherent properties of solution NMR impose a limitation on the protein size that is amenable to NMR studies. The classical high-resolution NMR methods are limited to a molecular size (mass) typically up to about 20 kDa (i.e., ~ 175 amino acids), provided the protein is appropriately  $^{13}\text{C}/^{15}\text{N}$ -labeled and soluble in water [118].

In addition to obtaining high-resolution structural data, solution NMR can be used to study the flexibility of the proteins and their dynamics over a wide range of time scales [119]. The interactions between a protein and its ligand can also be probed using solution NMR methods. For a membrane or lipid-associated protein, such as SP-B, NMR is a suitable method since the protein can be studied in detergent/lipid micelles which mimic its physiological environment. However, this is very challenging because the large size of protein/micelle complex substantially reduces the spectral intensity. Only relatively small proteins or protein fragments (up to ~ 150 amino acids) are thus amenable to study in micelles using solution NMR. Although recently developed solid-state NMR methods provide useful information about the structure and orientation of a membrane protein in lipid bilayers [120], the micelle-route using solution NMR is still the principal NMR technique to determine the high-resolution structure of a lipid-associated hydrophobic protein.

## 2.3 Basic Principles of NMR

All nuclei with an odd mass number (e.g.,  $^1\text{H}$ ,  $^{15}\text{N}$ ) or an even mass number and an odd atomic number (e.g.,  $^2\text{H}$ ,  $^{14}\text{N}$ ) possess spin angular momentum characterized by the spin quantum number  $I$  [121]. Nuclear magnetic resonance is a phenomenon which occurs when a group of nuclei with nonzero spin angular momentum is immersed in a static magnetic field inside the NMR spectrometer and exposed to RF pulses with appropriate energy [122]. Nuclei with zero spin (i.e.,  $I = 0$ ), such as  $^{12}\text{C}$  and  $^{16}\text{O}$ , are thus not observable by NMR. Nuclei with spin 1 or more (i.e.,  $I \geq 1$ ), such as  $^2\text{H}$  and  $^{14}\text{N}$ , are also not generally useful for structural studies in solution [123]. They possess electric quadrupole moments and the

lifetimes of their magnetic states are very short resulting in broad resonance lines which are difficult to observe. Nuclei with spin 1/2 (i.e.,  $I = 1/2$ ), such as  $^1\text{H}$ ,  $^{13}\text{C}$  and  $^{15}\text{N}$ , are the most useful nuclei for solution NMR [123]. For protein structural studies,  $^{12}\text{C}$  and/or  $^{14}\text{N}$  nuclei of the molecule are often replaced by their isotopes  $^{13}\text{C}$  and/or  $^{15}\text{N}$ , respectively.

In the absence of any external magnetic field, the spin 1/2 nuclei of a sample, which can be considered as tiny bar magnets, do not have any preferred orientation. However, when the sample is placed in the large static magnetic field of an NMR spectrometer, all spin 1/2 nuclei assume one of the two orientations, either in the same direction as, or opposed to, the external field. This is characterized by the two allowed quantum mechanical states given by the magnetic quantum number  $m = \pm 1/2$ . The two states have different energy levels known as Zeeman levels (Figure 2.3). In thermal equilibrium, these states are unequally populated, having some more nuclei in the lower energy state (ground state,  $m = 1/2$ ) than the higher energy state (excited state,  $m = -1/2$ ), as determined by the Boltzmann distribution. The small nuclear magnets may spontaneously flip from one orientation (energy state) to the other but the rate is extremely slow. However, when energy equal to the difference between the two states is applied, much more flipping is induced. This exemplifies a resonance phenomenon and is hence referred to as Nuclear Magnetic Resonance (NMR).

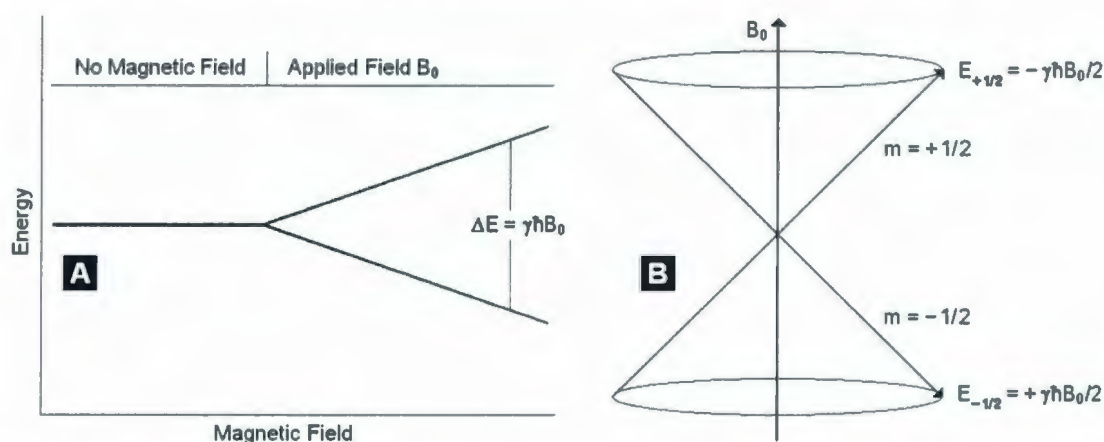


**Figure 2.3 :** Energy levels of a spin 1/2 nucleus in an external magnetic field. (A) The applied field  $B_0$  (the spectrometer field) causes the energy state of the nucleus to be split into two levels known as Zeeman levels. The energy difference between the levels is proportional to the external field strength. (B) The nucleus assumes one of the two quantum mechanically allowed energy states and a transition occurs by the absorption or emission of energy equal to the difference of the two states.

A nucleus with spin angular momentum  $\mathbf{I}$  also possesses nuclear magnetic moment  $\boldsymbol{\mu}$  (both are vector quantities as indicated by the boldface), and the relation between the two is

$$\boldsymbol{\mu} = \gamma \mathbf{I}, \quad (2.1)$$

where  $\gamma$  is the proportionality constant known as the gyromagnetic ratio of the nucleus. The magnitude of  $\gamma$ , in part, determines the receptivity of a nucleus in NMR spectroscopy since nuclei with larger gyromagnetic ratios (e.g.,  $^1\text{H}$  and  $^{19}\text{F}$ ) generate stronger NMR signals. However, the magnitude of the z-component of  $\mathbf{I}$  is specified by

$$I_z = m\hbar, \quad (2.2)$$

where  $\hbar = h/2\pi$  and  $h$  is Planck's constant. Therefore, the z-component of the nuclear magnetic moment is

$$\mu_z = \gamma m\hbar. \quad (2.3)$$

Now, in an external magnetic field  $\mathbf{B}$  along the z-axis, the energy of a spin state is

$$E = -\boldsymbol{\mu} \cdot \mathbf{B} = -\mu_z B. \quad (2.4)$$

The energy of a particular spin state  $m$  is then

$$E_m = -m\hbar\gamma B. \quad (2.5)$$

Thus the energy difference between the two Zeeman levels of a spin 1/2 nucleus placed in an external static magnetic field  $\mathbf{B}_0$  applied along the z-axis is

$$\begin{aligned} \Delta E &= E_{-1/2} - E_{+1/2} = - [(-1/2)\hbar\gamma B_0 - (1/2)\hbar\gamma B_0], \\ \text{or} \quad \Delta E &= \gamma\hbar B_0. \end{aligned} \quad (2.6)$$

This is also the irradiation energy required to cause transition between the two Zeeman states. Now, the Bohr condition,

$$\Delta E = h\nu, \quad (2.7)$$

enables the frequency of nuclear transition, known as the Larmor frequency, to be written as

$$\nu_0 = (1/2\pi)\gamma B_0, \quad (2.8)$$

$$\text{or} \quad \omega_0 = \gamma B_0. \quad (2.9)$$

in units of Hz or rad/s, respectively. Hence, the irradiation energy depends on both  $\gamma$  and  $B_0$ . In practice, it is in the radiofrequency range and is typically applied as a short pulse.

Table 2.1 lists the gyromagnetic ratios and the Larmor frequencies of selected NMR-active bio-nuclei in an 11.74 T field [119, 123].

**Table 2.1** : Properties of nuclei commonly used in bio-NMR [119, 123].

Nucleus	Natural abundance (%)	I	$\gamma$ (T·s) <sup>-1</sup>	$\omega_0$ at $B_0 = 11.74$ T (MHz)
<sup>1</sup> H	99.98	1/2	$2.68 \times 10^8$	500
<sup>2</sup> H	0.02	1	$4.11 \times 10^7$	77
<sup>13</sup> C	1.11	1/2	$6.73 \times 10^7$	125.7
<sup>15</sup> N	0.36	1/2	$-2.72 \times 10^7$	50.7
<sup>19</sup> F	100	1/2	$2.52 \times 10^8$	488.4
<sup>31</sup> P	100	1/2	$1.08 \times 10^7$	201.5

In an external magnetic field, the Zeeman splitting of the magnetic states of a group of spin 1/2 nuclei at thermal equilibrium also leads to a net bulk magnetization  $\mathbf{M}_0$  since the two states are unequally populated. It is the bulk magnetization from the whole ensemble that determines the NMR signal, not the magnetic moment of any individual nucleus. Conventionally, the direction of the external field  $\mathbf{B}_0$  is taken as the z-axis of the coordinate system. So,  $\mathbf{M}_0$  is also aligned along the z-axis.

During NMR experiments, the bulk magnetization  $\mathbf{M}_0$  is manipulated by an RF pulse, which is a time varying magnetic field,  $\mathbf{B}_1$ , oscillating at the same Larmor frequency  $\omega_0$  (Figure 2.4). The pulse applies a torque on the longitudinal bulk magnetization and tips it from the z-axis. If  $\mathbf{B}_1$  is a  $90^\circ$  pulse applied along the y-axis, the longitudinal magnetization converts to a transverse magnetization along the x-axis following a rotation in the ZX-plane. However, immediately after the pulse, the transverse magnetization starts precessing about the z-axis in the XY-plane with frequency  $\omega_0$  under the influence of the external field  $\mathbf{B}_0$ . The precession induces an electric current in the detection coil of the spectrometer. In the absence of any further perturbing RF pulses, relaxation processes bring the spin system to thermal equilibrium over time with the magnetization oriented back along the z-axis. During this period, the transverse magnetization decays with time and consequently the induced current also decays. The free induction decay (FID) of the induced current is recorded as a function of time over a certain acquisition period. The FID is thus a time-domain signal with contributions typically from different nuclei with slightly different frequency caused by the variations of the local chemical environment surrounding each nucleus. The usual frequency-domain NMR spectrum is obtained by computing the Fourier transformation of the FID.

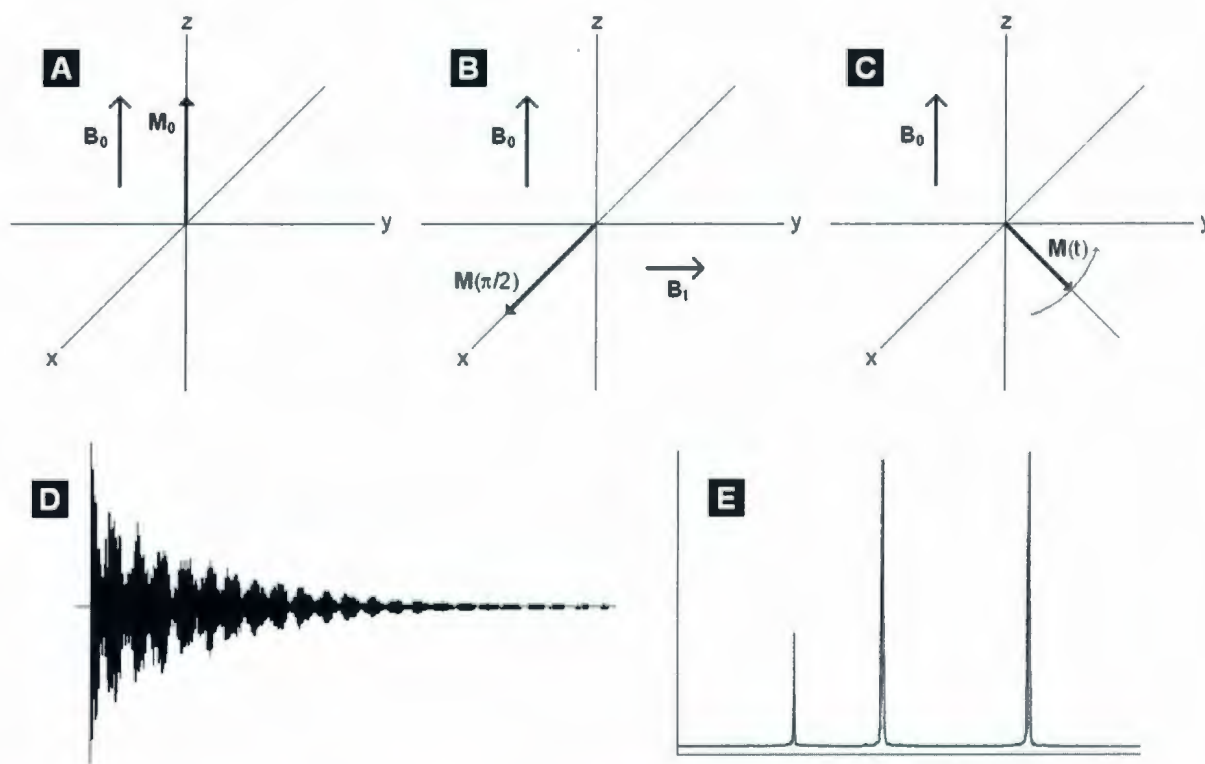


**Figure 2.4 :** Steps of a simple one-pulse 1D NMR experiment. In a static external field  $B_0$ , the net bulk magnetization  $M_0$  lies along the z-axis at thermal equilibrium (A). A  $90^\circ$  RF pulse, applied along the y-axis, rotates  $M_0$  to the x-axis where it is renamed as  $M(\pi/2)$  (B). Immediately after the pulse,  $M(\pi/2)$  starts precessing in the XY-plane under the influence of  $B_0$  and relaxations also start. The time-varying magnetic field  $M(t)$  induces a current in the spectrometer coil (C). The induced current is measured as a function of time during the acquisition period following the pulse in the form of free induction decay (FID) (D). The subsequent Fourier transformation of the FID gives the normal NMR spectrum with absorption peaks at frequencies corresponding to the energy differences between the ground and excited states of the nuclei at different chemical environments (E).

## 2.4 Basic NMR Parameters

### 2.4.1 Relaxation Times ( $T_1$ and $T_2$ )

Relaxation is the process by which a nuclear spin system, perturbed by absorbing an RF energy, returns back to thermal equilibrium. There are two relaxation processes; spin-lattice or longitudinal relaxation, characterized by the time  $T_1$  and spin-spin or transverse relaxation, characterized by the time  $T_2$  [119, 123]. At equilibrium, the net magnetization

vector  $\mathbf{M}_0$  lies along the z-axis, so there are no transverse components present and the longitudinal component represents the total magnetization, i.e.,  $M_Z = M_0$  and  $M_X = M_Y = 0$ . A  $90^\circ$  RF pulse (of the order of  $10 \mu\text{s}$ ) with appropriate energy and phase rotates the magnetization from the z-axis and diminishes  $M_Z$  to zero. After the pulse, the spin system gradually (of the order of 1 s for a typical protein) returns back to the thermal equilibrium and  $M_Z$  regains its original magnitude. The time constant which describes how  $M_Z$  returns to its equilibrium value is called the spin-lattice relaxation time  $T_1$ . The equation governing this behavior as a function of time  $t$  after the displacement is

$$M_Z(t) = M_0 (1 - e^{-t/T_1}). \quad (2.10)$$

Also, when the longitudinal bulk magnetization is rotated from the z-axis by the application of a  $90^\circ$  RF pulse, it evolves as transverse magnetization and starts precessing in the XY-plane under the influence of the static external field. However, the magnetizations of individual nuclei belonging to a particular ensemble immediately start to dephase (fan out) causing the net magnetization to gradually shrink. Fluctuating local fields which perturb the energy levels of the spin states cause the dephasing. The longer the elapsed time the greater the dephasing, till the transverse magnetization diminishes to zero upon saturation of the whole plane. The time constant that describes how the net transverse magnetization,  $M_{XY}$ , decays from its initial value  $M_{XY0}$  to zero over time is called the spin-spin relaxation time  $T_2$ . This is governed by

$$M_{XY}(t) = M_{XY0} e^{-t/T_2}. \quad (2.11)$$

There are actually two factors that contribute to the decay of transverse magnetization; mutual exchange of spin energies (leading to a pure  $T_2$  molecular effect) and variations in the static external field  $\mathbf{B}_0$  (leading to an inhomogeneous  $T_2$  effect). The combination of these two factors is what actually results in the decay of the transverse magnetization. The combined time constant is called  $T_2^*$  and is expressed as

$$1/T_2^* = 1/T_{2\text{pure}} + 1/T_{2\text{inhomo}}. \quad (2.12)$$

In reality, both  $T_1$  and  $T_2$  processes occur simultaneously, the only restriction being that  $T_2$  is always less than or equal to  $T_1$ . Following a pulse sequence that perturbs the spin system from the thermal equilibrium,  $T_2$  governs the length of time during which the FID can be observed and  $T_1$  governs the minimum time required for equilibrium to be restored.

$T_2$  plays a crucial role in protein NMR studies. It is inversely proportional to the overall rotational correlation time ( $\tau_c$ ) of the particle and thus depends on the mass and shape of the protein (or protein complex). Typical values of  $T_1$ ,  $T_2$  and  $\tau_c$  for proteins in solution are of the order of 1, 0.1 and  $10^{-8}$  s, respectively.

## 2.4.2 Chemical Shift ( $\delta$ )

In NMR spectroscopy, nuclei of different elements (e.g.,  $^1\text{H}$ ,  $^{13}\text{C}$  or  $^{15}\text{N}$ ), because of their different gyromagnetic ratios, yield signals at completely different frequencies when placed in the same external magnetic field (Table 2.1). However, the observed resonance frequencies also depend on the local chemical environments of individual nuclei and hence, even for a single element, differ slightly from the frequencies predicted by Eq. 2.9. The difference between the predicted and observed resonance frequencies is referred to as a chemical shift. It provides the opportunity of distinguishing between nuclei that are identical, but for their location in different chemical environments. The phenomenon of chemical shift arises because the motions of electrons around nuclei, induced by the external magnetic field, generate secondary magnetic fields. The net local magnetic field experienced by a specific nucleus results from the combination of the external and the secondary fields. The effect of the secondary field, called nuclear shielding, can enhance or diminish the effect of the main field. Depending on the surrounding chemical environments, each nucleus experiences a slightly different degree of shielding causing a variation in the local magnetic fields [119, 123]. Consequently, the resonance condition is modified to

$$\omega_{\text{eff}} = \gamma B_{\text{local}} = \gamma B_0(1 - \sigma), \quad (2.13)$$

where  $\omega_{\text{eff}}$  is the effective resonance frequency due to the actual local field,  $B_{\text{local}}$ , experienced by the nucleus and  $\sigma$  is a dimensionless screening or shielding constant. However, it is difficult to determine the exact resonance frequency of a nucleus with absolute accuracy. It is rather much easier to determine the difference between the resonance frequencies of a nucleus of interest and a reference. Since the induced secondary field that causes the chemical shift is about a million times weaker than the applied main static field, the chemical shift is expressed in terms of parts per million (ppm) [119, 123]. This also

removes the dependence of the chemical shift on the applied field strength and makes it a dimensionless number  $\delta$  (Figure 2.5) given by

$$\delta = [(\omega_{\text{int}} - \omega_{\text{ref}})/\omega_0] \times 10^6, \quad (2.14)$$

where  $\omega_{\text{int}}$  and  $\omega_{\text{ref}}$  are the frequencies of the nucleus of interest and the reference nucleus, respectively, and  $\omega_0$  is the operating frequency of the spectrometer. For  $^1\text{H}$ , the reference frequency is usually set to 0 ppm so that  $\omega_{\text{ref}} = \omega_0$ . The most commonly used reference compounds are tetramethylsilane (TMS) and sodium 2,2-dimethyl-2-silapentane-5-sulfonate (DSS). TMS is often used as an external reference while DSS is used as an internal reference.

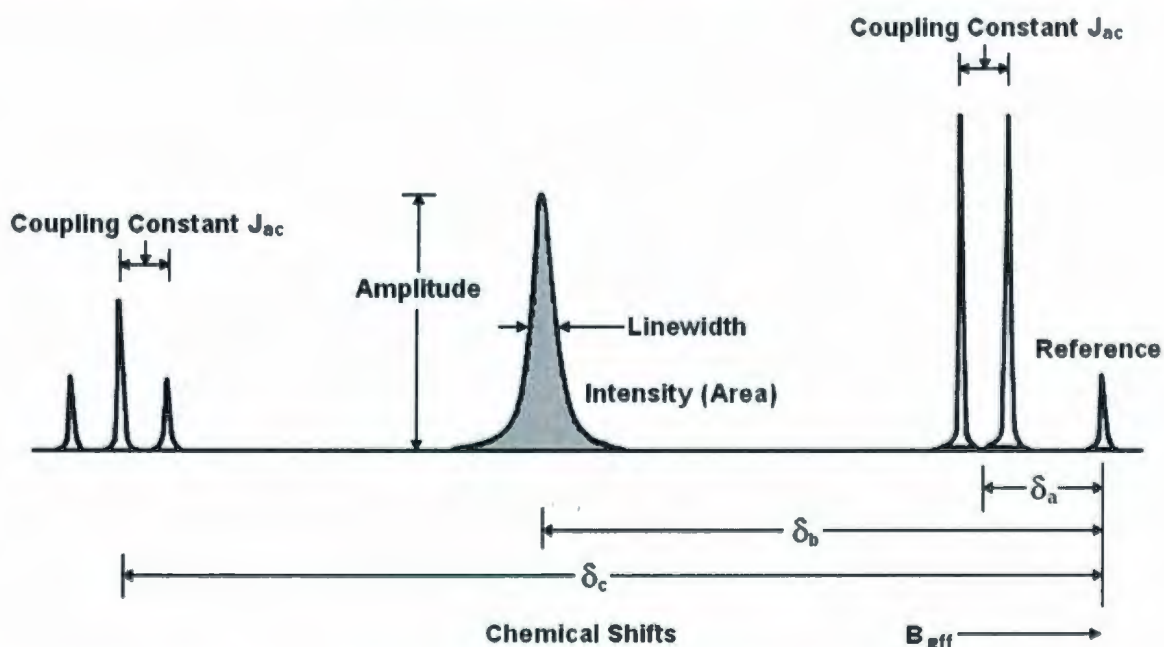


**Figure 2.5 :** Basic NMR spectral parameters. The reference signal is assigned a chemical shift of 0 ppm. The chemical shifts of other signals are measured from the reference and referred to as  $\delta_a$ ,  $\delta_b$  and so on. The height of a signal represents its amplitude and the area under the curve represents its intensity which is proportional to the number of nuclei contributing to the signal. The coupling constant represents the difference between two adjacent multiplets which results from scalar coupling.

### 2.4.3 Linewidth ( $\Delta\nu_{1/2}$ )

In an NMR spectrum, a series of absorption peaks or resonance signals representing resonance frequencies of various ensembles of nuclei belonging to different chemical environments are observed. Under ideal experimental conditions, the area of a signal (not the

height) is directly proportional to the number of nuclei contributing to the signal. The linewidth ( $\Delta\nu_{1/2}$ ) is defined as the full-width at half-height of a signal with Lorentzian lineshape (Figure 2.5) [119, 123]. The linewidth is a key factor affecting both resolution and signal to noise (S/N) ratio of the spectrum. It is exclusively dependent on the spin-spin or transverse relaxation time  $T_2$  and represented by

$$\Delta\nu_{1/2} = 1/\pi T_2. \quad (2.15)$$

The relaxation time  $T_2$ , however, is inversely proportional to the overall rotational correlation time  $\tau_c$  of the molecule in solution. Again,  $\tau_c$  depends on mass (and shape) of the molecule. Thus, the lines are inevitably broader for larger proteins. The line broadening, caused by a fast  $T_2$  relaxation, is the main factor that limits the size of a protein amenable to NMR studies. For smaller proteins, observed linewidths substantially larger than expected primarily indicate an increase in the rotational correlation time, likely caused by a molecular aggregation. If aggregates are large enough, the lines become too broad to observe.

#### 2.4.4 Scalar Coupling (J)

Scalar couplings between nuclei linked via a small number of covalent bonds in a chemical structure result in mutual splitting of the NMR signal from each nucleus into multiplets (Figure 2.5) [119, 123]. Scalar couplings arise from spin-spin interactions mediated by the electrons forming the chemical bonds between the nuclei. The coupling is ordinarily not important beyond three bonds. The two-bond coupling is termed geminal (e.g., H-C-H) while the three-bond coupling is termed vicinal (e.g., H-C-C-H). To a first approximation, the relative intensities of the multiplets are given by binomial coefficients; 1:1 for a doublet (i.e., for a nucleus interacting with another nucleus), 1:2:1 for a triplet (i.e., for a nucleus interacting with two other equivalent nuclei), 1:3:3:1 for a quartet (i.e., for a nucleus interacting with three other equivalent nuclei), and so on. The difference between any two adjacent components of a multiplet is the same and yields the magnitude of the scalar coupling constant (J) in Hz. This is independent of the magnetic field strength. To simplify a protein spectrum and to improve the S/N ratio, selective decoupling is often employed by irradiating the coupled nuclei with a weak RF field.

### 2.4.5 Nuclear Overhauser Effect (NOE)

The nuclear Overhauser effect (or enhancement) (NOE) is the fractional change in intensity of one NMR line when another resonance is irradiated in a double irradiation experiment [124]. It is customarily quoted in percent of the unperturbed resonance intensity. The NOEs are observed because of the dipolar cross-relaxation (through-space) between pairs of nuclei (proton-proton or proton-other spin 1/2) with sufficiently close spatial proximity (usually  $< 5 \text{ \AA}$ ). The intensity of an NOE is proportional to the inverse sixth power of the distance between the two nuclei and also depends on the dynamics of the molecule,

$$\text{NOE} = f(\text{dynamics}) \times 1/r^6. \quad (2.16)$$

Thus the NOEs observed between pairs of protons in a protein characterize inter-proton distances that are invaluable for the high-resolution structure determination. Another application of this effect is the information on a protein's internal dynamics since the NOE intensity is a function of the dynamics too. The dynamics arise since proteins are not rigid molecules and have a certain degree of conformational freedom which is often essential to their biological functions. From an NOE experiment performed for individual amino acids of a protein in physiologically relevant conditions, the rigidity or flexibility of its local backbone conformation can be determined in a quantitative manner [125].

## 2.5 Protein NMR Experiments

A suite of complex multi-dimensional NMR experiments, starting with a simple 1D experiment, are performed to determine the high-resolution structure of a protein as well as to probe its dynamics and interactions. Proton ( $^1\text{H}$ ) is the most useful nucleus in protein NMR studies because of its high natural abundance and large gyromagnetic ratio (Table 2.1). However, spin 1/2 carbon and/or nitrogen nuclei (i.e.,  $^{13}\text{C}$  and  $^{15}\text{N}$ ) are also regularly used in NMR studies by replacement of their natural isotopes ( $^{12}\text{C}$  and  $^{14}\text{N}$ ). The structure determination process begins with identifying which resonance frequency belongs to which magnetic nucleus in the chemical structure of the protein. Afterwards, NOEs are used to identify pairs of protons that are close in space. The NOE data is combined with a restrained

molecular dynamics simulation to provide the 3D atomic coordinates of the protein. Protocols for many protein NMR experiments have been developed over the years with new pulse sequences being developed all the time. Only the experiments used for this Ph.D. work are briefly described here.

In the simple 1D  $^1\text{H}$  experiment, the sample magnetization that lies along the z-axis at thermal equilibrium is rotated into the XY-plane by a  $90^\circ$  RF pulse, applied for  $\sim 10 \mu\text{s}$  at the powers typical of solution NMR probes. After the pulse, the transverse magnetization precesses about the z-axis and decays over time. The time-domain data are acquired by recording the FID during the acquisition period. The FID is then Fourier-transformed to yield the final frequency-domain spectrum. Because the resonance frequency is modulated by the chemical environment that an ensemble of protons finds itself in, the 1D spectrum shows a dispersion of signals resulted from protons at different sites in different amino acids. However, the protons in similar chemical groups (e.g., amide protons or  $\alpha$ -protons) have characteristic ranges of frequencies and hence chemical shifts (Figure 2.6) [119,123].

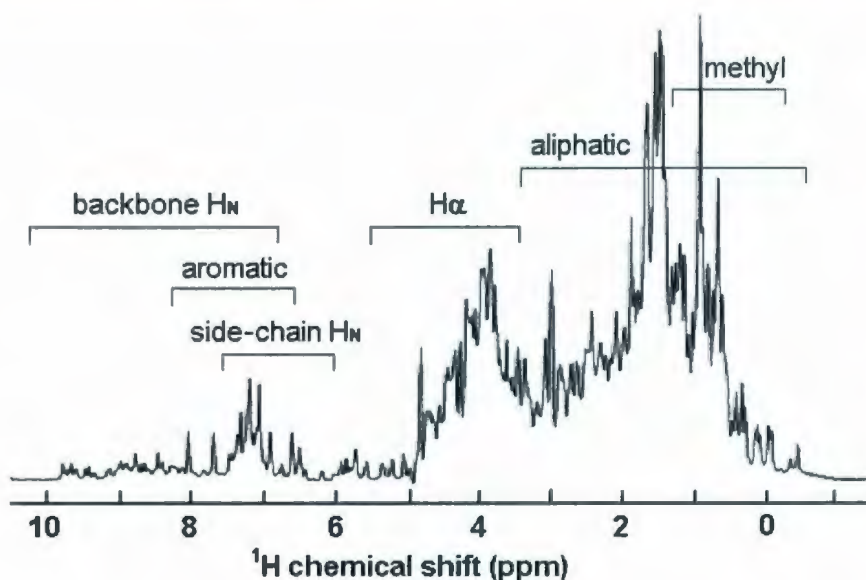


**Figure 2.6 :** Schematic representation of the 1D  $^1\text{H}$  NMR spectrum of a protein. Chemical shift ranges usually observed for the protons from different chemical groups are marked.

The second basic experiment, the proton-detected 2D Heteronuclear Single Quantum Correlation (HSQC), uses a magnetization transfer mechanism. For this experiment, at least some of the  $^{12}\text{C}$  and/or  $^{14}\text{N}$  nuclei must have been replaced by their spin 1/2 isotopes  $^{13}\text{C}$  and/or  $^{15}\text{N}$  during the protein production.  $^{13}\text{C}$  will not be mentioned any further as only  $^{15}\text{N}$

labels were used in this work. The magnetization is transferred from covalently linked  $^1\text{H}$  to  $^{15}\text{N}$  during a part of the pulse sequence called the mixing time. The peaks in the Fourier-transformed 2D spectra are usually shown as contour plots correlating the resonance frequencies of  $^{15}\text{N}$ - $^1\text{H}$  pairs (Figure 2.7) [119,123].

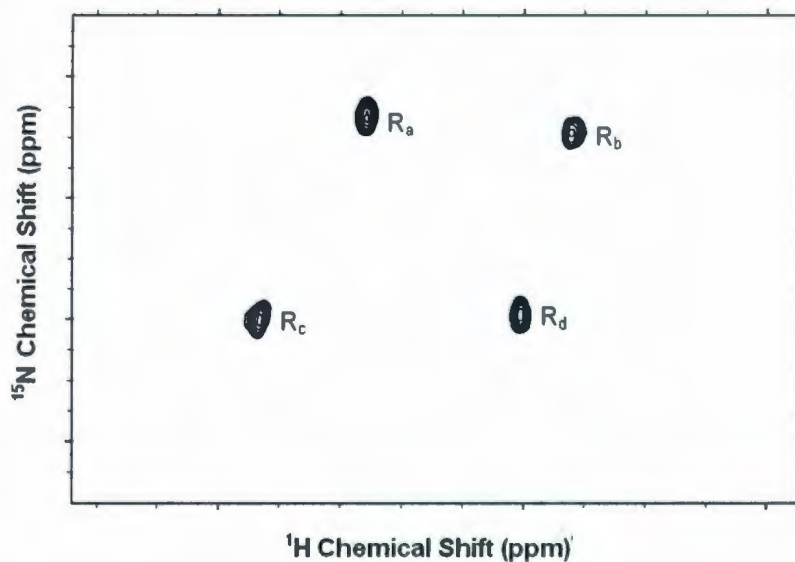


**Figure 2.7 :** Schematic representation of the 2D  $^{15}\text{N}$ - $^1\text{H}$  HSQC spectra of a protein with four  $^{15}\text{N}$ -labeled amino acids  $R_a$ ,  $R_b$ ,  $R_c$  and  $R_d$ . The peaks, represented as contour plots, correlate the resonance frequencies of the four covalently linked  $^{15}\text{N}$ - $^1\text{H}$  pairs.

The 1D  $^1\text{H}$  and 2D HSQC experiments are routinely done to optimize the sample conditions (concentration, pH, temperature, etc.) and to check the status of the sample before and after any long multi-dimensional experiments. These spectra also provide indications of the protein's structural homogeneity, molecular aggregation, dynamics and interactions. Furthermore, preliminary hints on the secondary structure ( $\alpha$ -helix/ $\beta$ -sheet) may be obtained since nuclei belonging to such structures exhibit characteristic frequency shifts with respect to the random coil configuration [126-128].

To determine the structure of a protein, the resonance frequencies of its magnetic nuclei must be determined first. Thus, a number of multi-dimensional homonuclear and heteronuclear experiments are performed leading to the complete resonance assignments. The 2D Total Correlation Spectroscopy (TOCSY) and Nuclear Overhauser Effect Spectroscopy (NOESY) are the standard homonuclear experiments for identifying spin-spin coupling connectivities between pairs of protons. These experiments rely on magnetization transfer along the proton networks, which take place during the mixing period of the pulse

sequence [129]. In TOCSY, the magnetization is transferred from one proton to another through covalent bonds (up to 3 bonds) via scalar coupling. In NOESY, on the other hand, the magnetization transfer is achieved through space (up to  $\sim 5 \text{ \AA}$ ) via dipolar coupling. The diagonal peaks of these 2D spectra reproduce the complete 1D  $^1\text{H}$  spectrum. The off-diagonal or cross-peaks, however, correlate pairs of protons between which the magnetization transfer takes place (Figure 2.8, only a few selected peaks are shown and two are labeled for clarity).

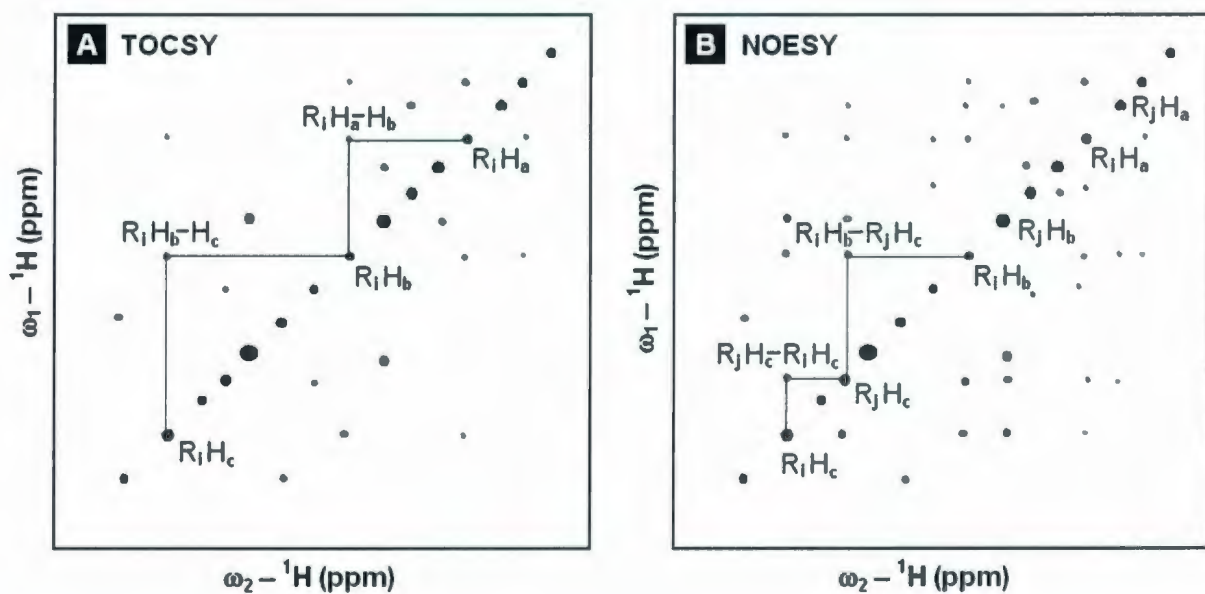


**Figure 2.8** : Schematic representations of the 2D homonuclear NMR spectra of a protein. In TOCSY, the cross-peaks result from the magnetization transfer between protons through covalent bonds (up to 3 bonds) (A). In NOESY, the cross-peaks result from the magnetization transfer between protons through space (up to  $\sim 5 \text{ \AA}$ ) (B). The NOESY spectra consist of peaks from both intra-residue and sufficiently close inter-residue proton pairs. The diagonal peaks reproduce the complete 1D  $^1\text{H}$  spectrum in both. The spectra are symmetrical with respect to the diagonal.

The NOEs (observed as the cross-peaks in the NOESY spectra) act as the primary source of structural information in protein NMR because they indicate the spatial proximity of protons within the molecule. The intensities of the NOEs vary approximately as the inverse sixth power of the inter-proton distances. However, there are difficulties in using the NOE intensity quantitatively since the intensity is also affected by spin diffusion, intra-protein motions and artifacts. Therefore, the intensities of all NOEs are classified into strong, medium and weak categories and, rather than being converted into discrete distances, are

given distance ranges large enough to allow for the effects of motion, etc. on NOE intensity. These distance restraints act as the most crucial inputs in the protein structure calculation. In addition to distance restraints, dihedral angle and hydrogen bond restraints are also generated for amino acids that can be clearly identified as having a particular secondary structure conformation by indicators such as selected NOEs (e.g., strong  $\text{HN}_i\text{-HN}_{i+1}$  indicates  $\alpha$ -helix, strong  $\text{Ha}_i\text{-HN}_{i+1}$  indicates  $\beta$ -sheet, etc.) and chemical shift perturbations of specific nuclei (e.g.,  $\text{Ha}$ ,  $\text{Ca}$ , etc.) based on the random coil chemical shifts [126].

As the 2D homonuclear spectra are crowded with cross-peaks (especially the NOESY), overlapping of peaks, that inevitably occurs in larger proteins, substantially hinders the resonance assignments. The 3D and 4D heteronuclear-edited NMR experiments resolve overlapped peaks according to the chemical shifts of the heteronuclei (e.g.,  $^{15}\text{N}$ ) bonded directly to the protons [130, 131]. In 3D experiments, the spectra are separated along a third dimension ( $^{15}\text{N}$  or  $^{13}\text{C}$ ), so that the  $^1\text{H}\text{-}^1\text{H}$  peaks are distributed throughout a cube instead of a plane. This spreading-out is achieved by combining an HSQC at the end of a TOCSY or NOESY in a single experiment. The FID data are collected after the HSQC instead of at the end of the TOCSY/NOESY [132]. The 4D experiments consist of the concatenation of a NOESY pulse sequence followed by two HSQC building blocks. The peaks in the 4D spectra are separated with respect to one heteronuclei first to generate 3D cubes which are then sliced further with respect to the other heteronuclei attached to the protons [133].

Diffusion-Ordered Spectroscopy (DOSY) provide a measure of the sizes of particles, such as micelles or protein-micelle complexes, undergoing free diffusion in solution by determining the translational diffusion coefficients (also known as diffusion constants) [134]. This method can be used to probe the protein-lipid or protein-protein interactions as the size would change upon binding. The DOSY data are acquired by attenuating the final  $^1\text{H}$  signals to about 5% of the initial amplitudes using gradient pulses. The signals are attenuated gradually by increasing the gradient strength from  $\sim 2\%$  to  $\sim 95\%$  of maximum amplitude in 16 or 32 steps. The conventional 2D DOSY spectra show approximate measures of the translational diffusion coefficients of various species present in the sample with respect to their  $^1\text{H}$  chemical shifts (Figure 2.9 A). The exact value of a diffusion coefficient is

determined from slope of the signal attenuation curve obtained from the underlying 1D  $^1\text{H}$  experiments (Figure 2.9 B). The equation for attenuation of the signal [135] is

$$S = S(0)\exp[-D\gamma^2g^2\delta^2(\Delta - \delta/3)], \quad (2.17)$$

$$\text{or } \ln[S(k)/S(0)] = -Dk, \quad (2.18)$$

$$\text{with } k = \gamma^2g^2\delta^2(\Delta - \delta/3). \quad (2.19)$$

Here  $S$  [or  $S(k)$ ] is the observed signal intensity,  $S(0)$  is the unattenuated signal intensity,  $D$  is the diffusion coefficient,  $\gamma$  is the gyromagnetic ratio of the observed nucleus ( $^1\text{H}$ ),  $g$  is the gradient strength,  $\delta$  is the gradient pulse length and  $\Delta$  is the diffusion time. The size of the particles can then be calculated using the Stokes-Einstein equation for spherical particles undergoing free diffusion in solution,

$$D = k_B T / 3\pi\eta d_H, \quad (2.20)$$

where  $k_B$  is the Boltzmann constant,  $T$  is the absolute temperature,  $\eta$  is the viscosity of the solution and  $d_H$  is the hydrodynamic diameter of the particle. The hydrodynamic diameter corresponds to the diameter of a sphere that would be diffusing at the same rate.

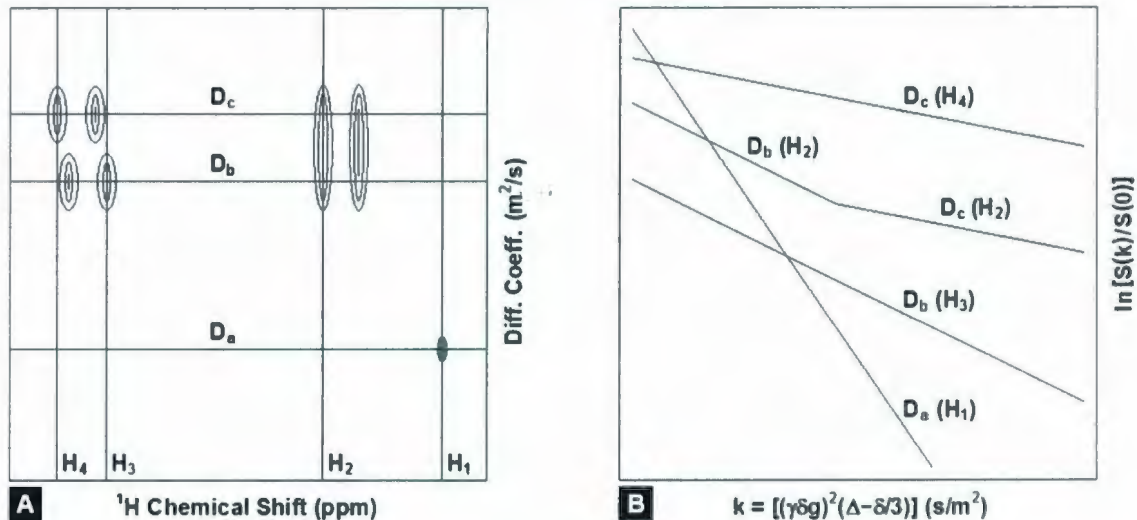


**Figure 2.9 :** Translational diffusion coefficients of the particles obtained from the DOSY data. (A) Schematic representation of the 2D DOSY spectra of a sample consisting of three species. Approximate measures of the diffusion coefficients  $D_a$ ,  $D_b$  and  $D_c$  are obtained from the horizontal positions of the  $^1\text{H}$  peaks. (B) Exact values of the diffusion coefficients are obtained from the slopes of the signal attenuation curves plotted using Eq. 2.18. The peaks at chemical shifts  $H_1$ ,  $H_3$  and  $H_4$  each yield a single linear fit (i.e., a single diffusion coefficient), but the peak at chemical shift  $H_2$  yield two linear fits (i.e., two diffusion coefficients). The hydrodynamic diameters are calculated using the Stokes-Einstein equation (Eq. 2.20).

## 2.6 Protein Structure Calculation

The high-resolution structure of a protein is calculated using computer programs that translate the NMR-derived proton-proton distances and the dihedral angle data into 3D molecular coordinates. The calculated structure reflects both the experimental data, as well as the restrictions on bond lengths, angles, etc. that are known from the chemical structure of the protein. Both the NMR data and the chemical structure data are implemented as empirical energy functions in a restrained molecular dynamics simulation. In practice, first an extended initial structure with ideal covalent geometry is generated using the known amino acid sequence. The computer program then refolds the initial structure in a way so that the experimentally determined distance and angle restraints are satisfied. To achieve this, each known parameter is assigned an energy potential. The program calculates a structure by minimizing the overall energy [136, 137].

Without the spatial restrictions imposed by the experimentally determined distance and dihedral angle restraints, the protein can adopt a huge number of conformations that are still consistent with the covalent geometry derived from its chemistry. It is therefore important to identify as many restraints from the NMR spectra as possible to restrict the conformational space to the subset of space actually sampled by the properly folded protein.

Simulated annealing, combined with the molecular dynamics simulation, is the most commonly used method for calculating the NMR-based structure of a protein in solution. In this method, the initial extended structure is heated to a high temperature in a simulation giving the atoms a high thermal mobility. During the subsequent cooling steps, the initial extended structure evolves towards the energetically favorable and properly folded final structure under the influence of a force field derived from the experimentally determined spatial restraints [136, 137]. In the calculation, the total energy is classified into two categories and given by,

$$E_{\text{Total}} = E_{\text{Empirical}} + E_{\text{Experimental}}, \quad (2.21)$$

$$\text{where } E_{\text{Empirical}} = E_{\text{Bond}} + E_{\text{Angle}} + E_{\text{van-der-Waals}} + E_{\text{Electrostatic}}, \quad (2.22)$$

$$\text{and } E_{\text{Experimental}} = E_{\text{NOE}} + E_{\text{Dihedral}} + E_{\text{H-bond}}. \quad (2.23)$$

The folded final structure is calculated using these energy functions and the simulated annealing protocol which finds the set of atomic coordinates that represents the minimum total energy [136, 137].  $E_{\text{NOE}}$ , the pseudo energy term corresponding to the NOEs, plays the most crucial role in the protein structure calculation. However, the NOE-derived inter-proton distances are imprecise and expressed by a range rather than a specific value. Therefore, many closely related structural models are consistent with the observations. Hence, an NMR-derived protein structure is usually reported as an ensemble of atomic coordinates. The conformational space sampled by the structural ensemble reflects the conformational space sampled by the protein in solution. It is thus beneficial if the experimental conditions match the native conditions.

## 2.7 Strategies for Studying SP-B Peptides

Despite the fact that approximately 30% of all proteins of currently sequenced genomes are associated with lipid membranes [138], structural information on these lipid-associated hydrophobic proteins lags far behind when compared to the water-soluble proteins [139]. This is largely due to the difficulties involved in expression, purification and preparation of physiologically relevant protein samples in lipid-like environments. SP-B is one such lipid-associated and water-insoluble hydrophobic protein which presents unique challenges to structure determination by solution NMR. Attempts for recombinant expression and chemical synthesis of the full-length or near-full SP-B have not succeeded yet. However, some of the successfully produced synthetic fragments have exhibited substantial biological activity when compared to the wild-type protein [109]. I have studied three such SP-B-based peptides in this Ph.D. work. I have used a variety of detergent and lipid micelles to mimic the lipid environment in which SP-B functions in the lungs.

Micelles are self-assembled aggregates of amphiphilic molecules, such as certain detergents and lipids, in water or other polar solvents (Figure 2.10). These amphiphiles contain a polar (hydrophilic) headgroup and one long or two short nonpolar (hydrophobic)

hydrocarbon tail(s) (acyl chain(s)). If the concentration of these molecules in aqueous solution is greater than a certain value, known as the critical micelle concentration (CMC), hydrophobic interactions force them to spontaneously form micelle structures [140, 141]. Under most circumstances, pure micelles are spherical or near-spherical in shape. However, depending on the headgroup area and acyl chain volume/length, other shapes, e.g., cylindrical, can also be adopted. The sizes of micelles vary substantially with composition. Even for a single detergent or lipid, the micelle-size varies considerably with changes in concentration, pH and/or temperature. However, in all types of micelles, the polar headgroups remain exposed to the water molecules and the nonpolar acyl chains get buried inside the core. Small lipid-associated proteins or polypeptides, such as the fragments of SP-B, likely interact with both headgroups and acyl chains of the micelles and fold into physiologically relevant 3D structures (Figure 2.10).

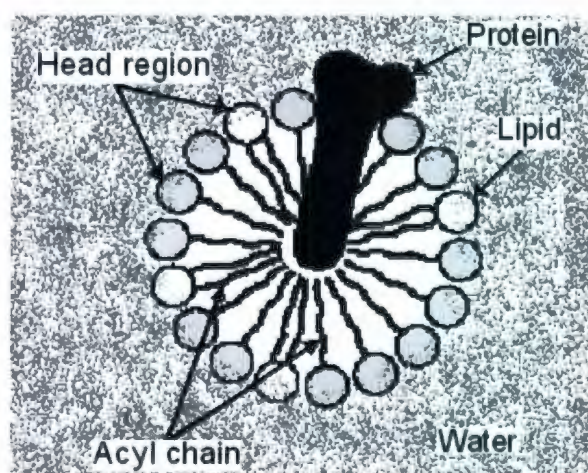


**Figure 2.10** : Schematic representation of a micelle-protein complex. When mixed in water in excess of CMC, amphiphiles with one long acyl chain or two short acyl chains form micelles. These micelles function as lipid environment mimetics for membrane or lipid-associated proteins. The proteins interact with the micelles and likely take on physiologically relevant 3D structures.

In general, the size of a micelle-protein complex is significantly larger than the size of the protein by itself. In aqueous solution, the larger complex tumbles more slowly because of the higher rotational correlation time and thus undergoes a more efficient transverse relaxation. The faster transverse relaxation rate in turn leads to broader lines in the NMR spectra and produces consequent decreases in both resolution and S/N ratio, as well as increases in peak overlap. Therefore, analysis of the NMR data of a micelle-bound protein is much more challenging when compared to a water-soluble protein consisting of the same number of amino acids.

To gain insight into the mechanisms of SP-B's essential roles in lung surfactant function, the conformations of the SP-B-based peptides, their interactions and consequences of oxidation were studied in both zwitterionic and anionic micelles. These micelles mimic the lung lipid environments created by the most abundant surfactant phospholipids with PC and PG headgroups. The work began with the structural studies of Mini-B in micelles composed of anionic detergent SDS. Mini-B's conformation and interactions were then investigated in a variety of micelle systems composed of surfactant phospholipid analogues, namely dodecylphosphocholine (DPC), lysomyristoylphosphatidylcholine (LMPC), lysomyristoylphosphatidylglycerol (LMPG) and an LMPC/LMPG mixture. Interactions of the most abundant surfactant protein SP-A were also investigated in all these micelle systems to aid in the later studies of Mini-B/SP-A interactions in the presence of lipids. Next, the impacts of tryptophan oxidation on the structure of SP-B<sub>8-25</sub> were probed in water alone, organic solvent HFIP, and SDS and DPC micelles. Lastly, the conformation of Maxi-B<sub>CT</sub> was investigated in HFIP and SDS micelles. Figure 2.11 shows the chemical structures of these lung lipid mimetics and the organic solvent.

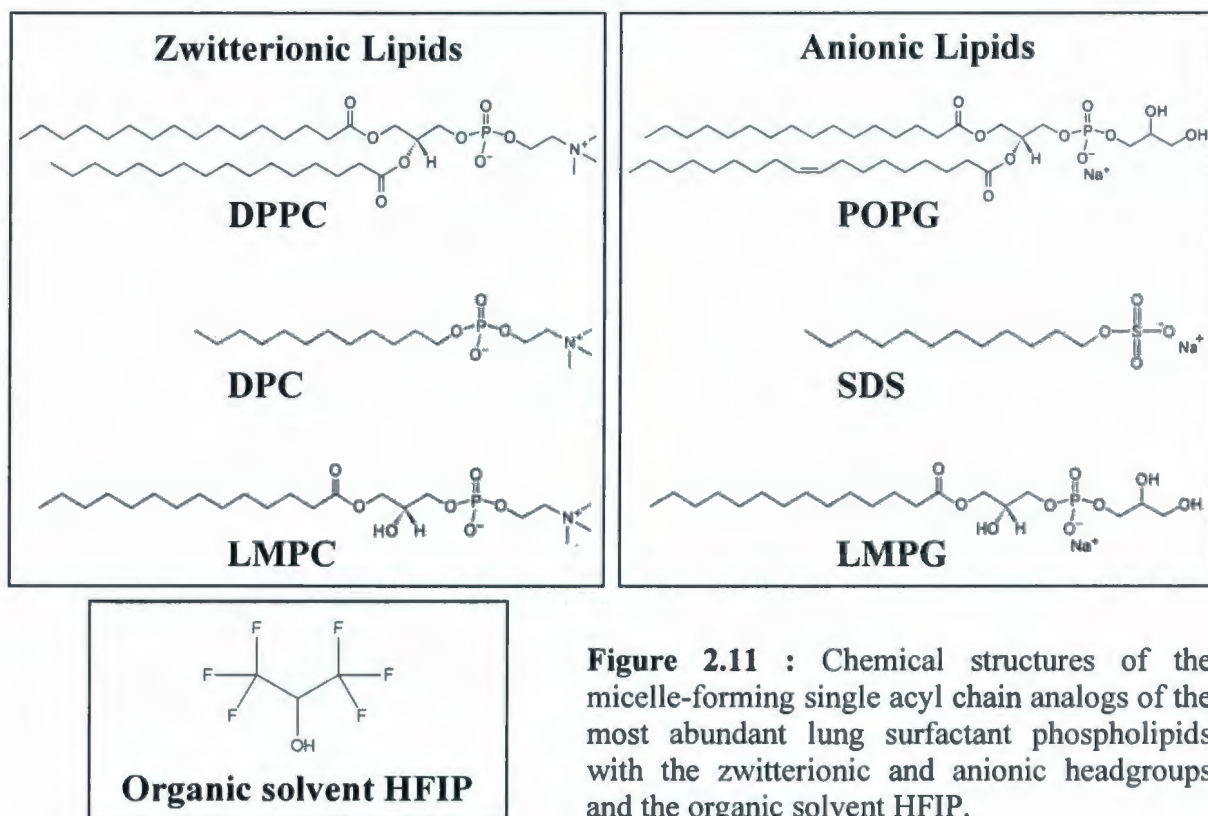


**Figure 2.11 :** Chemical structures of the micelle-forming single acyl chain analogs of the most abundant lung surfactant phospholipids with the zwitterionic and anionic headgroups and the organic solvent HFIP.

## *Chapter 3*

# **Structure of Mini-B, an N-Terminal – C-Terminal Construct of SP-B, in Detergent Micelles**

*Note : Mini-B was synthesized and purified by Prof. Alan J. Waring and his group (Waring lab, Medicine, UCLA). The work presented in this chapter has been published as : Sarker, M., Waring, A. J., Walther, F. J., Keough, K. M. W., and Booth, V. (2007) Structure of Mini-B, a Functional Fragment of Surfactant Protein B, in Detergent Micelles. Biochemistry 46, 11047-11056.*

### 3.1 Overview

Fragments of SP-B containing predicted individual helices or pairs of helices have been shown to retain substantial activity when compared to the full-length protein [101-107]. Mini-B, a 34 residue construct based on the sequence of the N- and C-terminal predicted helices of SP-B (Figure 3.1), demonstrated the most significant biological function among these fragments [109]. Surfactant deficient rats treated with model surfactant preparations containing Mini-B attain oxygenation and lung compliance values as good as, or better than, those achieved in the presence of native SP-B [109]. However, for the study in Ref. [109], the surfactant material was added exogenously and so the findings cannot speak to any additional requirements that may be required for SP-B in naturally produced surfactant, which must somehow travel from the lamellar bodies secreted by type II alveolar cells to the air-water interface. Nevertheless, high resolution structural studies of Mini-B can be expected to unveil at least some of the critical structural features that underlie the activity of SP-B in native lung conditions.

SP-B exhibits a strong cationic profile with nine positively charged and two negatively charged amino acids, yielding a net charge of +7 at neutral pH. Seven of the nine positively charged amino acids are concentrated in the regions covered by Mini-B, giving the same net charge of +7 to this peptide at neutral pH. In addition, about half (44%) of Mini-B amino acids are hydrophobic, which compares well with the 52% hydrophobic amino acids of SP-B. Mini-B also includes the only tryptophan (Trp9) present in the SP-B sequence. Furthermore, Mini-B possesses four of the six conserved cysteines that define the Saposin fold and thus, in its oxidized form, has two disulfide bridges linking the two predicted helices. The function of SP-B is thought to relate to its positive charges, amphipathic helical structure and tryptophan anchor [83, 106, 142]. All these structural features are retained in Mini-B and presumably this is what makes the peptide so functional in model surfactants.

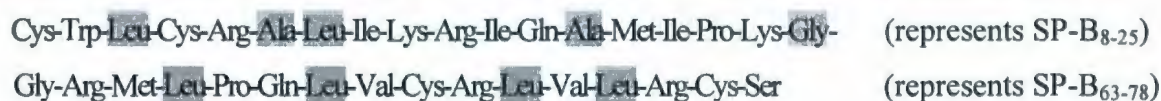
For this part of my work, I have used solution NMR to determine the high resolution structure of Mini-B in the presence of micelles composed from anionic detergent SDS. These



## 3.2 Materials and Methods

### 3.2.1 Peptide Synthesis and Purification

Mini-B was synthesized and purified by the Waring lab (Medicine, UCLA). The peptide was produced by solid phase chemical synthesis using *O*-fluorenylmethyloxycarbonyl (Fmoc) chemistry with nine <sup>15</sup>N-labels. <sup>15</sup>N-leucine was incorporated at positions 3, 7, 22, 25, 29 and 31; <sup>15</sup>N-alanine at positions 6 and 13; and <sup>15</sup>N-glycine at position 18. The primary structure of Mini-B is shown below with gray shading on the <sup>15</sup>N-labeled amino acids :



The peptide was produced with disulfide bonds between C1-C33 and C4-C27. Fmoc amino acids and coupling agents were purchased from AnaSpec (Fremont, CA). The <sup>15</sup>N-labeled amino acids were purchased from Cambridge Isotope Laboratories (Andover, MA) and converted to their Fmoc derivatives by AnaSpec. Organic solvents and other reagents used for the synthesis and purification were high performance liquid chromatography (HPLC) grade or better and purchased from Fisher Scientific (Ottawa, ON) and Aldrich Chemical (St. Louis, MO). The peptide was synthesized at a 0.25 mmol scale in an ABI 431A peptide synthesizer configured for FastMoc double-coupling cycles of all residues for optimum yield [143]. A prederivatized N-Fmoc-O-*tert*-butylserine HMP resin (AnaSpec) was used to assemble the peptide during synthesis. Deprotection and cleavage of the peptide from the resin were carried out using a TFA/thioanisole/EDT/phenol/water mixture (10/0.5/0.25/0.5/0.5 by volume) followed by cold precipitation with *tert*-butyl ether. The disulfide linkages were directed by selective deprotection of the Cys residues at amino acid positions 1 and 33 using trityl side chain protecting protocols and at positions 4 and 27 using acetamidomethyl groups [109]. The disulfide linkages were formed by air mediated oxidation of the peptide in structure-promoting solvents [109]. The crude product was purified by preparative reverse phase HPLC in a Vydac C-18 column using a water/acetonitrile linear gradient with 0.1% trifluoroacetic acid as the ion-pairing agent. The molecular weight of the peptide was

confirmed by fast atom bombardment or MALDI-TOF mass spectrometry. The purity (> 95%) of the final product was determined by analytical HPLC. The purified peptide was lyophilized and stored at 4 °C.

### 3.2.2 Sample Preparation

The sample of Mini-B in SDS micelles was prepared by dissolving 1.5 mM peptide and 150 mM detergent (98% deuterated) in 90% H<sub>2</sub>O and 10% D<sub>2</sub>O with 0.4 mM DSS and 0.2 mM NaN<sub>3</sub>. The deuterated SDS was purchased from Cambridge Isotope Laboratories. The pH of the sample was set at 5.0 using NaOH and HCl solutions, without taking the isotope effects into account. This pH was chosen in order to obtain the NMR spectra in a region where the amide proton/deuteron exchange rate is relatively slow.

### 3.2.3 NMR Data Collection

Solution NMR experiments were performed on Bruker Avance 500 MHz and 600 MHz spectrometers (at Memorial University of Newfoundland) and a Varian INOVA 800 MHz spectrometer (at NANUC, AB). All the spectrometers were equipped with z-gradients. The 1D <sup>1</sup>H experiments used presaturation [144], 2D <sup>15</sup>N-<sup>1</sup>H HSQC experiments used water flip-back [145], and 2D/3D TOCSY and NOESY experiments used water-gate [146] water suppression techniques. Initial 1D <sup>1</sup>H and 2D <sup>15</sup>N-<sup>1</sup>H HSQC experiments were done at three different temperatures (25, 35 and 45 °C using Bruker 500 MHz) to evaluate the temperature dependence of the peptide conformation. It was observed that the peptide exhibited improved conformational homogeneity and less signal overlap at 45 °C. Therefore, all subsequent NMR experiments were conducted at this temperature. Scalar-coupled spin systems were identified using 2D <sup>1</sup>H-<sup>1</sup>H TOCSY (mixing time 80 ms, Bruker 500 MHz). NOE data for structure restraints were obtained from 2D <sup>1</sup>H-<sup>1</sup>H NOESY (mixing time 200 ms, Bruker 500 MHz). Three-dimensional <sup>15</sup>N-edited TOCSY (mixing time 80 ms, Bruker 500 MHz) and three-dimensional <sup>15</sup>N-edited NOESY (mixing time 200 ms, Varian 800 MHz) were used to resolve overlapped peaks.

### 3.2.4 Data Processing and Structure Calculation

The NMR spectra were processed using NMRPipe 2.2 [147] and the frequency assignments were made using Sparky 3.110 [148]. The NOESY spectra were used for generating the distance restraints for the structure calculation. The NOEs were classified into strong, medium and weak categories depending on the peak intensities (heights) and assigned distance ranges accordingly (1.8-2.8 Å for strong, 1.8-3.4 Å for medium and 1.8-5.0 Å for weak). Dihedral angle and hydrogen bond restraints were added for residues that could clearly be identified as  $\alpha$ -helical from local NOE patterns, which were residues 3-14 and 23-32. Hydrogen bond restraints were set to 1.7-2.4 Å for  $O_i \cdots H_{Ni+4}$  and 2.5-3.5 Å for  $O_i \cdots N_{i+4}$ , and dihedral angles were set to  $\phi = -60^\circ \pm 30^\circ$  and  $\psi = -40^\circ \pm 40^\circ$  for these residues. Table 3.1 summarizes the experimental restraints used in the structure calculation. Structures of Mini-B were calculated using the simulated annealing algorithm within CNS 1.1 [149]. Although over half of the NOEs (339 out of 638) were intraresidue, those were not added into the CNS input as they contribute little structural information but their inclusion tends to over-constrain the structure calculation. Structures of Mini-B were viewed by MOLMOL 2k.2 [150]. Whenever possible, stereospecific assignments were made using distances derived from a preliminary structure calculation. A total of 500 structures were calculated for Mini-B. Ensembles of the lowest energy 15 structures were retained for further analysis and deposited to the Protein Data Bank (PDB) [ID 2DWF].

Restraints	Number
Total NOE distance restraints	638
Unambiguous	613
Intra-residue	339
Sequential ( $ i-j  = 1$ )	158
Medium-range ( $ i-j  \leq 5$ )	110
Long-range ( $ i-j  \geq 5$ )	6
Ambiguous (inter-residue)	25
Dihedral angle restraints	44
Hydrogen bond restraints	28
Disulfide bonds	2

**Table 3.1:** Mini-B Structural Restraints. All restraints except for the intra-residue restraints were input in the structure calculation.

### 3.3 Results

Mini-B is based on the N- and C-terminal predicted  $\alpha$ -helices of human SP-B and is composed of the human sequence residues 8-25 joined to 63-78 [109] (Figure 3.1). In full length SP-B, these two predicted helical segments are linked by a pair of cysteine-cysteine disulfide bonds. The structure of Mini-B with the two native-like disulfide bonds was determined in SDS micelles, which provide an environment similar to the lipid-water interfacial environment in which SP-B functions in the lungs. The peptide was produced by chemical synthesis and hence it was feasible to use only limited isotope labeling. Nine of Mini-B's 34 amino acids (6 leucines, 2 alanines and 1 glycine) had  $^{15}\text{N}$  labels.

The 2D  $^{15}\text{N}$ - $^1\text{H}$  HSQC spectra obtained at a variety of temperatures indicated that conformational inhomogeneity and spectral overlap were minimized at a temperature of 45 °C. Therefore, this temperature was chosen for the structural analysis. As expected, the HSQC peaks for Mini-B in SDS micelles are broad, given the large complex size, but at 45 °C they are well-dispersed and resolved (Figure 3.2 A). Eight of the peaks have comparable intensity but there are also some weaker peaks present. One of the weak peaks was later assigned to L3 and the other weak peaks likely arise from minor conformations of L7, G18 and L22. To probe the possibility that protein-protein interactions were responsible for the weak peaks, HSQC spectra were also acquired at lower peptide/micelle concentrations. There was no reduction in the intensity of the weak peaks as compared to the major peaks in either the 0.5 mM Mini-B/50 mM SDS sample or the 0.1 mM Mini-B/10 mM SDS sample (Figures 3.2 B and C). Hence, it does not appear that these weak peaks are the result of protein-protein binding. Rather, these are consistent with a degree of flexibility in SDS-bound Mini-B.

Frequency assignments for Mini-B were made primarily using 2D  $^1\text{H}$ - $^1\text{H}$  TOCSY and NOESY spectra (Figures 3.3 A and B) with the help from  $^{15}\text{N}$ -edited 3D experiments for the  $^{15}\text{N}$ -labeled amino acids. Although there was significant overlap in the spectra of the micelle-bound peptide, with the knowledge of side chain assignments of the reduced Mini-B in HFIP (Sarker, M., M.Sc. Thesis, Booth lab [110]), it was possible to identify the correlations to

confirm frequency assignments for all but  $H_{\alpha}$  of L3, L7 and L22 of the oxidized Mini-B in SDS. NOESY crosspeaks involving C1, W2, L3, C4 and R5 were weak and displayed only a few inter-residue correlations. The relatively weak peak intensity for residues 1 through 5 is consistent with dynamics on an intermediate time scale involving the N-terminal region of the peptide. NOEs indicative of secondary structure and  $H_{\alpha}$  chemical shift index (CSI) are shown in Figure 3.4.  $H_{\alpha_i}-HN_{i+3/i+4}$  NOEs and generally negative CSI values indicate an  $\alpha$ -helical conformation for residues 3-14 and 23-32 of Mini-B.

The structures of Mini-B in SDS micelles (Figure 3.5) were calculated from 299 inter-residue NOEs, plus 44 dihedral angle and 28 hydrogen bond restraints for the helical regions (Table 3.1). In the ensemble of the 15 lowest energy structures, 73% of the residues were found in the most favorable region of the Ramachandran plot, the overall backbone RMSD was 0.98 Å and the backbone RMSD of the helical regions (residues 3-14 and 23-32) was 0.78 Å. Unambiguous inter-helix NOEs were observed between residues R5 and R28, L7 and P23, I8 and C27, K9 and Q24 and W2 and S34. The two helices are packed close to each other and their relative positions are almost parallel.

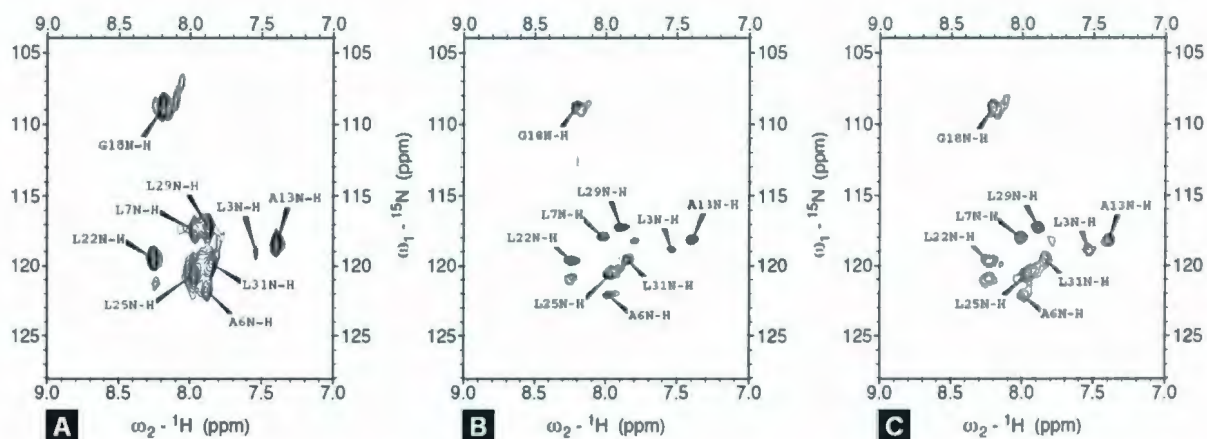


**Figure 3.2 :** 2D  $^{15}\text{N}$ - $^1\text{H}$  HSQC spectra of Mini-B in SDS at different concentrations (pH 5.0, temperature 45 °C). (A) 1.5 mM Mini-B in 150 mM SDS, acquired on a Bruker 500 MHz spectrometer with 16 scans. (B) 0.5 mM Mini-B in 50 mM SDS, acquired on a Bruker 600 MHz spectrometer with 48 scans. (C) 0.1 mM Mini-B in 10 mM SDS, acquired on a Bruker 600 MHz spectrometer with 240 scans. The base contour level shown in (A) is 3 and 4 times higher than that in (B) and (C), respectively. The number of increments acquired in the  $^{15}\text{N}$  dimension in (A) was half of that in (B) and (C) and hence the  $^{15}\text{N}$  lines are broader in (A).

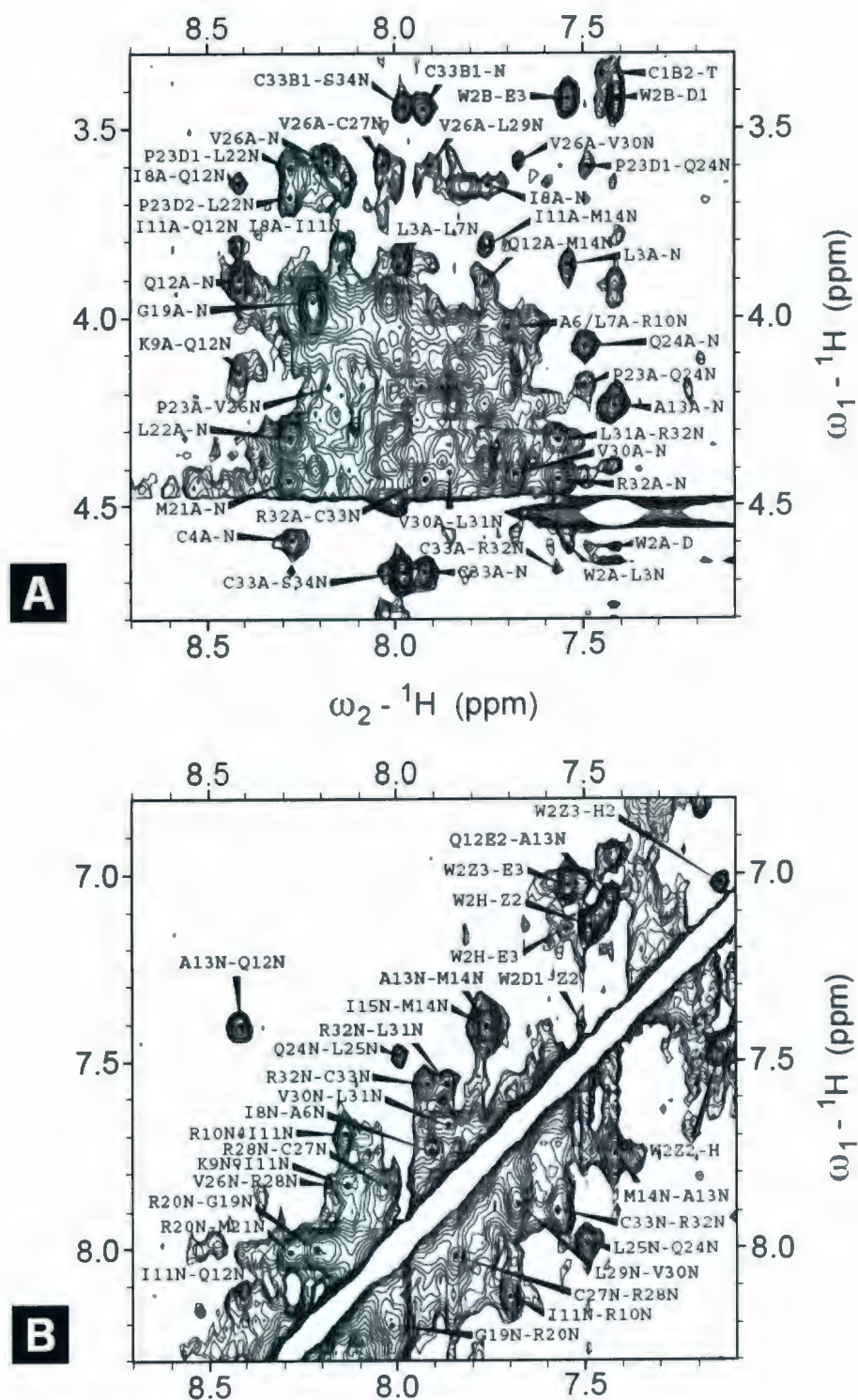


**Figure 3.3** : Portions of 2D  ${}^1\text{H}$ - ${}^1\text{H}$  NOESY spectra of Mini-B in SDS micelles, acquired on a Bruker 500 MHz spectrometer with a mixing time of 200 ms and 128 scans. (A)  $\text{H}\alpha$ -HN region and (B) HN-HN region. Note, all of the peaks displayed were assigned, but for clarity, not all have been labeled in these figures.

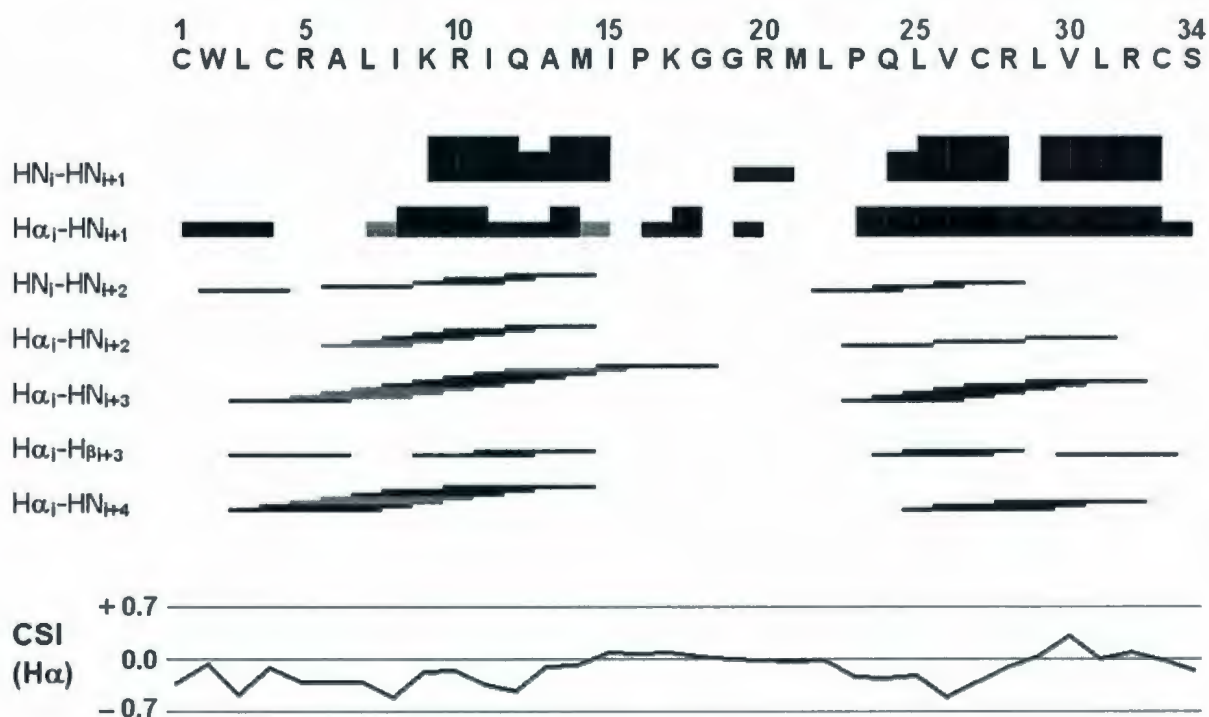


**Figure 3.4** : Secondary structure indicators for Mini-B in SDS micelles. Black bars represent unambiguously assigned NOEs and grey bars represent ambiguous NOEs. For sequential NOEs, the height of the bars corresponds to the intensity of the NOE. The chemical shift index (CSI) for the H $\alpha$  resonances are shown at the bottom. The CSI values were calculated using the random coil chemical shifts obtained from Ref. [151].

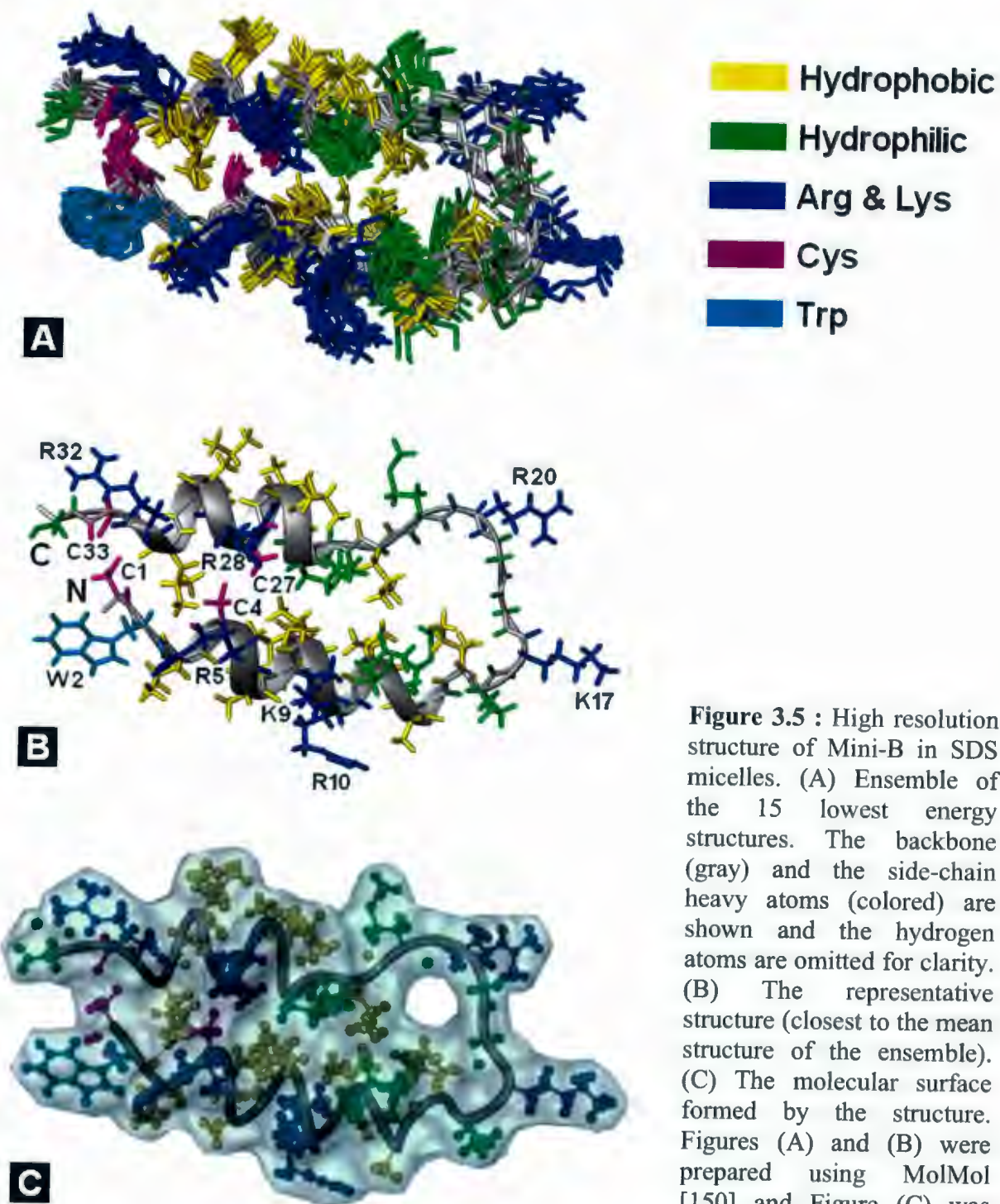


**Figure 3.5 :** High resolution structure of Mini-B in SDS micelles. (A) Ensemble of the 15 lowest energy structures. The backbone (gray) and the side-chain heavy atoms (colored) are shown and the hydrogen atoms are omitted for clarity. (B) The representative structure (closest to the mean structure of the ensemble). (C) The molecular surface formed by the structure. Figures (A) and (B) were prepared using MolMol [150] and Figure (C) was prepared using PPG [152].

### 3.4 Discussion

Although SP-B's contributions to lung function are clearly essential for life, the mechanism by which SP-B acts are still far from being understood. The current evidence points to SP-B-induced lipid restructuring, especially through interactions with anionic lipids, as being a key part of SP-B function [83, 86]. In order to help reveal the structural mechanisms that underlie SP-B's function, I have performed NMR structural studies of Mini-B, a SP-B based peptide that appears to retain much of the essential activities of native SP-B [109]. Mini-B is constructed from the N- and C-terminal helical regions of human SP-B (Figure 3.1). It contains 34 of SP-B's 79 amino acids and possesses the same net charge of +7 at neutral pH as full-length SP-B. Mini-B and native SP-B both contain a high proportion of hydrophobic residues (Ala, Val, Leu, Ile, Phe, and Trp), 41% in Mini-B and 52% in SP-B. The distribution of the positively charged and hydrophobic residues is of high interest since this distribution defines how Mini-B and SP-B interact with lipids. One major finding of this structural study is that Mini-B possesses a strikingly amphipathic surface with most of the positively charged residues localized to one face of the peptide and a large hydrophobic patch on the opposite face (Figure 3.6 A).

SP-B is a member of the Saposin superfamily of proteins whose common structural features are four to five helices and three internal disulfide bonds; two disulfide bonds between the terminal helices and the third one between the two middle helices [91-95]. Mini-B contains the N- and C-terminal predicted helical regions of SP-B and also four of the six cysteine residues that form two intrachain disulfide bonds as in native SP-B. The structure of Mini-B presented herein was determined in the presence of SDS micelles, which provide an anionic, lipid-like environment with a hydrophobic/hydrophilic interface. NMR data was also acquired for the reduced Mini-B in aqueous solution containing 40% HFIP (as part of my M.Sc. work, Booth lab) and used to guide in the spectral assignment of this native-like oxidized Mini-B in SDS micelles.

The experimental structures indicated that, in SDS, Mini-B folds into the predicted two  $\alpha$ -helical segments (Figure 3.5). The two helices are packed tightly together, with

interhelical interactions stabilized by the two disulfide bonds, as well as by several hydrophobic contacts. Ile 8, Ile 11, Ile 15, Leu 22, Pro 23, Leu 25 and Leu 31 are largely buried and make interleaved contacts across the interhelix interface that appear to stabilize the interaction between the helices. Given the extensive hydrophobic contacts, it does seem plausible that some helix-helix association could occur in a native-like lipid environment, even in the absence of disulfide bonds. This is consistent with the observation that reduced SP-B mimics the behavior of native SP-B in lipid-protein films subjected to dynamic compression-expansion cycling, but only in the presence of phosphatidylglycerol [153].

In water, at concentrations higher than the critical micelle concentration, the anionic detergent SDS forms micelles. These micelles are spherical structures of about 5 nm in diameter [154], with the hydrophobic chains on the inside and the negatively charged headgroups on the outside. Such micelles provide a mimic of the lipid environment in which SP-B is thought to function in the lungs. When in association with SDS micelles, Mini-B takes on a strikingly amphipathic structure (Figure 3.6 A). Five of the seven positively charged amino acids (Arg 5, Lys 9, Arg 10, Arg 28 and Arg 32) cluster into a positively charged patch on one face of the peptide. The remaining two cationic amino acids (Lys 17 and Arg 20) extend outwards from the loop connecting the two helices. A large hydrophobic patch, formed mainly by amino acids Leu 3, Leu 7, Val 26, Leu 29 and Val 30, is located on the face opposite to the positively charged patch. This marked partitioning of hydrophobic amino acids to one face and positively charged amino acids to the opposite face is likely key in the mechanism by which Mini-B, and presumably SP-B, functions.

Tryptophan is an amino acid that typically either contributes to the hydrophobic core of a protein or, in lipid-associated proteins, it may “anchor” the protein to the polar/apolar interface. In Mini-B, the tryptophan side chain does not appear to take part in any interhelix interactions (Figure 3.5 B) and therefore its role is most likely in interacting with lipids to help anchor Mini-B at the lipid-water interface. This role is consistent with tryptophan’s location between the hydrophobic face and the charged face of the 3D structure of Mini-B. A critical role for this tryptophan in positioning Mini-B and SP-B at the lipid interface is

supported by previous studies that have found that Trp9 of SP-B is critical for optimal interface affinity [107, 142]. It should be noted that although this tryptophan is at position 9 of SP-B, it is at position 2 of Mini-B and so it is conceivable, although unlikely, that it may take on a different structure when the first seven residues of SP-B are present.

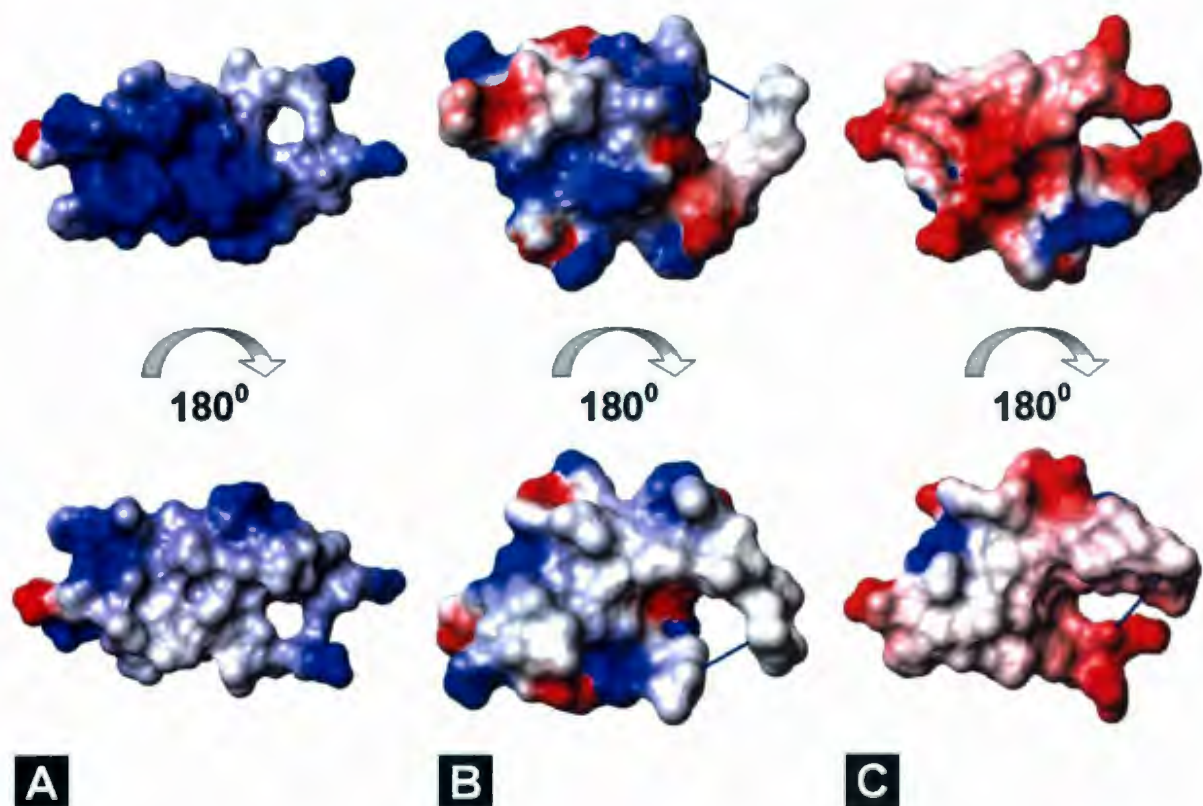


**Figure 3.6 :** Electrostatic potential surface of Mini-B (A) and the corresponding segments of NK-lysine (B) and Saposin C (C). NK-lysine and Saposin C segments are constructed from their PDB coordinates (1NKL [94] and 1SN6 [93], respectively). Positively charged regions are blue and the negatively charged regions are red. The orientation of Mini-B shown in the upper panel of Figure (A) is the same as the orientation used in Figure 3.5. These figures were prepared using MolMol [150].

The middle loop region of Mini-B is composed of part of the loop that connects helices 1 and 2 in full-length SP-B, and part of the loop that connects helices 3 and 4 in full-length SP-B. There are two positively charged amino acids in this loop of Mini-B (one from each of the parent loops of SP-B). The loop is unstructured in Mini-B, and it may be that these side chains are able to reconfigure in such a way as to interact optimally with lipid

molecules. Since the loop is unstructured in Mini-B, it is clear that the loop itself is not forcing any non-native contacts between the two helices. From the Mini-B structure it is not possible to draw any conclusions as to the characteristics of the corresponding loops in full-length SP-B; they may also be unstructured, or they may take on a more defined conformation than the Mini-B loop.

The NMR spectra showed evidence that the structure of some regions of Mini-B were dynamic on intermediate (on the order of milliseconds) and slower timescales. There were several weaker peaks in the HSQC spectra, likely representing minor conformations of amino acids L7, G18 and L22. These peaks did not change relative intensity as the concentration of Mini-B was reduced, and thus it appears that protein-protein binding is not responsible for the minor conformations. Additionally, the intensity of the peaks originating from residues 1 to 5 was relatively low in the NMR spectra, in comparison to the peaks from other parts of the peptide. These spectral features likely indicate a certain degree of plasticity in the regions of Mini-B covering the N-terminus, the N-terminal segment of the first helix, and the loop that connects the two helices. It is possible that this flexibility has a functional role, i.e., to allow Mini-B to form different types of associations with lipids.

Several high resolution structures have been determined for Saposin proteins, the family to which SP-B belongs. These are Saposin A [91], Saposin B [92], Saposin C [93], NK-lysin [94] and Amoebapore A [95], as well as the Saposin related protein Granulysin [96]. All these Saposin proteins form structures consisting of four to five helices, with interactions between the N- and C-terminal helices stabilized by two disulfide bonds and interactions between the middle helices stabilized by a third disulfide bond [Figure 3.1]. However, the structures differ significantly in how the termini helix-pair (which corresponds to the region covered by Mini-B) interacts with the middle helix-pair. In some proteins, such as Saposin A, NK-lysin, Amoebapore A and Granulysin, the two helix-pairs pack together tightly into a “closed” overall structure (Figure 3.7 A). On the other hand, in Saposin B and Saposin C, the pairs of helices do not pack closely together and the overall tertiary structure is relatively “open” (Figure 3.7 B). In Saposin B, the open type structure results in the formation of a large hydrophobic cavity that is likely responsible for its ability to extract

target lipids from membranes [92]. Saposin C, in complex with SDS micelles, also possesses an exposed hydrophobic pocket that is implicated in interactions with lipids [93]. Figure 3.6 shows the electrostatic surfaces for Mini-B and, for comparison, the corresponding regions of NK-lysin, as a representative of the closed type Saposin structure, and Saposin C, as a representative of the open type Saposin structure. The surfaces on the bottom row of Figure 3.6 represent the face of the termini helix-pair that is positioned to interact with the middle part of the protein. Mini-B more resembles the Saposin C helix-pair, which exhibits primarily hydrophilic (although negatively charged in this case) and hydrophobic opposite faces, than it does the NK-lysin structure which exhibits far a less amphiphilic surface.

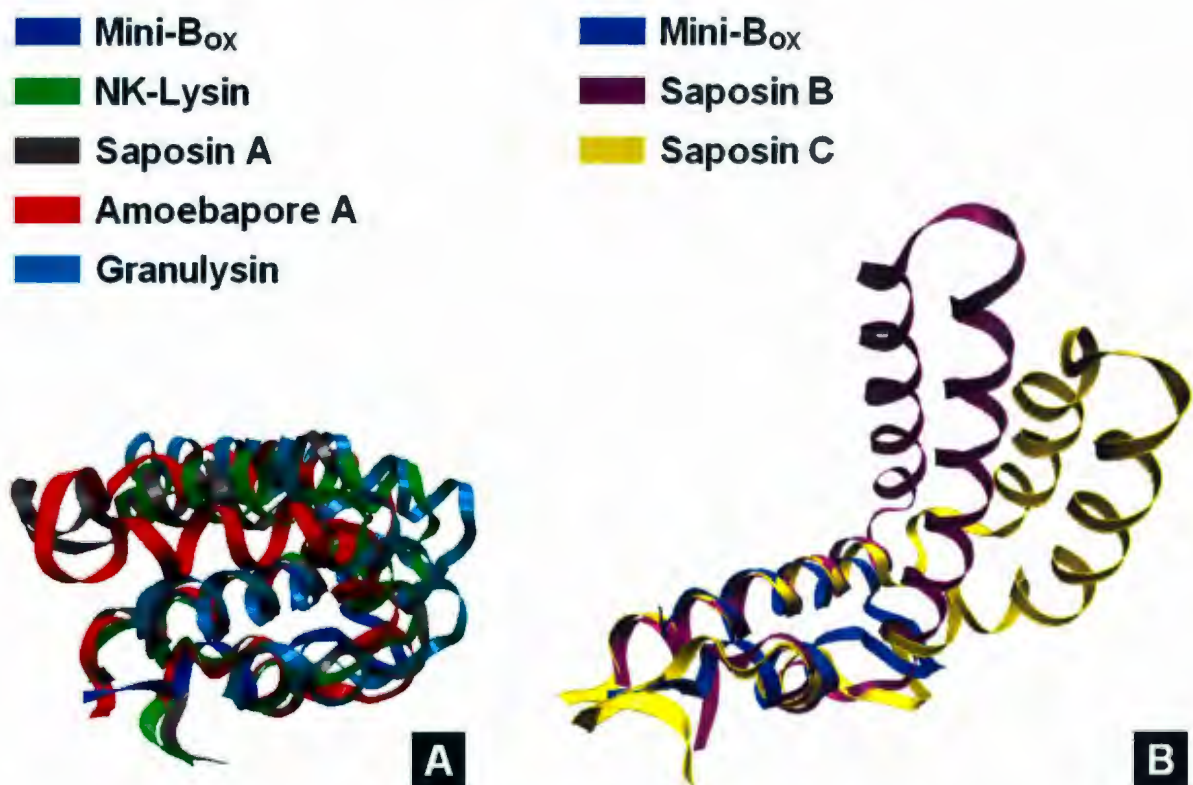


**Figure 3.7 :** Overlay of the backbone structures of Mini-B and other Saposin family proteins. (A) Mini-B and “closed-type” Saposins; NK-lysin [94], Saposin A [91], Amoebapore A [95] and Granulysin [96]. (B) Mini-B and “open-type” Saposins; Saposin B [92] and Saposin C [93]. This figure was prepared using VMD [155].

SP-B has been observed to exhibit a number of *in vitro* behaviors relating to its interactions with lipids, such as promoting phospholipid vesicle aggregation, fusion and lysis,

promoting rapid adsorption of surfactant material to an air-water interface, and re-adsorption of surfactant material to the interface during compression-expansion cycling [82]. These *in vitro* activities relate to three important properties of lung surfactant activity *in vivo*: rapid interfacial absorption, surface tension reduction during compression and re-spreading of the surface film during subsequent expansion. A number of potential molecular mechanisms for SP-B's essential contributions to these critical lung surfactant properties have been proposed [27]. SP-B may act as a bridge between bilayers and/or between bilayers and monolayers to keep components that are squeezed out during compression in close association with the interface for rapid respreading. SP-B may stabilize high-energy intermediates required for phospholipids to pass into the interfacial monolayer. SP-B may induce lipid-packing perturbations leading to transfer of surfactant material to the interface. SP-B may act as a sort of carrier, taking associating molecules with it to the interface. The structure of Mini-B in SDS, with its strikingly amphipathic surface and projecting tryptophan anchor, appears very well suited for making strong interactions with lipids, especially anionic species, at an interface. The hydrophobic face provides a surface for interactions with several lipid acyl chains, the positively charged face provides a surface for interactions with negatively charged lipid headgroups, and the tryptophan side chain, which is itself amphipathic, extends out from the surface in a position to anchor Mini-B at the interface. The relatively large extent of the positively charged patch suggests that this surface may be able to interact with a second lipid layer through electrostatic interactions, or at least reduce the electrostatic repulsion between negatively charged lipid layers, allowing them to stay in closer association.

Mini-B is considerably more effective in rat lung oxygenation and dynamic compliance assays than its unlinked N and C-terminal halves, even when they are added together [109]. This indicates that there is indeed extra functionality associated with Mini-B's relatively large hydrophobic and cationic surfaces. Now that Mini-B's structure and resonance frequency assignments are known, it will be possible in future studies to directly observe Mini-B's interactions with phospholipids and other proteins. In particular, it will be of interest to study Mini-B's structure and lipid interactions in more physiologically relevant systems than SDS micelles, such as phospholipid monolayers and bilayers.

## *Chapter 4*

# **Mini-B in Model Surfactant Lipids: Conformations and Interactions**

*Note : Mini-B was synthesized and purified by Prof. Alan J. Waring and his group (Waring lab, Medicine, UCLA).*

## 4.1 Overview

Biophysical studies have produced a long list of SP-B *in vitro* activities including membrane binding, membrane lysis, membrane fusion, promotion of lipid adsorption to air-water surfaces, stabilization of monomolecular surface films and respreading of films from collapsed phases [82]. Although it is not clear which of these activities, if any, underlies SP-B's essential roles *in vivo*, it is plausible that interactions between SP-B and phospholipids make crucial contributions to lung surfactant function. SP-B's profile of 52% nonpolar amino acids, as well as nine positively charged and two negatively charged amino acids, enables the protein to engage in both electrostatic interactions with lipid headgroups and hydrophobic interactions with lipid hydrocarbon acyl chains. However, the lack of knowledge of the high-resolution structure of SP-B hinders direct probing of its interactions with lipids at molecular and submolecular levels.

Mini-B, an N-terminal – C-terminal construct from SP-B, has been shown to provide excellent response in animal models [109]. Surfactant deficient rats treated exogenously with model surfactant preparations containing Mini-B attain oxygenation and dynamic lung compliance values as good as, or better than, those achieved in the presence of native SP-B [109]. This indicates that Mini-B likely represents the most functionally active region of the full-length protein. Now that the high-resolution structure of Mini-B in SDS micelles and the resonance frequencies of its amino acid spin systems are determined (Chapter 3 and [156]), it is possible to directly probe Mini-B's interactions with surfactant phospholipids and other proteins. In particular, it is of interest to study Mini-B's conformation and lipid interactions in more physiologically relevant systems. Thus, in this part of my work, I have used solution NMR to investigate the conformation of Mini-B in dodecylphosphocholine (DPC), lysomyristoylphosphatidylcholine (LMPC) and lysomyristoylphosphatidylglycerol (LMPG) micelles and probe its interactions with these lipids, alongside the SDS micelles. DPC and LMPC are analogues of DPPC, an abundant zwitterionic surfactant phospholipid generally considered to be of paramount importance in attaining low surface tension at the alveolar air-water interface [24]. LMPG, on the other hand, is an analogue for PGs, the anionic surfactant

phospholipids that SP-B is thought to preferentially bind in surface monolayers of surfactant films [83, 84]. Also studied were Mini-B's interactions with a mixed LMPC/LMPG micelle system containing approximately the physiological ratio of PC to PG (85% : 15%). Furthermore, the reduced version of Mini-B that lacks the two native-like disulfide bonds between the helices was studied in SDS and DPC micelles. The structure of this version was determined previously in organic solvent HFIP (Sarker, M., M.Sc. Thesis, Booth lab [110]). Since the reduced Mini-B also retains a considerable portion of the biological activity of full-length SP-B [109], it was worth looking at its conformation in micelle environments and learning about Mini-B's interactions with lipid mimetics, even in the absence of disulfide bonds. Figure 4.1 shows the chemical structures of the detergent mimetics and phospholipid analogues of PC and PG used in these studies.

In addition to observing Mini-B's conformation in physiologically relevant lipid systems and probing its interactions with model surfactant lipids, this part of my work provided a foundation for studying Mini-B/SP-A interaction in the presence of these surfactant phospholipid analogues that was carried out later (Chapter 6).

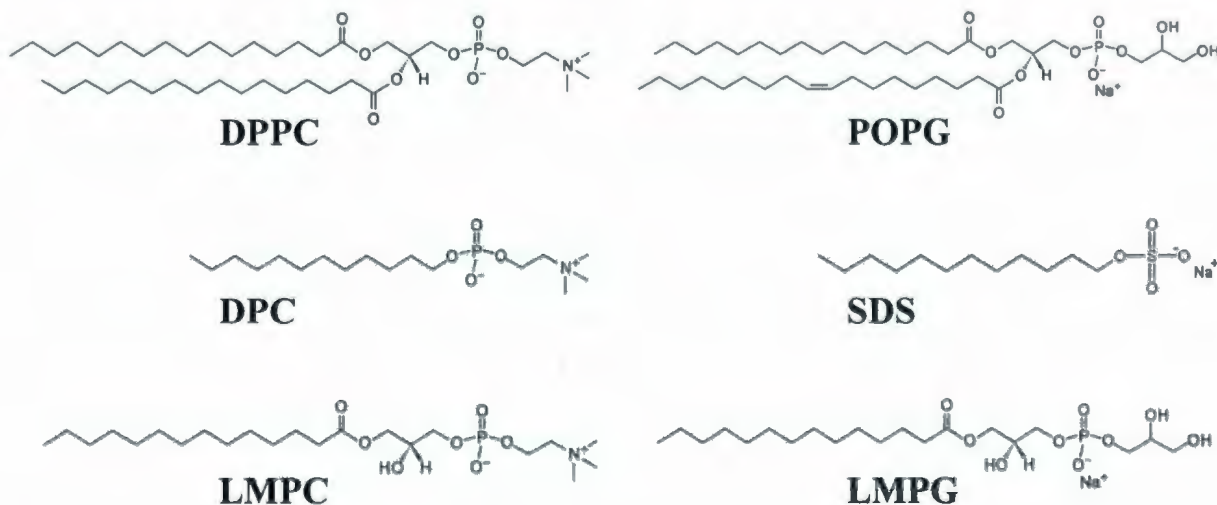


**Figure 4.1** : Chemical structures of the micelle-forming detergent mimetics and phospholipid analogues of the two most abundant zwitterionic and anionic lung surfactant phospholipids DPPC and POPG. The headgroups of DPPC and LMPC are identical while the neck region of DPC is slightly different. The headgroups of POPG and LMPG are also identical but that of SDS is different.

## 4.2 Materials and Methods

### 4.2.1 Peptide Synthesis and Purification

Mini-B was synthesized and purified by the Waring lab (Medicine, UCLA). The peptide was produced by solid phase chemical synthesis using *O*-fluorenylmethyloxycarbonyl (Fmoc) chemistry and purified by preparative reverse phase HPLC in a Vydac C-18 column as described previously (Chapter 3 and [156]). Two versions of Mini-B were synthesized. The oxidized version (termed as Mini-B<sub>OX</sub>) contained two disulfide bonds as in the native protein [156]. The other version was in reduced form (termed as Mini-B<sub>RED</sub>) and thus lacked the disulfide bonds [110]. Both versions of Mini-B possessed nine backbone <sup>15</sup>N-labeled amino acids as shown with gray shading in Chapter 3 (Section 3.2.1, Page 46).

### 4.2.2 Sample Preparation

Mini-B<sub>OX</sub> samples were prepared in DPC, LMPC, LMPG and mixed LMPC (85%)/LMPG (15%) micelles, alongside SDS micelles. Mini-B<sub>RED</sub> samples were prepared in SDS and DPC micelles only. At least two Mini-B samples were prepared for each micelle system with varying peptide/lipid ratios. The exact composition of each sample is described in the results section. First, a stock buffer solution was prepared in H<sub>2</sub>O/D<sub>2</sub>O (90%/10%) with 0.4 mM DSS, 0.2 mM NaN<sub>3</sub>, and 4.5 mM Hepes (except for the Mini-B<sub>RED</sub> samples). The final NMR samples were then prepared by dissolving required quantities of Mini-B and detergent/lipid in the buffer. For each sample, the molar concentration of the detergent/lipid was kept at least 100 times higher than the peptide. Deuterated (98%) SDS and DPC were purchased from Cambridge Isotope Laboratories (Andover, MA). Non-deuterated LMPC and LMPG, purchased from Avanti Polar Lipids (Alabaster, AL) were used, as deuterated versions of these lipids were not available commercially to date. Hepes was also in the non-deuterated form. The pH of the samples was set to 7.0, 6.9 or 5.0 (the exact value for

each sample is reported in the results section) using NaOH and HCl solutions without taking the isotope effects into account. The pH values were chosen in order to either match the physiological condition (~ 6.9) or to match with the Mini-B structural studies (5.0).

### 4.2.3 NMR Data Collection and Processing

A set of 1D  $^1\text{H}$ , 2D  $^{15}\text{N}$ - $^1\text{H}$  HSQC and 2D DOSY experiments was performed for Mini-B in each micelle system on a Bruker Avance II 14.1 Tesla (600 MHz) spectrometer (Billerica, MA) equipped with z-gradients and an inverse triple resonance TXI probe. The NMR data were collected and processed using the Bruker Topspin 2.0 software. The pulse length (P1) and the transmitter offset (O1) were optimized for each sample before running the full set of NMR experiments. The 1D  $^1\text{H}$  and 2D  $^{15}\text{N}$ - $^1\text{H}$  HSQC spectra were acquired at 37 °C to match the physiological temperature. In 1D  $^1\text{H}$  experiments, data were collected with 64 to 320 scans (indicated in the figure captions) using the water-gate water suppression technique [146] and processed using an exponential apodization function with 1 Hz line broadening. The 2D  $^{15}\text{N}$ - $^1\text{H}$  HSQC spectra were acquired with 64 to 320 scans (indicated in the figure captions) using the flip-back water suppression technique [145] and processed using the Qsine apodization function with a sine bell shift of 2. The 2D DOSY experiments were performed using pulsed field gradient (PFG) NMR [157]. The pulse sequence used a stimulated echo with bipolar gradient pulses and one spoil gradient [158], followed by a 3-9-19 pulse for water suppression [159]. The DOSY spectra of SDS and DPC samples were acquired at 37 °C. However, for LMPC and LMPG samples, the DOSY spectra were acquired at 25 °C to minimize the effect of thermal convection. The diffusion time was kept constant at 100 ms. The gradient pulse length was optimized for each sample and set between 3 and 8 ms. The maximum amplitude of the gradient strength was 35 G/cm and the  $^1\text{H}$  signals were attenuated in 32 steps. The translational diffusion coefficient was determined from the slope of the signal attenuation curve plotted using Eq. 2.17. The hydrodynamic diameter was calculated using the Stokes-Einstein equation [Eq. 2.20]. The viscosity of pure water was used for the viscosity of solution in the calculation and the values were  $8.91 \times 10^{-4}$  kg/m.s at 25 °C (298 K) and  $6.92 \times 10^{-4}$  kg/m.s at 37 °C (310 K).

## 4.3 Results

### 4.3.1 Mini-B in SDS Micelles

The SDS micelles used in the structural studies of Mini-B (Chapter 3) provided a first approximation of the physiological lipid environment of SP-B in the lungs and thus this micelle system was included in the analysis of Mini-B/lipid interactions. However, the experimental conditions used in the structural studies were optimized for the structure determination rather than to best mimic the lung conditions. Therefore, to best probe the lipid interactions, these conditions were modified to better reflect the *in vivo* conditions, and thus most of the SDS spectra were re-acquired at lower protein concentrations and physiological pH and temperature.

Figure 4.2 shows the 1D  $^1\text{H}$  spectra of both oxidized and reduced versions of Mini-B in SDS micelles. The signals seen in the 6-9 ppm region, enlarged and shown in the bottom panel, correspond mostly to the backbone amide protons (HNs) of Mini-B. The spectral dispersion and intensity of these signals indicate that both versions of Mini-B are structured in SDS micelles even under conditions that are different from the structural studies (Chapter 3 and [110]).

The 2D  $^{15}\text{N}$ - $^1\text{H}$  HSQC spectra, shown in Figure 4.3, also indicate a similar degree of structuring in more physiological conditions, as compared to the conditions used for the structural studies. The peaks seen in the HSQC spectra correspond to the backbone  $^{15}\text{N}$ - $^1\text{H}$  correlations. However, although Mini-B carries nine backbone  $^{15}\text{N}$ -labeled amino acids, there are eight strong peaks and about five additional weak peaks present for Mini-B<sub>OX</sub>. As is known from the structural studies, the eight strong peaks and one weak peak correspond to the nine  $^{15}\text{N}$ -labeled amino acids and represent the major conformation of Mini-B<sub>OX</sub>. The additional weak peaks likely represent minor conformations of some flexible regions of the peptide, as discussed in Chapter 3 (Section 3.4, Page 57). For Mini-B<sub>RED</sub>, nine strong peaks

are present only and there are no additional weak peaks seen. This suggests a homogeneous structuring of Mini-B<sub>RED</sub> in SDS micelles. Comparison of the HSQC spectra from the two Mini-B versions shows differences in chemical shift of at least two peaks (from Leu3 and Leu31) indicating a difference in the chemical environment for these amino acids between the oxidized and reduced versions. Thus, Mini-B<sub>OX</sub> and Mini-B<sub>RED</sub> exhibit differences in the conformational homogeneity and structures. However, both versions of the peptide appear to take on similar  $\alpha$ -helical secondary structures and the main difference is likely present in their tertiary structures.

The effect of Mini-B<sub>OX</sub> on the size or shape of SDS micelles is probed using the translational diffusion coefficients of pure SDS micelles and the Mini-B<sub>OX</sub>/SDS complex obtained from the 2D DOSY spectra (Figure 4.4). The DOSY data are acquired using the same molar concentrations of SDS and Mini-B<sub>OX</sub> as in the structural studies, i.e., 150 mM SDS and 1.5 mM Mini-B<sub>OX</sub>. Two values of average diffusion coefficients are measured for SDS micelles alone and for the Mini-B<sub>OX</sub>/SDS complex, from the attenuation of the two sharpest SDS peaks at 0.80 ppm (corresponding to CH<sub>3</sub>) and 1.22 ppm (corresponding to (CH<sub>2</sub>)<sub>3-11</sub>). The excellent linear fits shown in the plots of Figure 4.4 indicate that each sample is dominated by a particle of one distinct size. The diffusion coefficients of pure SDS micelles are  $1.388 \times 10^{-10}$  and  $1.385 \times 10^{-10}$  m<sup>2</sup>/s and those of the Mini-B<sub>OX</sub>/SDS complex are  $0.900 \times 10^{-10}$  and  $0.971 \times 10^{-10}$  m<sup>2</sup>/s, from the two peaks respectively. The corresponding hydrodynamic diameters, calculated using the Stokes-Einstein equation, are 4.73 and 4.74 nm for the micelles alone and 7.29 and 6.76 nm for the peptide/micelle complex.

The extraction of the hydrodynamic diameter of pure micelles from the translational diffusion coefficient is accurate only at low concentrations. Above CMC, the diffusion coefficients correspond to a weighted average of free and micelle-bound detergent/lipid molecules [218, 219]. Therefore, the measured hydrodynamic diameter corresponds to the lower size-limit for the micelles. In addition, at high concentrations, e.g., above  $\sim 100$  mM for SDS, the micelles experience an obstructed diffusion as a result of crowding [218]. The crowding produces an opposite effect to the observed diffusion coefficients and the measured hydrodynamic diameters of the micelles tend to be larger. Thus, at 150 mM SDS

concentration, both effects will take place simultaneously. A more complex behavior can be expected when Mini-B<sub>OX</sub> is bound to the micelles. All the same, the apparent size of the micelles increases substantially upon the inclusion of the peptide.

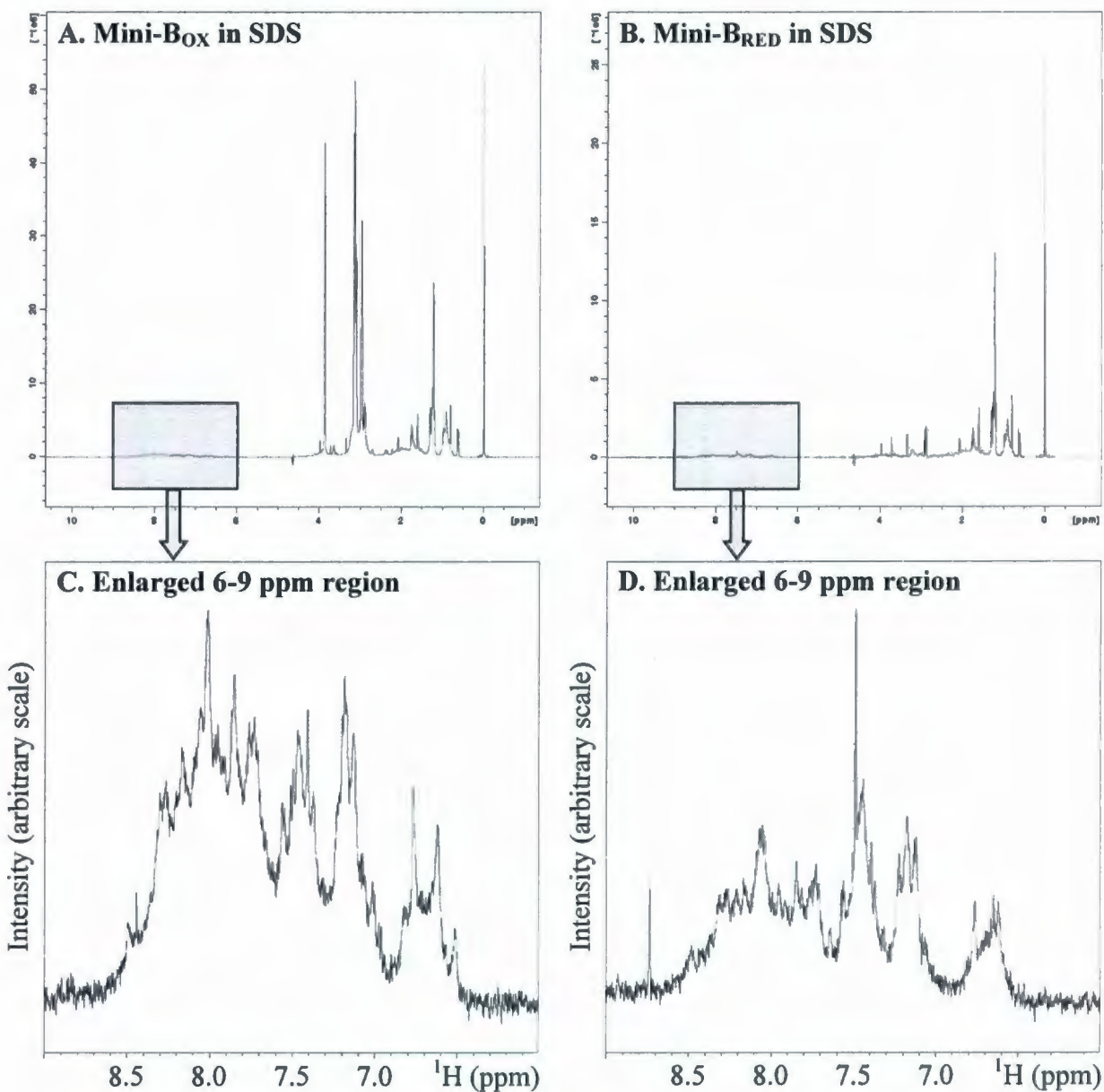


**Figure 4.2 :** 1D <sup>1</sup>H spectra of (A) 0.20 mM Mini-B<sub>OX</sub> in 40 mM SDS in the presence of 4.5 mM Hepes at pH 6.9 (acquired using 256 scans) and (B) 0.75 mM Mini-B<sub>RED</sub> in 75 mM SDS at pH 5 (acquired using 64 scans). Both experiments were performed at temperature 37 °C and the spectra were processed with 1 Hz line broadening. The intense peaks seen in the spectra are from DSS and Hepes. The 6-9 ppm regions, exhibiting the protein HN signals, are enlarged and shown in the bottom panels (C and D).

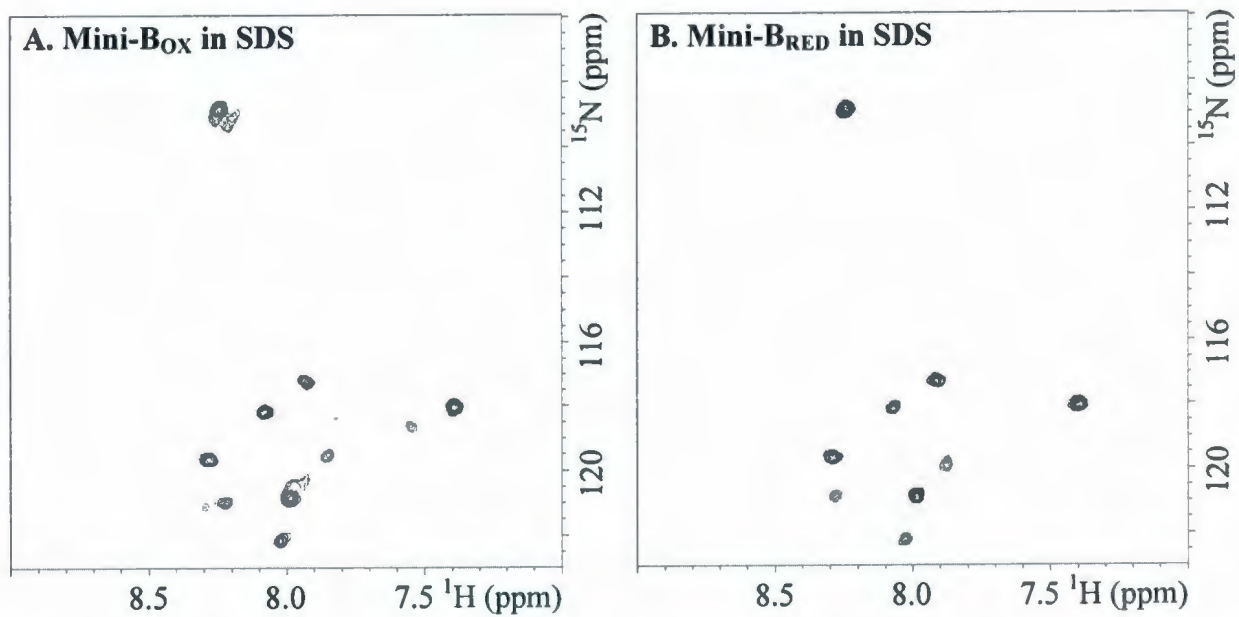
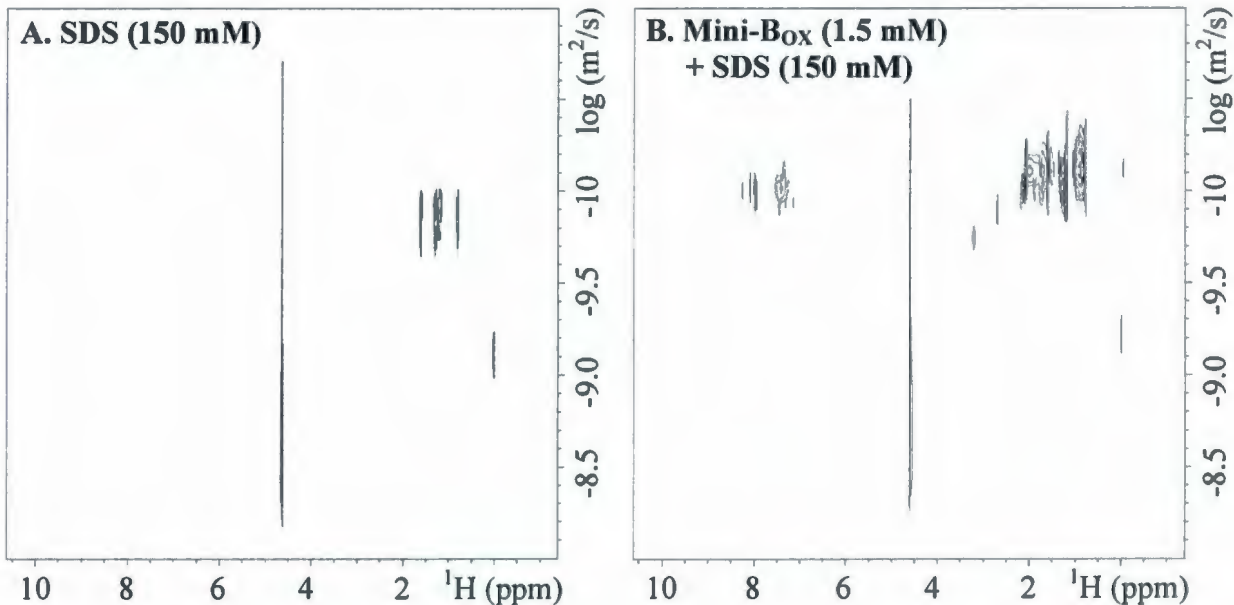
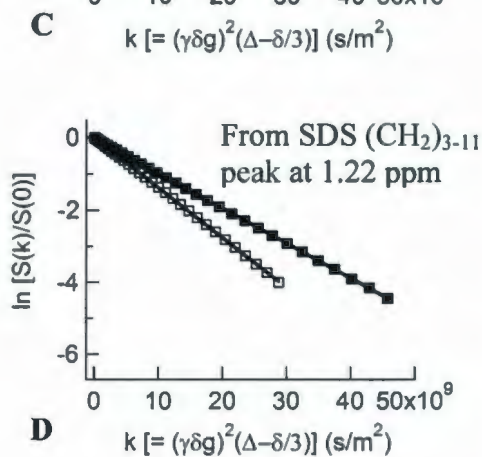
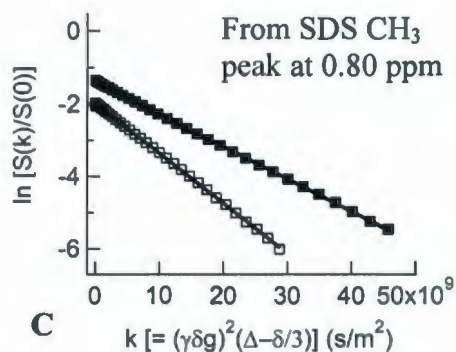


**Figure 4.3 :** 2D  $^{15}\text{N}$ - $^1\text{H}$  HSQC spectra of (A) 0.20 mM Mini-B<sub>OX</sub> in 40 mM SDS in the presence of 4.5 mM Hepes at pH 6.9 (acquired using 160 scans) and (B) 0.75 mM Mini-B<sub>RED</sub> in 75 mM SDS at pH 5 (acquired using 64 scans). Both experiments were performed at temperature 37 °C. The base contour level shown in (A) is two times higher than (B).



□□□□ SDS Micelles  
 ■■■■ Mini-B<sub>ox</sub>/SDS Complex



Peak at ppm	SDS (□□□)		Mini-B <sub>ox</sub> /SDS (■■■)	
	D. Coeff. ×10 <sup>-10</sup> (m <sup>2</sup> /s)	H. Dia. (nm)	D. Coeff. ×10 <sup>-10</sup> (m <sup>2</sup> /s)	H. Dia. (nm)
0.80	1.388 (± 0.004)	4.73	0.900 (± 0.002)	7.29
1.22	1.385 (± 0.002)	4.74	0.971 (± 0.001)	6.76

E

**Figure 4.4 :** SDS micelles (□□□) and Mini-B<sub>ox</sub>/SDS complex (■■■) sizes as indicated by translational diffusion. Upper panels show 2D DOSY spectra of (A) 150 mM SDS and (B) 1.5 mM Mini-B<sub>ox</sub> + 150 mM SDS, at pH 7 and temperature 37 °C. Linear fits (C and D) show the attenuation of the peaks at 0.80 and 1.22 ppm obtained from the DOSY data. The observed diffusion coefficients, represented by the slopes of the curves, and the corresponding hydrodynamic diameters, calculated using the Stokes-Einstein equation (Eq. 2.20), are shown in the table (E).

### 4.3.2 Mini-B in DPC Micelles

The DPC micelles mimic the native lung condition created by the most abundant surfactant phospholipids which have zwitterionic PC headgroups. The 1D  $^1\text{H}$  and 2D  $^{15}\text{N}$ - $^1\text{H}$  HSQC spectra (Figures 4.5 and 4.6) indicate an overall similar level of structure of Mini-B<sub>OX</sub> in DPC micelles, compared to the structure in SDS micelles. However, there exists a noticeable change in the HSQC spectra of Mini-B<sub>OX</sub> in DPC. Although the peptide contains nine  $^{15}\text{N}$ -labeled amino acids, only eight peaks are seen and the peak for Gly18 is missing as identified from the resonance frequency determined during the structural studies in SDS (Chapter 3). The position of Gly18 in the loop region makes it likely that its disappearance is due to the exchange between multiple conformations of this region of Mini-B<sub>OX</sub> occurring at an intermediate rate, i.e., of the order of chemical shift difference. On the other hand, all nine peaks, including the one for Gly18, are seen in the HSQC spectra of Mini-B<sub>RED</sub> indicating the conformational exchange is absent when the disulfide bonds are reduced. This view that the disulfide bonds are associated with increased conformational heterogeneity is also supported by the observation of much fewer weak peaks (indicative of additional conformations) in the HSQC spectra of Mini-B<sub>RED</sub> compared to Mini-B<sub>OX</sub>.

The structuring of cationic Mini-B in zwitterionic lipid environment is likely driven by its direct binding to DPC micelles. This is further indicated by the substantially slower translational diffusion of the micelles upon inclusion of Mini-B<sub>OX</sub>, and hence an increased size, as obtained from the 2D DOSY experiments (Figure 4.7). Two values of average diffusion coefficients are measured for pure DPC micelles and the Mini-B<sub>OX</sub>/DPC complex using the attenuation of the two sharpest DPC peaks at 0.80 ppm (corresponding to  $\text{CH}_3$ ) and 1.22 ppm (corresponding to  $(\text{CH}_2)_{3-11}$ ). The diffusion coefficients for the micelles alone are  $3.35 \times 10^{-10}$  and  $3.37 \times 10^{-10}$   $\text{m}^2/\text{s}$  and that for the peptide/micelle complex are  $2.58 \times 10^{-10}$  and  $2.65 \times 10^{-10}$   $\text{m}^2/\text{s}$ , respectively. The corresponding hydrodynamic diameters, calculated using the Stokes-Einstein equation, are 1.96 and 1.95 nm for pure micelles and 2.54 and 2.48 nm for the peptide/micelle complex. Although under same experimental conditions, the sizes of DPC and SDS micelles are unlikely to be drastically different [160, 161], the sizes of pure

DPC micelles and the Mini-B<sub>OX</sub>/DPC complex found in this study are substantially smaller than those found for pure SDS micelles and the Mini-B<sub>OX</sub>/SDS complex, respectively. Since the DOSY data corresponds to a weighted average from the free and micelle-bound lipid

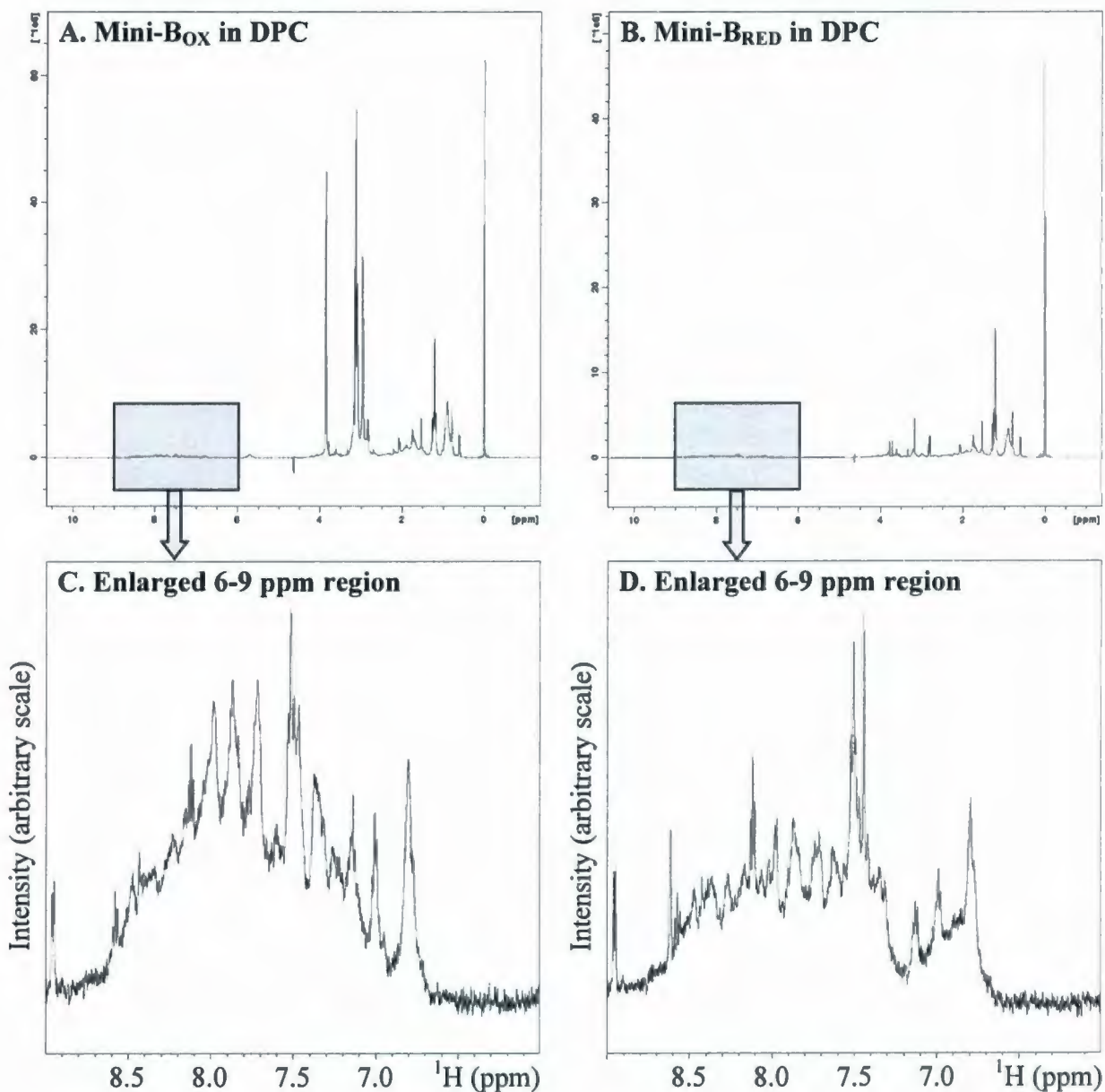


**Figure 4.5** : 1D <sup>1</sup>H spectra of (A) 0.20 mM Mini-B<sub>OX</sub> in 40 mM DPC in the presence of 4.5 mM Hepes at pH 6.9 (acquired using 256 scans) and (B) 0.75 mM Mini-B<sub>RED</sub> in 75 mM DPC at pH 5 (acquired using 64 scans). Both experiments were performed at temperature 37 °C and the spectra were processed with 1 Hz line broadening. The intense peaks seen in the spectra are from DSS and Hepes. The 6-9 ppm regions, exhibiting the protein HN signals, are enlarged and shown in the bottom panels (C and D).

molecules, the smaller apparent size may be the result of a rapid exchange between the two DPC species. This is likely due to the lower DPC concentration of 20 mM used in this study, as opposed to 150 mM concentration used for the SDS study.

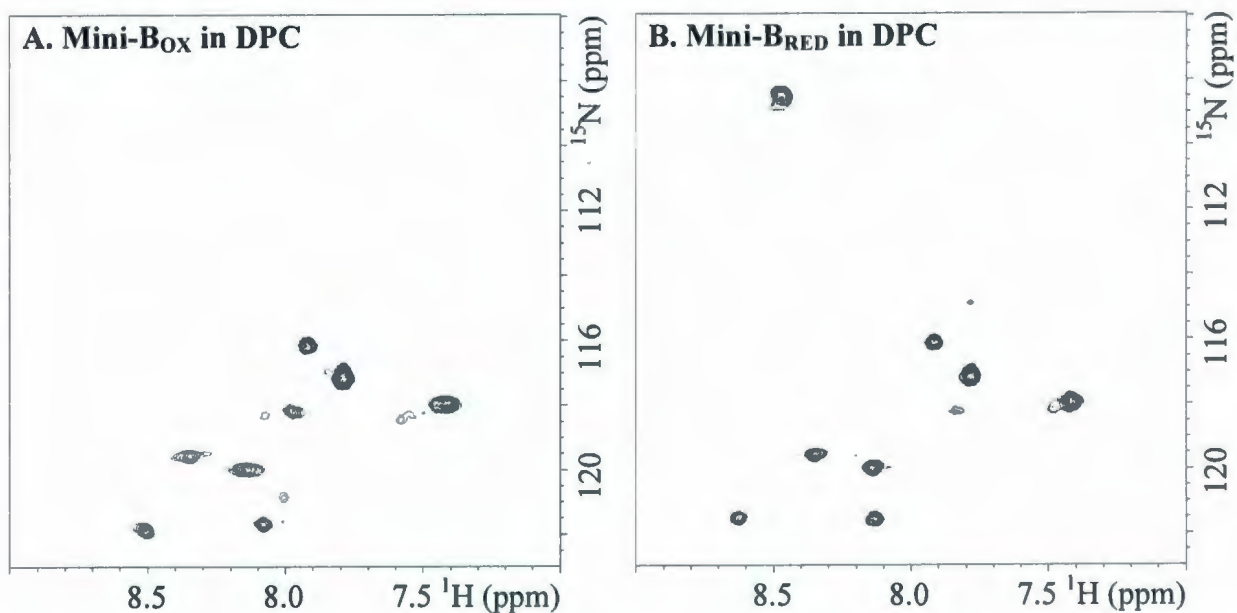
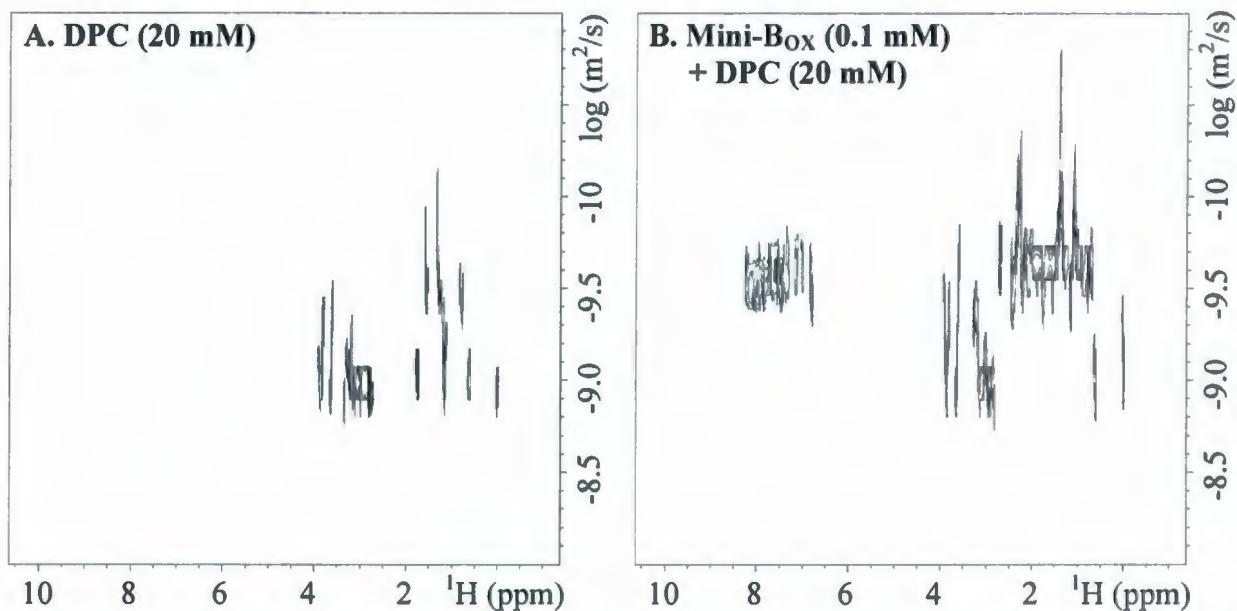
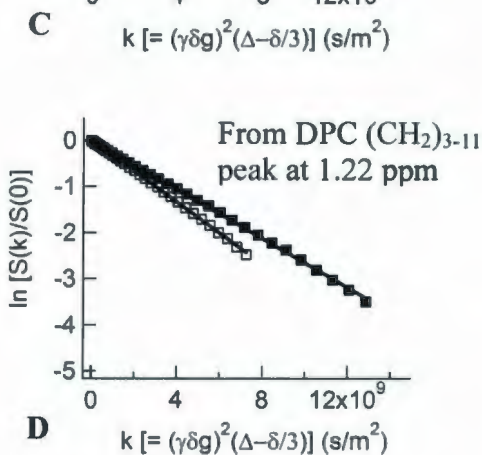
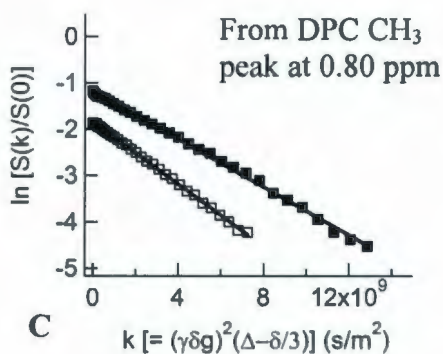


**Figure 4.6** : 2D  $^{15}\text{N}$ - $^1\text{H}$  HSQC spectra of (A) 0.20 mM Mini-B<sub>OX</sub> in 40 mM DPC in the presence of 4.5 mM Hepes at pH 6.9 (acquired using 160 scans) and (B) 0.75 mM Mini-B<sub>RED</sub> in 75 mM DPC at pH 5 (acquired using 64 scans). Both experiments were performed at temperature 37 °C. The base contour level shown in (A) is two times higher than (B).



□□□□ DPC Micelles  
 ■■■■ Mini-B<sub>ox</sub>/DPC Complex



Peak at ppm	DPC (□□□)		Mini-B <sub>ox</sub> /DPC (■■■)	
	D. Coeff. ×10 <sup>-10</sup> (m <sup>2</sup> /s)	H. Dia. (nm)	D. Coeff. ×10 <sup>-10</sup> (m <sup>2</sup> /s)	H. Dia. (nm)
0.80	3.35 (± 0.02)	1.96	2.58 (± 0.02)	2.54
1.22	3.37 (± 0.01)	1.95	2.65 (± 0.01)	2.48

**E**

**Figure 4.7 :** DPC micelles (□□□) and Mini-B<sub>ox</sub>/DPC complex (■■■) sizes as indicated by translational diffusion. Upper panels show 2D DOSY spectra of (A) 20 mM DPC and (B) 0.10 mM Mini-B<sub>ox</sub> + 20 mM DPC, at pH 7 and temperature 37 °C. Linear fits (C and D) show the attenuation of the peaks at 0.80 and 1.22 ppm obtained from the DOSY data. The observed diffusion coefficients, represented by the slopes of the curves, and the corresponding hydrodynamic diameters, calculated using the Stokes-Einstein equation (Eq. 2.20), are shown in the table (E).

### 4.3.3 Mini-B in LMPC Micelles

To gain an insight into Mini-B's conformation in a more physiologically relevant lipid environment and to probe Mini-B's interactions with surfactant phospholipid analogues, only the oxidized version of Mini-B was used in the remaining studies for this chapter. First studied was Mini-B<sub>OX</sub> in zwitterionic LMPC micelles. LMPC is a better mimetic for the most abundant surfactant phospholipid DPPC than DPC, as it contains identical head and neck regions to DPPC. The investigations were carried out at two different peptide/lipid ratios (indicated in the figure captions). The 1D <sup>1</sup>H and 2D <sup>15</sup>N-<sup>1</sup>H HSQC spectra look almost identical for both concentrations. The HN signals seen in the 1D <sup>1</sup>H spectrum are broader than SDS- or DPC-bound Mini-B<sub>OX</sub> and likely more overlapped (Figure 4.8). The <sup>15</sup>N-<sup>1</sup>H correlations seen in the 2D HSQC spectra are also broader (Figure 4.9). This is consistent with a larger complex-size of Mini-B<sub>OX</sub>/LMPC than Mini-B<sub>OX</sub>/SDS or Mini-B<sub>OX</sub>/DPC. Like Mini-B<sub>OX</sub> in DPC, eight strong HSQC peaks, along with some additional weak peaks, are seen and the Gly18 peak is missing. Comparison with the spectra in SDS and DPC micelles indicates that Mini-B<sub>OX</sub> is structured in LMPC micelle environment, along with additional minor conformations of some regions. However, some differences in the overall conformation of LMPC-bound Mini-B<sub>OX</sub> and SDS- or DPC-bound Mini-B<sub>OX</sub> are likely as the chemical shifts of most of the HSQC peaks are not exactly the same.

The effects of Mini-B<sub>OX</sub> on the structure of LMPC micelles are revealed from the 2D DOSY spectra (Figure 4.10). The ~ 7.2 nm hydrodynamic diameter of pure LMPC micelles, calculated using the observed translational diffusion coefficient of ~  $7.3 \times 10^{-11}$  m<sup>2</sup>/s, is indeed much larger than the diameters of pure SDS and DPC micelles. Interestingly, in contrast to the SDS and DPC results, the inclusion of Mini-B<sub>OX</sub> apparently decreases the diameter of LMPC micelles to ~ 6.7 nm since the observed diffusion coefficient of the peptide/micelle complex is increased to ~  $6.7 \times 10^{-11}$  m<sup>2</sup>/s. The faster diffusion of the complex may be a result of smaller size, changed shape and/or enhanced exchange between the free and micelle-bound LMPC molecules instigated by Mini-B<sub>OX</sub>.

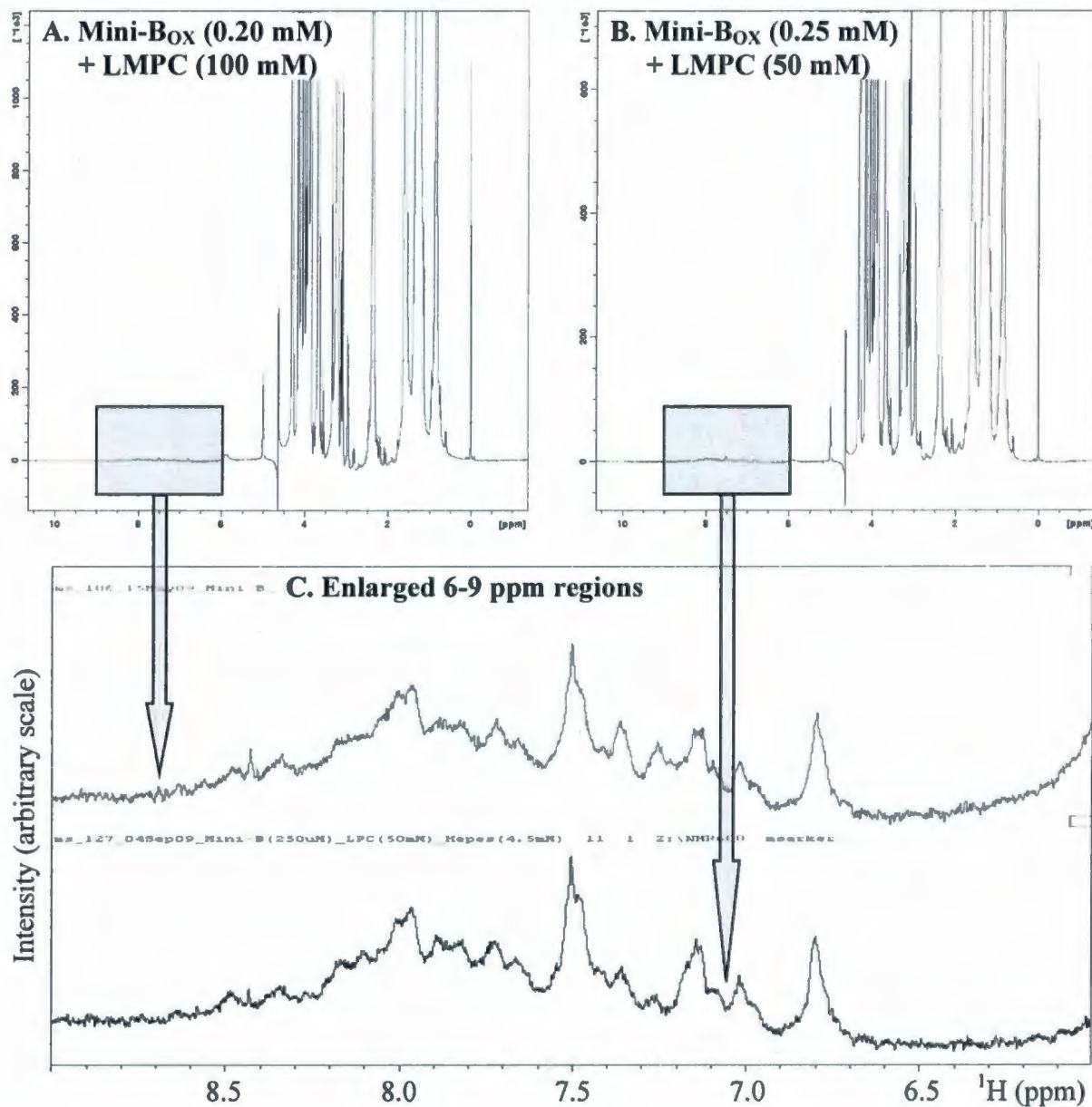


**Figure 4.8** : 1D <sup>1</sup>H spectra of (A) 0.20 mM Mini-BO<sub>X</sub> in 100 mM LMPC and (B) 0.25 mM Mini-BO<sub>X</sub> in 50 mM LMPC, in the presence of 4.5 mM Hepes. The pH of both samples was 6.9 and the experiments were performed at temperature 37 °C. The spectra were acquired using 160 scans and processed with 1 Hz line broadening. The intense peaks seen in the spectra are from LMPC, Hepes and DSS. The 6-9 ppm regions, exhibiting the protein HN signals, are enlarged and shown in the bottom panel (C).

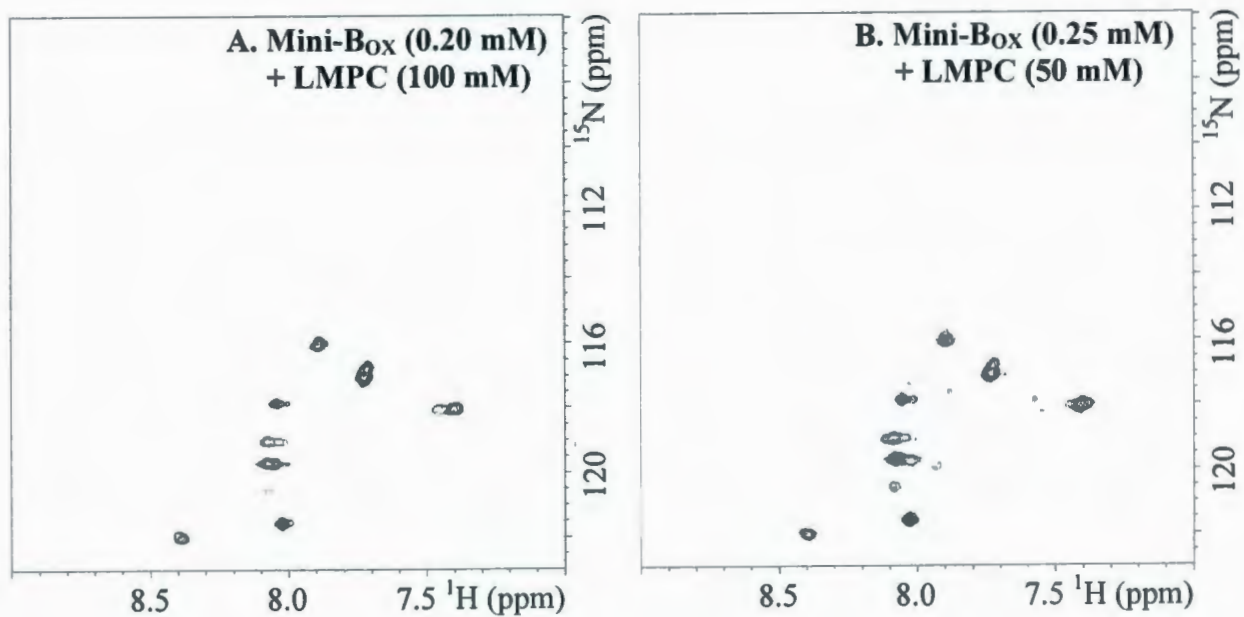
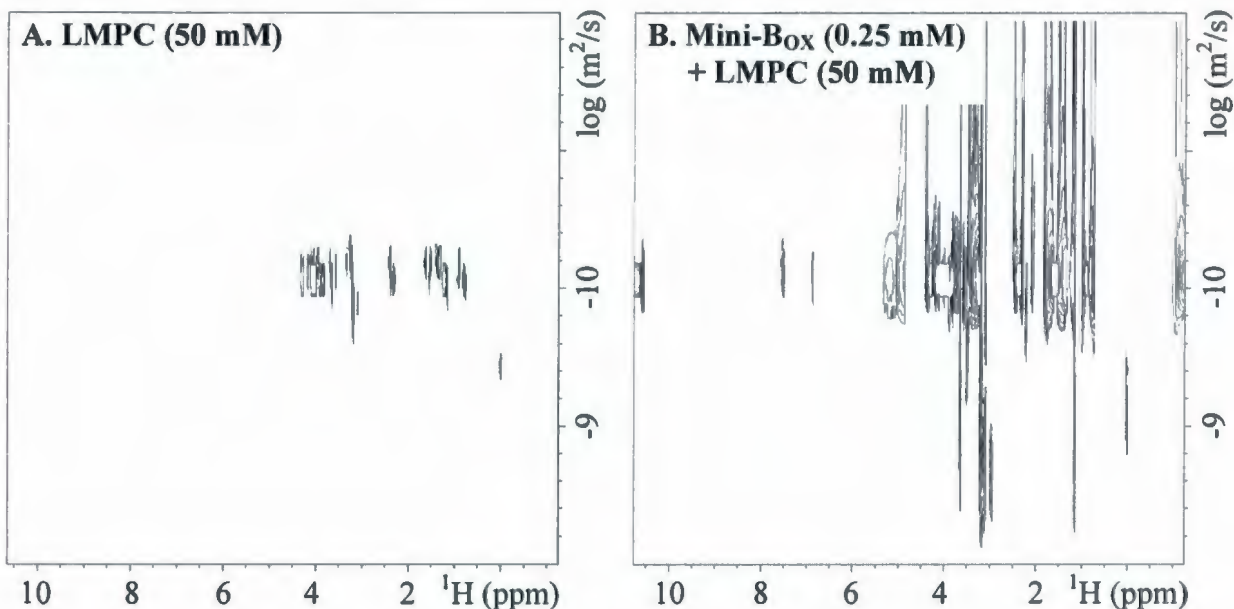
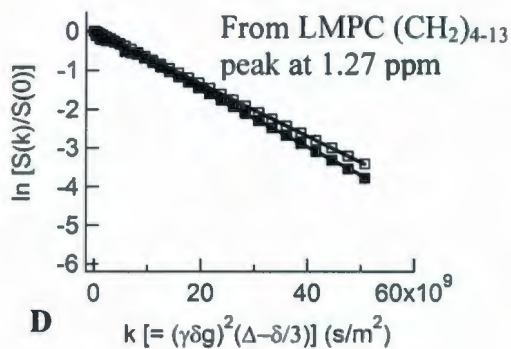
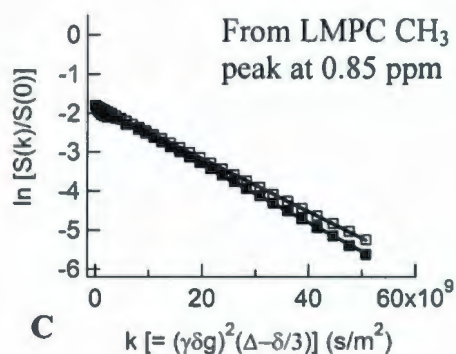


**Figure 4.9** : 2D  $^{15}\text{N}$ - $^1\text{H}$  HSQC spectra of (A) 0.20 mM Mini-BO<sub>X</sub> in 100 mM LMPC and (B) 0.25 mM Mini-BO<sub>X</sub> in 50 mM LMPC, in the presence of 4.5 mM Hepes. The pH of the samples was 6.9. The spectra were acquired at temperature 37 °C using 160 scans.



□□□□ LMPC Micelles  
 ■■■■ Mini-B<sub>OX</sub>/LMPC Complex



Peak at ppm	LMPC (□□□)		Mini-B <sub>OX</sub> /LMPC (■■■)	
	D. Coeff. ×10 <sup>-11</sup> (m <sup>2</sup> /s)	H. Dia. (nm)	D. Coeff. ×10 <sup>-11</sup> (m <sup>2</sup> /s)	H. Dia. (nm)
0.85	6.790 (± 0.006)	7.21	7.364 (± 0.047)	6.65
1.27	6.741 (± 0.003)	7.26	7.332 (± 0.043)	6.68

E

**Figure 4.10** : LMPC micelles (□□□) and Mini-B<sub>OX</sub>/LMPC complex (■■■) sizes as indicated by translational diffusion. Upper panels show 2D DOSY spectra of (A) 50 mM LMPC and (B) 0.25 mM Mini-B<sub>OX</sub> + 50 mM LMPC, at pH 6.9 and temperature 25 °C. Linear fits (C and D) show the attenuation of the peaks at 0.85 and 1.27 ppm obtained from the DOSY data. The observed diffusion coefficients, represented by the slopes of the curves, and the corresponding hydrodynamic diameters, calculated using the Stokes-Einstein equation (Eq. 2.20), are shown in the table (E).

#### 4.3.4 Mini-B in LMPG Micelles

The studies of the conformation and lipid interactions of Mini-B<sub>OX</sub> continued next with anionic LMPG micelles. LMPG contains an identical headgroup to surfactant PGs and hence is a much better mimetic than SDS. The NMR experiments were performed with two different peptide/lipid ratios (indicated in the figure captions) but the 1D <sup>1</sup>H and 2D <sup>15</sup>N-<sup>1</sup>H HSQC spectra are almost identical (Figures 4.11 and 4.12). The signals are broader than SDS- and DPC-bound Mini-B<sub>OX</sub> but similar to LMPC-bound Mini-B<sub>OX</sub>. The Gly18 HSQC peak, absent in zwitterionic DPC and LMPC but present in anionic SDS, is present in LMPG as well. Comparison with the spectra from other micelle systems indicates an overall similar structure of Mini-B<sub>OX</sub> in LMPG micelles.

The findings about the change in the structure of LMPG micelles brought by the inclusion of Mini-B<sub>OX</sub>, as obtained from the 2D DOSY experiments (Figure 4.13), are similar to the LMPC study. The observed translational diffusion coefficient of pure LMPG micelles increases from  $\sim 5.9 \times 10^{-11} \text{ m}^2/\text{s}$  to  $\sim 6.8 \times 10^{-11} \text{ m}^2/\text{s}$  when Mini-B<sub>OX</sub> is added. Thus, the hydrodynamic diameter of the micelles apparently decreases from  $\sim 8.3 \text{ nm}$  to  $\sim 7.2 \text{ nm}$  when bound to the peptide.

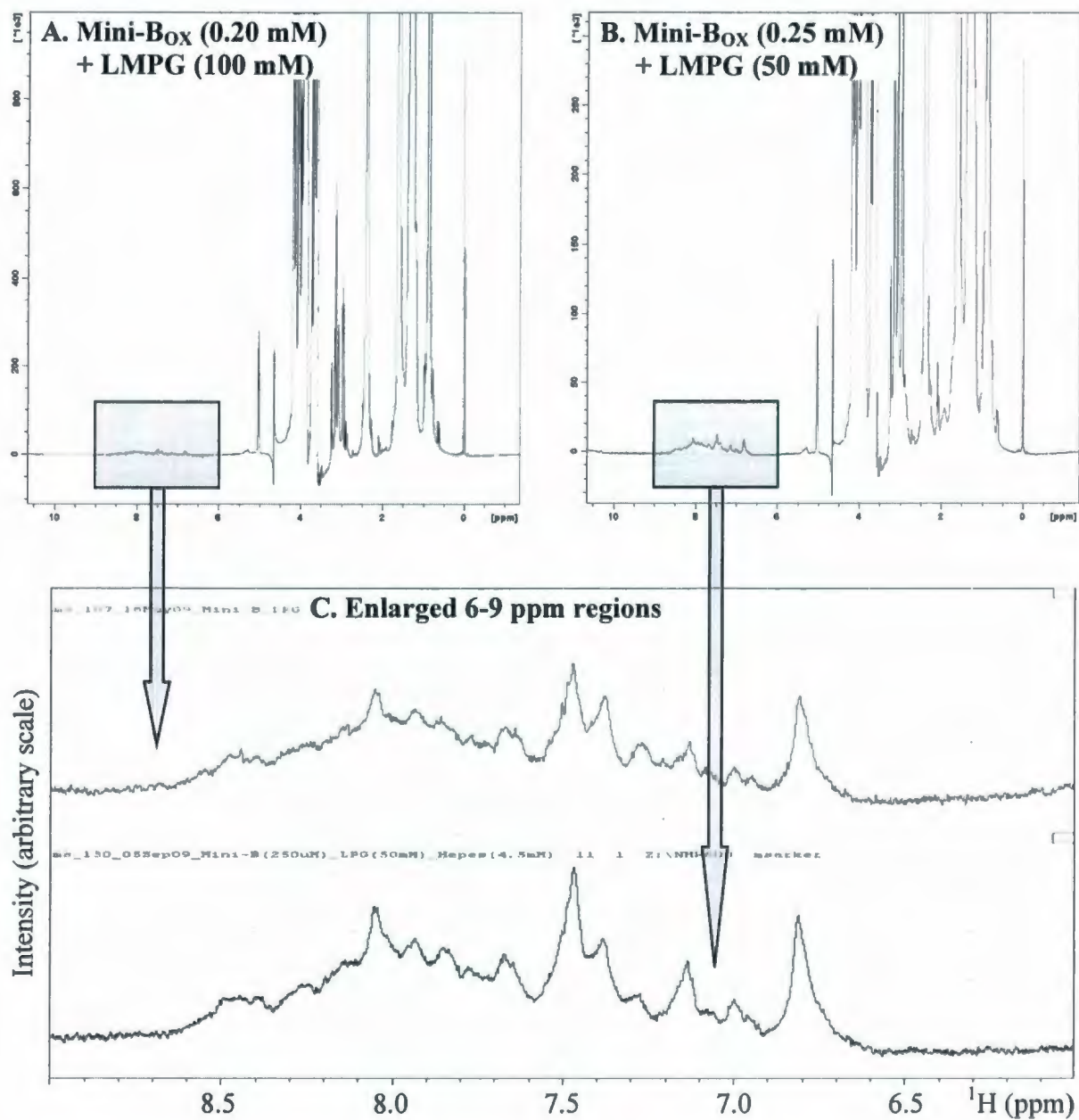


**Figure 4.11** : 1D <sup>1</sup>H spectra of (A) 0.20 mM Mini-B<sub>OX</sub> in 100 mM LMPG and (B) 0.25 mM Mini-B<sub>OX</sub> in 50 mM LMPG, in the presence of 4.5 mM Hepes. The pH of both samples was 6.9 and the experiments were performed at temperature 37 °C. The spectra were acquired using 160 scans and processed with 1 Hz line broadening. The intense peaks seen in the spectra are from LMPG, Hepes and DSS. The 6-9 ppm regions, exhibiting the protein HN signals, are enlarged and shown in the bottom panel (C).

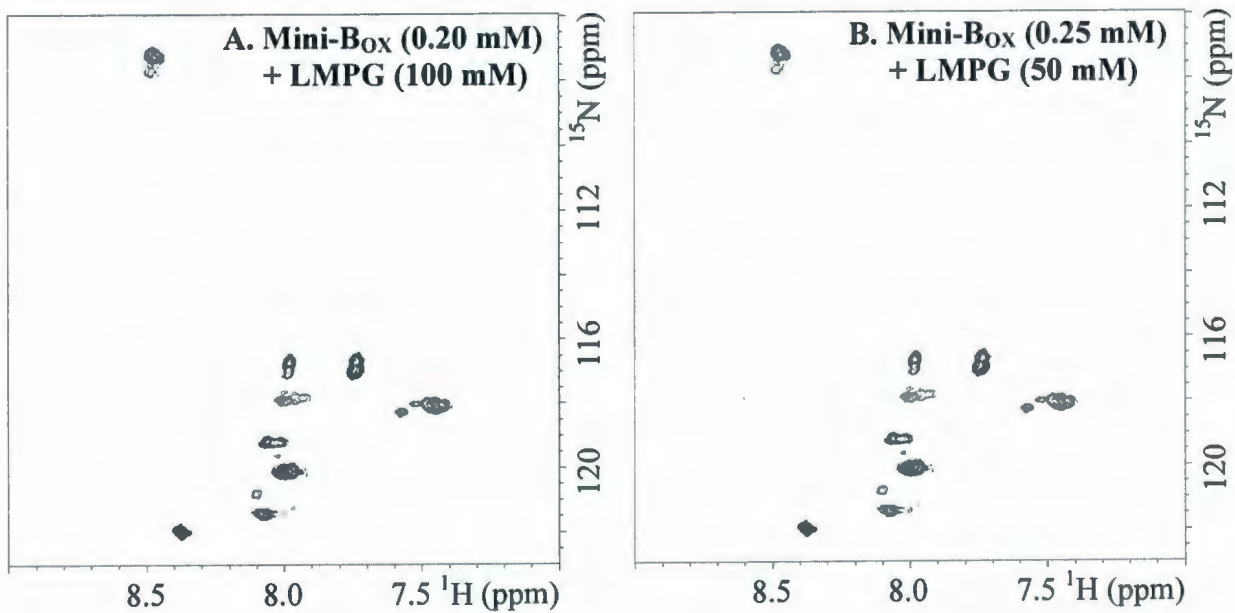
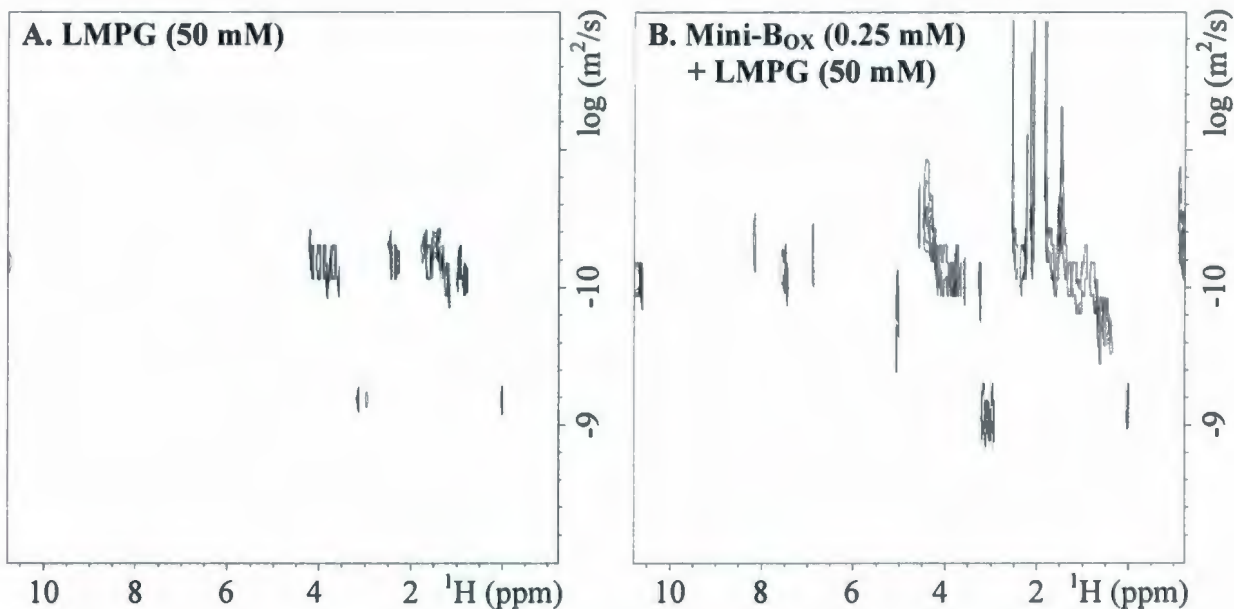
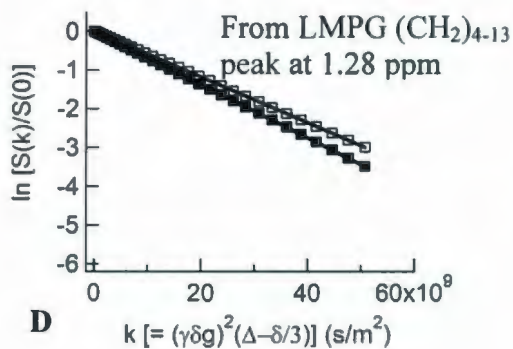
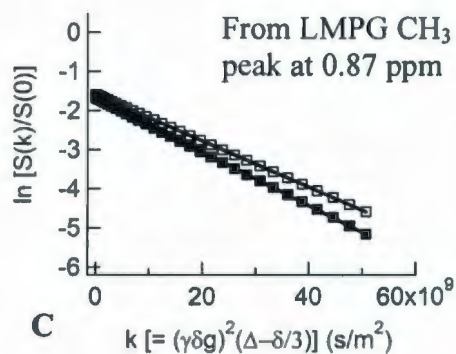


**Figure 4.12** : 2D <sup>15</sup>N-<sup>1</sup>H HSQC spectra of (A) 0.20 mM Mini-BO<sub>x</sub> in 100 mM LMPG and (B) 0.25 mM Mini-BO<sub>x</sub> in 50 mM LMPG, in the presence of 4.5 mM Hepes. The pH of the samples was 6.9. The spectra were acquired at temperature 37 °C using 160 scans.



□□□□ LMPG Micelles  
 ■■■■ Mini-B<sub>OX</sub>/LMPG Complex



Peak at ppm	LMPG (□□□)		Mini-B <sub>OX</sub> /LMPG (■■■)	
	D. Coeff. ×10 <sup>-11</sup> (m <sup>2</sup> /s)	H. Dia. (nm)	D. Coeff. ×10 <sup>-11</sup> (m <sup>2</sup> /s)	H. Dia. (nm)
0.87	5.907 (± 0.004)	8.29	6.841 (± 0.014)	7.16
1.28	5.909 (± 0.003)	8.29	6.849 (± 0.009)	7.15

E

**Figure 4.13** : LMPG micelles (□□□) and Mini-B<sub>OX</sub>/LMPG complex (■■■) sizes as indicated by translational diffusion. Upper panels show 2D DOSY spectra of (A) 50 mM LMPG and (B) 0.25 mM Mini-B + 50 mM LMPG, at pH 6.9 and temperature 25 °C. Linear fits (C and D) show the attenuation of the peaks at 0.87 and 1.28 ppm obtained from the DOSY data. The observed diffusion coefficients, represented by the slopes of the curves, and the corresponding hydrodynamic diameters, calculated using the Stokes-Einstein equation (Eq. 2.20), are shown in the table (E).

### 4.3.5 Mini-B in Mixed LMPC/LMPG Micelles

Lastly for this Chapter, conformation of Mini-B<sub>OX</sub> and its lipid interactions were investigated in a mixed LMPC/LMPG micelle system. Again, two different peptide/lipid concentrations were used (indicated in the figure captions) but the 8.5 : 1.5 ratio of PC to PG was maintained in both samples to match the physiological condition. The 1D <sup>1</sup>H and 2D <sup>15</sup>N-<sup>1</sup>H HSQC spectra indicate a structured Mini-B<sub>OX</sub> in the mixed zwitterionic/anionic environment when compared to the spectra in individual micelle systems (Figures 4.14 and 4.15). However, the HSQC spectra exhibit two more interesting features. Firstly, the Gly18 peak which was present in LMPG micelles but disappeared in LMPC micelles, reappears in the mixed micelles containing only 15% LMPG. Therefore, as little as 15% LMPG is enough to induce the same structure/dynamics of Mini-B<sub>OX</sub> loop region as 100% LMPG. Secondly, for at least two cases, the two peaks representing a single <sup>15</sup>N-labeled amino acid have similar intensities. This indicates the presence of multiple conformations of some regions of Mini-B<sub>OX</sub> with similar populations.

The 2D DOSY study confirms the formation of mixed micelles, containing both LMPC and LMPG molecules together, as there is only a single translational diffusion coefficient present for the LMPC/LMPG system (Figure 4.16). However, the change in the micelle structure caused by the inclusion of Mini-B<sub>OX</sub> follows the same trend as of Mini-B<sub>OX</sub>/LMPC and Mini-B<sub>OX</sub>/LMPG. The observed translational diffusion coefficient of micelles alone is  $\sim 5.9 \times 10^{-11} \text{ m}^2/\text{s}$  but that of the peptide/micelle complex is  $\sim 7.6 \times 10^{-11} \text{ m}^2/\text{s}$ . Thus the hydrodynamic diameter of the mixed micelles apparently decreases from  $\sim 8.3 \text{ nm}$  to  $\sim 6.5 \text{ nm}$  when bound to Mini-B<sub>OX</sub>.

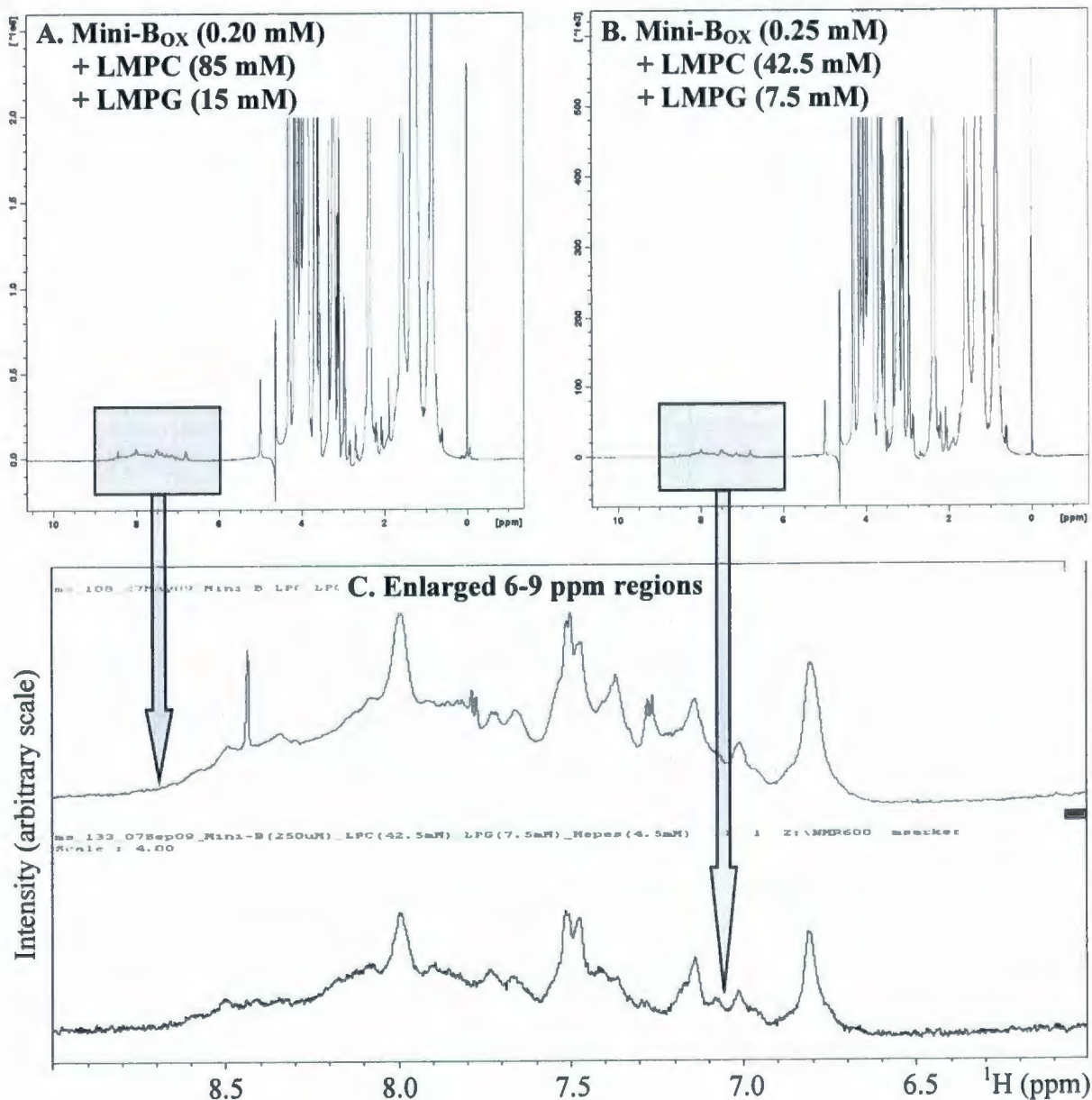


**Figure 4.14** : 1D <sup>1</sup>H spectra of (A) 0.20 mM Mini-B<sub>OX</sub> in 85 mM LMPC plus 15 mM LMPG and (B) 0.25 mM Mini-B<sub>OX</sub> in 42.5 mM LMPC plus 7.5 mM LMPG, in the presence of 4.5 mM Hepes. The pH of both samples was 6.9 and the experiments were performed at temperature 37 °C. The spectra were acquired using 160 scans and processed with 1 Hz line broadening. The intense peaks seen in the spectra are from LMPC, LMPG, Hepes and DSS. The 6-9 ppm regions, exhibiting the protein HN signals, are enlarged and shown in the bottom panel (C).

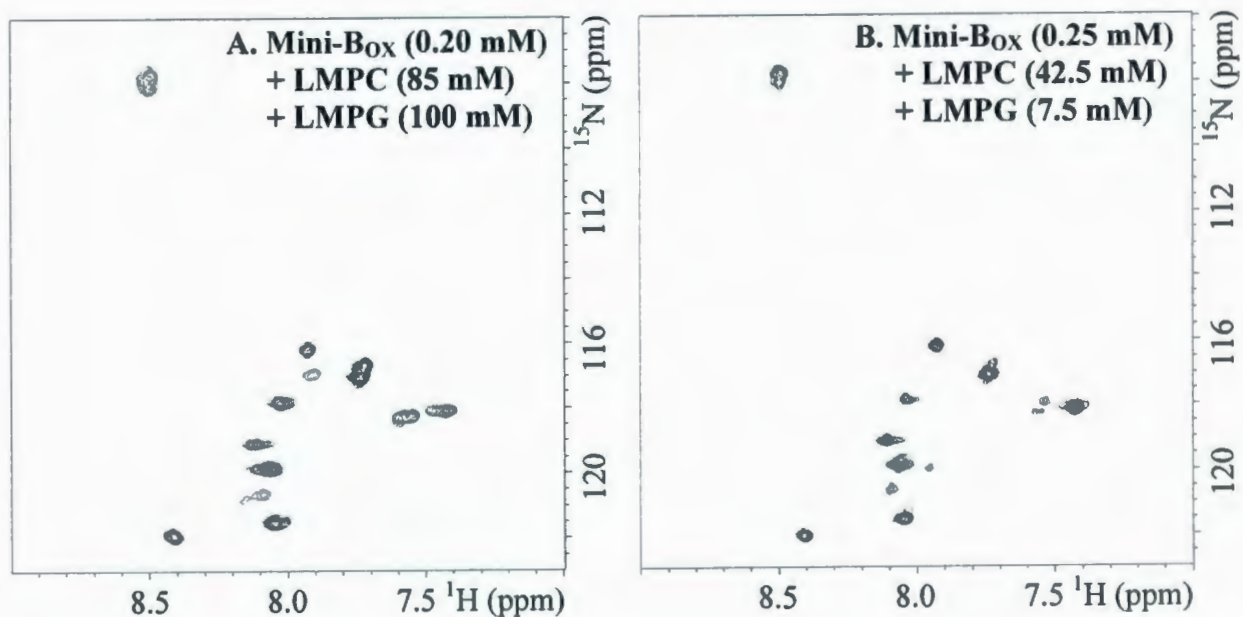
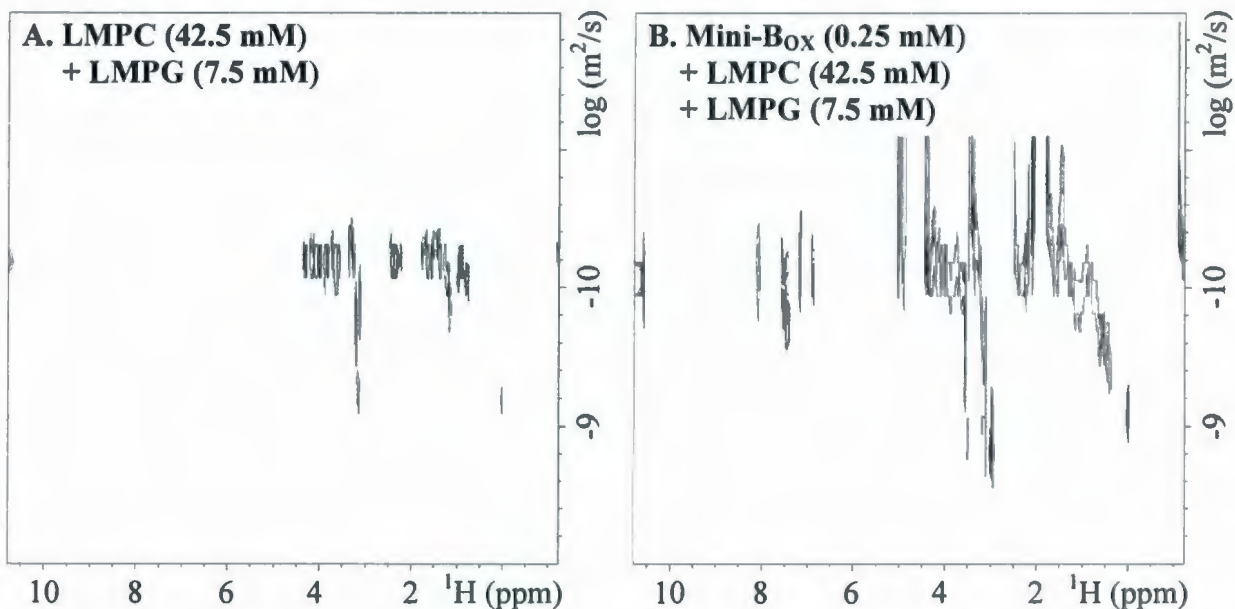
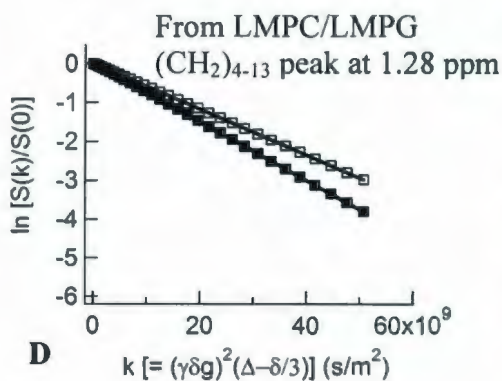
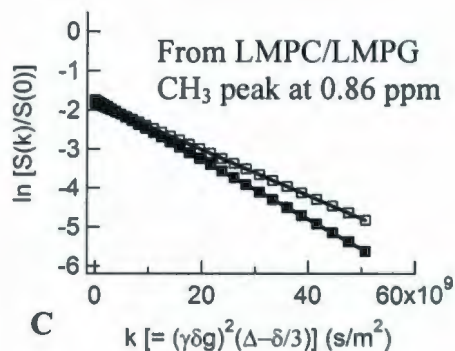


**Figure 4.15** : 2D  $^{15}\text{N}$ - $^1\text{H}$  HSQC spectra of (A) 0.20 mM Mini-Box in 85 mM LMPC plus 15 mM LMPG (acquired using 320 scans) and (B) 0.25 mM Mini-Box in 42.5 mM LMPC plus 7.5 mM LMPG (acquired using 160 scans), in the presence of 4.5 mM Hepes. The pH of the samples was 6.9 and the experiments were performed at temperature 37 °C.



□□□□ LMPC/LMPG Micelles  
 ■■■■ Mini-B<sub>Ox</sub>/LMPC/LMPG Complex



Peak at ppm	LMPC/LMPG (□□□)		Mini-B <sub>Ox</sub> /LMPC/LMPG (■■■)	
	D. Coeff. ×10 <sup>-11</sup> (m <sup>2</sup> /s)	H. Dia. (nm)	D. Coeff. ×10 <sup>-11</sup> (m <sup>2</sup> /s)	H. Dia. (nm)
0.86	5.910 (± 0.003)	8.29	7.635 (± 0.003)	6.41
1.28	5.866 (± 0.002)	8.35	7.504 (± 0.003)	6.53

E

**Figure 4.16** : LMPC/LMPG mixed micelles (□□□) and Mini-B<sub>Ox</sub>/LMPC/LMPG complex sizes (■■■) as indicated by translational diffusion. Upper panels show 2D DOSY spectra of (A) 42.5 mM LMPC + 7.5 mM LMPG and (B) 0.25 mM Mini-B + 42.5 mM LMPC + 7.5 mM LMPG, at pH 6.9 and temperature 25 °C. Linear fits (C and D) show the attenuation of the peaks at 0.86 and 1.28 ppm obtained from the DOSY data. The observed diffusion coefficients, represented by the slopes of the curves, and the corresponding hydrodynamic diameters, calculated using the Stokes-Einstein equation (Eq. 2.20), are shown in the table (E).

## 4.4 Discussion

SP-B's essential roles in lung surfactant function presumably come through its interactions with phospholipids [82-88]. A detailed mechanistic description of these interactions is still unavailable as the high resolution structure of full-length SP-B is not yet known. Biophysical studies suggest that SP-B facilitates large-scale rearrangements of lipids and stabilizes complex structures required for rapid adsorption of surfactant materials at the alveolar air-water interface, surface tension reduction during lung compression and respreading of the surface film during subsequent lung expansion [82-88]. Mini-B is a synthetic construct based on the N-terminal – C-terminal helical regions of SP-B that retains substantial biological activity of the full-length protein [109]. In this chapter, solution NMR was used to investigate the conformation of Mini-B and probe its interactions with a variety of micelle systems mimicking the lung lipid environment of SP-B. The micelles were composed of LMPC and LMPG, the analogues of the most abundant surfactant phospholipids with zwitterionic and anionic headgroups, as well as a mixture of both LMPC and LMPG at a physiological ratio. However, the studies began with smaller micelles composed of anionic detergent SDS and zwitterionic lipid DPC. Intriguing differences were found in how Mini-B interacts with the smaller DPC/SDS micelles compared to the larger LMPC/LMPG micelles, suggesting that differences in the lipid structure can substantially impact Mini-B/lipid interactions. Interesting differences in the overall conformation and dynamics of Mini-B in zwitterionic versus anionic environments were also noticed. Moreover, despite the similarity in structuring of Mini-B in DPC to LMPC and SDS to LMPG, subtle differences in Mini-B's interactions were observed.

Due to the high degree of hydrophobicity, SP-B and its peptide fragments are mostly insoluble and presumably unstructured in water alone. However, Mini-B takes on a well-defined and mostly homogeneous conformation, with two  $\alpha$ -helices connected by a loop, in the presence of organic solvent HFIP and detergent micelles composed of SDS ([110] and Chapter 3). Comparison of the 1D  $^1\text{H}$  and 2D  $^{15}\text{N}$ - $^1\text{H}$  HSQC spectra acquired for this chapter with similar spectra from the previous structural studies indicates that Mini-B is structured in

all DPC, LMPC, LMPG and mixed LMPC/LMPG micelle systems. Although small differences in the overall conformation would not be unexpected, as chemical shifts of some HSQC peaks are not identical, Mini-B likely adopts a generic amphipathic helical folding in all these physiologically relevant lipid environments. It is conceivable that the structuring is driven by Mini-B's direct interactions with both polar headgroups and hydrophobic core of the micelles. In native lung conditions, the corresponding terminal regions of full-length SP-B probably interact with surfactant phospholipids in a similar manner and also fold as amphipathic helices.

In addition to the dominant major conformation, some regions of Mini-B<sub>OX</sub> possess additional minor conformations in all micelle systems as indicated by the additional weak HSQC peaks of some <sup>15</sup>N-labeled amino acids. At least in SDS-bound Mini-B<sub>OX</sub>, these regions include the N-terminus and the middle loop (Chapter 3). In mixed LMPC/LMPG micelles, two or three <sup>15</sup>N-labeled amino acids each show two HSQC peaks with similar intensities. The regions containing these amino acids therefore exhibit two conformations with similar populations. There is likely a slow exchange taking place between these conformations. It is conceivable that this conformational heterogeneity allows Mini-B<sub>OX</sub> to form different types of associations with lipids and thus plays a functional role.

Mini-B<sub>RED</sub>, in contrast to Mini-B<sub>OX</sub>, does not appear to exhibit any significant conformational heterogeneity in either of SDS or DPC micelles since there are no additional weak peaks present in the HSQC spectra. The reduced Mini-B is an interesting SP-B based peptide for clinical applications. It has been shown that this version of Mini-B also retains some biological functions of SP-B in surfactant lavaged rat models [109]. It thus possesses a substantial therapeutic potential since making multiple disulfide bonds in synthetic SP-B based peptides is very challenging. However, in rat models, Mini-B<sub>RED</sub> exhibits lower activity than Mini-B<sub>OX</sub> (Figure 1.6 on Page 17 and [109]), which can probably be attributed to its different three dimensional conformation. The helices of Mini-B<sub>RED</sub> are not spatially constrained by disulfide bonds, as they are in Mini-B<sub>OX</sub>. Hence, in the presence of detergent/lipid molecules, Mini-B<sub>RED</sub>, in contrast to taking on a "compact" tertiary structure

like Mini-B<sub>OX</sub>, presumably takes on an entropically more favorable “open” tertiary structure through necessary reorientation of its helices. This assumption is favorably supported by the difference in chemical shifts of Leu3 and Leu31, two amino acids located at the interface between the helices and close to the termini, when the HSQC spectra of both versions are compared. Also, the lack of disulfide bonds likely allows Mini-B<sub>RED</sub> to form a more rigid association with both anionic and zwitterionic amphiphiles and thereby adopt a temporally stable homogeneous and single conformation. This further underscores Mini-B’s ability, irrespective of the disulfide bonds between its helices, to bind different lipid types.

Although the dynamics of Mini-B<sub>OX</sub> are not directly probed in these studies, based on the spectral features of HSQC, some inferences can be drawn about the flexibility of its regions exhibiting multiple conformations. For the regions that contain amino acids each with two (or more) HSQC peaks, there is either no chemical exchange taking place between the conformations or if there is any exchange going on that must be occurring at a rate much slower than the chemical shift difference. On the other hand, for the regions that contain amino acids each with a single peak which is weak as a result of line broadening, probably multiple conformations are still present but a chemical exchange is taking place at a rate close to the chemical shift difference, i.e. at an intermediate rate (of the order of a thousand per second). The peak for Gly18, which is located in the loop region connecting the helices, is completely missing from the HSQC spectra of Mini-B<sub>OX</sub> in DPC and LMPC micelles. Thus, in zwitterionic environment, the middle loop of Mini-B<sub>OX</sub> is most likely undergoing a conformational exchange at an intermediate rate very close to the chemical shift difference. In contrast, a strong Gly18 peak (and an additional weak peak) is present in the HSQC spectra of Mini-B<sub>OX</sub> in SDS, LMPG and mixed LMPC/LMPG micelles. Hence, the middle loop of Mini-B<sub>OX</sub>, though exhibiting a conformational heterogeneity, is probably rigid or at most exchanging very slowly in pure anionic or mixed lipid environments. In DPC micelles, although the Gly18 peak is missing for Mini-B<sub>OX</sub> indicating an intermediate conformational exchange of the loop region, interestingly, it is present for Mini-B<sub>RED</sub> indicating no such exchange for this version. Mini-B thus exhibits a distinctive structural flexibility which not only varies with the lipid environments but also depends on its own tertiary conformation.

The diffusion NMR spectroscopy reveals that the translational diffusion of all types of micelles changes upon the inclusion of Mini-B<sub>OX</sub>. This indicates a Mini-B<sub>OX</sub>-induced change of the micelle structure and provides an evidence of direct interactions between the peptide and the detergent/lipid molecules. However, the observations for SDS and DPC micelles, where Mini-B<sub>OX</sub> causes the micelles to diffuse more slowly, and the observations for LMPC, LMPG and mixed LMPC/LMPG micelles, where Mini-B<sub>OX</sub> causes the micelles to diffuse more quickly, are opposite. LMPC and LMPG each contain a 14-carbon acyl chain and a large headgroup (Figure 4.1, Page 62). On the other hand, DPC contains a 12-carbon acyl chain and a slightly smaller headgroup, while SDS also contains a 12-carbon acyl chain but a much smaller headgroup. From the translational diffusion measurements, SDS and DPC micelles are found to be much smaller in size than LMPC, LMPG or mixed LMPC/LMPG micelles. Hence, when Mini-B<sub>OX</sub> is added, the smaller SDS or DPC micelles are presumably substantially stretched to accommodate the peptide within them, which would explain the slower translational diffusion and increased size of the peptide/micelle complexes. However, the effects of Mini-B<sub>OX</sub>'s interactions are seemingly different for much larger LMPC, LMPG or mixed LMPC/LMPG micelles as these micelles diffuse faster when bound to Mini-B<sub>OX</sub>. There are three plausible explanations for this behavior. First, Mini-B<sub>OX</sub> may contract the surface of these large micelles and thereby yield more compact and smaller peptide/micelle complexes. The self-assembly of detergent/lipid micelles is primarily driven by the hydrophobic interactions of their nonpolar hydrocarbon acyl chains [140, 141]. As both LMPC and LMPG headgroups carry charges, inclusion of Mini-B<sub>OX</sub>, which also carries charges, may add an extra electrostatic component of interactions. This may bring a contraction at the surface of these micelles and thus causing the complexes to decrease in size. Second, pure LMPC/LMPG micelles may adopt a largely non-spherical shape and Mini-B<sub>OX</sub> may induce an increased curvature by restructuring these micelles to a more spherical shape that encounters decreased viscous drag in solution. This may be related to some predicted physiological functions of SP-B. One major proposed function depicts that SP-B squeezes out unsaturated phospholipids from the surface film during compression, which would require its association with highly curved lipid structures [86]. In addition, *in vitro* reconstitution of tubular myelin (TM) requires both SP-A and SP-B, where the positioning of

SP-B is likely in the highly curved corners of TM [17]. Mini-B<sub>OX</sub>, being a biologically active fragment of SP-B, may thus be involved in inducing an increased curvature to the micelle surfaces formed from surfactant phospholipid analogues. Third, Mini-B<sub>OX</sub>, without changing the size or shape of the micelles substantially, may trigger a faster exchange between the free and micelle-bound LMPC/LMPG molecules present in these samples. Since the diffusion coefficient obtained from the DOSY data is a weighted average from the free and micelle-bound lipid molecules, the faster exchange would also result in a quicker translational diffusion of the peptide/micelle complex. All of these possibilities, whether it is the change of micelle size, micelle shape, or lipid exchange rate, suggest that Mini-B<sub>OX</sub> is capable of instigating a large-scale rearrangement of the lipid structures.

The interactions between Mini-B and micelles are likely both electrostatic and hydrophobic in nature. The electrostatic interactions likely occur between the anionic amino acids of the peptide and the cationic or zwitterionic headgroups of the micelles, while the hydrophobic interactions likely occur between the nonpolar amino acids of the peptide and the core of the micelles formed by the hydrocarbon acyl chains. Given the strikingly amphipathic structure of Mini-B<sub>OX</sub> and consequently presumed strong electrostatic interactions between cationic amino acids of Mini-B and anionic headgroups of SDS and LMPG micelles, it is possible that Mini-B<sub>OX</sub> is comparatively tightly bound to these anionic micelles. Thus the positioning of Mini-B<sub>OX</sub> may be relatively deep inside the anionic micelles. On the other hand, the electrostatic interactions between the same anionic amino acids and zwitterionic headgroups of DPC and LMPC micelles are unlikely to be so strong, and hence Mini-B<sub>OX</sub> may be relatively loosely bound to these zwitterionic micelles. Therefore, the positioning of Mini-B<sub>OX</sub> may be relatively shallow in the zwitterionic micelles. This hypothesis is favorably supported by the observation that SP-B<sub>63-78</sub>, consisting of the C-terminal half of Mini-B, takes a deeper position inside anionic phospholipid-containing bilayers than purely zwitterionic bilayers [162]. However, despite the differences in electrostatic component of peptide/micelle interactions, the helical secondary structure of Mini-B<sub>OX</sub> is unlikely to be drastically different in two micelle environments.

The presence of Gly18 peak in the HSQC spectra of Mini-B<sub>OX</sub> in pure anionic or mixed micelles, but its disappearance from the spectra in pure zwitterionic micelles may directly be attributed to Mini-B<sub>OX</sub>'s differential electrostatic interactions with different micelle types. It is conceivable that the two Gly18-flanking positively charged amino acids, Lys17 and Arg20, experience strong electrostatic attractions from negatively charged headgroups of SDS and LMPG micelles. As a result, although the middle loop may be structurally flexible, the exchange between the conformations in these micelles, if any, is very slow, as pointed out earlier. In contrast, since DPC and LMPC headgroups contain both positive and negative charges, their interactions with positively charged Lys17 and Arg20 would be much weaker and hence the loop region may be much more flexible. Thus, an exchange between conformations is likely occurring in these micelles at an intermediate rate which, due to substantial line broadening, causes the Gly18 HSQC peak to disappear.

An additional novel result from this part of my research is an indication about the formation of the mixed LMPC/LMPG micelles. From the DOSY experiments, for each type of micelles and peptide/micelle complex, two separate values of translational diffusion coefficients are calculated using the attenuation of the two sharpest proton peaks. For LMPC, LMPG and LMPC/LMPG mixture, each signal attenuation curve constitutes a single linear fit with less than 0.05% standard deviation and hence yields a single diffusion coefficient. Also, the two diffusion coefficients for each micelle type, including the LMPC/LMPG mixture, vary by less than 1% and thus are virtually the same. Therefore, there is only one homogeneous micelle structure present for each of the LMPC, LMPG or mixed LMPC/LMPG systems. The hydrodynamic diameters of these micelles, calculated using the measured diffusion coefficients, are ~ 7.2, ~ 8.3 and ~ 8.3 nm, respectively. The diameters of pure LMPC and LMPG micelles are quite different, but interestingly, the diameters of LMPG micelles and LMPC/LMPG mixture are equivalent, although the mixture only contains 15% LMPG. Hence, the mixture sample consists of micelles formed from LMPC and LMPG together rather than their own separate micelles. Reappearance of the strong Gly18 peak in the HSQC spectra of Mini-B<sub>OX</sub> in LMPC/LMPG mixture also indicates to the formation of a mixed micelle system. Had there been separate micelles in the mixture, the

Gly18 peak would not be present or would be very weak, since in LMPC micelles, which would then represent 85% of the micelle population in the mixture, the peak is absent.

The strong reappearance of Mini-B<sub>OX</sub>'s Gly18 HSQC peak in the mixed LMPC/LMPG system has another important implication. It shows that as little as 15% LMPG is enough to induce the same structure/dynamics of the middle loop as is seen in 100% LMPG. This likely indicates Mini-B's specificity, or at least a preference of interaction, for anionic amphiphiles over zwitterionic amphiphiles. In native lung conditions, the full-length SP-B may also exhibit similar behavior and preferentially bind lipids with PG headgroup from a pool that includes lipids with PC headgroup too. However, Mini-B interacts with PC-type lipid molecules as well. The parent protein SP-B may thus bind DPPC or other PCs also and contribute to the large scale rearrangement of lipids and stabilization of complex structures required for optimum surfactant function.

Given the amphipathic profile of Mini-B, it is not unusual that the peptide would interact with amphiphiles such as detergents or lipids and take on a folded conformation in micelle environments. What is more intriguing, the peptide interacts differentially with anionic and zwitterionic surfactant phospholipid analogues. The strength of cationic Mini-B's binding with the micelles apparently depends on the charge profile of the micelle headgroups. Due to the variation in electrostatic component of interactions, Mini-B is probably loosely bound to the zwitterionic micelles and stays close to the surface but tightly bound to the anionic micelles and lies much deeper. There also exist subtle differences in Mini-B's structures in various micelle systems. The tertiary structures of oxidized and reduced Mini-B, however, appear substantially dissimilar even in a particular micelle environment. Mini-B<sub>RED</sub> takes on a single structure but Mini-B<sub>OX</sub> exhibits a degree of conformational heterogeneity in all micelle systems. Furthermore, the structural flexibility or dynamics of Mini-B<sub>OX</sub> are quite different in anionic versus zwitterionic micelles, at least for the middle loop. These findings about Mini-B, the most biologically active fragment of SP-B produced so far, help in figuring out some key features of SP-B, such as its conformation in native lung conditions and its interactions with different surfactant phospholipids.

## *Chapter 5*

# **SP-A in Model Surfactant Lipids: Conformations and Interactions**

*Note : SP-A was collected from cow lungs supplied by Ray Bishop (Bishops Meat, Foxtrap, NL). Isolation and purification of the protein was performed by Donna Jackman (Booth lab, Biochemistry, MUN).*

## 5.1 Overview

Surfactant protein A (SP-A) is a glycoprotein and, by weight, the most abundant protein component of the lung surfactant system [163]. Under native conditions, SP-A is presumed to be an octadecamer constructed by six trimers [164] although other smaller oligomers also coexist [165]. The monomer of human SP-A, and also of the bovine SP-A used in this study, consists of 248 amino acids [56] but its molecular weight varies from ~ 28 to ~ 36 kDa depending on the extent of post-translational modifications [166]. SP-A belongs to the structurally homologous family of innate immune defense proteins known as collectins, so named for their collagen-like and lectin domains. SP-A consists of four structural domains: (1) a short N-terminal domain involved in intermolecular disulfide bond formation, (2) a proline-rich collagen-like domain important for oligomerization, (3) an  $\alpha$ -helical coiled coil neck domain involved in trimerization, and (4) a globular C-terminal carbohydrate recognition domain (CRD) [17, 53, 167]. Figure 5.1 shows a schematic diagram of the structural domains of SP-A and how its octadecameric structure is assembled.

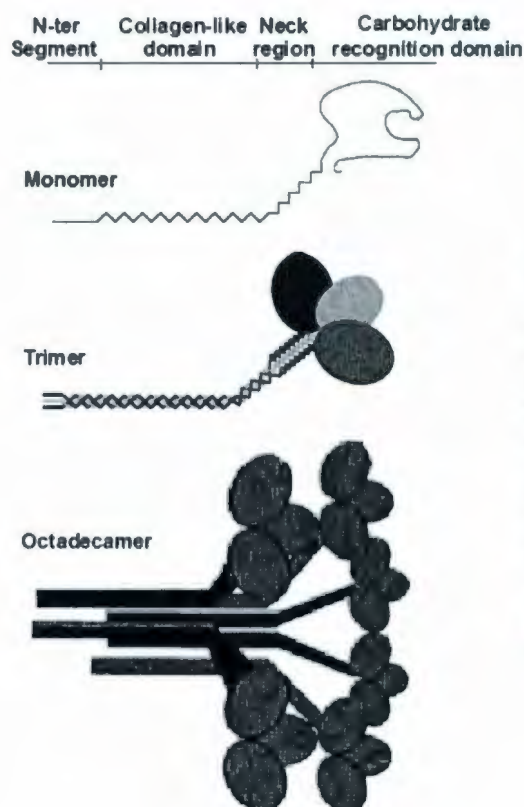


**Figure 5.1** : A model for SP-A monomer, trimer and octadecamer, based on Ref. [53]. The protein consists of four distinct structural domains [17, 53]. The neck domains of three monomers become associated as a rigid  $\alpha$ -helical coiled-coil and the collagen-like domains fold into a staggered collagen triple-helix. A trimeric subunit is tethered by disulfide linkages in the N-terminal domains. Six trimeric subunits further assemble as an octadecamer by lateral association of the N-terminal halves of the triple-helices forming a stem.

Substantial evidence indicates that SP-A is a major player in innate host-defense and inflammatory immunomodulator processes of the lung [5, 57]. SP-A has been shown to bind to a broad range of microorganisms, including bacteria, fungi, viruses and mite extracts [168, 169]. The binding neutralizes, agglutinates and/or enhances the uptake of pathogens by phagocytes of the innate immune system [17]. *In vitro* studies have also presented a long list of SP-A's surfactant-related activities. SP-A mediates the formation of tubular myelin when added to DPPC, PG and SP-B mixtures in the presence of  $\text{Ca}^{2+}$  [59, 170], enhances adsorption of phospholipids along the air-water interface in a concerted action with SP-B [62, 171], induces  $\text{Ca}^{2+}$  dependent aggregation of lipid vesicles with or without SP-B or SP-C [172, 173] and reduces inhibition of surfactant activity by foreign lipid binding proteins or serum lipoproteins [174, 175].

Several biophysical studies have indicated an *in vitro* interaction, either direct or indirect, between SP-B and SP-A [59, 62, 170, 171] that may be important in lung surfactant function. I have attempted to directly probe the interaction between Mini-B and SP-A in the presence of micelles composed of model surfactant lipids LMPC, LMPG and mixed LMPC/LMPG, alongside SDS and DPC (Chapter 6). In Chapter 4, I have reported the findings on Mini-B's interactions with these micelles along with its conformation. In this chapter, I report the findings on SP-A's conformation and lipid interactions under the same micelle conditions obtained using proton and diffusion NMR. These two chapters provide the foundation for investigating Mini-B/SP-A interaction, if any, in the presence of surfactant lipid analogues.

## **5.2 Materials and Methods**

### **5.2.1 Protein Isolation and Purification**

The natural bovine SP-A used in these studies were collected from the lungs of young cows slaughtered at a local farm (Bishops Meat, Foxtrap, Newfoundland). Isolation and purification of SP-A were conducted by Donna Jackman (Booth lab, Biochemistry, Memorial

University of Newfoundland). The lungs were lavaged with 0.15 M NaCl solution and the lavage was centrifuged at 800g for 10 minutes. The supernatant was centrifuged at 7000g for 60 minutes. The pellet was resuspended in 5 mM Tris-HCl/100 mM NaCl/1.64 M NaBr (pH 7.4) and centrifuged overnight at 81500g. The pellicle was resuspended in 5 mM Tris-HCl/100 mM NaCl (pH 7.4) and centrifuged at 65000g for 2 hours. SP-A was purified from the surfactant pellet by the method of Haagsman *et al.* [176] as follows. The surfactant pellet suspended in water was injected into stirred 1-butanol and then centrifuged at 10000g for 20 minutes. The precipitate was dried under nitrogen and washed twice in 10 mM Hepes/100 mM NaCl/20 mM octyl  $\beta$ -D-glucopyranoside (pH 7.4). Each wash was followed by centrifugation at 100000g for 30 minutes. The material that was insoluble in the above buffer was suspended in 5 mM Hepes (pH 7.4) and the solution was dialyzed against 5 mM Hepes (pH 7.4). The dialyzed material was centrifuged at 100000g for 30 minutes and the supernatant, which contained the purified SP-A, was concentrated using Amicon ultra centrifugal filters (Fisher Scientific, Ottawa, ON) and stored at -20 °C. The molecular mass of the final product was confirmed by SDS-polyacrylamide gel electrophoresis (PAGE) or matrix-assisted laser desorption/ionization -time-of-flight (MALDI-TOF) mass spectrometry performed at the CREAT Network facility at Memorial University of Newfoundland. The concentration of SP-A in Hepes buffer was confirmed by spectrophotometric analysis.

### 5.2.2 Sample Preparation

The NMR samples used in these studies were prepared from different preparations of SP-A. First, samples of SP-A alone (i.e., without detergents/lipids) were prepared in aqueous solution (90% H<sub>2</sub>O plus 10% D<sub>2</sub>O) containing 0.4 mM DSS, 0.2 mM NaN<sub>3</sub> and 4.5 mM Hepes. SP-A/micelle samples were then prepared by adding the required amounts of detergents/lipids. At least two samples were prepared for each micelle system (except for SDS) with varying ratios of the protein and detergent/lipid using different SP-A preparations. However, for each sample, the molar concentration of the lipid was kept at least 200 times higher than the monomeric concentration of the protein. The exact composition of each

sample is described in the results section with SP-A molar concentration specified as if it were 100% monomeric. Deuterated (98%) SDS and DPC were purchased from Cambridge Isotope Laboratories (Andover, MA). Non-deuterated LMPC and LMPG, purchased from Avanti Polar Lipids (Alabaster, AL) were used, as deuterated versions of these lipids are not available commercially to date. Hepes was also in the non-deuterated form. The pH of the samples was set at 6.9 to match the physiological condition in the lung. The pH was set using NaOH and HCl solutions without taking the isotope effects into account.

### 5.2.3 NMR Data Collection and Processing

A set of 1D  $^1\text{H}$  and 2D DOSY experiments were performed for SP-A alone, individual micelle systems and SP-A/micelle complexes on a Bruker Avance II 14.1 Tesla (600 MHz) spectrometer (Billerica, MA) equipped with z-gradients and an inverse triple resonance TXI probe. The NMR data were collected and processed using the Bruker Topspin 2.0 software. The pulse length (P1) and the transmitter offset (O1) were optimized for each sample before running the full set of NMR experiments. The 1D  $^1\text{H}$  spectra were acquired at 37 °C to match the physiological temperature. In 1D  $^1\text{H}$  experiments, data were collected with either 256 or 160 scans (indicated in the figure captions) using the water-gate water suppression technique [146] and processed using an exponential apodization function with 1 Hz line broadening. The 2D DOSY spectra of SP-A alone and SP-A in SDS/DPC micelles were acquired at 37 °C. However, the DOSY spectra of SP-A in LMPC/LMPG micelles were acquired at 25 °C to minimize the effect of thermal convection. The diffusion time was kept constant at 100 ms. The gradient pulse length was optimized for each sample and set between 5 and 8 ms. The maximum amplitude of the gradient strength was 35 G/cm and the  $^1\text{H}$  signals were attenuated in 32 steps. The translational diffusion coefficient was determined from the slope of the signal attenuation curve plotted using Eq. 2.17. The hydrodynamic diameter was calculated using the Stokes-Einstein equation [Eq. 2.20]. The viscosity of pure water was used for the viscosity of solution in the calculation and the values were  $8.91 \times 10^{-4}$  kg/m.s at 25 °C (298 K) and  $6.92 \times 10^{-4}$  kg/m.s at 37 °C (310 K).

## 5.3 Results

### 5.3.1 SP-A Alone in Aqueous Solution

Before studying the conformation of SP-A in lipid mimetic micelle environments and its interactions with surfactant lipid analogues, I first investigated its conformation when alone in the aqueous environment (90% H<sub>2</sub>O and 10% D<sub>2</sub>O). Also, since SP-A was collected from a natural source (cow lungs) and the protein preparation (isolation and purification) was performed using different batches as required, acquisition of a 1D <sup>1</sup>H spectrum was routinely performed for each preparation of SP-A in aqueous solution to check the consistency of the samples. The 1D <sup>1</sup>H spectra of all SP-A preparations looked almost identical confirming the consistency among different protein preparations. Figure 5.2 shows one such 1D <sup>1</sup>H spectrum of SP-A alone in 90% H<sub>2</sub>O and 10% D<sub>2</sub>O in the presence of 4.5 mM Hepes. The intense proton signals are mostly generated by Hepes and DSS. However, a few broad signals from SP-A, having a much lower intensity, are also present. The overall appearance of the spectrum is consistent with a high molecular mass protein specimen. The observed protein signals, including the 2 or 3 peaks in the amide proton region, are likely generated by some highly mobile region(s) of SP-A (e.g., a flexible loop) undergoing fast motion or conformational exchange. Therefore, under this condition, SP-A is likely present in a large oligomeric form, perhaps the long-presumed native octadecameric form with a molecular weight of ~ 550 kDa. If there are any smaller subunits also present, such as monomers or trimers, those are most probably associated with the large structures.

The size(s) of SP-A particles in the aqueous solution, as determined from translational diffusion measurements, confirm the presence of a large structure of the protein. Two values of the diffusion coefficients of SP-A are determined from the 2D DOSY spectra (Figure 5.3) using the attenuation of the peak at 2.03 ppm and the HN region. The observed diffusion coefficients are  $5.40 \times 10^{-11}$  and  $6.52 \times 10^{-11}$  m<sup>2</sup>/s, respectively. The corresponding hydrodynamic diameters, calculated using the Stokes-Einstein equation (Eq. 2.20), are 12.15

and 10.06 nm, respectively. The apparent faster diffusion implied by the HN region is likely a result of the exchange between the labile amide protons and the solvent protons/deuterons. Thus the translational diffusion measurements indicate that the hydrodynamic diameter of SP-A alone is greater than 12 nm under the conditions used in this study.

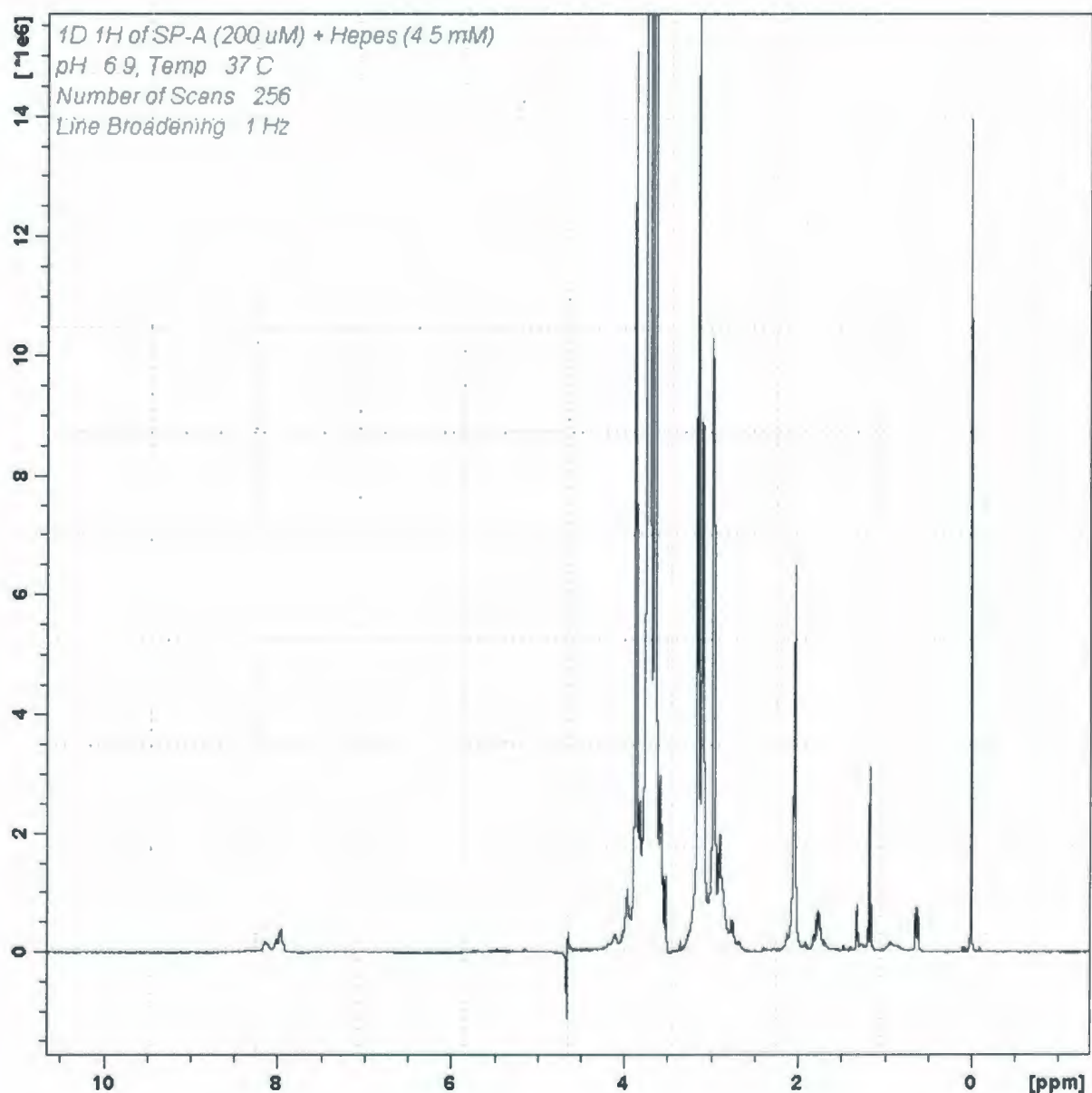


**Figure 5.2 :** 1D  $^1\text{H}$  spectrum of 0.2 mM SP-A in 90%  $\text{H}_2\text{O}$  and 10%  $\text{D}_2\text{O}$ , in the presence of 4.5 mM Hepes at pH 6.9 and temperature 37 °C. The molar concentration of SP-A corresponds to the monomeric form of the protein. The spectrum was acquired using 256 scans and processed with 1 Hz line broadening.

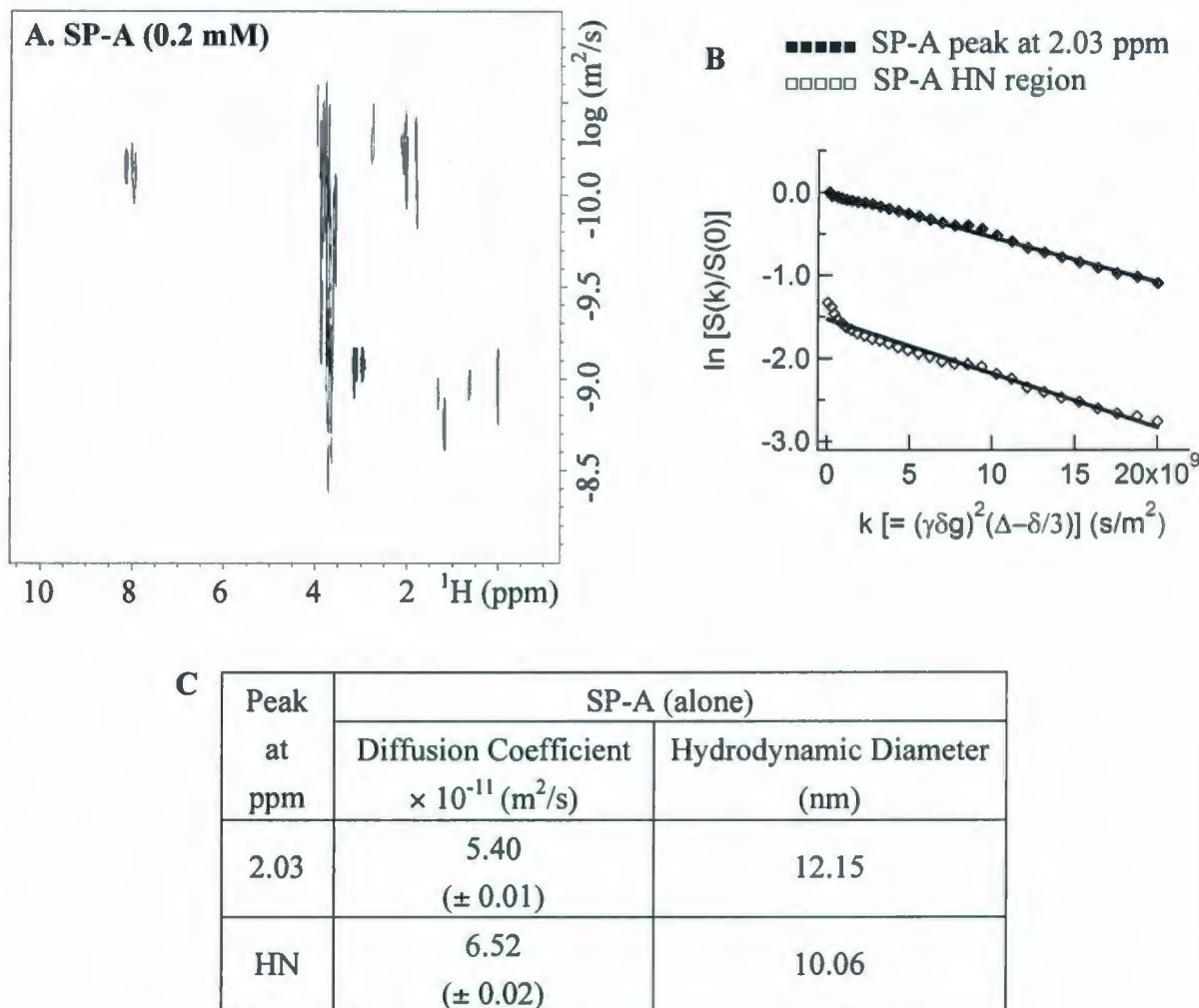


**Figure 5.3** : Size of SP-A as indicated by translational diffusion. Left panel (A) shows 2D DOSY spectra of 0.2 mM SP-A in aqueous solution (90% H<sub>2</sub>O plus 10% D<sub>2</sub>O), in the presence of 4.5 mM Hepes at pH 7 and temperature 37 °C. Linear fits in the right panel (B) show the attenuation of the peaks at 2.03 ppm and HN region obtained from the DOSY data. The observed diffusion coefficients, represented by the slopes of the signal attenuation curves, and the corresponding hydrodynamic diameters, calculated using the Stokes-Einstein equation (Eq. 2.20), are shown in the table (C).

### 5.3.2 SP-A in SDS Micelles

Studies of SP-A's conformation in the micelle environments and its lipid interactions began with smaller anionic micelles composed from the detergent SDS. Figure 5.4 shows the 1D  $^1\text{H}$  spectrum of SP-A in SDS micelles. Surprisingly, SP-A displays a major conformational change with the addition of SDS as the enlarged 6-9 ppm region shows a lot more signals from the backbone amide protons with increased intensity when compared to SP-A alone. The signals are broad and overlapped, as would be expected from a multimeric protein consisting of 248 amino acids and bound to a micelle, but well-dispersed. As elaborated in the discussion, the well-dispersed HN signals may arise from a subpopulation of the protein having a lower molecular mass and hence a smaller oligomeric form that dissociate from the higher molecular mass oligomers in the presence of SDS micelles.

The translational diffusion coefficients, obtained from the 2D DOSY spectra (Figure 5.5), confirm the presence of lower molecular mass SP-A species when the protein is bound to the micelles. The observed diffusion coefficient of SP-A/SDS complex, determined from the attenuation of the HN signals, is  $1.166 \times 10^{-10} \text{ m}^2/\text{s}$ , which represents a hydrodynamic diameter of 5.63 nm. Thus the apparent size of SP-A/SDS complex is substantially smaller than the size of SP-A alone (hydrodynamic diameter  $\sim 12.2 \text{ nm}$ ). The DOSY data also illustrates the effect of SP-A on the size or shape of SDS micelles. The diffusion coefficient of micelles, determined from the SDS peak at 1.22 ppm, decreases from  $5.323 \times 10^{-10}$  to  $1.670 \times 10^{-10} \text{ m}^2/\text{s}$  upon binding to SP-A. Therefore the hydrodynamic diameter of SDS micelles apparently increases from 1.23 to 3.93 nm as a result of SP-A binding.

The apparent size of SDS micelles found in this study is substantially smaller than that of earlier study (Chapter 4, Page 69). Since the DOSY data corresponds to a weighted average from the free and micelle-bound molecules, the smaller apparent size may be the result of a faster exchange between the two SDS species. This is likely due to the lower SDS concentration of 40 mM used in this study, as opposed to 150 mM concentration used in the previous study. The faster exchange of SDS molecules may also be the reason for the difference in the apparent hydrodynamic diameter of SP-A/SDS complex, which is 5.63 nm when determined from the protein HN region, but 3.93 nm when determined from the SDS

1.22 ppm peak. Also, the signal attenuation curves of pure SDS micelles, plotted using either of the peaks at 0.80 or 1.22 ppm, are not fit well by a single linear fit (Figure 5.5). This likely indicates the presence of multi-size SDS assemblies at lower concentrations and a relatively

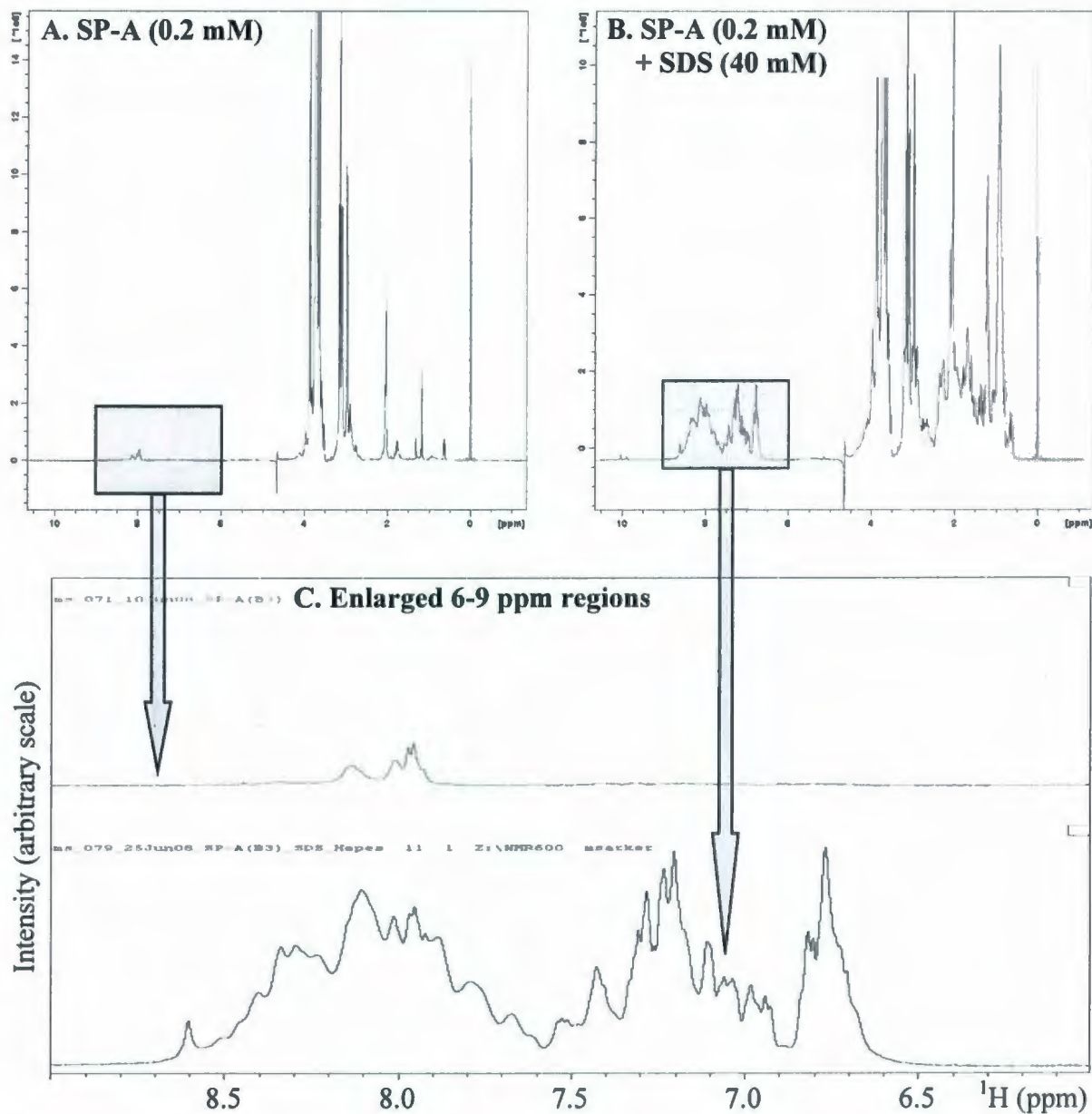
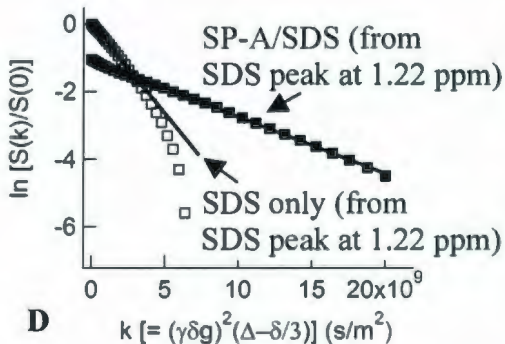
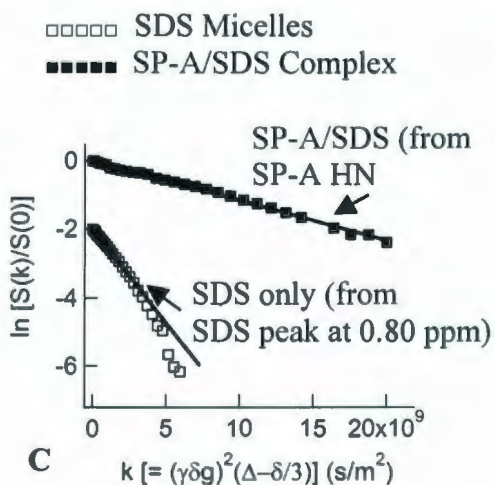
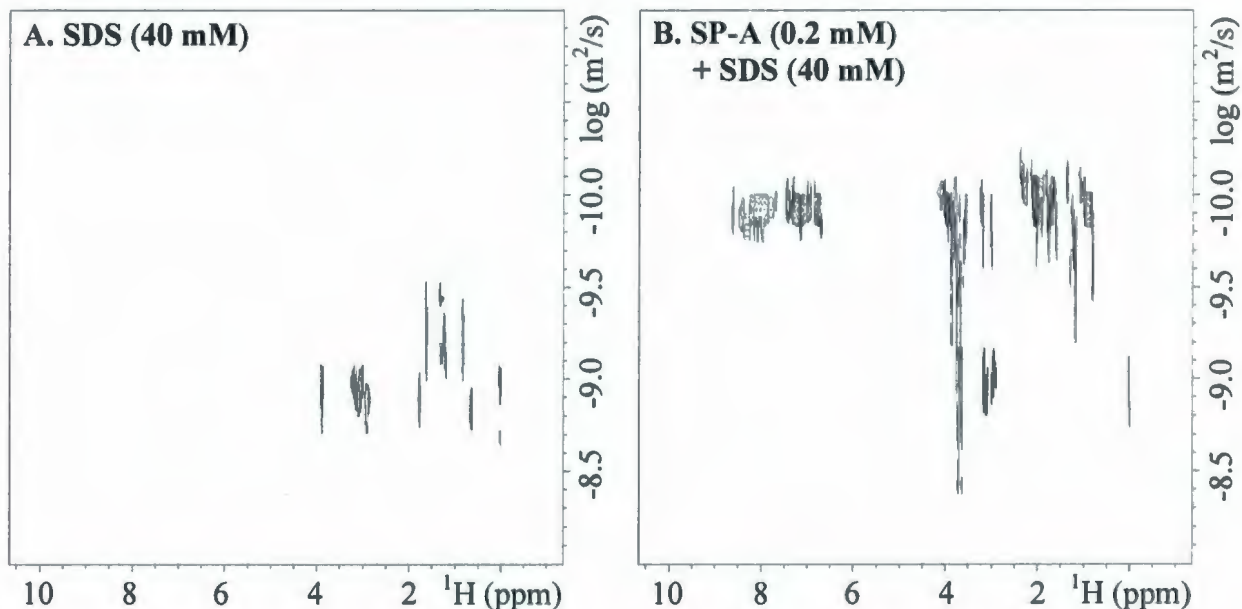


**Figure 5.4** : 1D  $^1\text{H}$  spectra of (A) 0.2 mM SP-A (alone) and (B) 0.2 mM SP-A in 40 mM SDS, in the presence of 4.5 mM Hepes. The pH of both samples was 6.9 and the experiments were performed at 37 °C. The spectra were acquired using 256 scans and processed with 1 Hz line broadening. The intense peaks seen in the spectrum (B) are from DSS and Hepes. The 6-9 ppm regions, exhibiting the protein HN signals, are enlarged and shown in the bottom panel (C).

slower exchange between the species. However, the single linear fits for the SDS/SP-A complex indicate a single average size and a relatively fast exchange between the species.



Peak at ppm	SDS (□□□)		SP-A/SDS (■ ■ ■)	
	D. Coeff. $\times 10^{-10}$ (m <sup>2</sup> /s)	H. Dia. (nm)	D. Coeff. $\times 10^{-10}$ (m <sup>2</sup> /s)	H. Dia. (nm)
0.80/ HN	5.466 ( $\pm 0.043$ )	1.20	1.166 ( $\pm 0.014$ )	5.63
1.22	5.323 ( $\pm 0.027$ )	1.23	1.670 ( $\pm 0.008$ )	3.93

E

**Figure 5.5 :** SDS micelles (□□□) and SP-A/SDS complex (■ ■ ■) sizes as indicated by translational diffusion. Upper panels show 2D DOSY spectra of (A) 40 mM SDS and (B) 0.2 mM SP-A + 40 mM SDS, at pH 7 and temperature 37 °C. Linear fits (C and D) show the attenuation of the SDS peaks at 0.80 and 1.22 ppm and the protein HN region obtained from the DOSY data. For SDS micelles, the fits correspond to the larger size only. The observed diffusion coefficients, represented by the slopes of the curves, and the corresponding hydrodynamic diameters, calculated using the Stokes-Einstein equation (Eq. 2.20), are shown in the table (E).

### 5.3.3 SP-A in DPC Micelles

The conformation of SP-A and its lipid interactions were studied next in the zwitterionic DPC micelle system. The 1D  $^1\text{H}$  spectra of two SP-A samples, with different protein/lipid concentrations (indicated in the figure captions), look almost identical (Figure 5.6). As in SDS, SP-A displays a major conformational change in DPC micelles when compared to SP-A alone. The enlarged 6-9 ppm region shows well-dispersed signals with increased intensity, although, as expected, the signals are broad and overlapped. Again, the proton signals are generated most probably by a subpopulation of lower molecular mass SP-A species that are dissociated from the large oligomers in the presence of DPC micelles.

Furthermore, similar to SDS, the translational diffusion measurements support the presence of smaller molecular mass SP-A species and formation of a complex through interactions between SP-A and DPC micelles. The observed diffusion coefficient of pure DPC micelles, as determined from the attenuation of the DPC peak at 1.22 ppm, decreases from  $3.37 \times 10^{-10}$  to  $1.92 \times 10^{-10} \text{ m}^2/\text{s}$  upon binding to SP-A. This corresponds to an apparent increase of the micelle hydrodynamic diameter from 1.95 to 3.42 nm. The observed diffusion coefficient of the complex, when determined from the attenuation of the SP-A HN region, is  $1.62 \times 10^{-10} \text{ m}^2/\text{s}$  and the corresponding hydrodynamic diameter is 4.05 nm. Thus the apparent size of the SP-A/DPC complex is much smaller than SP-A alone (~ 12.2 nm).

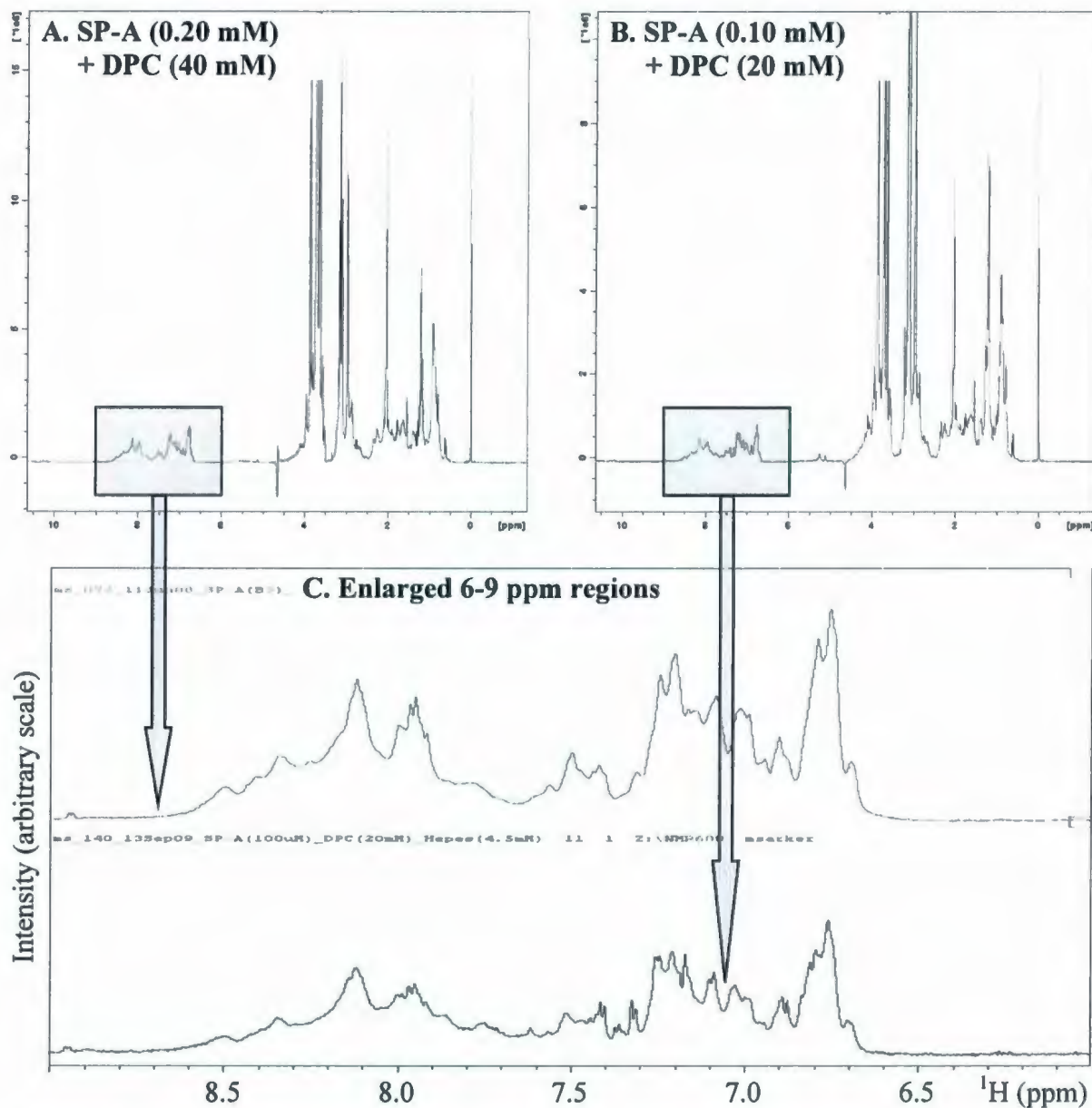
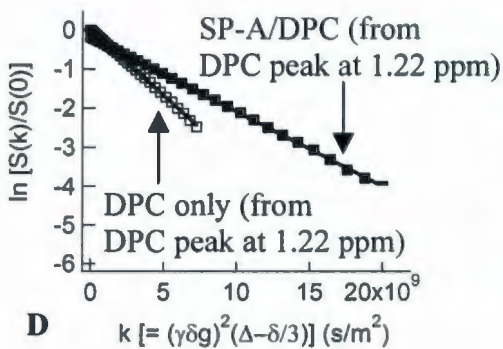
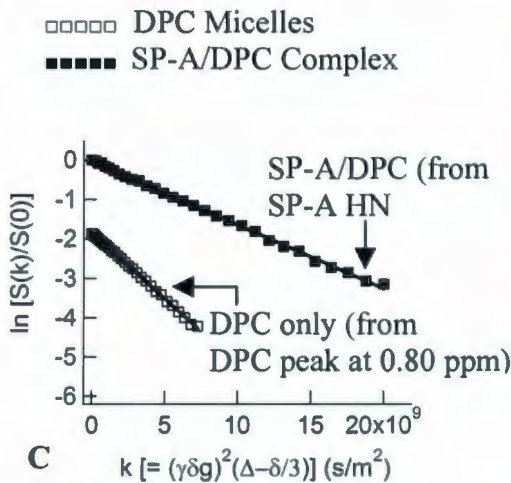
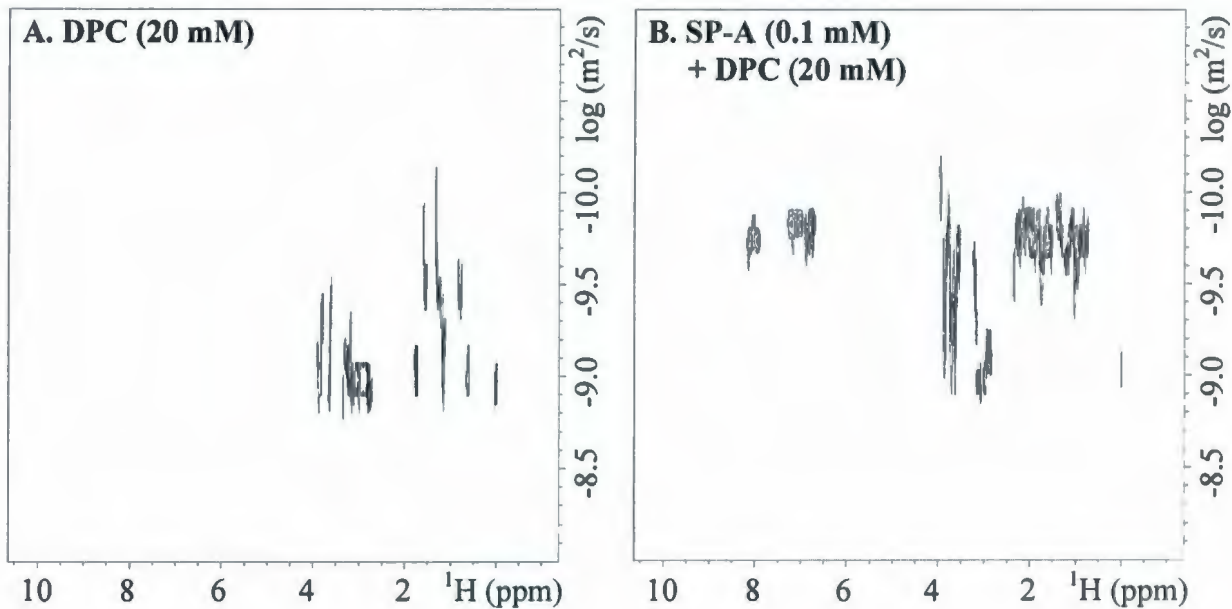


**Figure 5.6 :** 1D  $^1\text{H}$  spectra of (A) 0.20 mM SP-A in 40 mM DPC (acquired using 256 scans) and (B) 0.10 mM SP-A in 20 mM DPC (acquired using 160 scans), in the presence of 4.5 mM Hepes. Samples were made from two different preparations of SP-A. The pH of both samples was 6.9 and the experiments were performed at 37 °C. The spectra were processed with 1 Hz line broadening. The intense peaks seen in the spectra are from DSS and Hepes. The 6-9 ppm regions, exhibiting the protein HN signals, are enlarged and shown in the bottom panel (C).



Peak at ppm	DPC (□□□)		SP-A/DPC (■■■)	
	D. Coeff. $\times 10^{-10} \text{ (m}^2\text{/s)}$	H. Dia. (nm)	D. Coeff. $\times 10^{-10} \text{ (m}^2\text{/s)}$	H. Dia. (nm)
0.80/ HN	3.35 $(\pm 0.02)$	1.96	1.62 $(\pm 0.01)$	4.05
1.22	3.37 $(\pm 0.01)$	1.95	1.92 $(\pm 0.01)$	3.42

E

**Figure 5.7** : DPC micelles (□□□) and SP-A/DPC complex (■■■) sizes as indicated by translational diffusion. Upper panels show 2D DOSY spectra of (A) 20 mM DPC and (B) 0.10 mM SP-A + 20 mM DPC, at pH 7 and temperature 37 °C. Linear fits (C and D) show the attenuation of the DPC peaks at 0.80 and 1.22 ppm and the protein HN region obtained from the DOSY data. The observed diffusion coefficients, represented by the slopes of the curves, and the corresponding hydrodynamic diameters, calculated using the Stokes-Einstein equation (Eq. 2.20), are shown in the table (E).

#### 5.3.4 SP-A in LMPC Micelles

To gain an insight into SP-A's conformation in a more physiologically relevant lipid environment and to probe SP-A's interactions with surfactant phospholipid analogues, the investigations continued with LMPC, LMPG and mixed LMPC/LMPG micelles. First studied was SP-A in zwitterionic micelles composed of LMPC that mimic the lung lipid environment created by the most abundant surfactant phospholipid DPPC. Figure 5.8 shows the 1D  $^1\text{H}$  spectra of two SP-A samples having two different protein/lipid ratios (indicated in the figure captions). The enlarged 6-9 ppm regions of both samples look almost identical. The HN signals of SP-A in LMPC are also not substantially different from those in DPC. However, the signals are slightly broader and likely more overlapped as SP-A is now bound to the larger LMPC micelles. The overall appearance of the 1D  $^1\text{H}$  spectrum further indicates the dominance of a lower molecular mass SP-A subpopulation in the LMPC micelle environment.

The 2D DOSY experiments (Figure 5.9) confirm the presence of a smaller SP-A oligomer in LMPC micelles. The  $\sim 10.3$  nm hydrodynamic diameter of SP-A/LMPC complexes, calculated using the observed translational diffusion coefficient of  $\sim 4.8 \times 10^{-11}$   $\text{m}^2/\text{s}$ , is much larger than the SP-A/SDS or SP-A/DPC complexes, but still smaller than SP-A alone ( $\sim 12.2$  nm). The increase from the  $\sim 7.3$  nm hydrodynamic diameter of pure micelles upon addition of SP-A, calculated using the observed diffusion coefficient of  $\sim 6.8 \times 10^{-11}$   $\text{m}^2/\text{s}$ , confirms the binding of LMPC micelles to SP-A molecules.

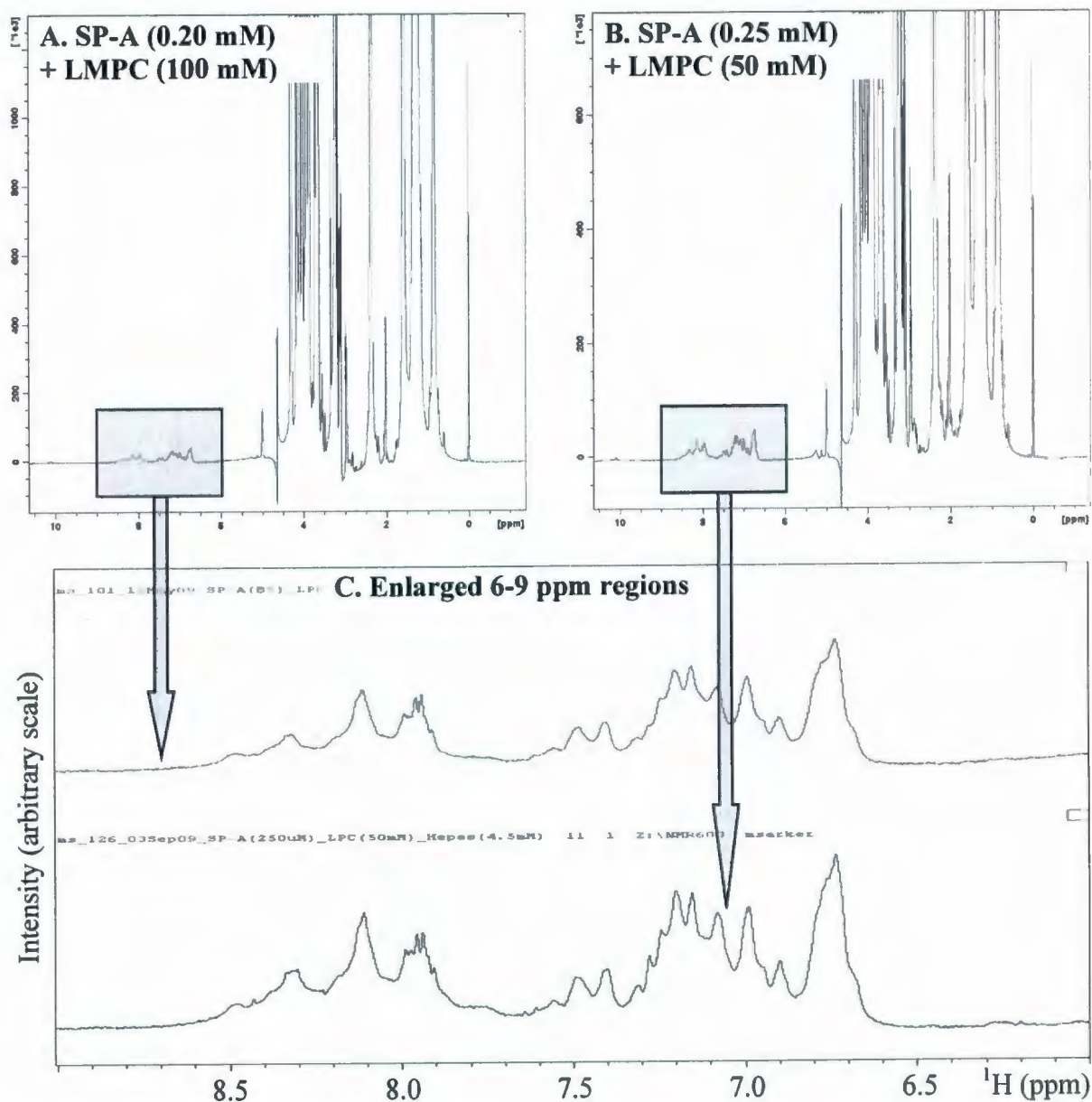
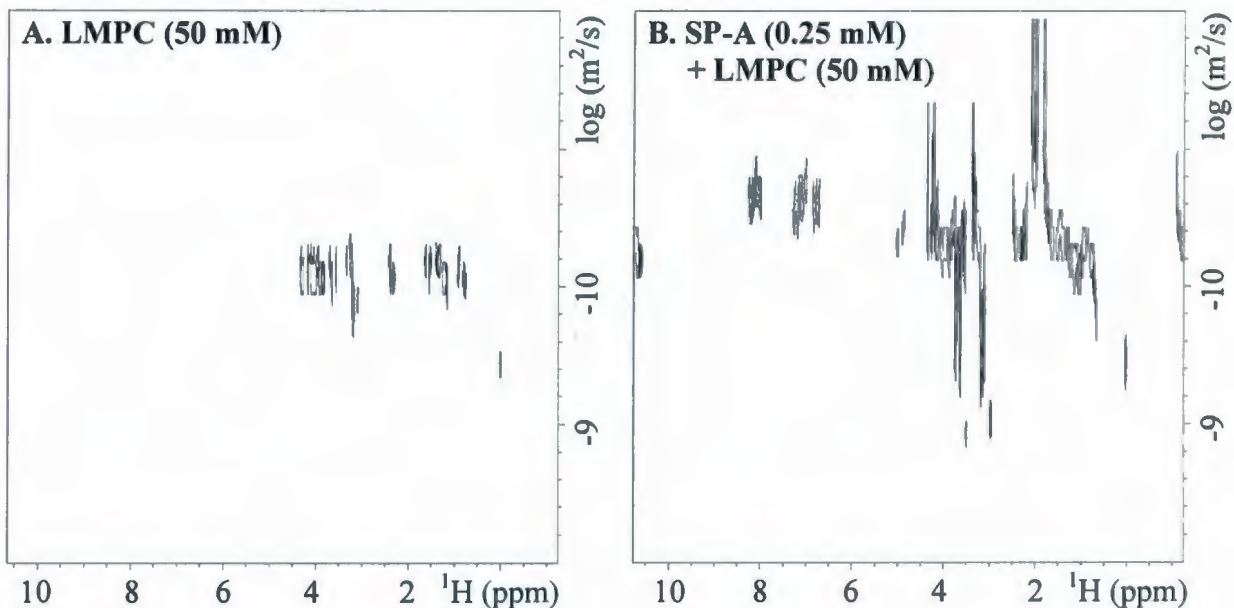
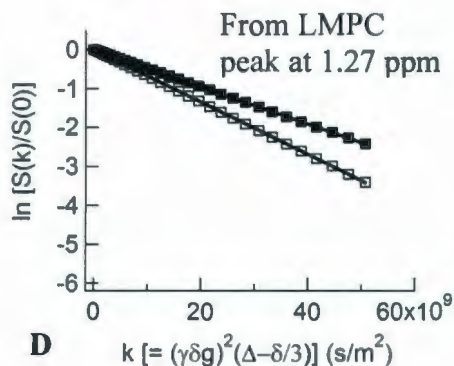
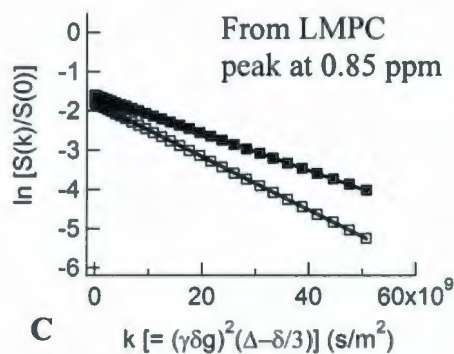


**Figure 5.8** : 1D  $^1\text{H}$  spectra of (A) 0.20 mM SP-A in 100 mM LMPC and (B) 0.25 mM SP-A in 50 mM LMPC, in the presence of 4.5 mM Hepes. Samples were made from two different preparations of SP-A. The pH of both samples was 6.9 and the experiments were performed at 37 °C. The spectra were acquired using 160 scans and processed with 1 Hz line broadening. The intense peaks seen in the spectra are from LMPC, Hepes and DSS. The 6-9 ppm regions, exhibiting the protein HN signals, are enlarged and shown in the bottom panel (C).



□□□□ LMPC Micelles  
 ■■■■ SP-A/LMPC Complex



Peak at ppm	LMPC (□□□)		SP-A/LMPC (■■■)	
	D. Coeff. $\times 10^{-11}$ (m <sup>2</sup> /s)	H. Dia. (nm)	D. Coeff. $\times 10^{-11}$ (m <sup>2</sup> /s)	H. Dia. (nm)
0.85	6.790 ( $\pm 0.006$ )	7.21	4.774 ( $\pm 0.007$ )	10.26
1.27	6.741 ( $\pm 0.003$ )	7.26	4.783 ( $\pm 0.003$ )	10.25

E

**Figure 5.9 :** LMPC micelles (□□□) and SP-A/LMPC complex (■■■) sizes as indicated by translational diffusion. Upper panels show 2D DOSY spectra of (A) 50 mM LMPC and (B) 0.25 mM SP-A + 50 mM LMPC, at pH 6.9 and temperature 25 °C. Linear fits (C and D) show the attenuation of the peaks at 0.85 and 1.27 ppm obtained from the DOSY data. The observed diffusion coefficients, represented by the slopes of the curves, and the corresponding hydrodynamic diameters, calculated using the Stokes-Einstein equation (Eq. 2.20), are shown in the table (E).

### 5.3.5 SP-A in LMPG Micelles

The investigations on the conformation and lipid interactions of SP-A continued next with anionic micelles composed of LMPG that mimic the lung lipid environment created by the surfactant phospholipids with PG headgroups. Again, the 1D  $^1\text{H}$  spectra were acquired for two different samples of SP-A having two different protein/lipid ratios (indicated in the figure captions) and both spectra look almost identical (Figure 5.10). Besides, as in the previously studied micelle systems, the dispersion and intensity of backbone HN signals indicate the presence of a smaller molecular mass species of SP-A in the LMPG micelle environment as well.

The findings about the interactions between SP-A and LMPG micelles and the complex size, as obtained from the 2D DOSY experiments (Figure 5.11), are similar to the LMPC study. The observed translational diffusion coefficient of pure LMPG micelles decreases from  $\sim 5.9 \times 10^{-11} \text{ m}^2/\text{s}$  to  $\sim 4.4 \times 10^{-11} \text{ m}^2/\text{s}$  when SP-A is added. Thus, the hydrodynamic diameter of the micelles apparently increases from  $\sim 8.3 \text{ nm}$  to  $\sim 11.2 \text{ nm}$  when bound to the protein, which is still smaller than SP-A alone ( $\sim 12.2 \text{ nm}$ ).

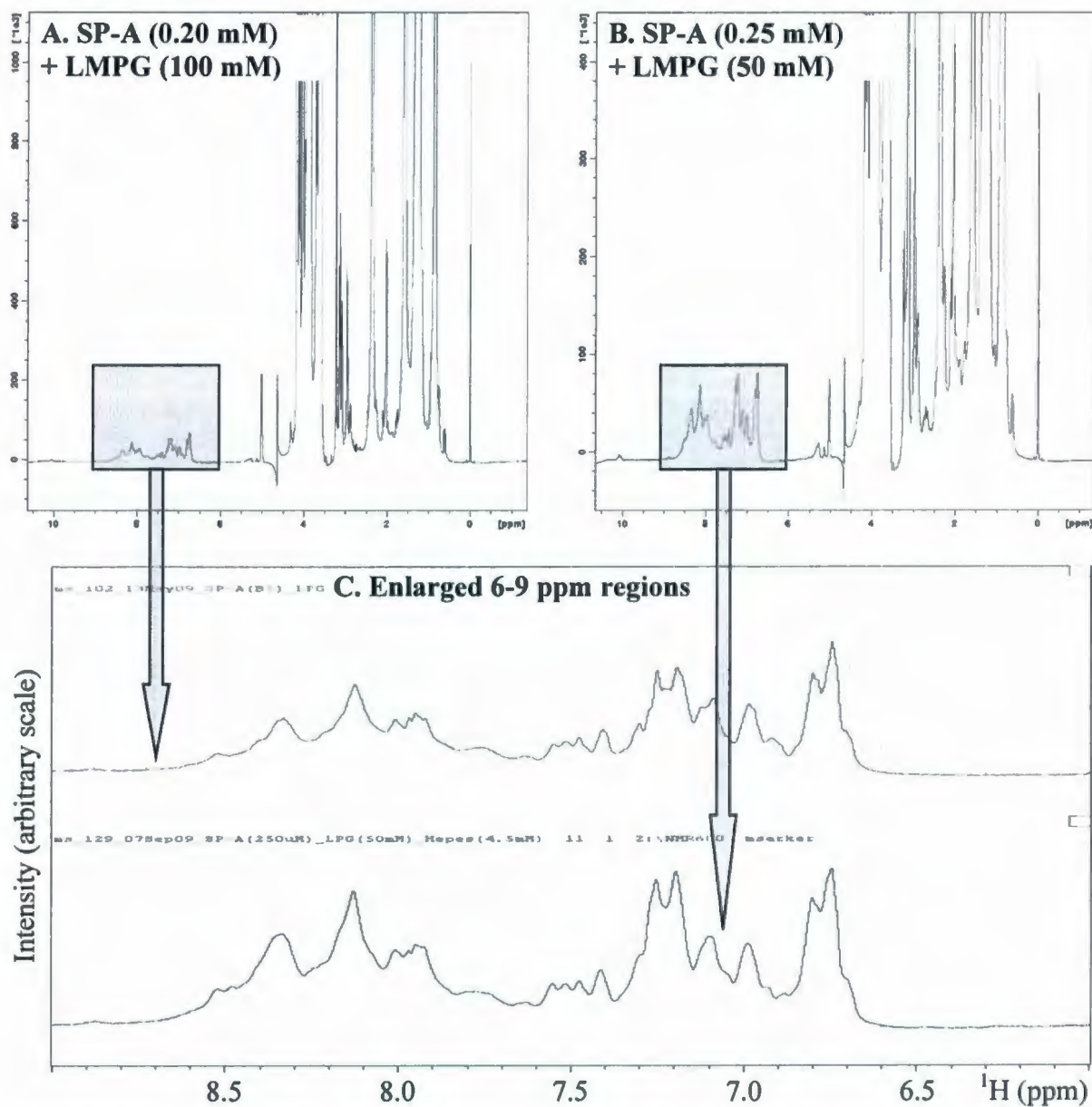
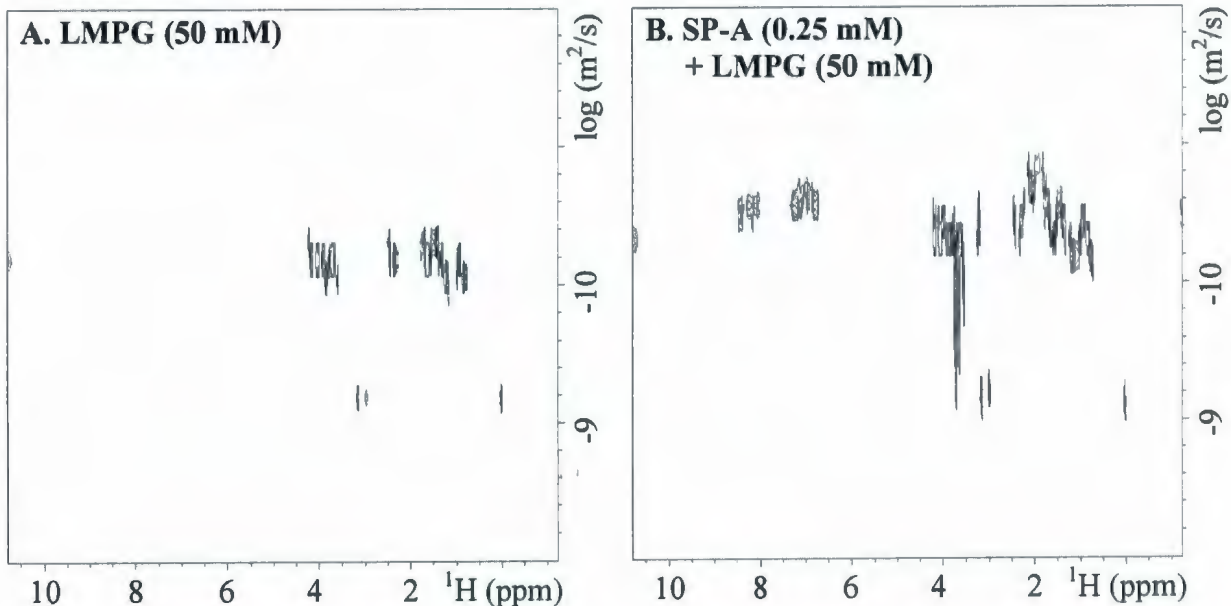
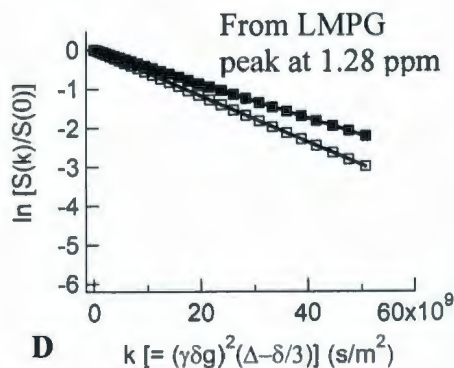
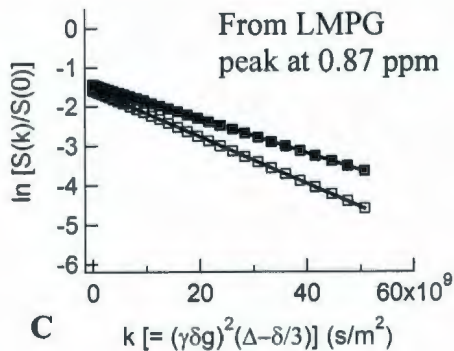


**Figure 5.10** : 1D  $^1\text{H}$  spectra of (A) 0.20 mM SP-A in 100 mM LMPG and (B) 0.25 mM SP-A in 50 mM LMPG, in the presence of 4.5 mM Hepes. Samples were made from two different preparations of SP-A. The pH of both samples was 6.9 and the experiments were performed at 37 °C. The spectra were acquired using 160 scans and processed with 1 Hz line broadening. The intense peaks seen in the spectra are from LMPG, Hepes and DSS. The 6-9 ppm regions, exhibiting the protein HN signals, are enlarged and shown in the bottom panel (C).



□□□□ LMPG Micelles  
 ■■■■ SP-A/LMPG Complex



Peak at ppm	LMPG (□□□)		SP-A/LMPG (■■■)	
	D. Coeff. $\times 10^{-11}$ (m <sup>2</sup> /s)	H. Dia. (nm)	D. Coeff. $\times 10^{-11}$ (m <sup>2</sup> /s)	H. Dia. (nm)
0.87	5.907 ( $\pm 0.004$ )	8.29	4.359 ( $\pm 0.005$ )	11.23
1.28	5.909 ( $\pm 0.003$ )	8.29	4.374 ( $\pm 0.005$ )	11.20

E

**Figure 5.11** : LMPG micelles (□□□) and SP-A/LMPG complex (■■■) sizes as indicated by translational diffusion. Upper panels show 2D DOSY spectra of (A) 50 mM LMPG and (B) 0.25 mM SP-A + 50 mM LMPG, at pH 6.9 and temperature 25 °C. Linear fits (C and D) show the attenuation of the peaks at 0.87 and 1.28 ppm obtained from the DOSY data. The observed diffusion coefficients, represented by the slopes of the curves, and the corresponding hydrodynamic diameters, calculated using the Stokes-Einstein equation (Eq. 2.20), are shown in the table (E).

### 5.3.6 SP-A in Mixed LMPC/LMPG Micelles

Lastly for this chapter, the conformation of SP-A and its lipid interactions were investigated in a mixed LMPC/LMPG micelle system. As usual, two different protein/lipid concentrations were used (indicated in the figure captions) but 8.5 : 1.5 ratio of PC to PG was maintained to match the physiological conditions. The 1D  $^1\text{H}$  spectra of both SP-A samples look almost identical (Figure 5.12). The dispersion and intensity of the backbone HN signals, when compared to SP-A alone, indicate the presence of a lower molecular mass species of SP-A also in the mixed micelle environment.

The smaller size of SP-A/micelle complex than SP-A alone is confirmed again by the 2D DOSY experiments (Figure 5.13). The size-increase of mixed LMPC/LMPG micelles, caused by the inclusion of SP-A, follows the same trend as of SP-A/LMPC and SP-A/LMPG. The observed translational diffusion coefficient of micelle alone is  $\sim 5.9 \times 10^{-11} \text{ m}^2/\text{s}$  but that of protein/micelle complex is  $\sim 4.6 \times 10^{-11} \text{ m}^2/\text{s}$ . Thus the hydrodynamic diameter of the mixed micelles apparently increases from  $\sim 8.3 \text{ nm}$  to  $\sim 10.7 \text{ nm}$  when bound to SP-A. The size of SP-A/ LMPC/LMPG complex still remains smaller than SP-A alone ( $\sim 12.2 \text{ nm}$ ).

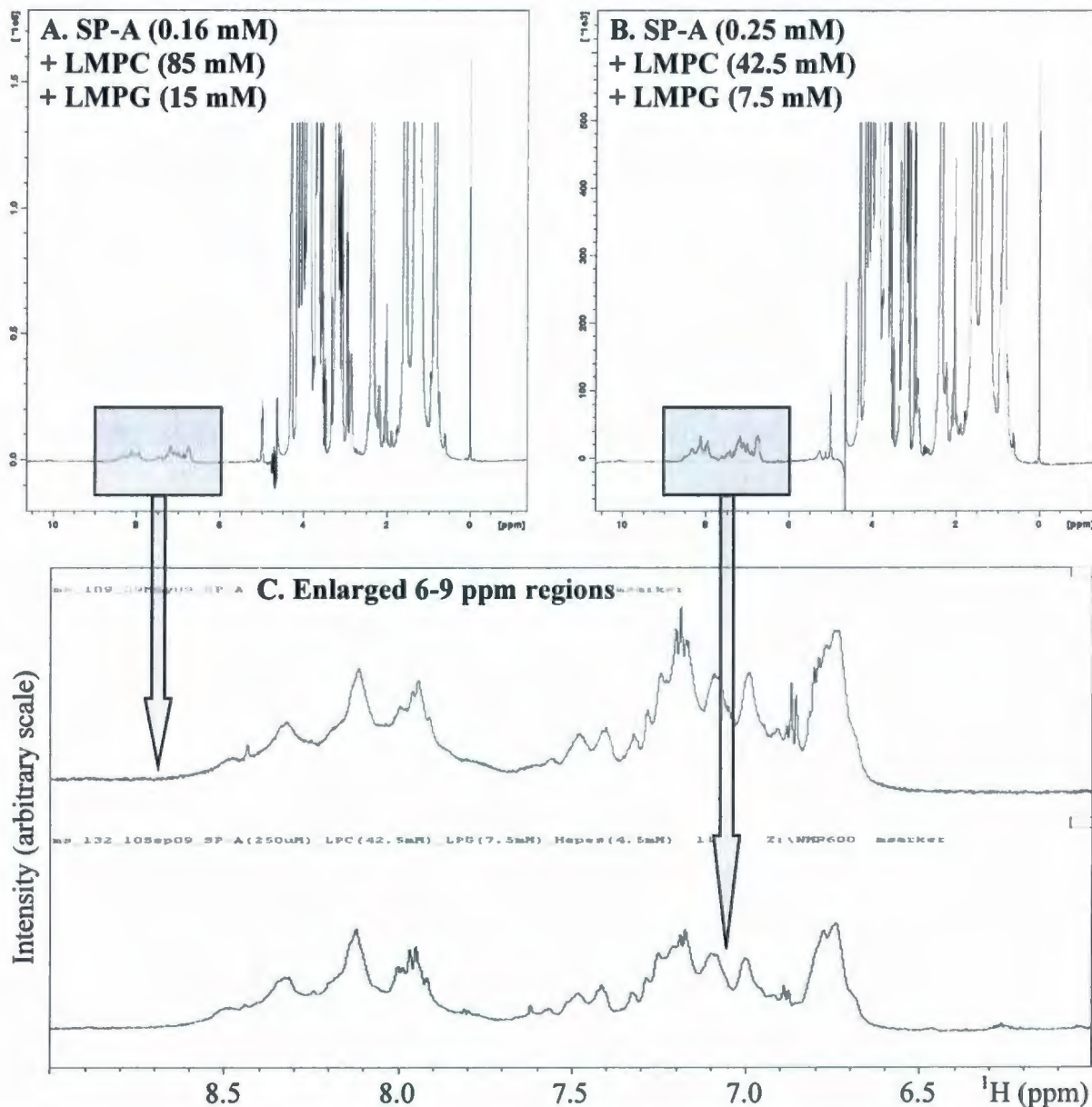
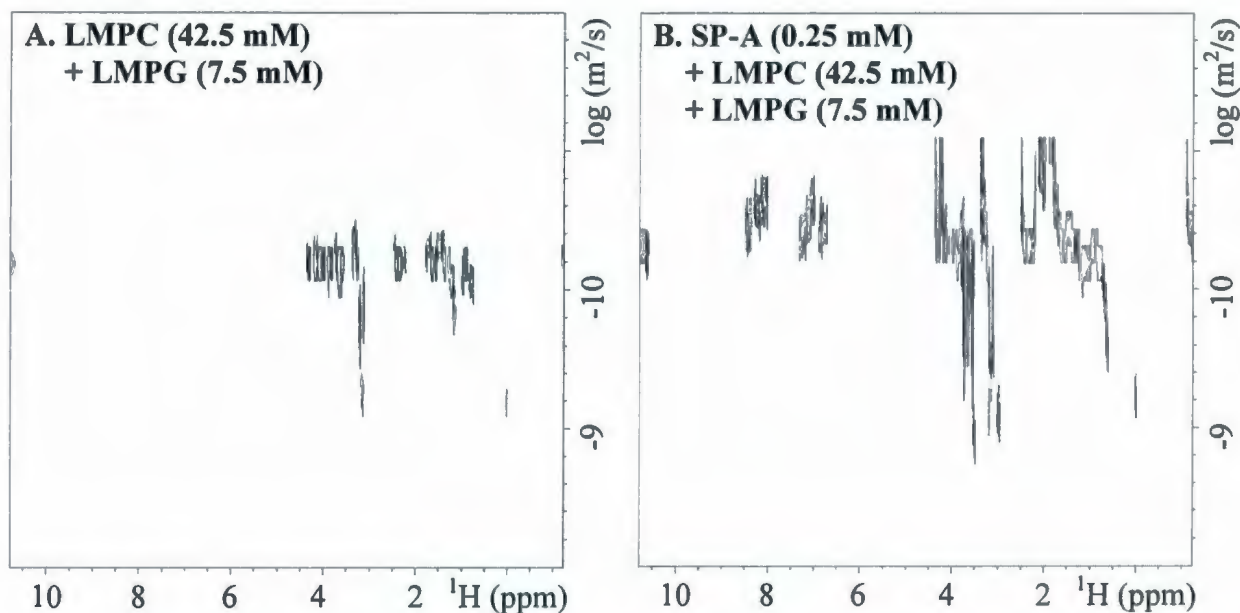
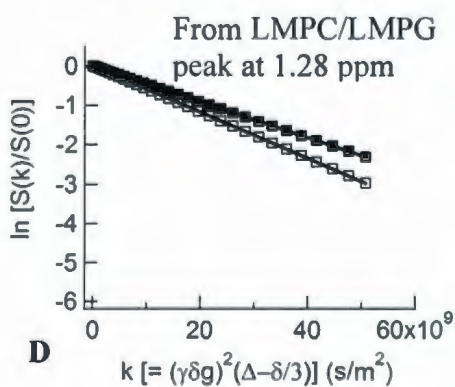
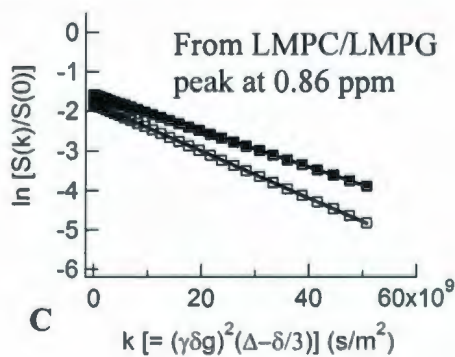


**Figure 5.12** : 1D  $^1\text{H}$  spectra of (A) 0.16 mM SP-A in 85 mM LMPC plus 15 mM LMPG and (B) 0.25 mM SP-A in 42.5 mM LMPC plus 7.5 mM LMPG, in the presence of 4.5 mM HEPES. Samples were made from two different preparations of SP-A. The pH of both samples was 6.9 and the experiments were performed at 37 °C. The spectra were acquired using 160 scans and processed with 1 Hz line broadening. The intense peaks seen in the spectra are from LMPC, LMPG, HEPES and DSS. The 6-9 ppm regions, exhibiting the protein HN signals, are enlarged and shown in the bottom panel (C).



□□□□ LMPC/LMPG Micelles  
 ■■■■ SP-A/LMPC/LMPG Complex

Peak at ppm	LMPC/LMPG (□□□)		SP-A/PC/PG (■■■)	
	D. Coeff. ×10 <sup>-11</sup> (m <sup>2</sup> /s)	H. Dia. (nm)	D. Coeff. ×10 <sup>-11</sup> (m <sup>2</sup> /s)	H. Dia. (nm)
0.86	5.910 (± 0.003)	8.29	4.564 (± 0.006)	10.73
1.28	5.866 (± 0.002)	8.35	4.571 (± 0.003)	10.71



**E**

**Figure 5.13 :** LMPC/LMPG mixed micelles (□□□) and SP-A/LMPC/LMPG complex (■■■) sizes as indicated by translational diffusion. Upper panels show 2D DOSY spectra of (A) 42.5 mM LMPC + 7.5 mM LMPG and (B) 0.25 mM SP-A + 42.5 mM LMPC + 7.5 mM LMPG, at pH 6.9 and temperature 25 °C. Linear fits (C and D) show the attenuation of the peaks at 0.86 and 1.28 ppm obtained from the DOSY data. The observed diffusion coefficients, represented by the slopes of the curves, and the corresponding hydrodynamic diameters, calculated using the Stokes-Einstein equation (Eq. 2.20), are shown in the table (E).

## 5.4 Discussion

The innate host defense activity that SP-A performs in alveolar airspaces is essential to maintain the sterile condition of the respiratory surface [27, 177]. In addition, SP-A may also contribute to the surface activity of lung surfactant. The presence of SP-A is necessary for the formation of tubular myelin, considered one of the possible structural intermediates in constructing the surface film. Tubular myelin enhances surfactant adsorption although it is not essential for normal breathing in *in vivo* models [58]. SP-A has also been shown to improve the surface activity of the surfactant under several challenging conditions such as low surfactant concentrations [178] or presence of inhibitory plasma proteins [174] or oxidants [179]. The binding capabilities of SP-A to surfactant phospholipids, pathogen-associated molecular patterns and receptors on cell surfaces depend on its complex oligomeric structure [180]. As presumed by the current models, SP-A assembles as a hexamer of trimeric subunits, i.e., a total of 18 SP-A molecules join together to form the quaternary structure [53]. However, there is evidence that the protein also coexists as a tetramer of trimers (i.e., 12 molecules), dimer of trimers (i.e., 6 molecules), just dimer (i.e., 2 molecules) and even monomer (i.e., a single molecule) [165]. According to the structural models, the trimerization of a subunit occurs through the collagen-like and neck domains and a lateral association at the N-terminal region stem to form higher octadecameric structures [17, 53]. The oligomers are further stabilized by interchain disulfide bonds formed at the short N-terminal domains [167]. Researchers believe that the oligomerization of SP-A occurs in a zipper-like fashion along the C-terminal to N-terminal axis [181]. The high-resolution crystal structures of trimeric carbohydrate recognition and neck domains of rat SP-A, in both native and ligand-bound forms, have been determined (PDB IDs 1R13 and 1R14, [73]) but the complete structures of the full protein or its higher oligomers are still unavailable.

The primary structure of mature SP-A is highly conserved among different mammalian species [182]. The 248-residue bovine SP-A, used in the present work, consists of 30 negatively charged and 26 positively charged amino acids, yielding a net charge of  $-4$  at neutral pH. The high proportion of charged amino acids, along with an abundance of other

polar amino acids, makes SP-A largely hydrophilic and hence soluble in water. However, in the lungs, approximately 90% of SP-A is lipid-associated, the bulk of which is within tubular myelin, and only 10% is in the fluid phase [183]. Therefore, interactions with phospholipids are presumably essential for SP-A's biological function(s). This work attempts to investigate the conformation of the wild-type SP-A in both aqueous and micelle environments and probe its lipid interactions using solution NMR. The studies start with a lipid-free simple aqueous solution, then proceed to the anionic and zwitterionic micelles composed of model surfactant lipids, and end in a mixed micelle system. The wide array of the micelle systems enable exploring the effects that different detergents/lipids have on the conformation of SP-A as well as the effects that SP-A has on the micelle structures.

To my knowledge, this is the first attempt to study SP-A in detergent/lipid micelles using solution NMR. Since, there is no prior information available with which to compare the results obtained from my NMR experiments, theoretical values of some basic NMR parameters, calculated for different oligomeric forms of SP-A, help in interpreting the spectral features. Table 5.1 lists the predicted hydrodynamic diameter ( $d_H$ ), rotational correlation time ( $\tau_c$ ), proton linewidth ( $\Delta\nu_{1/2}$ ) and relative intensity (I) for six different oligomeric forms of SP-A from monomer to octadecamer. The MALDI-TOF mass spectrometry of purified SP-A showed a monomeric molecular mass of  $\sim 29$  kDa. In the calculation, the masses of oligomeric forms of SP-A are predicted from the number of molecules involved without taking the effects of post-translational modifications (e.g., glycosylation) into account. The hydrodynamic diameter ( $r_H$ ) is calculated from the equation (Eq. 1.45, Page 21, Ref. [123]),

$$r_H = [(3VM)/(4\pi N_A)]^{1/3} + r_w, \quad 5.1$$

where, V is the specific volume of the protein (taken to be  $0.73 \text{ cm}^3 \cdot \text{g}^{-1}$ ), M is the molecular mass of the protein ( $29000 \text{ g} \cdot \text{mol}^{-1}$  and its multiples),  $N_A$  is Avogadro's number ( $6.022 \times 10^{23} \text{ mol}^{-1}$ ) and  $r_w$  is the thickness of one hydration shell (taken to be  $3.2 \text{ \AA}$ ). The rotational correlation time ( $\tau_c$ ) is determined from Stoke's law ((Eq. 1.44, Page 21, Ref. [123]),

$$\tau_c = (4\pi\eta_w r_H^3)/(3K_B T), \quad 5.2$$

in which  $\eta_w$  is the viscosity of the solvent,  $K_B$  is the Boltzmann constant ( $1.38 \times 10^{-23} \text{ J/K}$ )

and T is the absolute temperature (310 K). The solvent is considered to be pure H<sub>2</sub>O, ignoring the effect of 10% D<sub>2</sub>O, and the viscosity value used is 6.92 x 10<sup>-4</sup> kg/m.s (at 310 K or 37 °C). The proton resonance linewidth ( $\Delta\nu_{1/2}$ ) is determined from the equation,

$$\Delta\nu_{1/2} = 1.2\tau_c + 0.3. \quad 5.3$$

This equation is developed using the linear fit representing the proton linewidth (in Hz) as a function of rotational correlation time (in ns) (Figure 1.6, Page 20, Ref. [123]). The spin-spin or transverse relaxation time ( $T_2$ ) is determined from the equation (Page 18, Ref. [123]),

$$\Delta\nu_{1/2} = 1/\pi T_2. \quad 5.4$$

The relaxation processes follow a first-order rate equation, characterized by a characteristic time constant (T) or a rate constant (R) (Page 16, Ref. [119]),

$$I(t) = I_0 \exp(-t/T) = I_0 \exp(-Rt). \quad 5.5$$

Thus the relative signal intensity of SP-A<sub>Multimer</sub> ( $I_{\text{Multimer}}$ ) with respect to SP-A<sub>Monomer</sub> ( $I_{\text{Monomer}}$ ) can be calculated from,

$$I_{\text{Multimer}}/I_{\text{Monomer}} = T_{2(\text{Multimer})}/T_{2(\text{Monomer})}. \quad 5.6$$

The theoretical calculation indicates, if SP-A is present in the octadecameric form, the proton signal linewidth would be ~ 147 Hz (i.e., 0.245 ppm on a 600 MHz spectrometer) and thus the weak signal intensity caused by the massive line-broadening would probably bury almost all signals under the noise. However, if SP-A is present in the monomeric form, the signal linewidth would be ~ 11 Hz (i.e., 0.018 ppm on the same 600 MHz spectrometer) and hence intense signals would appear in the 1D <sup>1</sup>H spectrum. For the intermediate oligomers of SP-A, the 1D <sup>1</sup>H spectra would probably contain a number of signals but they would likely be substantially broad and overlapped. The intensity of proton peaks would also decrease as SP-A oligomers become larger. For example, in comparison with SP-A<sub>Monomer</sub>, SP-A<sub>Octadecamer</sub> would retain only 7% of the relative peak intensity.

Since the 1D <sup>1</sup>H spectrum of SP-A alone in aqueous solution (Figure 5.2) contains only a few weak HN signals, the spectrum is consistent with a high molecular mass species of SP-A, presumably the wild-type octadecameric form. The observed signals are likely generated by some highly mobile regions of the protein (e.g., flexible loops) that are

exhibiting fast motions on the NMR time-scale due to conformational exchange or other internal dynamics. Prevalence of large assemblies of SP-A, when alone in water, is not unexpected as the protein is isolated and purified from a natural source and is not exposed to any denaturing treatment. It is difficult to comment on the degree of SP-A's structuring when alone in water from such low-signal 1D  $^1\text{H}$  spectrum. However, since SP-A is known to be water-soluble and the protein preparation followed the same procedure as previously used in all kinds of functional studies, it is plausible that SP-A is properly folded in the aqueous environment but, as predicted from the theoretical calculation, the overall size of the oligomeric assembly is too large to yield any well-dispersed and intense HN signals.

**Table 5.1 :** Estimates of rotational correlation times, proton linewidths and relative signal intensities for SP-A oligomers at 37 °C. The increase of SP-A's mass due to post-translational modifications is not taken into account. The calculations are performed using the equations and plot from Refs. [123] and [119].

Oligomeric Form of SP-A	No. of SP-A Molecules	Molecular Mass (Da)	Hydrodynamic Diameter (nm)	Rotational Correlation Time (ns)	Proton Linewidth (Hz)	Relative Intensity (%)
Monomer	1	29000	4.7	8.8	10.9	100
Dimer	2	58000	5.8	16.2	19.7	55
Trimer	3	87000	6.5	23.3	28.3	39
Hexamer	6	174000	8.0	43.8	52.9	21
Dodecamer	12	348000	9.9	83.4	100.3	11
Octadecamer	18	522000	11.3	122.0	146.7	7

Much to my surprise, the 1D  $^1\text{H}$  spectra of SP-A in all types of micelles exhibit strikingly strong and dispersed HN signals when compared to SP-A alone (Figures 5.14 A and B). This implies that the protein/micelle complex is substantially smaller than the protein alone and tumbles much faster in the solution (Table 5.1). The spectra of micelle-bound SP-A are thus consistent with a lower molecular mass species, i.e., a smaller oligomeric form of the protein. However, the HN signals are still broad and severely overlapped. Again, this is not unexpected from a large micelle-bound protein, especially when the protein is likely present in multimeric forms. The spectral features also indicate that SP-A is structured in all micelle environments.

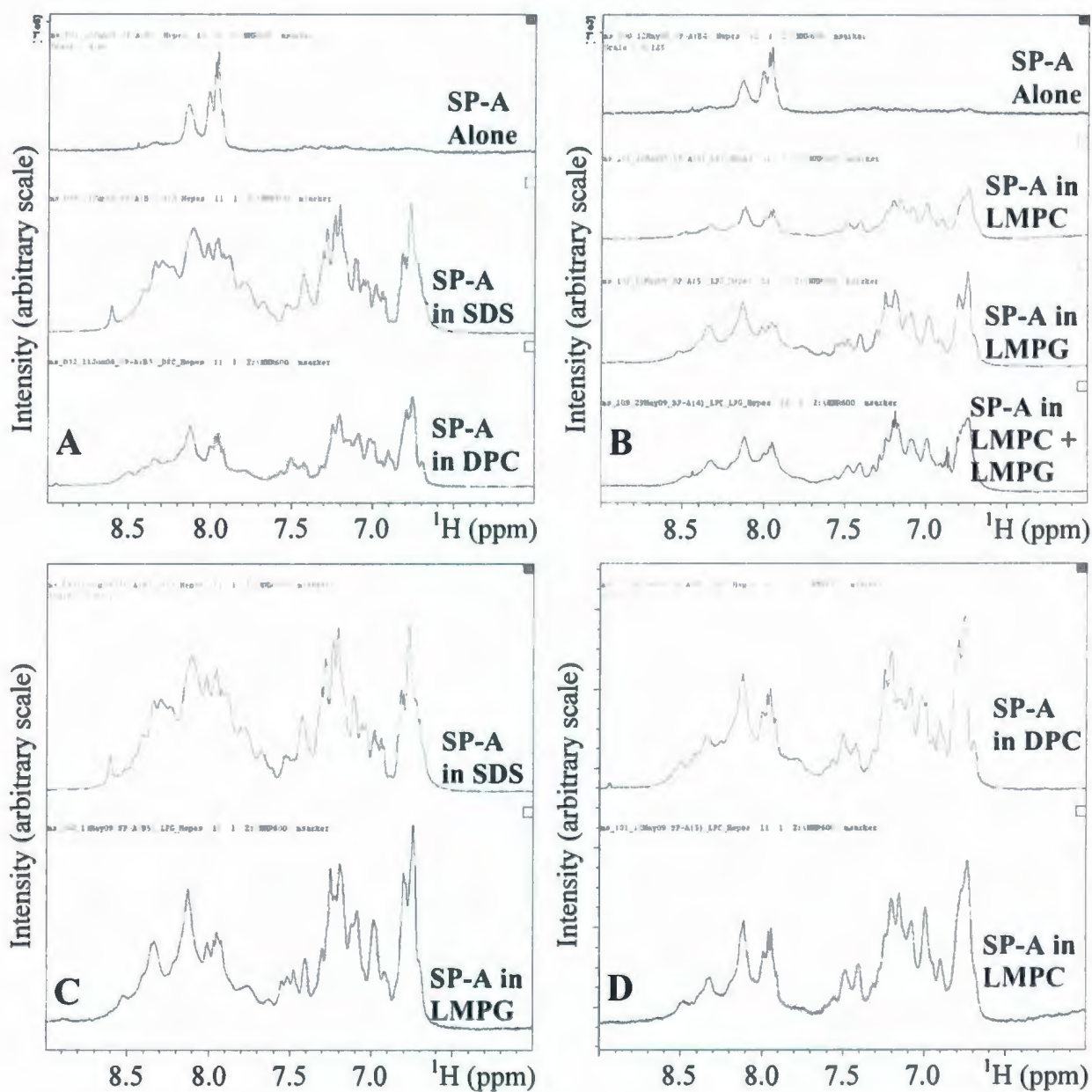


**Figure 5.14** : Overlay of the HN (6-9 ppm) regions of 1D  $^1\text{H}$  spectra of SP-A in different environments. The spectra are the same as presented in the Results section. The height of the top spectrum in each panel has been scaled to match the other(s).

Translational diffusion measurements confirm a substantial reduction in the size of SP-A, and hence in its mass and oligomeric state, when the micelles are added. Table 5.2 shows the molecular masses of in-water and in-micelle SP-A species, estimated from the experimentally determined translational diffusion coefficients ( $D_C$ ), and the matching

oligomeric states of the protein. For the micelle-bound form, the molecular mass of SP-A is determined as follows. The structures of pure micelles, as well as SP-A/micelle complexes, are considered to be perfectly spherical. The volume of the sphere (V) is determined from the hydrodynamic diameter ( $d_H$ ) calculated from the translational diffusion coefficient ( $D_C$ ),

$$d_H = (K_B T) / (3\pi\eta D_C), \quad 5.6$$

and 
$$V = (4/3)\pi(d_H/2)^3. \quad 5.7$$

The volume of SP-A ( $V_{SP-A}$ ) is determined from its contribution to the SP-A/micelle complex,

$$V_{SP-A} = V_{SP-A/Micelle} - V_{Micelle}. \quad 5.8$$

The molecular mass of SP-A ( $M_{SP-A}$ ) is calculated from its volume using the average protein density ( $\rho_{Protein}$ , taken to be 1.37 g/cm<sup>3</sup>),

$$M_{SP-A} = \rho_{Protein} \times V_{SP-A}. \quad 5.9$$

**Table 5.2** : Molecular masses of SP-A species, calculated using the experimentally determined translational diffusion coefficients, and their matching oligomeric states.

Sample Composition	Complex Volume (cm <sup>3</sup> )	Micelle Volume (cm <sup>3</sup> )	SP-A Volume (cm <sup>3</sup> )	Estimated SP-A Mass		Matching Oligomeric State
				(g)	(Da)	
SP-A Alone	9.39E-19	xxx	9.39E-19	1.29E-18	774,799	18+
SP-A/SDS	9.34E-20	9.74E-22	9.25E-20	1.27E-19	76,284	~ 2-3
SP-A/DPC	3.48E-20	3.88E-21	3.09E-20	4.23E-20	25,493	~1
SP-A/LMPC	5.64E-19	2.00E-19	3.63E-19	4.98E-19	299,892	~ 6-9
SP-A/LMPG	7.36E-19	2.98E-19	4.37E-19	5.99E-19	360,789	~ 6-9
SP-A/LMPC/LMPG	6.43E-19	3.05E-19	3.38E-19	4.64E-19	279,185	~ 6-9

As per the estimation, SP-A, when alone in the aqueous solution, predominantly exists in an octadecameric or even larger form. However, when the smaller SDS/DPC micelles are added, the large SP-A assembly appears to dissociate and the protein takes on a much smaller form in the monomer to trimer range. In contrast to both extremes, when the larger LMPC/LMPG micelles are added, SP-A apparently takes on an intermediate multimeric form between two and three trimers. Since this diffusion-based mass-estimation relies on many approximations, such as spherical structures of the particles, free diffusion

and the same number of detergent/lipid molecules in both pure micelles and protein/micelle complexes, as well as ignores the effects of post-translational modifications and exchanges between free and micelle-bound species, an exact measure of the molecular mass is not expected. However, the calculation clearly illustrates that the mass of SP-A species are reduced substantially when the micelles are added to the aqueous form of the protein. The reduction of SP-A mass, and hence its oligomeric state, is also verified by a non-reducing SDS-PAGE that demonstrates a large assembly of the protein when alone but between monomers and trimers in the presence of SDS and DPC (data not shown).

The question that immediately emerges is what is causing the larger SP-A species to dissociate when the micelles are added? Most likely not all of the monomers in the supramolecular SP-A assembly are covalently attached by disulfide bonds and many of the subunits are associated only through non-covalent protein-protein interactions. The addition of amphipathic lipids/detergents appears to disrupt these non-covalent interactions thus causing the sub-units to dissociate. It is plausible that the electrostatic interactions, and perhaps the hydrophobic interactions as well, between the protein and the lipid/detergent molecules overwhelm many of SP-A's inter-subunit non-covalent interactions and thus micelle complexes containing smaller SP-A oligomers are formed. However, the protein-micelle interactions may not dissociate all of the subunits and a subpopulation of octadecameric SP-A species may still prevail in the micelle environments but just that the complexes are too large to generate any observable NMR signals. Also, the oligomeric state of SDS/DPC-bound SP-A species (between a monomer and a trimer) appears to be substantially smaller than LMPC/LMPG-bound SP-A species (between two and three trimers). This indicates, the larger the size of micelles, the less affected the supramolecular assembly of the protein and, presumably, the less affected the non-covalent interactions among the protein subunits. Despite the dramatic effects of the micelles on the degree of SP-A's oligomerization, it is extremely unlikely that SP-A monomers that are covalently attached through disulfide bonds also dissociate as a result of protein-micelle interactions.

The next question that arises is why SP-A is present in smaller oligomeric forms in the micelles when its predominant conformation is widely referred to as octadecameric? The

long-presumed octadecameric structure of SP-A is elucidated by analytical methods such as gel filtration analysis and sedimentation equilibrium studies [184] and also verified by transmission electron microscopy (TEM) [185]. However, these studies are performed with purified SP-A and in lipid-free aqueous environments. In contrast, the gel filtration and sucrose density gradient centrifugation of unpurified SP-A show that the protein does not exist purely as fully assembled octadecamers but is consistently found in smaller oligomeric forms [165]. The TEM image of recombinant SP-A by itself also displays smaller aggregates like tetramers, trimers and dimers, and even monomers under mild reducing condition [185]. The TEM image of tubular myelin, on the other hand, shows X-shaped structures in the square lattice regions [61] which are modeled as SP-A octadecamers [17]. Thus the commonly referred pure octadecameric assembly of SP-A appears to be an oversimplification about the quaternary structure of the protein.

Another question would be about the differences in SP-A's conformation and lipid interactions between the micelle systems. The HN signals seen in the 1D  $^1\text{H}$  spectra of SP-A in DPC, LMPC and LMPG are quite similar but noticeably different from SDS (Figures 5.14 C and D). Hence, SP-A likely takes on a similar tertiary structure in DPC/LMPC/LMPG micelles that contain identical headgroups to surfactant PC and PG, but may take on a different structure in SDS micelles that contain a non-surfactant headgroup. Moreover, the DOSY data reveals that the oligomeric state of SP-A in the larger micelles (LMPC/LMPG) are substantially higher than the smaller micelles (SDS/DPC). SP-A's micelle interactions thus appear to be dependent on the size of the micelles. These intriguing differences in the conformation and mechanisms of lipid interactions may be important for SP-A's functions in the native lung environment.

Many of SP-A's biological functions are thought to come about via its interactions with a broad range of amphipathic lipids present in lung surfactant and cellular membranes or bacterial envelopes [186]. Several studies indicate that SP-A binds avidly to DPPC but less strongly to unsaturated PCs [187, 188]. SM is also demonstrated as a preferred ligand of SP-A [189]. However, there are reports that claim SP-A does not bind to PG, except to DPPG, and to PI, PE or PS [53]. Morphological studies show that *in vitro* reconstitution of SP-A

with DPPC-rich phospholipid bilayers containing SP-B in the presence of calcium produces a lattice-like array of bilayer structures similar to that of the native tubular myelin [59, 60]. Other than phospholipids, SP-A binds to many carbohydrates, preferentially to mannose and fucose that are commonly found on fungal and microbial surfaces [190]. SP-A also interacts with rough lipopolysaccharide (Re-LPS) and permeabilizes bacterial membrane through self-aggregation [191]. In relation to the surface activity, interactions of SP-A with lipid extract surfactant (LES), an organic extract of lung surfactant containing all of the phospholipids and SP-B and SP-C, has been shown to reduce the minimum surface tension that the surfactant films can achieve when they are cyclically compressed and expanded [174].

SP-A's biological roles, in relation to either anti-microbial activities or surfactant biophysical activities, are almost always attributed to its octadecameric structure and preferential interactions with DPPC [17, 53, 56]. However, this part of my work demonstrates at least two novel features about SP-A's conformation and lipid interactions. First, the micelle-bound SP-A exists predominantly as smaller oligomers, in sharp contrast to octadecamers (or even larger) when alone in the aqueous environment. Second, SP-A binds not only to zwitterionic micelles but also to anionic micelles. The investigations are carried out in pure micelles composed of the analogues of surfactant PC and PG, as well as in a mixed micelle system where the ratio of two lipids is kept close to the physiological level. Moreover, the experimental conditions, such as the pH and the temperature, are appropriately matched with the real lung conditions. The findings thus appear to lead towards a new thinking on the *in vivo* properties of SP-A. Perhaps, the current octadecameric SP-A models require some modifications to portray how SP-A may function as smaller oligomers.

## *Chapter 6*

# **Interaction between Mini-B and SP-A in Model Surfactant Lipids**

*Note : Mini-B was synthesized and purified by Prof. Alan J. Waring and his group (Waring lab, Medicine, UCLA). SP-A was collected from cow lungs supplied by Ray Bishop (Bishops Meat, Foxtrap, NL). Isolation and purification of SP-A was done by Donna Jackman (Booth lab, Biochemistry, MUN).*

## 6.1 Overview

Several studies have indicated interactions, either direct or indirect, between SP-A, the most abundant protein of lung surfactant by weight [163], and SP-B, an indispensable protein for lung surfactant function [37, 38], in model surfactant systems. Although the presence of SP-A is not strictly required for the biophysical function of lung surfactant [58], SP-A improves the surface activity of lipid-protein preparations only if SP-B is present, and especially in the presence of anionic phospholipids [62, 192]. Synergy between SP-A and SP-B observed in the process of phospholipid membrane fusion has been attributed to specific calcium-dependent SP-A/SP-B interactions [193, 194]. The perturbation of model surfactant bilayers prepared using DPPC/DPPG mixtures by SP-A and SP-B together is different from that of individual proteins, which is likely an outcome of the two proteins' interactions [195]. The proteins demonstrate a cooperative calcium-dependent action in improving the resistance to surfactant inhibition by blood and plasma proteins [196]. Formation of specific SP-A/SP-B complexes has been observed in lipid-protein interfacial films [197]. However, probably the most dramatic exhibition of a concerted action of SP-A and SP-B is the *in vitro* reconstitution of tubular myelin when SP-A is added to the mixtures of DPPC, PG and SP-B in the presence of calcium [59-61].

A direct examination of SP-A/SP-B interaction, even in laboratory experimental conditions, has long been hampered by the lack of a clear understanding regarding the structure-function relationships of both proteins, especially that of SP-B. Knowledge of the high-resolution structure of Mini-B, a synthetic construct that presumably corresponds to the key functional regions of full-length SP-B, provides an opportunity to directly probe Mini-B/SP-A interaction in the presence of model surfactant phospholipids. The findings from such a study may unveil critical features of SP-A/SP-B interactions and their consequences in native lung conditions. The conformations of Mini-B and SP-A and their lipid interactions have been characterized individually using an array of five different micelle systems. Based on those findings, I have attempted to investigate the interaction between Mini-B and SP-A, if any, in the presence of same model surfactant phospholipids.

## 6.2 Materials and Methods

### 6.2.1 Protein Preparation

The synthetic Mini-B was produced and purified by the Waring lab (Medicine, UCLA). The peptide was produced by solid phase chemical synthesis using *O*-fluorenylmethyloxycarbonyl (Fmoc) chemistry and purified by preparative reverse phase HPLC in a Vydac C-18 column as described previously (Chapter 3 and [156]). The natural bovine SP-A was collected from the lungs of young cows slaughtered at a local farm (Bishops Meat, Foxtrap, Newfoundland). The protein was isolated and purified by Donna Jackman (Booth lab, Biochemistry, Memorial University of Newfoundland) from the surfactant pellet by extraction with 1-butanol as described previously (Chapter 5).

### 6.2.2 Sample Preparation

No new NMR samples were prepared exclusively for this chapter but the corresponding Mini-B and SP-A samples, used for their individual studies presented in Chapters 4 and 5, were mixed together. Thus, like the individual proteins, at least two mixtures of Mini-B and SP-A were obtained for each micelle system with varying peptide/lipid ratios. However, in all samples, molar concentrations of the detergents/lipids still remained at least 100 times higher than the proteins. The exact composition of each sample is described in the results section with protein molar concentrations specified as if they were 100% monomeric. Mini-B<sub>OX</sub>/SP-A samples were prepared with SDS, DPC, LMPC, LMPG and mixed LMPC(85%)/LMPG(15%) micelles but Mini-B<sub>RED</sub>/SP-A samples were prepared with SDS and DPC micelles only. Consistent with the samples containing individual proteins, the pH of the Mini-B<sub>OX</sub>/SP-A samples was found to be 6.9. However, the pH of the original Mini-B<sub>RED</sub> samples was 5.0 and hence that of Mini-B<sub>RED</sub>/SP-A samples was raised to 7.0 using NaOH solution without taking the isotope effects into account. The pH of all samples thus closely matched the native condition of alveolar water hypophase.

### 6.2.3 NMR Data Collection and Processing

A set of 1D  $^1\text{H}$ , 2D  $^{15}\text{N}$ - $^1\text{H}$  HSQC and 2D DOSY experiments was performed for each of the Mini-B/SP-A samples on a Bruker Avance II 14.1 Tesla (600 MHz) spectrometer (Billerica, MA) equipped with z-gradients and an inverse triple resonance TXI probe. The NMR data were collected and processed using the Bruker Topspin 2.0 software. The pulse length (P1) and the transmitter offset (O1) were optimized for each sample before running the full set of NMR experiments. The 1D  $^1\text{H}$  and 2D  $^{15}\text{N}$ - $^1\text{H}$  HSQC spectra were acquired at 37 °C to match the physiological temperature. In 1D  $^1\text{H}$  experiments, data were collected with 128 to 320 scans (indicated in the figure captions) using the water-gate water suppression technique [146] and processed using an exponential apodization function with 1 Hz line broadening. The 2D  $^{15}\text{H}$ - $^1\text{H}$  HSQC spectra were acquired with 160 to 640 scans (indicated in the figure captions) using the flip-back water suppression technique [145] and processed using the Qsine apodization function with a sine bell shift of 2. The 2D DOSY experiments were performed using PFG NMR [157]. The pulse sequence used a stimulated echo with bipolar gradient pulses and one spoil gradient [158], followed by a 3-9-19 pulse for water suppression [159]. The DOSY spectra were acquired for SDS and DPC samples at 37 °C. However, for LMPC and LMPG samples, the DOSY spectra were acquired at 25 °C to minimize the effect of thermal convection. The diffusion time was kept constant at 100 ms. The gradient pulse length was optimized for each sample and set between 3 and 8 ms. The maximum amplitude of the gradient strength was 35 G/cm and the  $^1\text{H}$  signals were attenuated in 32 steps. The translational diffusion coefficient was determined from the slope of the signal attenuation curve plotted using Eq. 2.17. The hydrodynamic diameter was calculated using the Stokes-Einstein equation [Eq. 2.20]. The viscosity of pure water was used for the viscosity of solution in the calculation and the values were  $8.91 \times 10^{-4}$  kg/m.s at 25 °C (298 K) and  $6.92 \times 10^{-4}$  kg/m.s at 37 °C (310 K).

Although NMR data were acquired for at least two separately prepared mixtures of Mini-B and SP-A in each micelle system, spectra of both samples essentially looked identical and hence only one is shown in the results section. For the ease of comparison, the spectra of individual proteins acquired under the same micelle condition are also included in the figures.

## 6.3 Results

### 6.3.1 Mini-B and SP-A in SDS Micelles

As previously done for studying the conformations and lipid interactions of the proteins individually, the examination of Mini-B/SP-A interaction began with smaller anionic micelles composed of the detergent SDS. The study was performed using both Mini-B<sub>OX</sub> and Mini-B<sub>RED</sub>. SP-A was added to both versions of Mini-B at a monomeric ratio of 1:1, calculated assuming SP-A as a monomer. Figures 6.1 and 6.2 show the 1D <sup>1</sup>H spectra of Mini-B<sub>OX</sub> and Mini-B<sub>RED</sub>, respectively, plus SP-A in SDS micelles, along with the corresponding spectra of the individual proteins. The signals seen in the 6-9 ppm region, enlarged and displayed in the bottom panels, correspond mostly to backbone amide protons (HNs) of the proteins. However, the signals from Mini-B/SP-A mixtures, for both Mini-B versions, look almost identical to that of SP-A alone. This is not unexpected as SP-A (248 amino acids) is over 7 times larger than Mini-B (34 amino acids) and thus the signals of Mini-B are buried under the many signals of SP-A. A comparison of the spectral dispersion and intensity of HN signals indicates that the structure of SDS-bound SP-A remains essentially unchanged in the presence of SDS-bound Mini-B.

The structures of SDS-bound Mini-B<sub>OX</sub> and Mini-B<sub>RED</sub> also remain the same in the presence of SDS-bound SP-A. This is revealed by the 2D <sup>15</sup>N-<sup>1</sup>H HSQC spectra (Figures 6.3 and 6.4) which show that all nine major peaks corresponding to the <sup>15</sup>N-labeled amino acids of Mini-B, and even the additional weaker peaks in most cases, remain unaffected by the inclusion of SP-A. Addition of more SDS, followed by CaCl<sub>2</sub>, does not change the position or intensity of Mini-B HSQC peaks either (Figure 6.3 C and D).

The 1D <sup>1</sup>H and 2D HSQC spectra appear to provide no evidence of interactions between Mini-B and SP-A in SDS micelles. However, the 2D DOSY spectra of Mini-B<sub>OX</sub>/SP-A, when compared to the individual proteins, indicate a somewhat different scenario

(Figures 6.5 & 6.6 and Table 6.1). A total of four signal attenuation curves are produced, two from the SDS peaks at 0.80 and 1.22 ppm and two from the protein peaks at 0.92 ppm and HN region, but only two are shown in Figure 6.5 (from 1.22 ppm and HN region). Interestingly, the signal attenuation curve does not fit well with a single line (i.e., a single component). However, approximately the first and the last halves of the data are fit reasonably well with two lines having two different slopes. Thus, two observed translational diffusion coefficients are obtained and there are, at least, two distinct populations of protein/micelle complexes present in the solution. The apparent hydrodynamic diameters of the subpopulations are  $\sim 6.8$  nm [from HN Fit 1 ( $\sim$  first half of the data)] and  $\sim 19.4$  nm [from HN Fit 2 ( $\sim$  last half of the data)]. Although the first subpopulation is not substantially different in size from the SP-A/SDS complex ( $\sim 5.6$  nm), the second is much larger. A fraction of the total Mini-B<sub>OX</sub> and SP-A molecules present in the mixture hence form large protein/micelle complexes. The approximate ratio of the small-to-large subpopulations is 85% : 15%, as estimated from the y-axis (relative signal intensity) intercepts of the two linear fits representing the two diffusion coefficients. The average hydrodynamic diameter, which is not an arithmetic average of the two sizes, but calculated from the average linear fit of the HN signal attenuation data, is  $\sim 9.3$  nm. This apparent size is also larger than the sizes obtained for the individual proteins. For both Fit 1 and Fit 2 of the Mini-B<sub>OX</sub>/SP-A mixture, the diffusion coefficients, and hence the corresponding hydrodynamic diameters, obtained from the SDS peaks are different from that obtained from the protein peaks. For Fit 2, the apparent hydrodynamic diameters calculated from the SDS peaks are  $\sim 13$  nm while that from the protein peaks are  $\sim 20$  nm. As observed previously for the individual proteins, the smaller apparent size of the complex when calculated from the detergent peaks is likely the result of a rapid exchange between the free and micelle-bound SDS species.

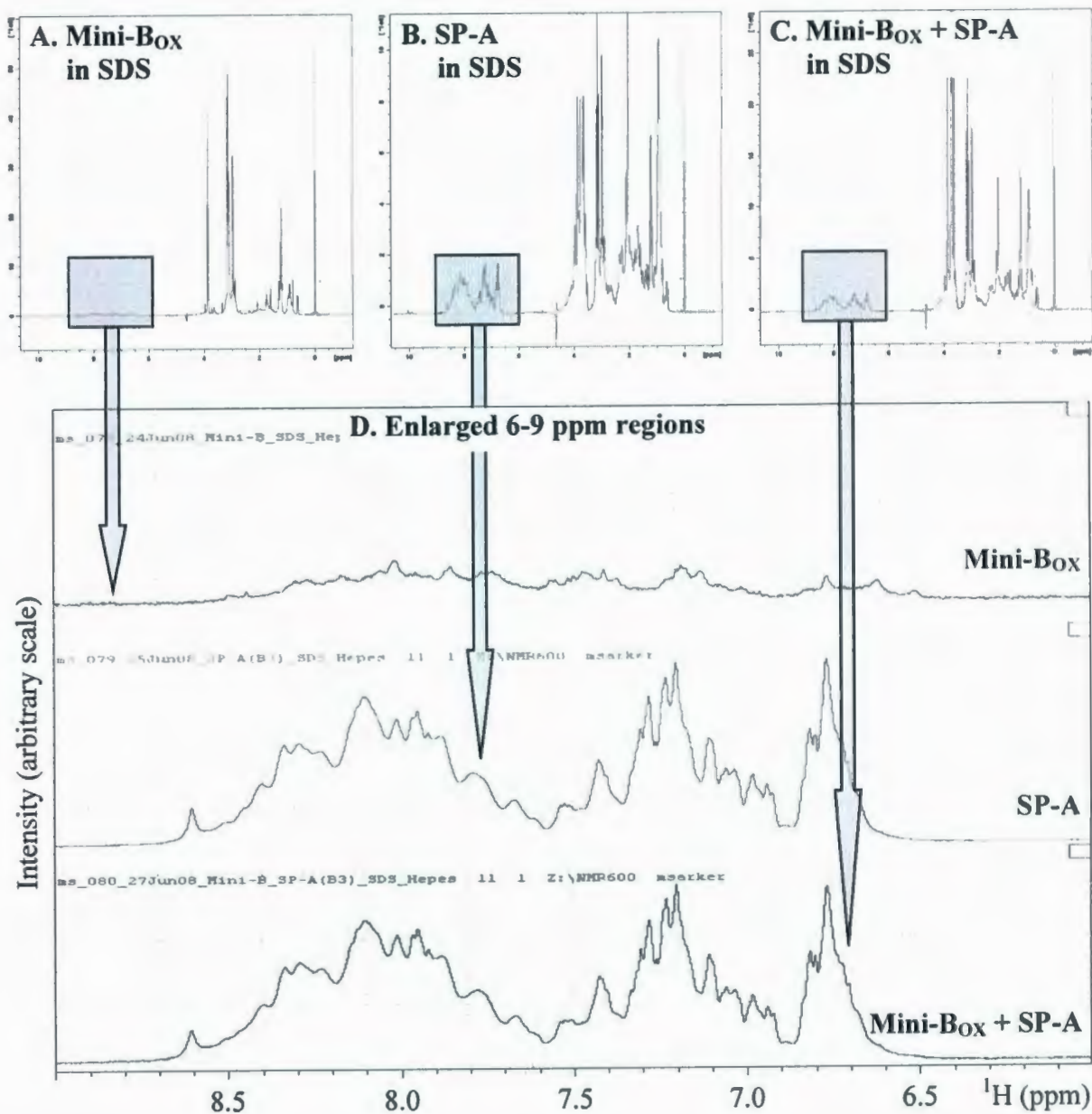


**Figure 6.1** : 1D  $^1\text{H}$  spectra of (A) 0.2 mM Mini-Box, (B) 0.2 mM SP-A and (C) 0.1 mM Mini-Box + 0.1 mM SP-A in 40 mM SDS, in the presence of 4.5 mM Hepes at pH 6.9 and temperature 37 °C. The spectra were acquired using 256 scans and processed with 1 Hz line broadening. The 6-9 ppm regions of all spectra are enlarged and shown in the bottom panel (D).

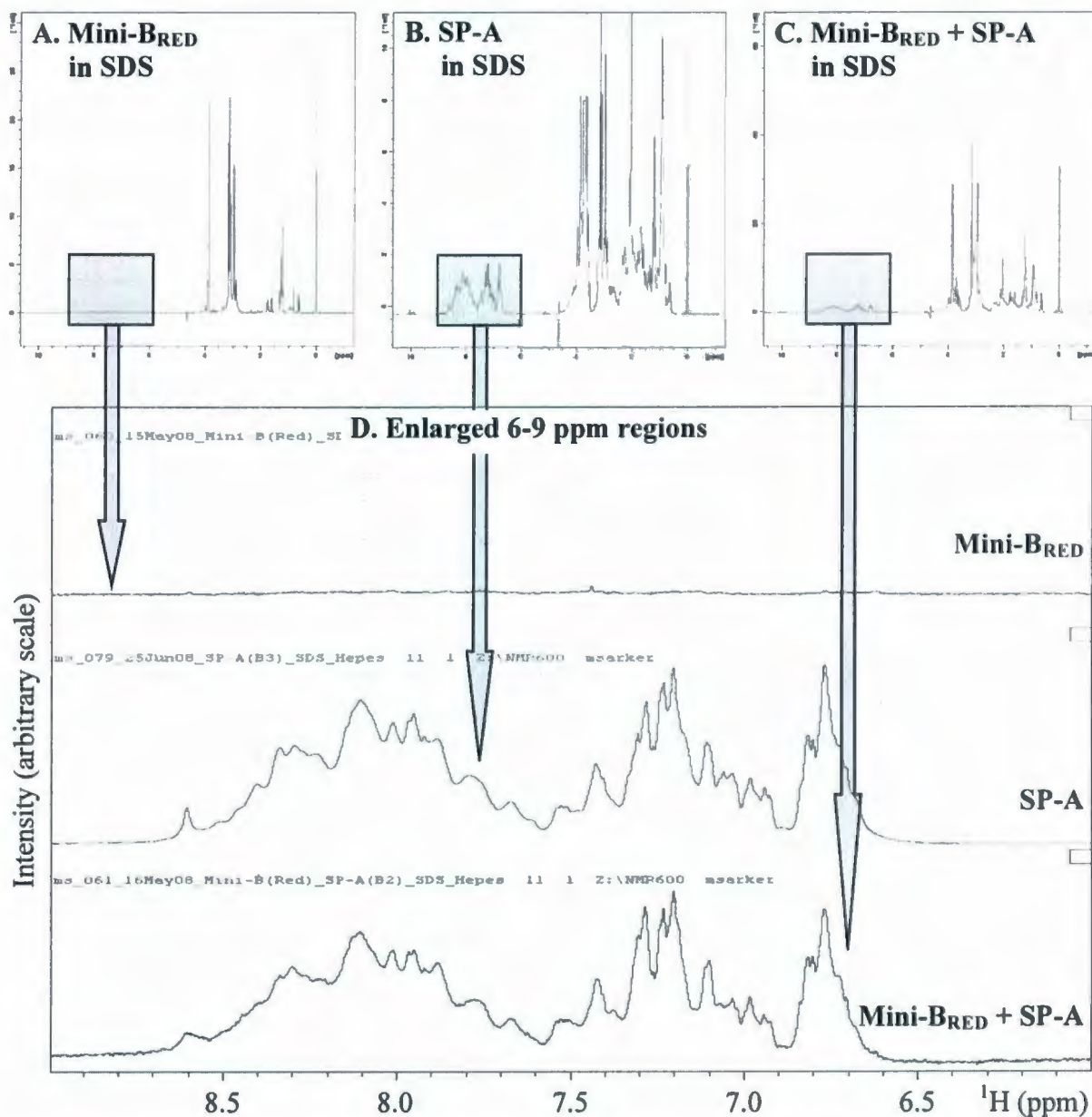


**Figure 6.2** : 1D  $^1\text{H}$  spectra of (A) 0.15 mM Mini-BRED in 30 mM SDS (acquired using 128 scans), (B) 0.2 mM SP-A in 40 mM SDS (acquired using 256 scans) and (C) 0.075 mM Mini-BRED + 0.08 mM SP-A in 15 mM SDS (acquired using 128 scans), in the presence of 4.5 mM Hepes at pH 7.0 and temperature 37  $^\circ\text{C}$ . The spectra were processed with 1 Hz line broadening. The 6-9 ppm regions of all spectra are enlarged and shown in the bottom panel (D).

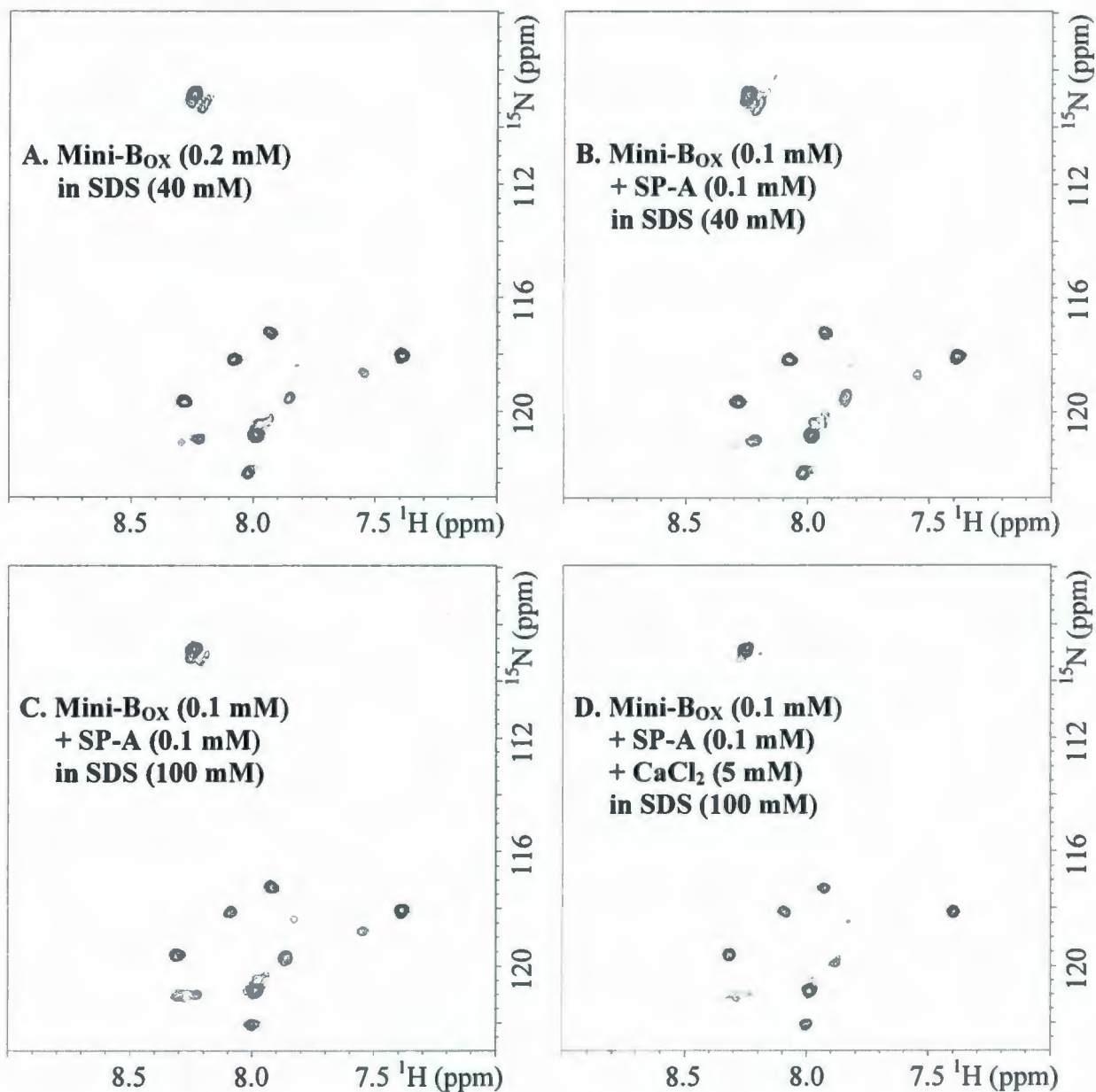


**Figure 6.3** : 2D  $^{15}\text{N}$ - $^1\text{H}$  HSQC spectra of (A) 0.2 mM Mini-B<sub>OX</sub> in 40 mM SDS (acquired using 160 scans), (B) 0.1 mM Mini-B<sub>OX</sub> + 0.1 mM SP-A in 40 mM SDS (acquired using 640 scans), (C) 0.1 mM Mini-B<sub>OX</sub> + 0.1 mM SP-A in 100 mM SDS (acquired using 320 scans) and (D) 0.1 mM Mini-B<sub>OX</sub> + 0.1 mM SP-A in 100 mM + 5 mM CaCl<sub>2</sub> (acquired using 320 scans), in the presence of 4.5 mM Hepes at pH 6.9 and temperature 37 °C. The base contour level shown in (B) is 2 times higher than others.

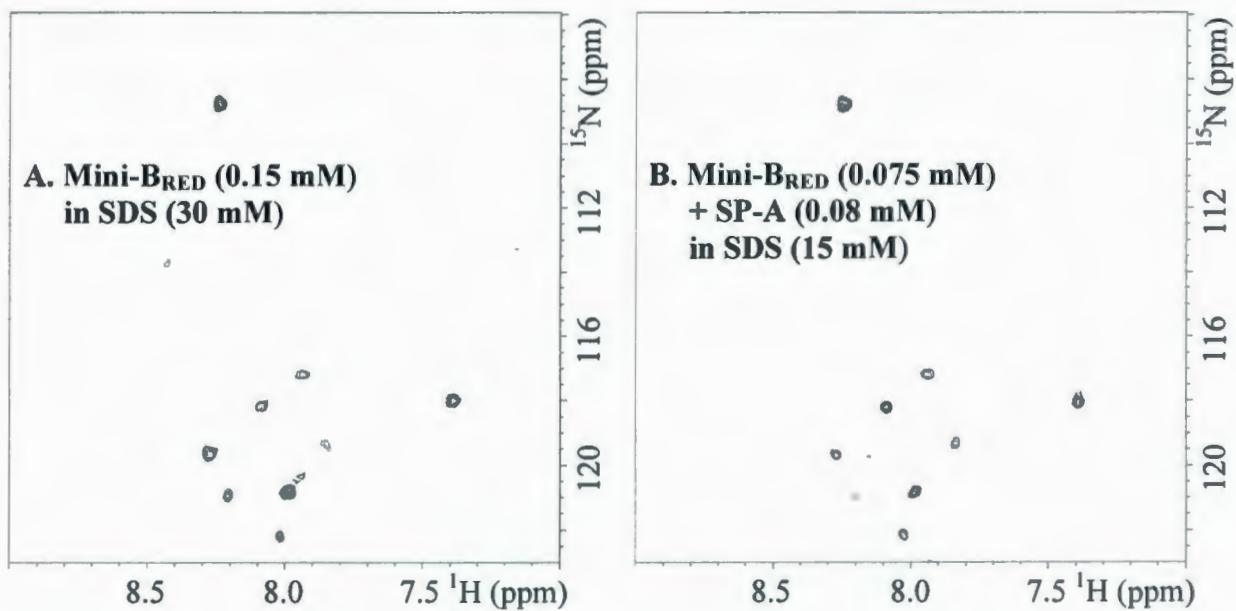


**Figure 6.4 :** 2D  $^{15}\text{N}$ - $^1\text{H}$  HSQC spectra of (A) 0.15 mM Mini-B<sub>RED</sub> in 30 mM SDS (acquired using 160 scans) and (B) 0.075 mM Mini-B<sub>RED</sub> + 0.08 mM SP-A in 15 mM SDS (acquired using 320 scans), in the presence of 4.5 mM Hepes at pH 7.0 and temperature 37 °C. The base contour level shown in (B) is 1.5 times higher than (A).

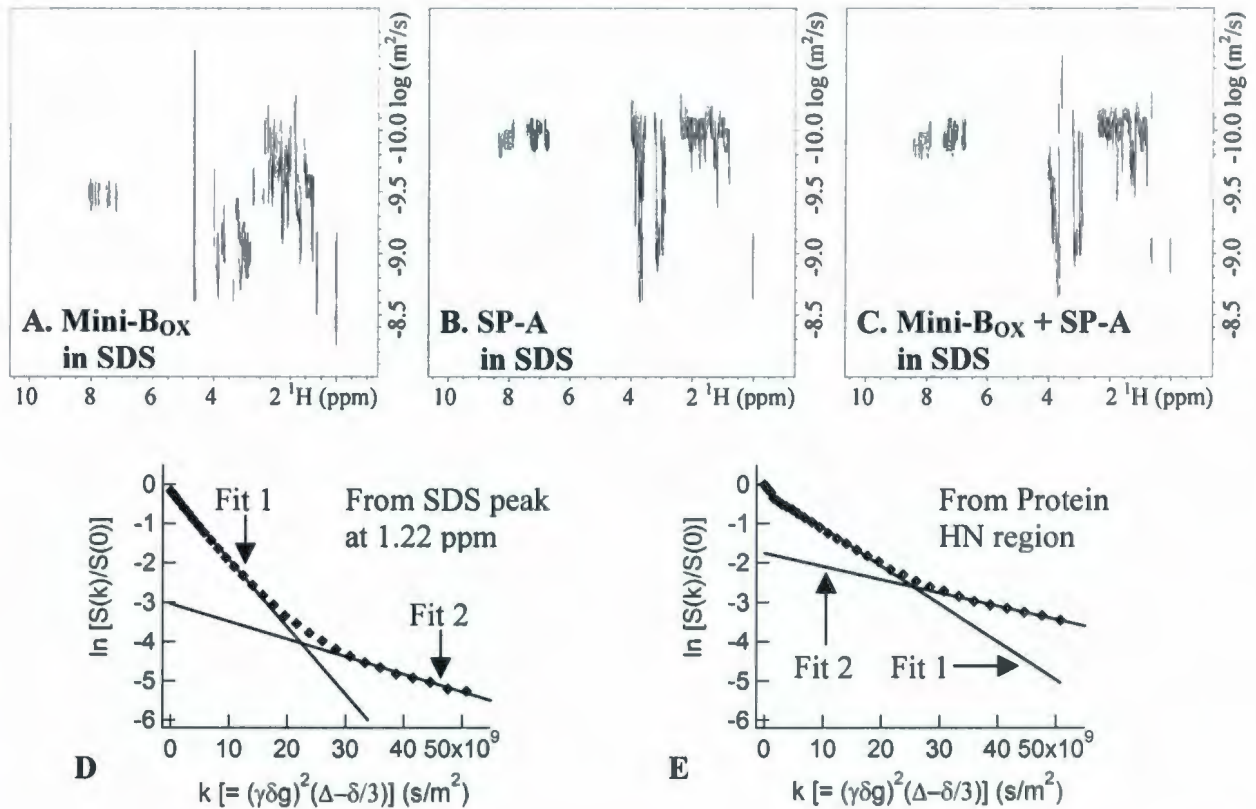


**Figure 6.5** : Translational diffusion measurements of Mini-BO<sub>X</sub> and SP-A in SDS. Top panels show the 2D DOSY spectra of 0.2 mM Mini-BO<sub>X</sub> (A), 0.2 mM SP-A (B) and 0.1 mM Mini-BO<sub>X</sub> + 0.1 mM SP-A (C) in 40 mM SDS, in the presence of 4.5 mM Hepes at pH 6.9 and temperature 37 °C. The observed diffusion coefficients are determined from the slopes of the <sup>1</sup>H signal attenuation curves using two SDS signals (at 0.80 and 1.22 ppm) and two protein signals (0.92 ppm and HN regions). Only two signal attenuation curves for the Mini-BO<sub>X</sub>/SP-A/SDS complexes, obtained from the SDS peak at 1.22 ppm (D) and the protein HN region (E), are shown in the bottom panels. None of the signal attenuation curves for Mini-BO<sub>X</sub>/SP-A/SDS complexes fit well with a single line. However, approximately the first and the last halves of the data are fit reasonably well with two lines having two different slopes.

**Table 6.1** : Observed translational diffusion coefficients and the corresponding hydrodynamic diameters of pure SDS micelles and protein/SDS complexes. The diffusion coefficients are represented by the slopes of the  $^1\text{H}$  signal attenuation linear fits obtained from the 2D DOSY data. The hydrodynamic diameters are calculated using the Stokes-Einstein equation (Eq. 2.20).

Micelle/Complex Composition	Diff. Coeff. $\times 10^{-10}$ ( $\text{m}^2/\text{s}$ ) from Peak at				Hydro. Dia. (nm) from Peak at			
	0.80 ppm	1.22 ppm	0.92 ppm	HN region	0.80 ppm	1.22 ppm	0.92 ppm	HN region
Pure SDS Micelle	5.466 $\pm 0.043$	5.323 $\pm 0.027$	X	X	1.20	1.23	X	X
Mini-B <sub>OX</sub> /SDS Complex	3.497 $\pm 0.061$	3.423 $\pm 0.037$	2.885 $\pm 0.047$	2.507 $\pm 0.087$	1.88	1.92	2.27	2.62
SP-A/SDS Complex	2.512 $\pm 0.037$	1.670 $\pm 0.008$	0.943 $\pm 0.005$	1.166 $\pm 0.014$	2.61	3.93	6.96	5.63
Mini-B <sub>OX</sub> /SP-A/ SDS (Average)	0.896 $\pm 0.038$	1.096 $\pm 0.048$	0.701 $\pm 0.027$	0.705 $\pm 0.025$	7.32	5.98	9.36	9.30
Mini-B <sub>OX</sub> /SP-A/ SDS (Fit 1)	1.610 $\pm 0.016$	1.712 $\pm 0.019$	1.022 $\pm 0.006$	0.964 $\pm 0.021$	4.07	3.83	6.42	6.80
Mini-B <sub>OX</sub> /SP-A/ SDS (Fit 2)	0.521 $\pm 0.017$	0.481 $\pm 0.021$	0.318 $\pm 0.008$	0.338 $\pm 0.010$	12.59	13.64	20.63	19.41

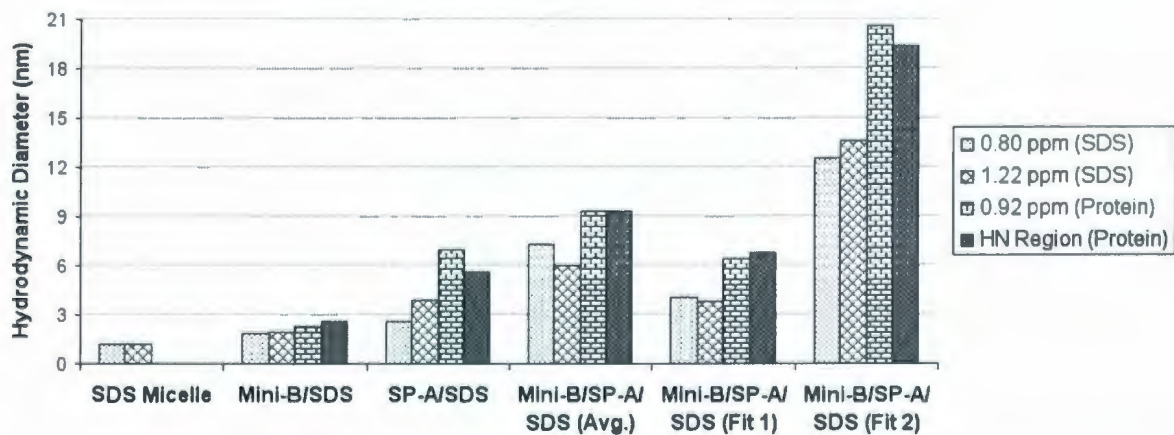


**Figure 6.6** : Bar graphs representing the apparent hydrodynamic diameters of pure SDS micelles and protein/SDS complexes, as presented in Table 6.1.

### 6.3.2 Mini-B and SP-A in DPC Micelles

The interaction between Mini-B and SP-A was studied next in smaller zwitterionic micelles composed of DPC. Again, this was investigated for both versions of Mini-B. SP-A was added to Mini-B<sub>RED</sub> in one step at the monomeric ratio of 1:1. However, Mini-B<sub>OX</sub> was titrated with SP-A in three steps, starting with a monomeric ratio of 4:1 and ending at 1:1. Figures 6.7 and 6.8 show the 1D <sup>1</sup>H spectra of Mini-B<sub>OX</sub> and Mini-B<sub>RED</sub>, respectively, plus SP-A in DPC micelles, along with the corresponding spectra of the individual proteins. As in SDS, the backbone HN signals from Mini-B/SP-A mixtures in DPC are almost identical to that of SP-A alone. Therefore, the conformation of SP-A likely remains the same in the presence of Mini-B, even if the proteins interact with each other.

Interestingly, the intensity of 2D <sup>15</sup>N-<sup>1</sup>H HSQC peaks of Mini-B<sub>OX</sub> gradually decrease with the addition of SP-A but their positions (chemical shifts) do not change (Figures 6.9 A-C). At the last step of titration, i.e., at 1:1 monomeric ratio of Mini-B<sub>OX</sub> to SP-A, all of the Mini-B<sub>OX</sub> peaks essentially disappear leaving much weaker traces of only one or two (Figure 6.9 D). The HSQC peaks of Mini-B<sub>RED</sub> also disappear in the presence of SP-A (Figure 6.10). This likely indicates all or most of Mini-B are bound in complexes, presumably complexes of SP-A plus DPC, which are too large to yield the HSQC signals. Since there are enough DPC present to provide about 7 times as many micelles as Mini-B molecules, it seems that Mini-B has a strong preference to interact with SP-A/DPC complexes over DPC micelles without SP-A. This interpretation is supported by the absence of any changes in the HSQC spectra of Mini-B<sub>OX</sub> when more DPC is added (Figure 6.9 E). However, a subsequent addition of CaCl<sub>2</sub>, at a concentration 50 times more than the proteins, causes the HSQC peaks of Mini-B<sub>OX</sub> to reappear (Figure 6.9 F). In this condition, the large Mini-B<sub>OX</sub>/SP-A/DPC complexes likely disassemble and the smaller Mini-B<sub>OX</sub>/DPC complexes reform.

The translational diffusion measurements confirm the formation of larger particles in the mixture of Mini-B<sub>OX</sub> and SP-A when compared to the individual proteins (Figures 6.11 & 6.12 and Table 6.2). As in SDS, the signal attenuation curves of Mini-B<sub>OX</sub>/SP-A/DPC, produced from the 2D DOSY spectra, do not fit well with a single line but reasonably well

with two lines based on approximately the first and the last halves of the data (Figure 6.11). Thus, two different observed translational diffusion coefficients are obtained. The hydrodynamic diameters calculated from both fits,  $\sim 12.8$  nm [from HN Fit 1 ( $\sim$  first half of the data)] and  $\sim 20.4$  [from HN Fit 2 ( $\sim$  last half of the data)], are much larger than SP-A/DPC ( $\sim 4.1$  nm) and Mini-B<sub>OX</sub>/DPC ( $\sim 2.3$  nm) complexes. The approximate ratio of small-to-large subpopulations of Mini-B<sub>OX</sub>/SP-A/DPC is 62% : 38%, as estimated from the y-axis (relative signal intensity) intercepts of the two linear fits. The average diameter of  $\sim 14.9$  nm, calculated from the average linear fit, is also much larger than the individual protein/micelle complexes. Thus, the two proteins likely interact and form larger complexes, but with heterogeneous sizes. As in SDS, the apparent sizes of the complexes are smaller when calculated from the DPC peaks ( $\sim 12$  nm, from Fit 2) than when calculated from the protein peaks ( $\sim 20$  nm, from Fit 2). Again, this is likely the result of a rapid exchange between the free and micelle-bound DPC species.

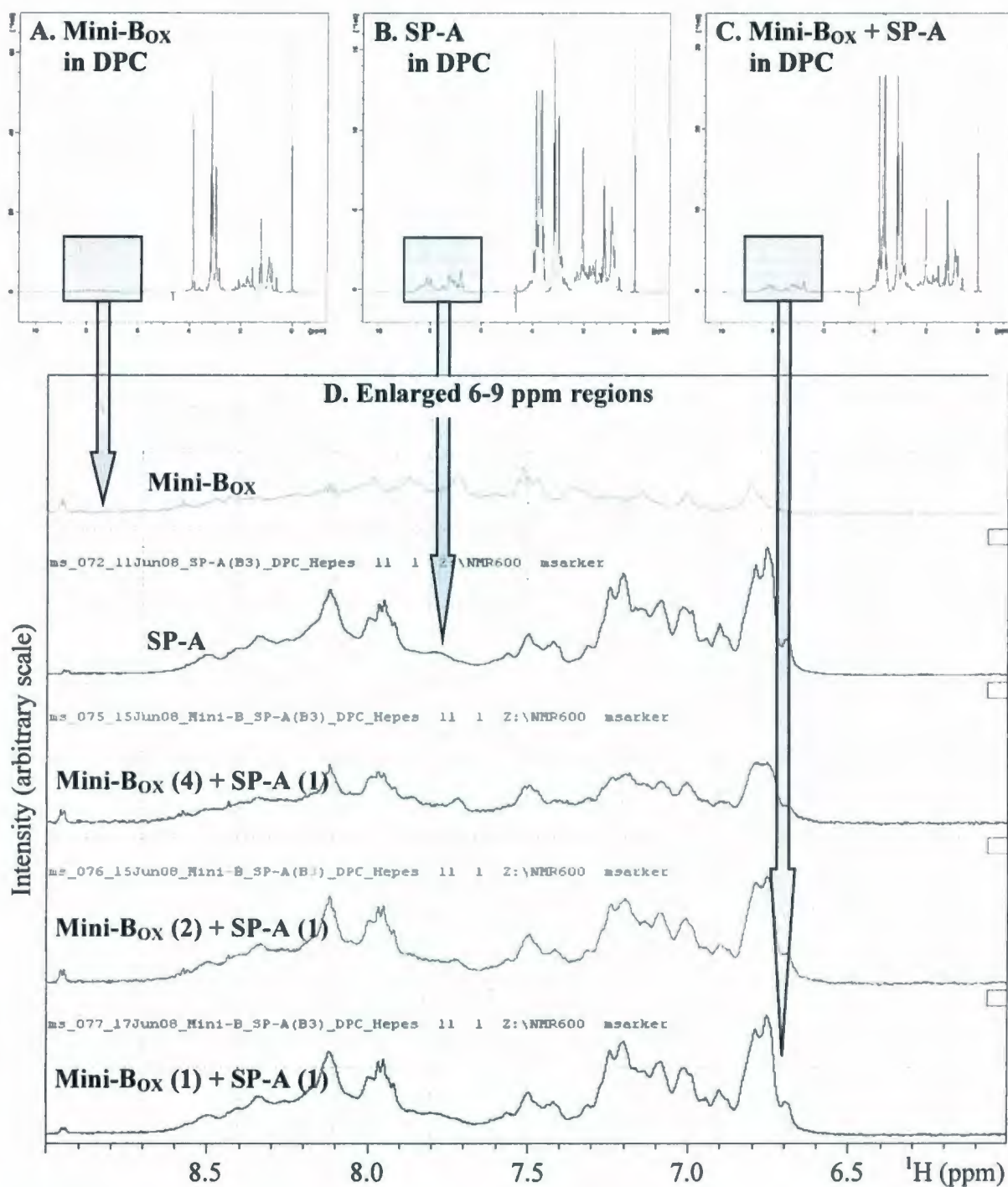


**Figure 6.7** : 1D  $^1\text{H}$  spectra of (A) 0.2 mM Mini-BoX, (B) 0.2 mM SP-A and (C) 0.1 mM Mini-BoX + 0.1 mM SP-A in 40 mM DPC, in the presence of 4.5 mM Hepes at pH 6.9 and temperature 37  $^{\circ}\text{C}$ . The spectra were acquired using 256 scans and processed with 1 Hz line broadening. The 6-9 ppm regions of all spectra are enlarged and shown in the bottom panel (D), including that from 0.16 mM Mini-BoX + 0.04 mM SP-A and 0.133 mM Mini-BoX + 0.67 mM SP-A samples.

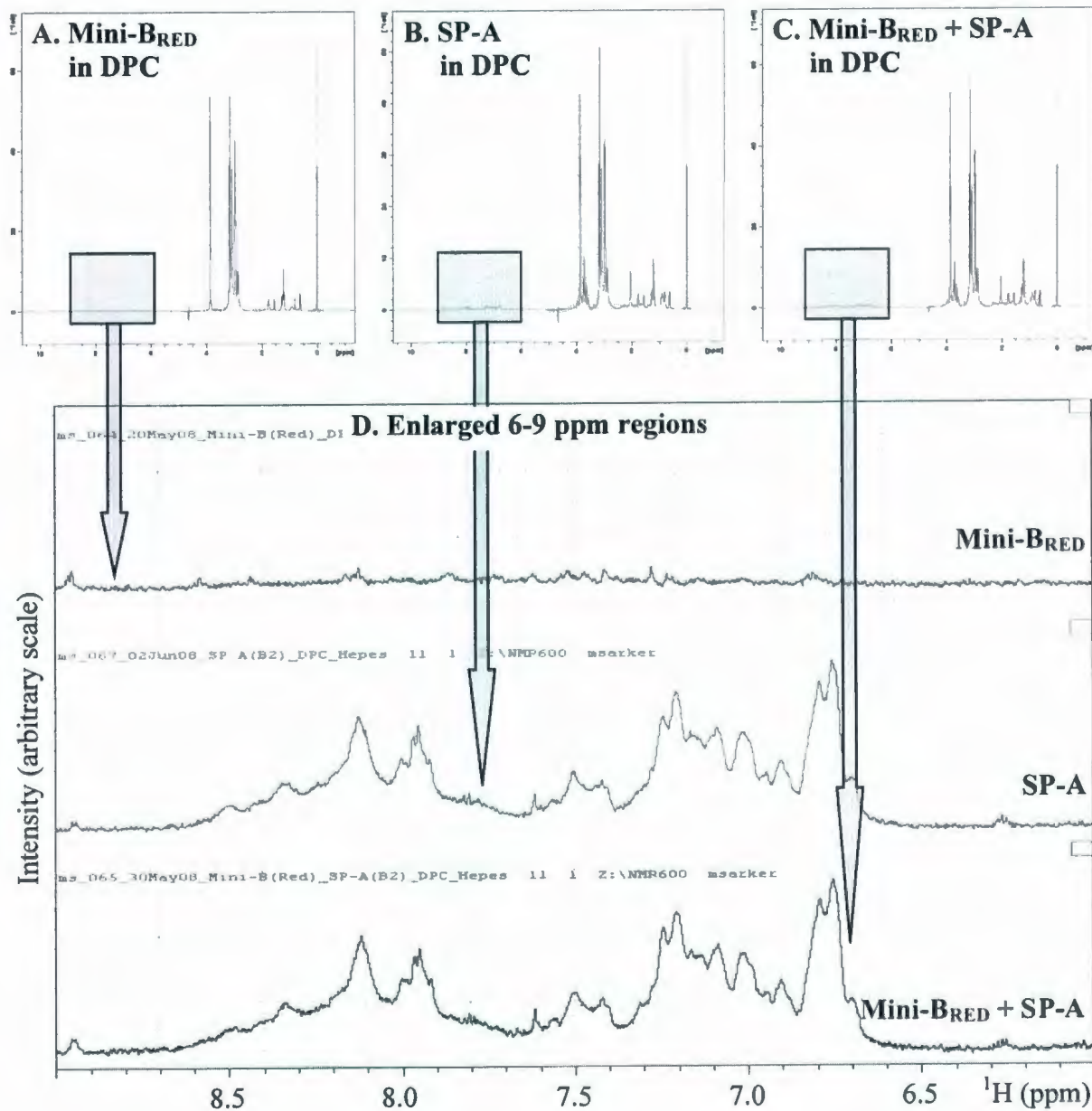


**Figure 6.8** : 1D  $^1\text{H}$  spectra of (A) 0.075 mM Mini-B<sub>RED</sub>, (B) 0.08 mM SP-A and (C) 0.075 mM Mini-B<sub>RED</sub> + 0.08 mM SP-A in 15 mM DPC, in the presence of 4.5 mM Hepes at pH 7.0 and temperature 37 °C. The spectra were acquired using 256 scans and processed with 1 Hz line broadening. The 6-9 ppm regions of all spectra are enlarged and shown in the bottom panel (D).

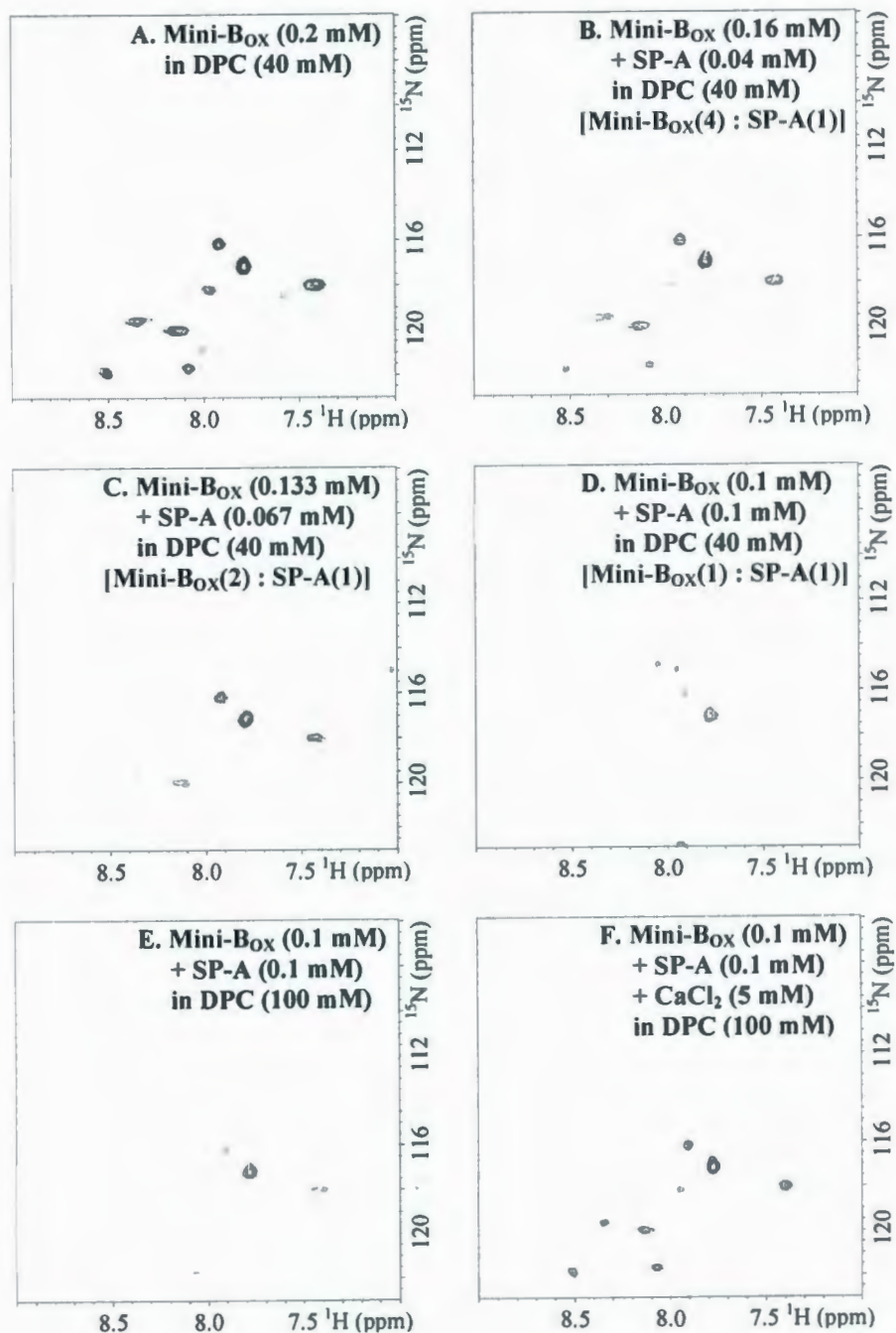


**Figure 6.9** : 2D  $^{15}\text{N}$ - $^1\text{H}$  HSQC spectra of (A) 0.2 mM Mini-B<sub>OX</sub> in 40 mM DPC (acquired using 160 scans), (B) 0.16 mM Mini-B<sub>OX</sub> + 0.04 mM SP-A in 40 mM DPC (acquired using 240 scans), (C) 0.133 mM Mini-B<sub>OX</sub> + 0.067 mM SP-A in 40 mM DPC (acquired using 352 scans), (D) 0.1 mM Mini-B<sub>OX</sub> + 0.1 mM SP-A in 40 mM DPC (acquired using 640 scans), (E) 0.1 mM Mini-B<sub>OX</sub> + 0.1 mM SP-A in 100 mM DPC (acquired using 320 scans) and (F) 0.1 mM Mini-B<sub>OX</sub> + 0.1 mM SP-A in 100 mM DPC + 5 mM CaCl<sub>2</sub> (acquired using 320 scans), in the presence of 4.5 mM Hepes at pH 6.9 and temperature 37 °C.

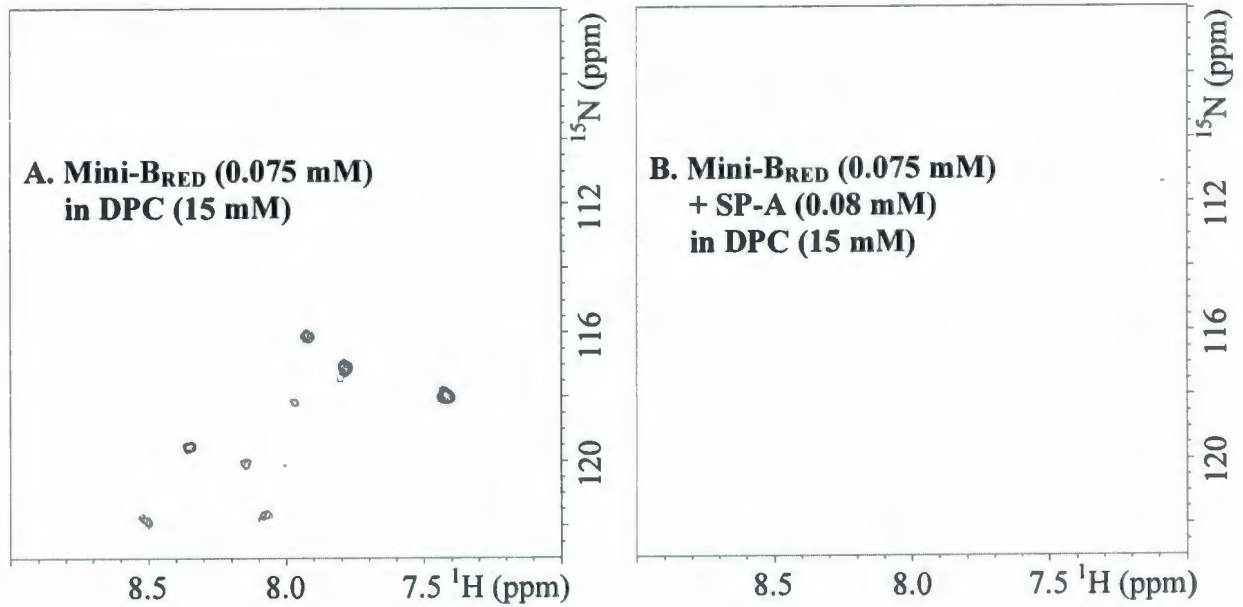


**Figure 6.10** : 2D  $^{15}\text{N}$ - $^1\text{H}$  HSQC spectra of (A) 0.075 mM Mini-B<sub>RED</sub> and (B) 0.075 mM Mini-B<sub>RED</sub> + 0.08 mM SP-A in 15 mM DPC, in the presence of 4.5 mM Hepes at pH 7.0 and temperature 37 °C. Both spectra were acquired using 320 scans.

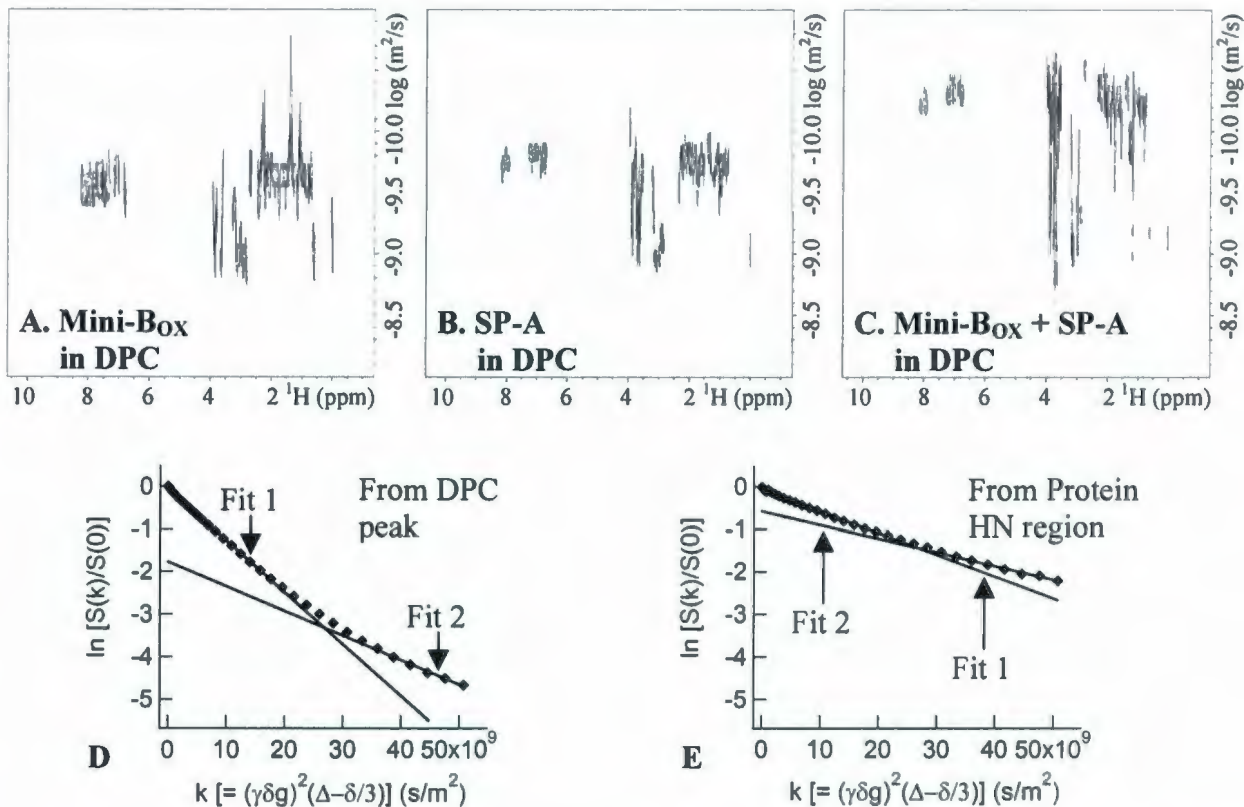


**Figure 6.11** : Translational diffusion measurements of Mini-BO<sub>X</sub> and SP-A in DPC. Top panels show the 2D DOSY spectra of 0.1 mM Mini-BO<sub>X</sub> in 20 mM DPC (A), 0.1 mM SP-A in 20 mM DPC (B) and 0.1 mM Mini-BO<sub>X</sub> + 0.1 mM SP-A in 40 mM DPC (C), in the presence of 4.5 mM Hepes at pH 6.9 and temperature 37 °C. The observed diffusion coefficients are determined from the slopes of the <sup>1</sup>H signal attenuation curves using two DPC signals (at 0.80 and 1.22 ppm) and two protein signals (0.92 ppm and HN regions). Only two signal attenuation curves for the Mini-BO<sub>X</sub>/SP-A/DPC complexes, obtained from the DPC peak at 1.22 ppm (D) and the protein HN region (E), are shown in the bottom panels. None of the signal attenuation curves for Mini-BO<sub>X</sub>/SP-A/DPC complexes fit well with a single line. However, approximately the first and the last halves of the data are fit reasonably well with two lines having two different slopes.

**Table 6.2 :** Observed translational diffusion coefficients and the corresponding hydrodynamic diameters of pure DPC micelles and protein/DPC complexes. The diffusion coefficients are represented by the slopes of the  $^1\text{H}$  signal attenuation linear fits obtained from the 2D DOSY data. The hydrodynamic diameters are calculated using the Stokes-Einstein equation (Eq. 2.20).

Micelle/Complex Composition	Diff. Coeff. $\times 10^{-10}$ ( $\text{m}^2/\text{s}$ ) from Peak at				Hydro. Dia. (nm) from Peak at			
	0.80 ppm	1.22 ppm	0.90 ppm	HN region	0.80 ppm	1.22 ppm	0.90 ppm	HN region
Pure DPC Micelle	3.356 $\pm 0.021$	3.367 $\pm 0.010$	X	X	1.96	1.95	X	X
Mini-B <sub>OX</sub> /DPC Complex	2.585 $\pm 0.023$	2.657 $\pm 0.013$	2.337 $\pm 0.015$	2.844 $\pm 0.061$	2.54	2.48	2.81	2.31
SP-A/DPC Complex	1.759 $\pm 0.011$	1.915 $\pm 0.004$	1.511 $\pm 0.008$	1.620 $\pm 0.011$	3.72	3.42	4.34	4.05
Mini-B <sub>OX</sub> /SP-A/ DPC (Average)	0.724 $\pm 0.018$	0.971 $\pm 0.022$	0.501 $\pm 0.010$	0.440 $\pm 0.008$	9.06	6.76	13.09	14.91
Mini-B <sub>OX</sub> /SP-A/ DPC (Fit 1)	0.922 $\pm 0.007$	1.214 $\pm 0.011$	0.610 $\pm 0.004$	0.511 $\pm 0.007$	7.11	5.40	10.75	12.84
Mini-B <sub>OX</sub> /SP-A/ DPC (Fit 2)	0.522 $\pm 0.009$	0.575 $\pm 0.027$	0.332 $\pm 0.013$	0.322 $\pm 0.012$	12.57	11.41	19.76	20.37

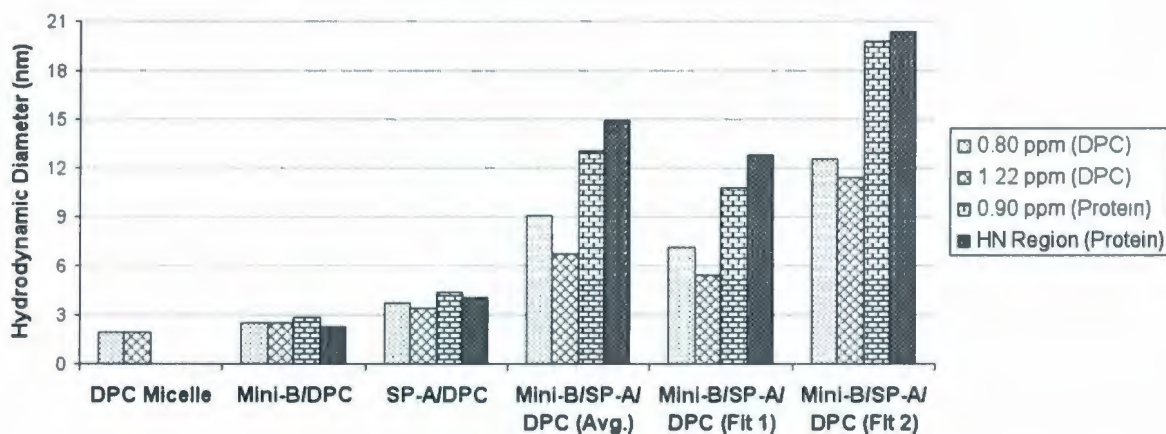


**Figure 6.12 :** Bar graphs representing the apparent hydrodynamic diameters of pure DPC micelles and protein/DPC complexes, as presented in Table 6.2.

### 6.3.3 Mini-B and SP-A in LMPC Micelles

To gain an insight into Mini-B/SP-A interaction in a more physiologically relevant lipid environment, the investigations continued with LMPC, LMPG and mixed LMPC/LMPG micelles. For these micelles, the studies were performed using Mini-B<sub>OX</sub> only. SP-A was added to Mini-B<sub>OX</sub> in one step at a monomeric ratio of 1:1. First studied were Mini-B<sub>OX</sub> and SP-A in zwitterionic micelles composed of LMPC that mimic the lung lipid environment created by the most abundant surfactant phospholipid DPPC. Again, the 1D <sup>1</sup>H spectrum of Mini-B<sub>OX</sub>/SP-A in LMPC looks almost identical to SP-A in LMPC indicating that the Mini-B<sub>OX</sub> signals are buried under the much stronger SP-A signals (Figure 6.13). The observed changes in the 2D <sup>15</sup>N-<sup>1</sup>H HSQC spectra are quite similar to that of the smaller zwitterionic micelles of DPC (Figure 6.14). The HSQC peaks of Mini-B<sub>OX</sub> disappear with the addition of SP-A leaving behind just a few much weaker traces.

The translational diffusion measurements in LMPC, however, demonstrate a result which is quite different from that of DPC or SDS (Figures 6.15 & 6.16 and Table 6.3). Again, four signal attenuation curves are produced from the 2D DOSY spectra, but now all are obtained from the lipid peaks since the protein signals are too weak to produce meaningful signal attenuation curves in the presence of nondeuterated LMPC (Figure 6.15). Unlike in SDS or DPC, each of the signal attenuation curves constitutes a single linear fit and hence yields a single translational diffusion coefficient. Thus, protein/lipid complexes of only a single homogeneous size are apparently present in the Mini-B<sub>OX</sub>/SP-A mixture in LMPC. Interestingly, the hydrodynamic diameter of the mixed complexes, calculated using the observed translational diffusion coefficient, is ~ 8.5 nm, which is smaller than SP-A/LMPC complexes (~ 10.3 nm) but larger than Mini-B<sub>OX</sub>/LMPC complexes (~ 6.7 nm). As elaborated in the discussion, this may be an outcome of rearrangements of the protein/lipid structures induced by the protein-protein interactions.

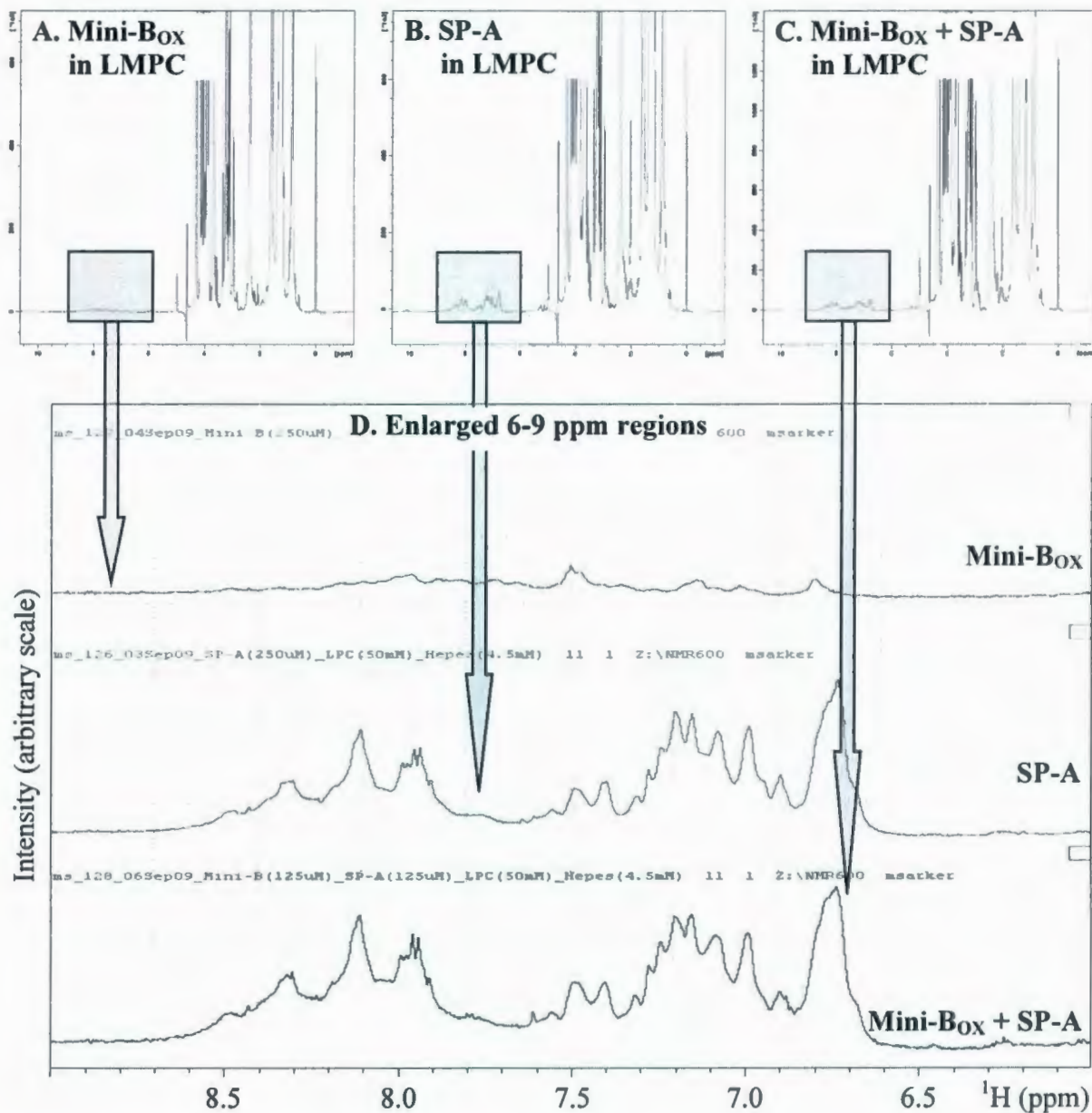


**Figure 6.13** : 1D  $^1\text{H}$  spectra of (A) 0.25 mM Mini-Box (acquired using 160 scans), (B) 0.25 mM SP-A (acquired using 160 scans) and (C) 0.125 mM Mini-Box + 0.125 mM SP-A (acquired using 320 scans) in 50 mM LMPC, in the presence of 4.5 mM Hepes at pH 6.9 and temperature 37 °C. The spectra were processed with 1 Hz line broadening. The 6-9 ppm regions of all spectra are enlarged and shown in the bottom panel (D).

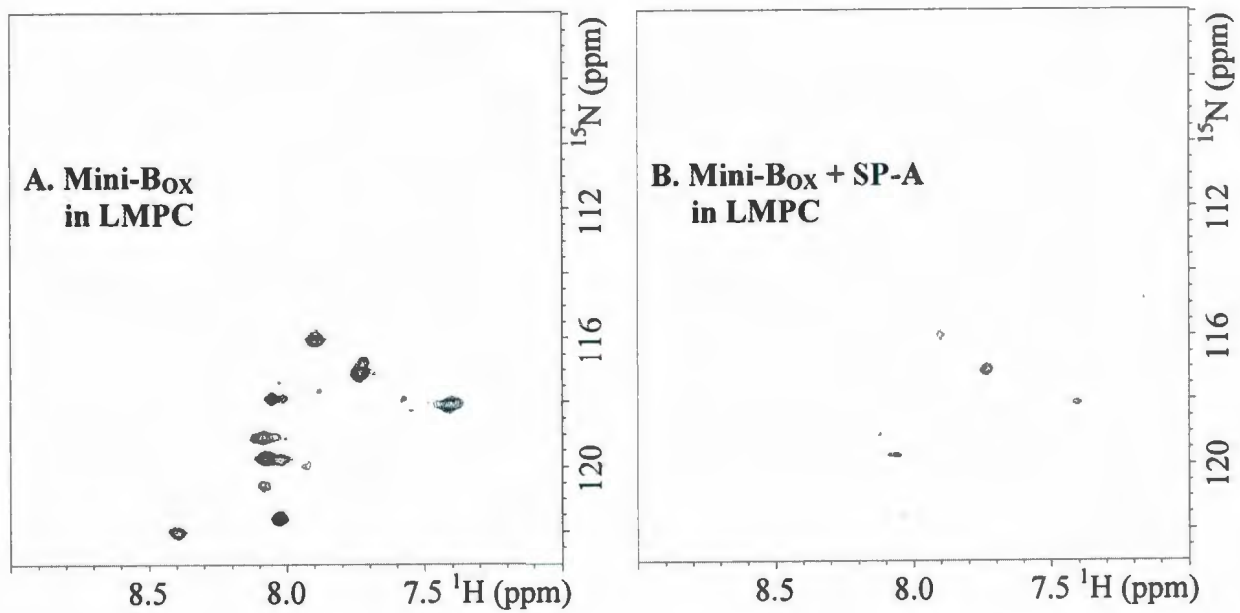


**Figure 6.14** : 2D  $^{15}\text{N}$ - $^1\text{H}$  HSQC spectra of (A) 0.25 mM Mini-B<sub>ox</sub> (acquired using 160 scans) and (B) 0.125 mM Mini-B<sub>ox</sub> + 0.125 mM SP-A (acquired using 320 scans) in 50 mM LMPC, in the presence of 4.5 mM Hepes at pH 6.9 and temperature 37 °C.

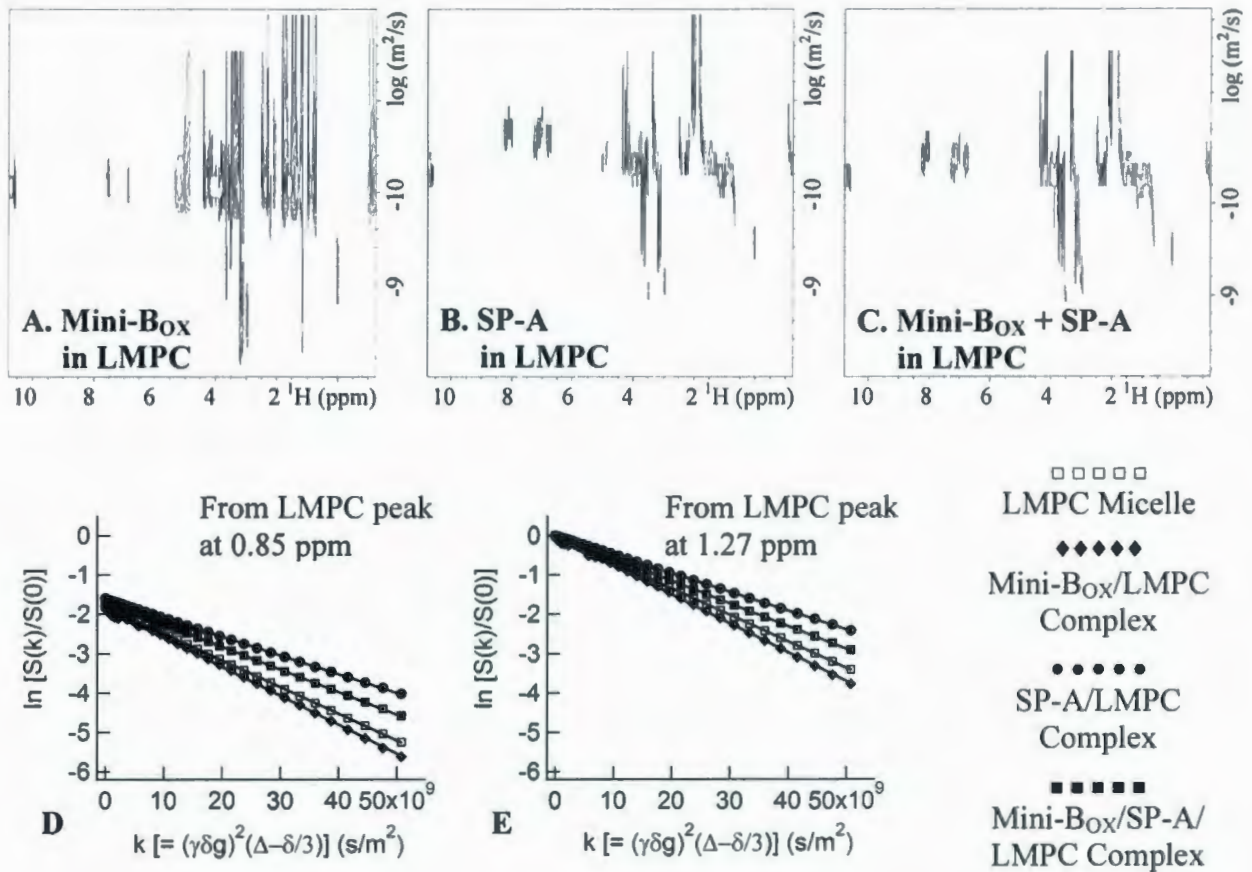


**Figure 6.15 :** Translational diffusion measurements of Mini-B<sub>OX</sub> and SP-A in LMPC. Top panels show the 2D DOSY spectra of 0.25 mM Mini-B<sub>OX</sub> (A), 0.25 mM SP-A (B) and 0.125 mM Mini-B<sub>OX</sub> + 0.125 mM SP-A (C) in 50 mM LMPC, in the presence of 4.5 mM Hepes at pH 6.9 and temperature 25 °C. The observed diffusion coefficients are determined from the slopes of the <sup>1</sup>H signal attenuation curves using four LMPC peaks (at 0.85, 1.27, 1.58 and 2.36 ppm). Only two sets of signal attenuation curves for pure micelle and protein/micelle complexes, obtained from the peaks at 0.85 ppm (D) and 1.27 ppm (E), are shown in the bottom panels.

**Table 6.3** : Observed translational diffusion coefficients and the corresponding hydrodynamic diameters of pure LMPC micelles and protein/LMPC complexes. The diffusion coefficients are represented by the slopes of the  $^1\text{H}$  signal attenuation linear fits obtained from the 2D DOSY data. The hydrodynamic diameters are calculated using the Stokes-Einstein equation (Eq. 2.20).

Micelle/Complex Composition	Diff. Coeff. $\times 10^{-11}$ ( $\text{m}^2/\text{s}$ ) from Peak at				Hydro. Dia. (nm) from Peak at			
	0.85 ppm	1.27 ppm	1.58 ppm	2.36 ppm	0.85 ppm	1.27 ppm	1.58 ppm	2.36 ppm
Pure LMPC Micelle	6.790 $\pm 0.006$	6.741 $\pm 0.003$	6.578 $\pm 0.014$	6.735 $\pm 0.004$	7.21	7.26	7.44	7.27
Mini-B <sub>ox</sub> /LMPC Complex	7.364 $\pm 0.047$	7.332 $\pm 0.043$	7.390 $\pm 0.055$	7.373 $\pm 0.042$	6.65	6.68	6.63	6.64
SP-A/LMPC Complex	4.774 $\pm 0.007$	4.783 $\pm 0.003$	4.580 $\pm 0.015$	4.755 $\pm 0.011$	10.26	10.24	10.69	10.30
Mini-B <sub>ox</sub> /SP-A/ LMPC Complex	5.762 $\pm 0.008$	5.760 $\pm 0.005$	5.609 $\pm 0.013$	5.764 $\pm 0.008$	8.50	8.50	8.73	8.50

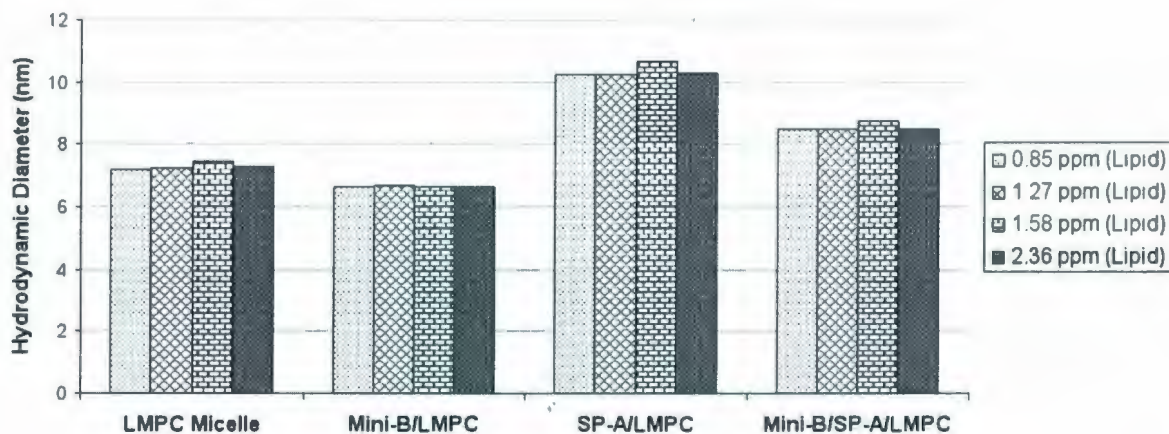


**Figure 6.16** : Bar graphs representing the apparent hydrodynamic diameters of pure LMPC micelles and protein/LMPC complexes, as presented in Table 6.3.

### 6.3.4 Mini-B and SP-A in LMPG Micelles

The interaction between Mini-B<sub>OX</sub> and SP-A was assessed next in anionic micelles composed of LMPG that mimic the lung lipid environment created by the surfactant phospholipids with PG headgroups. Again, in the 1D <sup>1</sup>H spectrum of Mini-B<sub>OX</sub>/SP-A in LMPG, the signals from Mini-B<sub>OX</sub> are buried under the intense signals of SP-A and the spectrum looks identical to SP-A in LMPG (Figure 6.17). The Mini-B<sub>OX</sub> peaks in the 2D <sup>15</sup>N-<sup>1</sup>H HSQC spectra remain unchanged with the addition of SP-A (Figure 6.18), which is similar to Mini-B<sub>OX</sub>/SP-A in SDS but different from Mini-B<sub>OX</sub>/SP-A in DPC or LMPC.

The translational diffusion measurements in LMPG, obtained using the 2D DOSY spectra, provide a similar result to that in LMPC (Figures 6.19 & 6.20 and Table 6.4). Each of the four signal attenuation curves constitutes a single linear fit and hence indicates a single particle size. Again, the apparent hydrodynamic diameter of the complexes in Mini-B<sub>OX</sub>/SP-A mixture, calculated using the observed translational diffusion coefficient, is ~ 9.1 nm, which is smaller than SP-A/LMPG complexes (~ 11.2 nm) but larger than Mini-B<sub>OX</sub>/LMPC complexes (~ 7.2 nm). As in LMPC, this may be caused by rearrangements of the protein/lipid structures induced by the Mini-B<sub>OX</sub>/SP-A interactions.

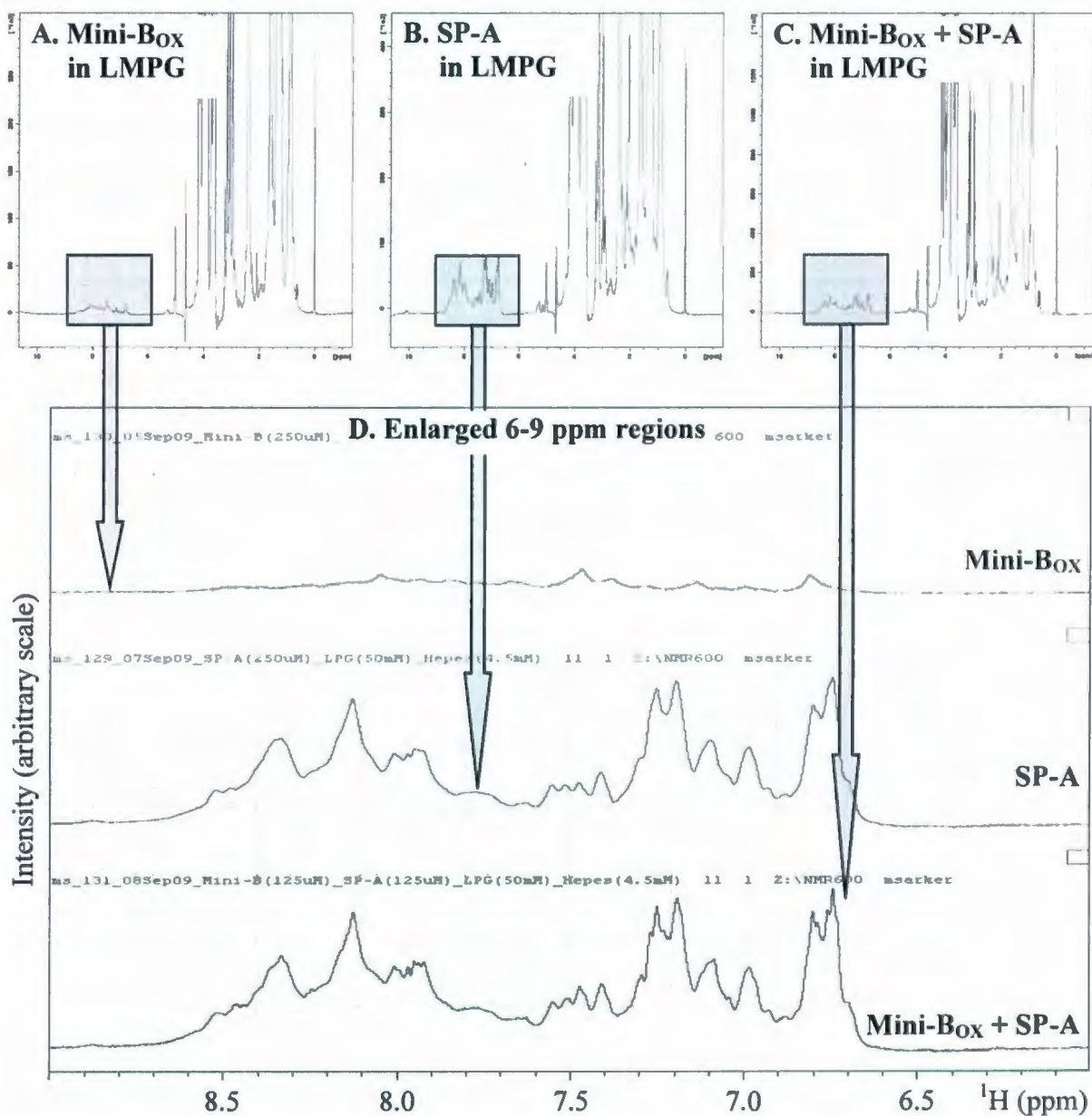


**Figure 6.17** : 1D  $^1\text{H}$  spectra of (A) 0.25 mM Mini-Box (acquired using 160 scans), (B) 0.25 mM SP-A (acquired using 160 scans) and (C) 0.125 mM Mini-Box + 0.125 mM SP-A (acquired using 320 scans) in 50 mM LMPG, in the presence of 4.5 mM Hepes at pH 6.9 and temperature 37 °C. The spectra were processed with 1 Hz line broadening. The 6-9 ppm regions of all spectra are enlarged and shown in the bottom panel (D).

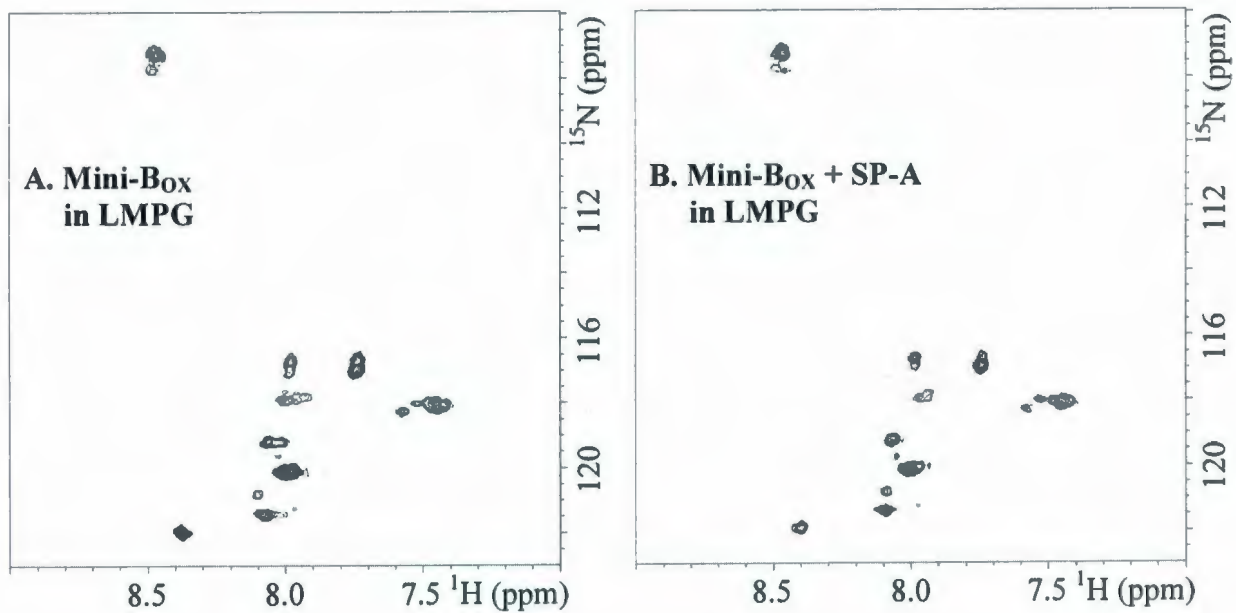


**Figure 6.18** : 2D  $^{15}\text{N}$ - $^1\text{H}$  HSQC spectra of (A) 0.25 mM Mini-Box (acquired using 160 scans) and (B) 0.125 mM Mini-Box + 0.125 mM SP-A (acquired using 320 scans) in 50 mM LMPG, in the presence of 4.5 mM Hepes at pH 6.9 and temperature 37 °C.

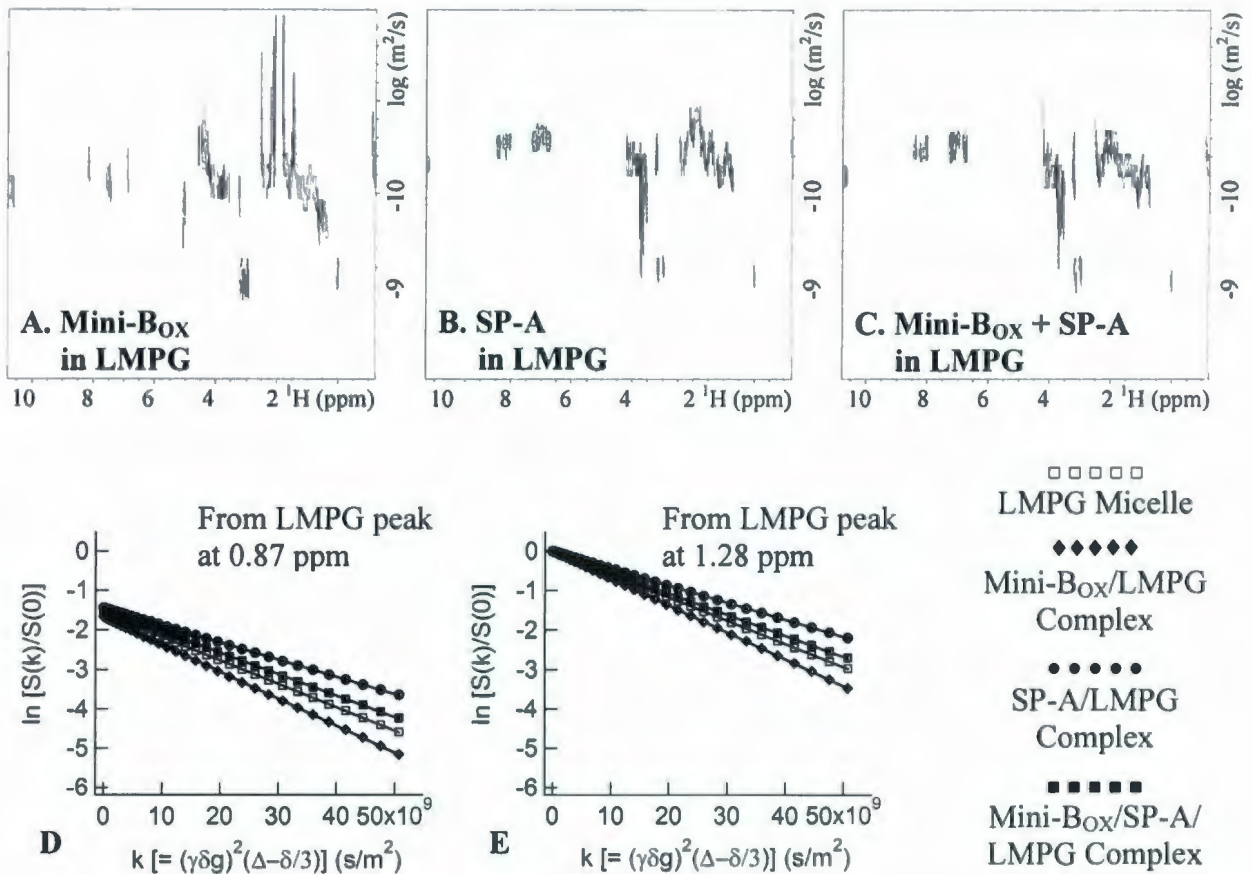


**Figure 6.19** : Translational diffusion measurements of Mini-B<sub>OX</sub> and SP-A in LMPG. Top panels show the 2D DOSY spectra of 0.25 mM Mini-B<sub>OX</sub> (A), 0.25 mM SP-A (B) and 0.125 mM Mini-B<sub>OX</sub> + 0.125 mM SP-A (C) in 50 mM LMPG, in the presence of 4.5 mM Hepes at pH 6.9 and temperature 25 °C. The observed diffusion coefficients are determined from the slopes of the <sup>1</sup>H signal attenuation curves using four LMPG peaks (at 0.87, 1.28, 1.60 and 2.38 ppm). Only two sets of signal attenuation curves for pure micelle and protein/micelle complexes, obtained from the peaks at 0.87 ppm (D) and 1.28 ppm (E), are shown in the bottom panels.

**Table 6.4** : Observed translational diffusion coefficients and the corresponding hydrodynamic diameters of pure LMPG micelles and protein/LMPG complexes. The diffusion coefficients are represented by the slopes of the  $^1\text{H}$  signal attenuation linear fits obtained from the 2D DOSY data. The hydrodynamic diameters are calculated using the Stokes-Einstein equation (Eq. 2.20).

Micelle/Complex Composition	Diff. Coeff. $\times 10^{-11}$ ( $\text{m}^2/\text{s}$ ) from Peak at				Hydro. Dia. (nm) from Peak at			
	0.87 ppm	1.28 ppm	1.60 ppm	2.38 ppm	0.87 ppm	1.28 ppm	1.60 ppm	2.38 ppm
Pure LMPG Micelle	5.907 $\pm 0.004$	5.909 $\pm 0.003$	5.861 $\pm 0.003$	5.891 $\pm 0.003$	8.29	8.29	8.36	8.31
Mini-Box/LMPG Complex	6.841 $\pm 0.014$	6.849 $\pm 0.009$	6.744 $\pm 0.007$	6.851 $\pm 0.013$	7.16	7.15	7.26	7.15
SP-A/LMPG Complex	4.359 $\pm 0.005$	4.374 $\pm 0.005$	4.300 $\pm 0.008$	4.345 $\pm 0.004$	11.23	11.20	11.39	11.27
Mini-Box/SP-A/ LMPG Complex	5.441 $\pm 0.009$	5.367 $\pm 0.006$	5.274 $\pm 0.004$	5.390 $\pm 0.006$	9.00	9.12	9.29	9.09

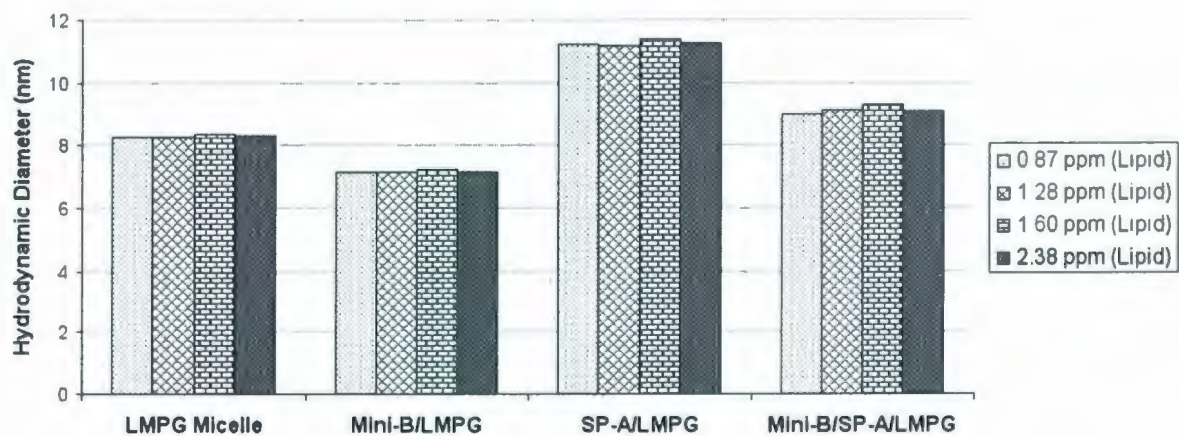


**Figure 6.20** : Bar graphs representing the apparent hydrodynamic diameters of pure LMPG micelles and protein/LMPG complexes, as presented in Table 6.4.

### 6.3.5 Mini-B and SP-A in Mixed LMPC/LMPG Micelles

Lastly for this chapter, the interaction between Mini-B<sub>OX</sub> and SP-A was probed in a mixed LMPC/LMPG micelle system. As usual, the 1D <sup>1</sup>H spectrum of Mini-B<sub>OX</sub>/SP-A mixture looks almost identical to that of SP-A alone (Figure 6.21). Interestingly, the Mini-B<sub>OX</sub> peaks in the 2D <sup>15</sup>N-<sup>1</sup>H HSQC spectra remain unchanged with the addition of SP-A (Figure 6.22), which matches the result obtained in 100% LMPG although only 15% LMPG is present in the mixed micelle system.

The change in the size of the protein/micelle complexes in the mixed micelle system, as obtained from the 2D DOSY spectra, follows the same trend as that of individual LMPC and LMPG systems (Figures 6.23 & 6.24 and Table 6.5). The hydrodynamic diameter of the particles present in the Mini-B<sub>OX</sub>/SP-A mixture, calculated using the observed translational diffusion coefficient, is ~ 9.0 nm, which is smaller than SP-A/LMPC/LMPG complexes (~ 10.7 nm) but larger than Mini-B<sub>OX</sub>/LMPC/LMPC complexes (~ 6.5 nm). Again, the protein-protein interactions may be responsible for rearrangements of the protein/lipid structures.

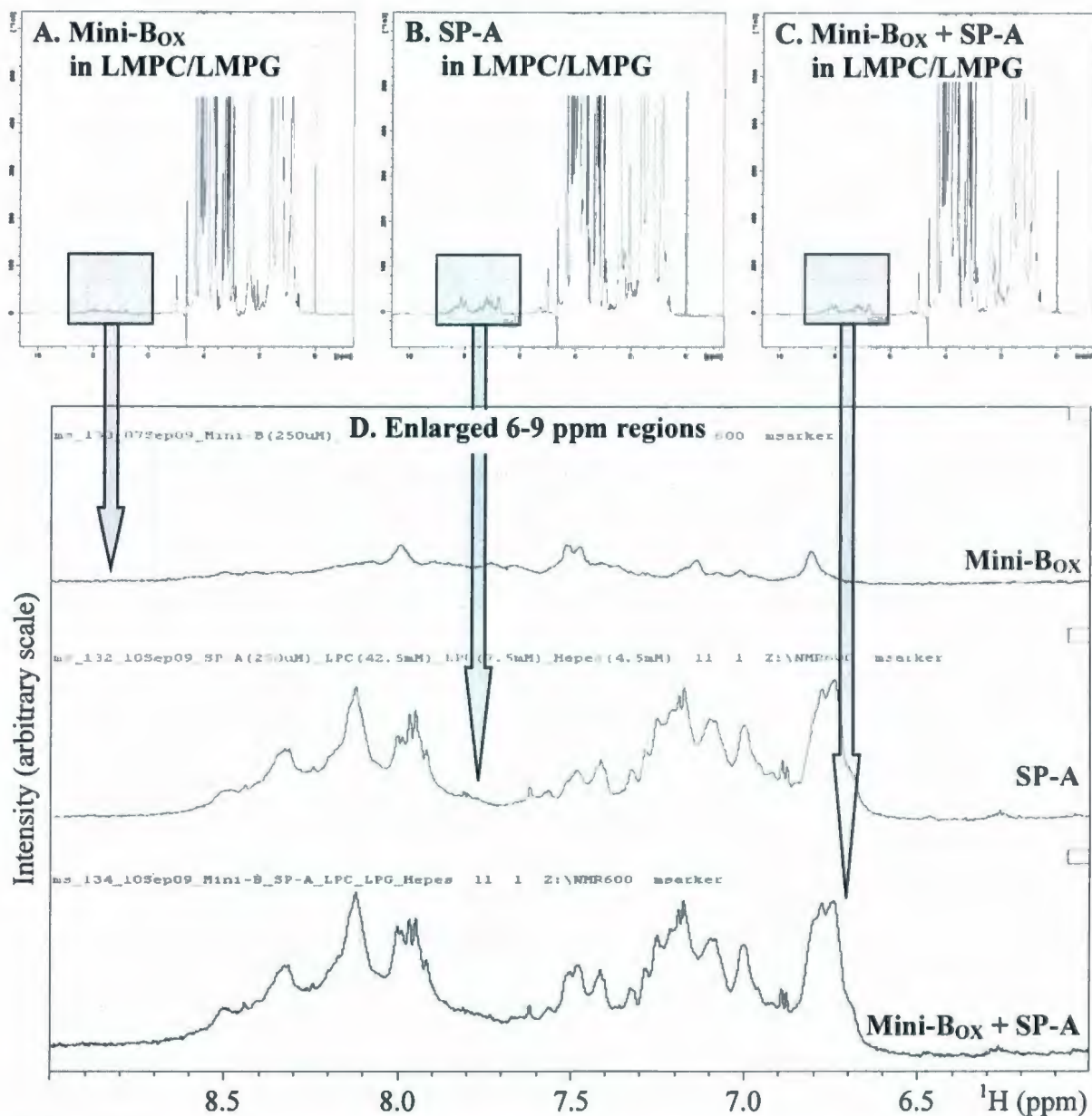


**Figure 6.21 :** 1D  $^1\text{H}$  spectra of (A) 0.25 mM Mini-Box (acquired using 160 scans), (B) 0.25 mM SP-A (acquired using 160 scans) and (C) 0.125 mM Mini-Box + 0.125 mM SP-A (acquired using 320 scans) in 42.5 LMPC + 7.5 mM LMPG, in the presence of 4.5 mM Hepes at pH 6.9 and temperature 37 °C. The spectra were processed with 1 Hz line broadening. The 6-9 ppm regions of all spectra are enlarged and shown in the bottom panel (D).

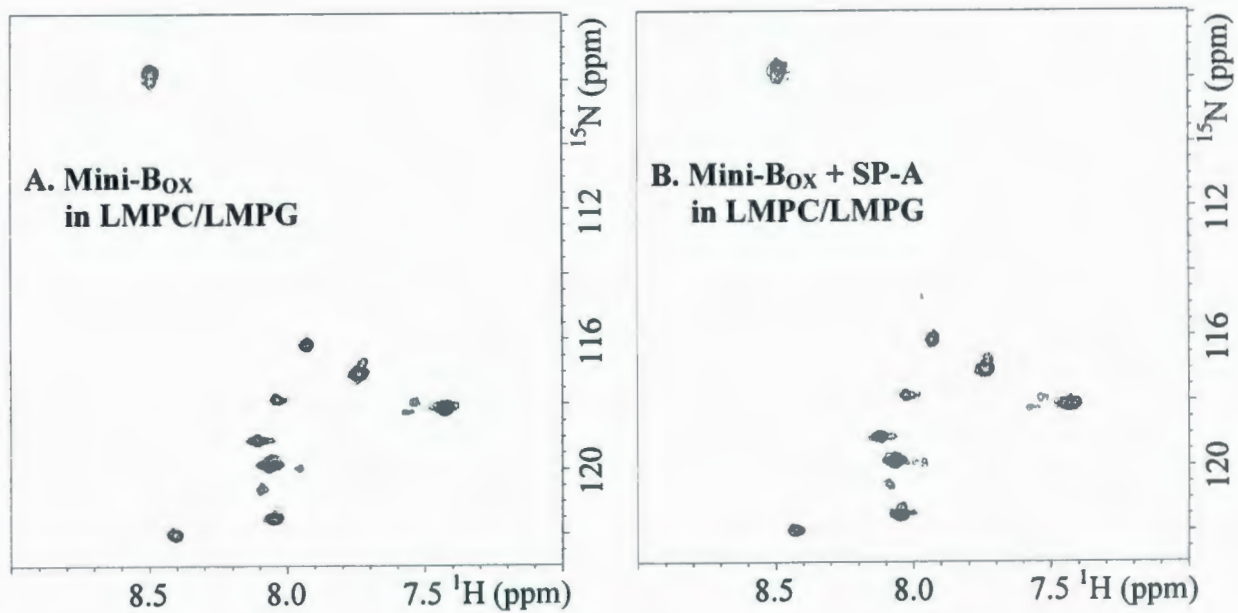


**Figure 6.22** : 2D  $^{15}\text{N}$ - $^1\text{H}$  HSQC spectra of (A) 0.25 mM Mini-Box (acquired using 160 scans) and (B) 0.125 mM Mini-Box + 0.125 mM SP-A (acquired using 320 scans) in 42.5 mM LMPC + 7.5 mM LMPG, in the presence of 4.5 mM HEPES at pH 6.9 and temperature 37 °C.

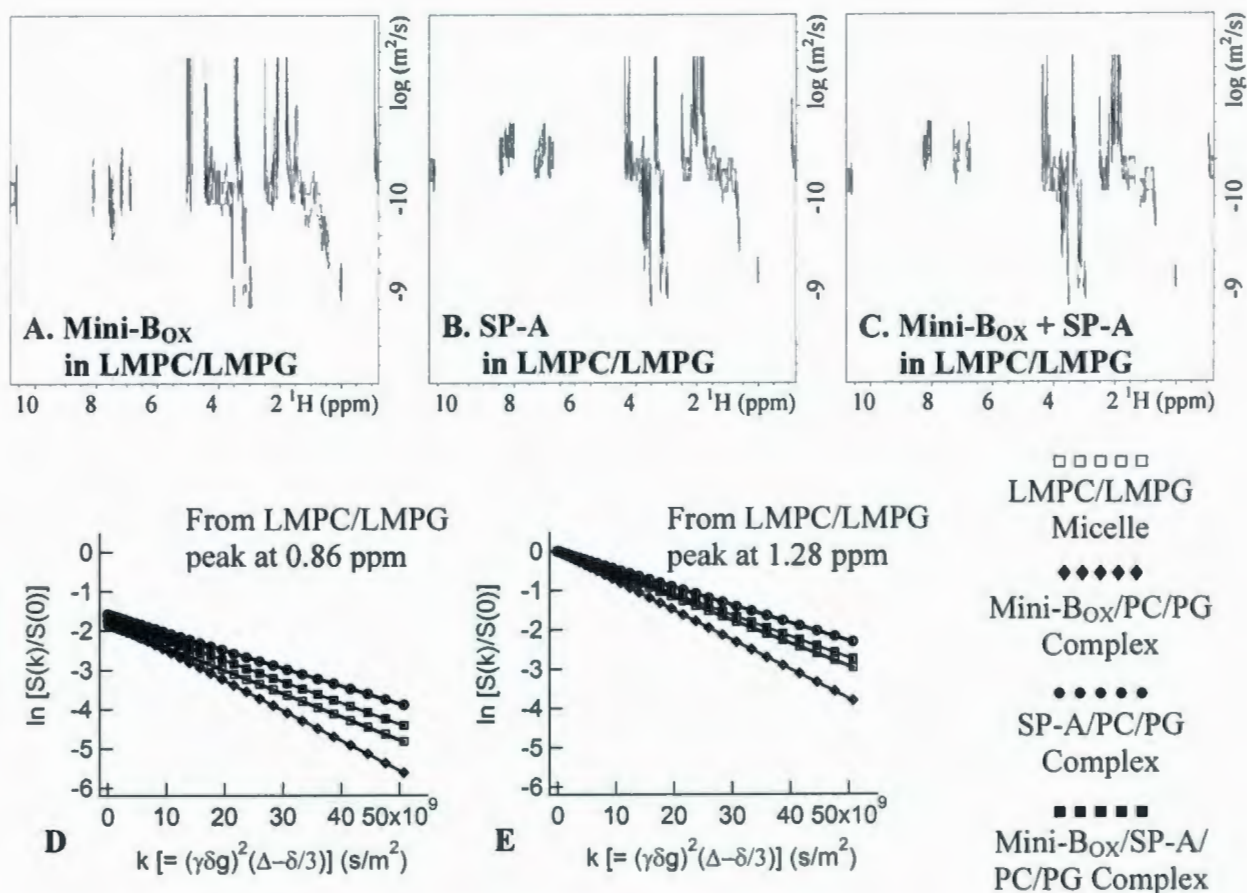


**Figure 6.23 :** Translational diffusion measurements of Mini-B<sub>OX</sub> and SP-A in LMPC/LMPG. Top panels show the 2D DOSY spectra of 0.25 mM Mini-B<sub>OX</sub> (A), 0.25 mM SP-A (B) and 0.125 mM Mini-B<sub>OX</sub> + 0.125 mM SP-A (C) in 42.5 mM LMPC + 7.5 mM LMPG, in the presence of 4.5 mM Hepes at pH 6.9 and temperature 25 °C. The observed diffusion coefficients are determined from the slopes of the <sup>1</sup>H signal attenuation curves using four LMPC/LMPG peaks (at 0.86, 1.28, 1.59 and 2.37 ppm). Only two sets of signal attenuation curves for pure micelle and protein/micelle complexes, obtained from the peaks at 0.86 ppm (D) and 1.28 ppm (E), are shown in the bottom panels.

**Table 6.5** : Observed translational diffusion coefficients and the corresponding hydrodynamic diameters of pure LMPC/LMPG micelles and protein/LMPC/LMPG complexes. The diffusion coefficients are represented by the slopes of the  $^1\text{H}$  signal attenuation linear fits obtained from the 2D DOSY data. The hydrodynamic diameters are calculated using the Stokes-Einstein equation (Eq. 2.20).

Micelle/Complex Composition	Diff. Coeff. $\times 10^{-11}$ ( $\text{m}^2/\text{s}$ ) from Peak at				Hydro. Dia. (nm) from Peak at			
	0.86 ppm	1.28 ppm	1.59 ppm	2.37 ppm	0.86 ppm	1.28 ppm	1.59 ppm	2.37 ppm
Pure LMPC/ LMPG Micelle	5.910 $\pm 0.003$	5.866 $\pm 0.002$	5.706 $\pm 0.012$	5.854 $\pm 0.004$	8.29	8.35	8.58	8.37
Mini-B <sub>OX</sub> /LMPC/ LMPG Complex	7.635 $\pm 0.003$	7.504 $\pm 0.003$	7.134 $\pm 0.012$	7.541 $\pm 0.005$	6.41	6.53	6.86	6.49
SP-A/LMPC/ LMPG Complex	4.564 $\pm 0.006$	4.571 $\pm 0.003$	4.387 $\pm 0.019$	4.563 $\pm 0.009$	10.73	10.71	11.16	10.73
Mini-B <sub>OX</sub> /SP-A/ LMPC/LMPG	5.436 $\pm 0.007$	5.427 $\pm 0.004$	5.252 $\pm 0.013$	5.415 $\pm 0.006$	9.01	9.02	9.32	9.04

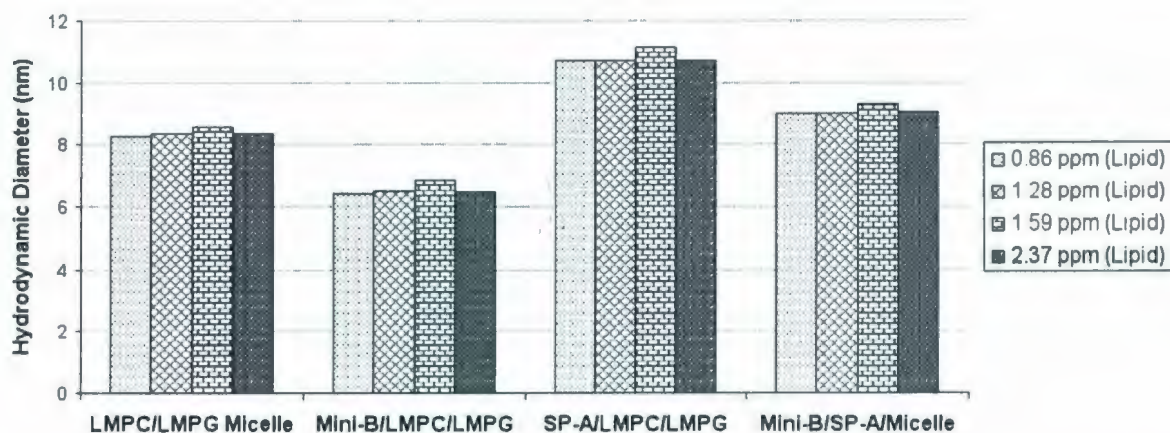


**Figure 6.24** : Bar graphs representing the apparent hydrodynamic diameters of pure LMPC/LMPG micelles and protein/LMPC/LMPG complexes, as presented in Table 6.5.

## 6.4 Discussion

Protein-protein interactions play vital roles in many biological processes. For optimal function of surfactant materials in the lung, interactions between SP-B and SP-A may also play important roles. Although mechanistic descriptions of the events that take place at the molecular and submolecular levels in lung surfactant function are still unavailable, a few models have been proposed portraying the mechanisms of SP-B- and SP-A-induced rearrangement and stabilization of phospholipid structures on an individual basis [70, 17] as well as through their concerted actions [12, 23, 198]. Formation of tubular myelin [59-61], enhancement of lipid adsorption along the air-water interface [62, 63], fusion of lipid membranes [193, 194] and inhibition of blood and plasma proteins [196] are well-established *in vitro* demonstrations of concerted actions between SP-A and SP-B. However, it is still unknown if the two proteins interact directly to accomplish these results or if these are achieved by their indirect interactions mediated through the lipids. Knowledge of the high-resolution structure of Mini-B provides a tool to probe its interactions with SP-A, if any, in model surfactant lipids and thus enhances our understanding of the ramifications of SP-B/SP-A interactions in the lung.

The interactions between Mini-B and SP-A are investigated by assessing the changes in the features of NMR spectra when the two proteins are mixed at equal molar concentrations. Like the individual proteins, these investigations are carried out in an array of five micelle systems mimicking various lipid components found in lung surfactant. Two of the micelle systems are anionic, composed from the detergent SDS and the surfactant PG-analogue LMPG, two are zwitterionic, composed from the lipid DPC and the surfactant PC-analogue LMPC, and the remaining one is a mixed micelle system composed of 85% LMPC and 15% LMPG, in keeping with the physiological ratio of PC to PG in the lung.

For all micelle systems, the 1D  $^1\text{H}$  spectra of Mini-B + SP-A look almost identical to SP-A alone (Figures 6.1, 6.2, 6.7, 6.8, 6.13, 6.17 and 6.21). The 1D  $^1\text{H}$  spectra of the mixed sample is expected to be dominated by the signals from SP-A since an SP-A monomer (248

amino acids) has more than 7 times the number of amino acids as a Mini-B monomer (34 amino acids). Thus the signals from Mini-B are completely buried under the many more intense signals of SP-A. However, lack of any observable differences between the 1D  $^1\text{H}$  spectra of SP-A and Mini-B + SP-A gives a primary indication that, in all micelle systems, the overall conformation of SP-A does not change with the addition of Mini-B. This, however, does not rule out an interaction between Mini-B and SP-A because the proton signals of SP-A are already very broad and overlapped and thus the SP-A signal intensity may not change much even if the relatively smaller Mini-B and SP-A are bound within the same micelle complex.

Since Mini-B consists of nine  $^{15}\text{N}$ -labeled amino acids, the 2D  $^{15}\text{N}$ - $^1\text{H}$  HSQC spectra provide an opportunity to assess the SP-A effects on the Mini-B conformation as a result of any interactions between the two proteins. Interestingly, upon addition of SP-A, the intensity of Mini-B<sub>OX</sub> HSQC peaks decreases drastically for zwitterionic DPC and LMPC micelles (Figures 6.9 and 6.14) but remains mostly unaffected for anionic SDS and LMPG and mixed LMPC/LMPG micelles (Figures 6.3, 6.18 and 6.22). The same results are also observed for Mini-B<sub>RED</sub> + SP-A in DPC and SDS micelles (Figures 6.10 and 6.4). Therefore, in zwitterionic micelles, a much larger subpopulation of Mini-B<sub>OX</sub> and the entire population of Mini-B<sub>RED</sub> appear to be bound in complexes that are too large to yield the HSQC signals, presumably complexes of SP-A-bound micelles. Since there are enough DPC/LMPC present to provide at least 4 times as many micelles as Mini-B molecules, it seems that Mini-B has a strong preference to interact with SP-A-bound DPC/LMPC complexes over SP-A-free DPC/LMPC micelles. This interpretation is supported by the absence of any changes in the HSQC spectra when more DPC is added (Figure 6.9 D and E). For the anionic micelles, the scenario appears to be substantially different. The absence of any apparent change in the HSQC peak intensity indicates that Mini-B does not interact with the SP-A/micelle complex and remains bound to its own micelle. Surprisingly, in mixed LMPC/LMPG micelles, Mini-B behaves similarly to that in pure LMPG micelles although the mixed micelles comprise 85% LMPC. It is, however, possible that even in the anionic and mixed micelle systems, a much smaller subpopulation of Mini-B interacts with SP-A and that does not cause an observable reduction in the overall HSQC peak intensity.

Indeed, the 2D DOSY spectra indicate the presence of larger complexes in both DPC and SDS micelle systems although the overall results are different between DPC and SDS. In DPC, the Mini-B<sub>OX</sub>/SP-A mixture contains two populations of different sizes as indicated by the two translational diffusion coefficients. The apparent hydrodynamic diameters are ~ 12.8 and 20.4 nm as calculated from the attenuation of the protein HN signals. Both of these sizes are much larger than the apparent hydrodynamic diameters of the complexes containing the proteins individually, ~ 2.3 nm for Mini-B<sub>OX</sub>/DPC and ~ 4.1 nm for SP-A/DPC. The approximate ratio of the small-to-large subpopulations of Mini-B<sub>OX</sub>/SP-A/DPC is 62% : 38% as estimated from the y-axis (relative signal intensity) intercepts of the two linear fits representing the two diffusion coefficients (Figure 6.11). However, as both species of Mini-B<sub>OX</sub> + SP-A in DPC are much larger than Mini-B<sub>OX</sub> alone, the intensity of the HSQC peaks decreases markedly (Figure 6.9). On the other hand, the mixed Mini-B<sub>OX</sub>/SP-A sample in SDS also contains two species but the apparent hydrodynamic diameters are ~ 6.8 and 19.4 nm. The approximate ratio of small-to-large subpopulations of Mini-B<sub>OX</sub>/SP-A/SDS is 85% : 15%. Moreover, the size of the predominant smaller species in this case is not very different from the ~ 5.6 nm apparent hydrodynamic diameter of SP-A/SDS alone. Therefore, only a smaller fraction of the total number of Mini-B molecules present in the SDS sample seems to be bound to SP-A. This likely explains why the HSQC peaks of Mini-B<sub>OX</sub> + SP-A do not noticeably lose intensity when compared to Mini-B<sub>OX</sub> alone (Figure 6.3). The apparent sizes of the DPC- and SDS-bound protein(s) mentioned here are estimated from the attenuation of the protein HN signals. Although the numbers are different when the estimation is done from the attenuation of the micelle peaks, the trend of the size-change remains the same between the mixed and individual protein samples. Therefore, almost the entire population of Mini-B<sub>OX</sub> presumably interacts with SP-A when in zwitterionic DPC micelles but only a subpopulation of Mini-B<sub>OX</sub> interacts with SP-A when in anionic SDS micelles.

In contrast to the results obtained for smaller DPC/SDS micelles, the 2D DOSY spectra of Mini-B<sub>OX</sub> + SP-A in larger LMPC/LMPG micelles do not provide a clear indication about the formation of bigger complexes containing both proteins together. Surprisingly, the apparent sizes of the particles present in Mini-B<sub>OX</sub> + SP-A samples,

calculated from the translational diffusion coefficients, consistently come in between the sizes of the particles present in individual protein samples (Figures 6.13, 6.16 and 6.19). For example, the apparent hydrodynamic diameter of Mini-B<sub>OX</sub>/SP-A/LMPC is ~ 8.5 nm, whereas that of Mini-B<sub>OX</sub>/LMPC and SP-A/ LMPC are ~ 6.7 and 10.3 nm, respectively. It should be mentioned that the apparent sizes of the protein/lipid complexes in these larger micelle systems are estimated from the lipid peaks only. As deuterated versions of LMPC and LPMG are not commercially available to date, the signals from the protonated lipids overwhelm the signals from the protein(s), as the lipid-protein ratio is 400 : 1, and hence the protein HN signals are too weak to produce meaningful signal attenuation curves.

It is not clear why, in LMPC and LMPG samples, Mini-B<sub>OX</sub> + SP-A diffuses more rapidly than SP-A alone (Figures 6.13, 6.16 and 6.19). However, my previous studies of Mini-B<sub>OX</sub> alone show that Mini-B<sub>OX</sub> induces either a size decrease, a shape change, or a faster exchange of free and micelle-bound amphiphiles for the larger micelles composed of LMPC or LMPG, which results in a faster diffusion of the Mini-B<sub>OX</sub>/micelle complexes than pure micelles (Chapter 4). Perhaps something similar takes place even when SP-A is present. Also surprising is the observation that the excellent single fits of the signal attenuations curves for Mini-B<sub>OX</sub> + SP-A in LMPC and LMPG indicate a single translational diffusion coefficient, and hence apparently one size, for each system. In comparison with SDS or DPC, large amphiphiles like LMPC and LMPG are much less used in the NMR studies of proteins. Many of the physical properties of these micelles, such as the shape and the size, are not well characterized to date. It is possible that the shape of pure LMPC and LMPG micelles is largely nonspherical and when bound to the protein(s) the shape may further deviate either way. This effect may be more prominent for a small amphipathic peptide like Mini-B and may result in an apparently unusual faster diffusion of the peptide/micelle complexes, even when the much larger SP-A is present. Another possibility is a Mini-B<sub>OX</sub> induced further reduction of SP-A oligomeric states, e.g., from 2~3 trimers to single trimers or even smaller, in LMPC and LMPG systems causing the Mini-B<sub>OX</sub>/SP-A/micelle complexes to diffuse more rapidly than the SP-A/micelle complexes. This may be a very interesting demonstration of Mini-B<sub>OX</sub>-induced rearrangement of not only the lipid structures but also the SP-A structures.

How exactly Mini-B interacts with SP-A is a matter of discussion. Since, in all cases, the chemical shifts of the Mini-B HSQC peaks (or their much weaker traces) remain unchanged, most likely the interactions between the two proteins do not occur directly but are mediated through the micelles. It is plausible that the Mini-B/micelle complexes fuse with the SP-A/micelle complexes but the two proteins remain apart in the final assembly. However, it is also possible that Mini-B directly interacts with SP-A but the complexes representing the directly interacting subpopulation are so large that they are completely absent from the HSQC spectra and hence the corresponding chemical shift changes of the peaks can not be tracked.

Electrostatic interaction between the positively charged Mini-B (net charge +7) and negatively charged SP-A (net charge -4) is most likely at the root of the fusion of the complexes containing the individual proteins. However, since both proteins are initially bound to their own micelles, the charges of lipid/detergent headgroups are expected to greatly influence the fusion process. Thus in the context of zwitterionic micelles, it is reasonable to think that electrostatic interaction between Mini-B and SP-A would be relatively strong, while in anionic micelles, the repulsion between micelles could substantially reduce the interaction between the two proteins. Moreover, as discussed in Chapter 4 (Page 90), Mini-B appears to be more compactly and deeply bound to anionic micelles than zwitterionic micelles. Therefore when within an anionic micelle, perhaps Mini-B does not experience a strong attraction toward SP-A which is bound to another anionic micelle. However, the Brownian motion and random collision in solution may bring instantaneous changes in the overall electrostatic profile of the individual protein complexes and thus a smaller subpopulation of the two proteins may become bound to the same anionic micelle complexes. In contrast, when bound to the zwitterionic micelles, whose own net charge is zero, the oppositely charged Mini-B and SP-A complexes likely experience a much stronger attraction and may easily fuse to form single Mini-B/SP-A/micelle complexes for the entire population, even if the two proteins do not directly bind each other. The apparent relatively superficial positioning of Mini-B in zwitterionic micelles may further enhance the complex formation process.

Comparison of the apparent particle sizes containing Mini-B<sub>OX</sub> and SP-A jointly and individually indicates that, at least in DPC and SDS, the protein-protein complexes are not formed as just one Mini-B<sub>OX</sub> plus one SP-A. Both subpopulations of Mini-B<sub>OX</sub>/SP-A/DPC and the larger subpopulation of Mini-B<sub>OX</sub>/SP-A/SDS are presumably formed by binding multiple subunits of the two proteins in a single complex.

In summary, the degree of interaction between Mini-B and SP-A appears to be dependent on the type of detergent/lipid headgroup. For the model surfactant lipids used in this study, most likely the interaction is not a direct protein-protein interaction, but rather is mediated via the detergent/lipid micelles. While the atomistic understanding of Mini-B/SP-A interaction is not complete, a lipid-dependent interaction between native SP-B and SP-A may have important implications in lung surfactant function.

## *Chapter 7*

# **Modifications to SP-B<sub>8-25</sub> Structure and Lipid Interactions upon Tryptophan Oxidation**

*Note : Peptides used in this study were synthesized and purified by Donna Jackman (Booth lab, Biochemistry, MUN). CD data were acquired and analyzed with help of Prof. David H. Heeley (Heeley lab, Biochemistry, MUN) and Dr. Michael Hayley (Booth lab, Biochemistry, MUN).*

## 7.1 Overview

Acute respiratory distress syndrome (ARDS) and acute lung injury (ALI) can arise from a variety of insults of the lung including oxidative stress caused by an increase in reactive oxygen species (ROS) [199-202]. ROS-induced modifications result in dysfunction of lung surfactant (LS) and can lead to its complete inactivation [202-205]. Several studies have examined the disruptive effects of ROS on both individual LS components, namely lipids and proteins, and overall alterations of surfactant biophysical activity [179, 205-210]. However, the most deleterious effects are observed for ROS-induced modifications of SP-B, which appear to make the most severe contributions to surfactant inactivation [202, 206, 210]. *In vitro* studies have shown that the oxidation of SP-B involves modification of a maximum of three amino acids; the two methionines and the only tryptophan [211]. Analysis of fusogenic, lytic and surface tension reducing activities of SP-B-based peptides demonstrates that Trp9 is critical for optimal interface affinity of SP-B [107, 142]. It is therefore crucial to characterize the changes to the structure and lipid interactions of SP-B caused by the oxidative modification of Trp9 which potentially leads to the loss of protein function.

Tryptophan is an amino acid that typically either contributes to the hydrophobic core of a globular protein or anchors a lipid-associated protein to a polar/apolar interface [212]. From the structure of Mini-B, determined in detergent micelles composed of SDS, the sidechain of Trp9 (W2 in Mini-B) does not appear to contribute to the interhelix hydrophobic contacts and therefore its role is most likely in interacting with the lipids to help anchor Mini-B at the lipid/water interface (Chapter 3 and [156]).

In this part of my research, I have studied the conformations of Wild-Type and Trp-Oxidized SP-B<sub>8-25</sub>, an 18 amino acid peptide that consists of the N-terminal helical segment of SP-B (i.e., the N-terminal half of Mini-B). The objectives were to investigate if the oxidation of Trp9 destroys the helical structure or makes the peptide unable to anchor inside lipids only, or results in both. The structural differences between the two peptide versions were probed in lung lipid mimetic SDS and DPC micelles, in organic solvent HFIP, as well as in water alone, using solution NMR and circular dichroism (CD).

## 7.2 Materials and Methods

### 7.2.1 Peptide Synthesis and Purification

SP-B<sub>8-25</sub> consists of human SP-B amino acids 8 to 25. Two versions of the peptide were synthesized and purified by Donna Jackman (Booth lab, Biochemistry, MUN). The wild-type version [SP-B<sub>8-25</sub> (Wild-Type)] retained the native tryptophan at position 2, which corresponds to position 9 in the natural protein. In the oxidized version [SP-B<sub>8-25</sub> (Trp9Kyn)], tryptophan was replaced by one of its oxidized forms, kynurenine [Figure 7.1]. The amino acid sequences are :

SP-B<sub>8-25</sub> (Wild-Type) : Cys-**Trp**-Leu-Cys-Arg-Ala-Leu-Ile-Lys-Arg-Ile-Gln-Ala-Met-Ile-Pro-Lys-Gly

SP-B<sub>8-25</sub> (Trp9Kyn) : Cys-**Kyn**-Leu-Cys-Arg-Ala-Leu-Ile-Lys-Arg-Ile-Gln-Ala-Met-Ile-Pro-Lys-Gly

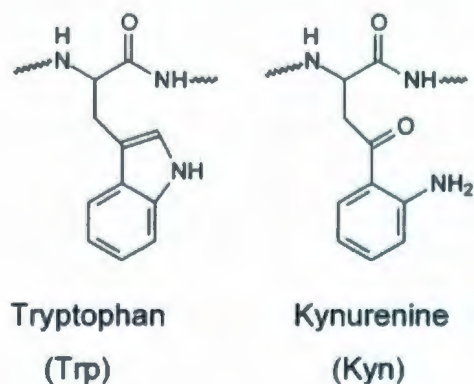


**Figure 7.1** : Chemical structures of tryptophan (Trp) and one of its oxidized forms kynurenine (Kyn).

Both versions of SP-B<sub>8-25</sub> were synthesized in a CS336X peptide synthesizer (C S Bio Co., Menlo Park, CA) following manufacturer's instructions. The peptides were produced by solid phase peptide synthesis method employing O-fluorenylmethyloxycarbonyl (Fmoc) chemistry. All Fmoc amino acids and coupling agents were purchased from C S Bio Co. with the exception of Fmoc kynurenine that was purchased from Advanced ChemTech (Louisville, KY). Organic solvents and other reagents used for the synthesis and purification were high performance liquid chromatography (HPLC) grade or better and purchased from Fisher Scientific (Ottawa, ON) and Aldrich Chemical (St. Louis, MO). The peptides were

synthesized at a 0.2 mmol scale using a single coupling. A prederivatized Rink amide resin was used to assemble the peptides during synthesis. At completion, deprotection and cleavage of the peptides from the resin were carried out with a TFA/Water (95/5 by volume) cleavage cocktail followed by cold precipitation with *tert*-butyl ether. The crude products were then purified by preparative reverse-phase HPLC in a Vydac C-8 column by use of a water/acetonitrile linear gradient with 0.1% trifluoroacetic acid as the ion-pairing agent. The molecular weight of the peptides were confirmed by matrix-assisted laser desorption/ionization - time of flight (MALDI-TOF) mass spectrometry performed at the CREAT Network facility (MUN). Finally, the purified peptides were lyophilized and stored at 4 °C.

### 7.2.2 Sample Preparation

Four samples were prepared for each version of SP-B<sub>8-25</sub>. First a stock buffer solution was prepared in H<sub>2</sub>O/D<sub>2</sub>O (90%/10%) with 0.4 mM DSS and 0.2 mM NaN<sub>3</sub>. The final samples were then prepared by dissolving peptides and other contents in the buffer. For samples in water, 1 mM peptide was dissolved in the buffer. Samples in HFIP also contained 1 mM peptide but the buffer was adjusted to have 40% HFIP (98% deuterated; Cambridge Isotope, Andover, MA) plus 50% H<sub>2</sub>O and 10% D<sub>2</sub>O. For samples in SDS or DPC, 1 mM peptide and 100 mM detergent (98% deuterated; Cambridge Isotope, Andover, MA) were dissolved in the buffer. One mM DTT was also added to all eight samples from a freshly prepared DTT stock solution. The pH of the samples was set to 7.0 by use of NaOH and HCl, without taking the isotope effects into account. Only one sample of each composition was made and the same sample was used for both NMR and CD experiments.

### 7.2.3 NMR Data Collection and Processing

A set of 1D <sup>1</sup>H, 2D <sup>1</sup>H-<sup>1</sup>H TOCSY, 2D <sup>1</sup>H-<sup>1</sup>H NOESY and 2D DOSY experiments was performed for each SP-B<sub>8-25</sub> sample on a Bruker Avance II 14.1 Tesla (600 MHz) spectrometer (Billerica, MA) equipped with z-gradients and an inverse triple resonance TXI

probe. The NMR data were collected and processed using the Bruker Topspin 2.0 software. The pulse length (P1) and the transmitter offset (O1) were optimized for each sample before running the full set of NMR experiments. The 1D  $^1\text{H}$ , 2D  $^1\text{H}$ - $^1\text{H}$  TOCSY and 2D  $^1\text{H}$ - $^1\text{H}$  NOESY spectra were acquired at temperature 37 °C to match the physiological temperature. All these experiments used the water-gate water suppression technique [146]. In 1D  $^1\text{H}$  experiments, data were collected with 32 scans and processed using an exponential apodization function with 1 Hz line broadening. The 2D  $^1\text{H}$ - $^1\text{H}$  TOCSY experiments used a 60 ms mixing time and were run with 80 or 128 scans (indicated in the figure captions). A total of 2048/512 data points were collected in F2/F1 dimensions and the processed spectra had 1024 points in both dimensions. The 2D  $^1\text{H}$ - $^1\text{H}$  NOESY experiments used a 200 ms mixing time and were run with 128 scans. A total of 2048/512 data points were collected in F2/F1 dimensions and the processed spectra had 1024 points in both dimensions. All TOCSY and NOESY spectra were processed using the Qsine apodization function with a sine bell shift of 2. The 2D DOSY experiments were performed using PFG NMR [157]. The pulse sequence used a stimulated echo with bipolar gradient pulses and one spoil gradient [158], followed by a 3-9-19 pulse for water suppression [159]. The DOSY spectra were acquired for SDS samples at 37 °C. However, for DPC samples, the DOSY spectra were acquired at 25 °C to minimize the effect of thermal convection. The diffusion time was kept constant at 100 ms. The gradient pulse length was optimized for each sample and set between 4 and 6 ms. The maximum amplitude of the gradient strength was 35 G/cm and the  $^1\text{H}$  signals were attenuated in 32 steps. The translational diffusion coefficient was determined from the slope of the signal attenuation curve plotted using Eq. 2.17. The hydrodynamic diameter was calculated using the Stokes-Einstein equation [Eq. 2.20]. The viscosity of pure water was used for the viscosity of solution in the calculation and the values were  $8.91 \times 10^{-4}$  kg/m.s at 25 °C (298 K) and  $6.92 \times 10^{-4}$  kg/m.s at 37 °C (310 K).

## 7.2.4 CD Data Collection and Processing

The CD spectra, in the far-ultraviolet (far-UV) region (from 260 to 190 nm), were recorded for all eight SP-B<sub>8-25</sub> samples using a Jasco-810 spectropolarimeter (Easton, MD). The CD data were acquired at 37 °C using a quartz cuvette with 0.1 mm path length. The NMR samples were transferred to the cuvette without making any changes in the sample conditions. The temperature was controlled by a CTC-345 circulating water bath. The scanning speed of the instrument was set at 100 nm/min with normal sensitivity. Five accumulations were collected for each sample in 0.1 nm steps. The Molar ellipticity [ $\theta$ ] was calculated using the equation suggested by Heeley *et al.* [213],

$$[\theta] = \theta_{\text{obs}}/(10LC), \quad (7.1)$$

where  $\theta_{\text{obs}}$  is the observed ellipticity,  $L$  is the path length of the cell (0.01 cm) and  $C$  is the number of amino acids multiplied by the molar concentration of the peptide (0.018 M). The secondary structural content was calculated from the molar ellipticity data using a computer program following the method of Yang *et al.* [214]. Although the computer program calculated the structure percentages as  $\alpha$ -helix,  $\beta$ -sheet,  $\beta$ -turn and random coil, SP-B<sub>8-25</sub> is unlikely to contain a  $\beta$ -sheet which requires two or more strands hydrogen-bonded together. It is more plausible that the  $\beta$ -sheet content indicated by the computer program actually represents an extended conformation and hence is reported as such in the CD results sections.

## 7.3 Results

### 7.3.1 NMR Spectra of SP-B<sub>8-25</sub> in SDS

Figure 7.2 shows the 1D <sup>1</sup>H spectra of SP-B<sub>8-25</sub> (Wild-Type) and SP-B<sub>8-25</sub> (Trp9Kyn) in SDS micelles, a mimetic for the lung surfactant phospholipids with anionic headgroups. The signals seen for SP-B<sub>8-25</sub> (Wild-Type) in the enlarged 6-9 ppm region, corresponding to the backbone and sidechain amide protons (HNs), are broad and possibly overlapped in some cases but well dispersed. This level of line-broadening and overlap is not unexpected as the peptide is bound to a detergent micelle. The spectral dispersion and intensity of backbone HN signals indicate SP-B<sub>8-25</sub> (Wild-Type) is structured in SDS. The 6-9 ppm region of SP-B<sub>8-25</sub> (Trp9Kyn), on the other hand, looks substantially different. There are fewer signals present and the signals are less intense and less resolved, although the 7-7.5 ppm region has some peaks with greater intensity likely from sidechain HN signals. Overall, the 1D <sup>1</sup>H spectrum of SP-B<sub>8-25</sub> (Trp9Kyn) is atypical for a structured peptide.

Similarly, the HA-HN regions of 2D <sup>1</sup>H-<sup>1</sup>H TOCSY and 2D <sup>1</sup>H-<sup>1</sup>H NOESY spectra (data not shown) show fewer cross peaks for SP-B<sub>8-25</sub> (Trp9Kyn) than for SP-B<sub>8-25</sub> (Wild-Type). The overall appearance of these spectra is consistent with Wild-Type peptide being well structured and Trp9Kyn peptide exhibiting far less structure. This interpretation is further supported by the examination of HN-HN regions of 2D <sup>1</sup>H-<sup>1</sup>H NOESY spectra of SP-B<sub>8-25</sub> (Wild-Type) and SP-B<sub>8-25</sub> (Trp9Kyn) in SDS (Figure 7.3). About 9 backbone HN-HN cross peaks and some sidechain HN-HN cross peaks are seen for SP-B<sub>8-25</sub> (Wild-Type). The ~ 9 intense backbone HN-HN correlations result from short HN-HN distances and indicate an  $\alpha$ -helical folding of the peptide for about 10 amino acids (i.e., about 3 helical turns). However, for SP-B<sub>8-25</sub> (Trp9Kyn), only ~ 2 backbone HN-HN cross peaks are seen. This indicates that SP-B<sub>8-25</sub> (Wild-Type) contains a helical region comprised of only about 3 amino acids (i.e., approximately 1 helical turn).

Next, diffusion NMR spectroscopy is used to indicate differences in the peptide/micelle complex sizes. The 2D DOSY spectra of SP-B<sub>8-25</sub> (Wild-Type) and SP-B<sub>8-25</sub> (Trp9Kyn) in SDS (Figure 7.4) display <sup>1</sup>H signals resulted from translational diffusion. The

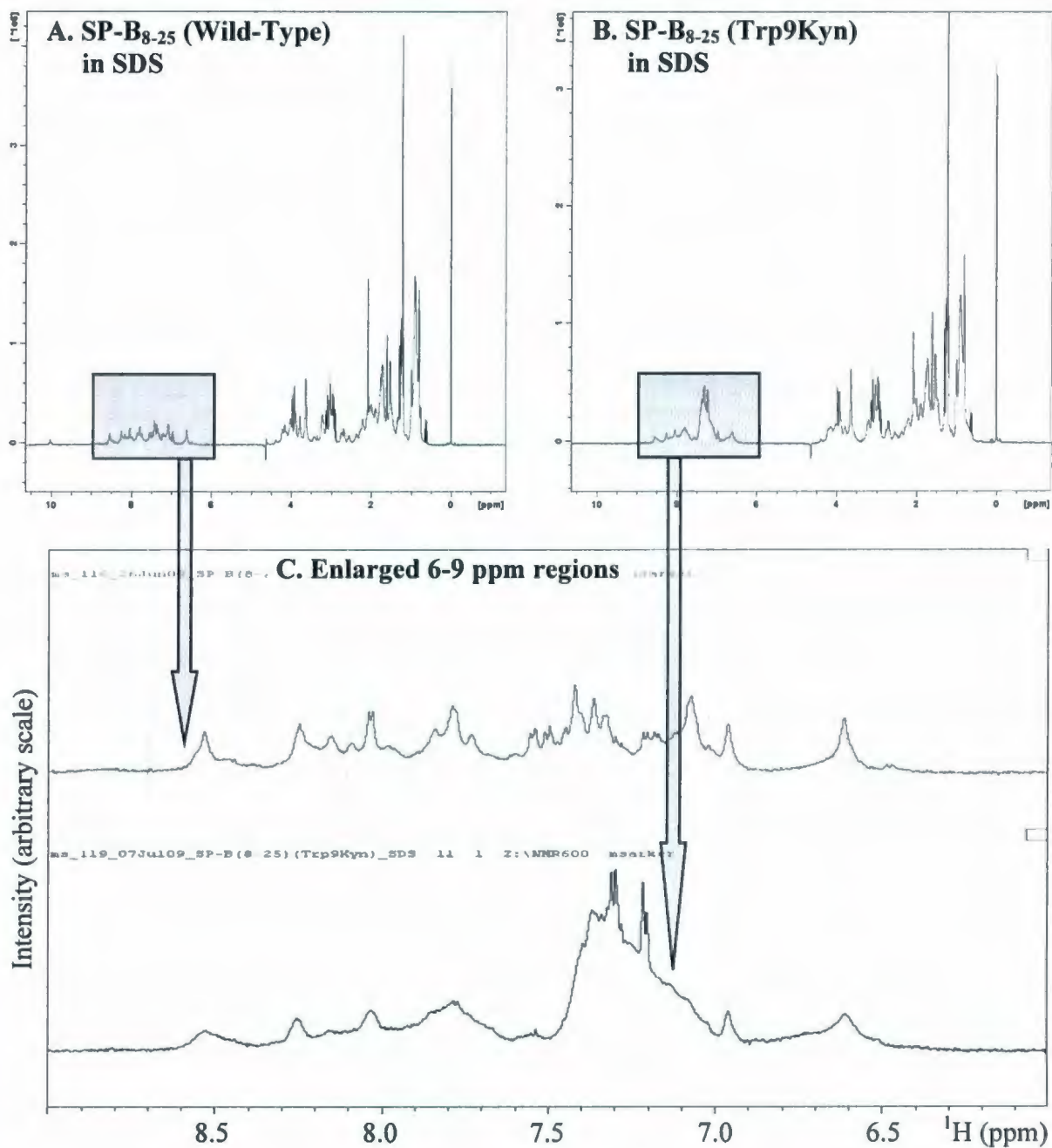


**Figure 7.2** : 1D <sup>1</sup>H spectra of (A) 1 mM SP-B<sub>8-25</sub> (Wild-Type) and (B) 1 mM SP-B<sub>8-25</sub> (Trp9Kyn) in 100 mM SDS at pH 7.0 and temperature 37 °C, acquired using 32 scans. The 6-9 ppm regions of both spectra are enlarged and shown in the bottom panel (C).

translational diffusion coefficients are represented by the slopes of the signal attenuation curves, obtained from the underlying 1D  $^1\text{H}$  experiments, for the two sharpest SDS peaks at 0.80 ppm (corresponding to  $\text{CH}_3$ ) and 1.22 ppm (corresponding to  $(\text{CH}_2)_{3-11}$ ), as well as the SP-B<sub>8-25</sub> HN regions (6-9 ppm). The observed diffusion coefficients, along with the hydrodynamic diameters calculated using the Stokes-Einstein equation, are reported in the table of Figure 7.4. The diameters are 2.82, 2.85 and 2.71 nm, respectively, for SP-B<sub>8-25</sub> (Wild-Type)/SDS complex and 3.93, 3.77 and 3.45 nm, respectively, for SP-B<sub>8-25</sub> (Trp9Kyn)/SDS complex. Therefore, the micelle complex containing SP-B<sub>8-25</sub> (Trp9Kyn) appears substantially larger than the micelle complex containing SP-B<sub>8-25</sub> (Wild-Type).

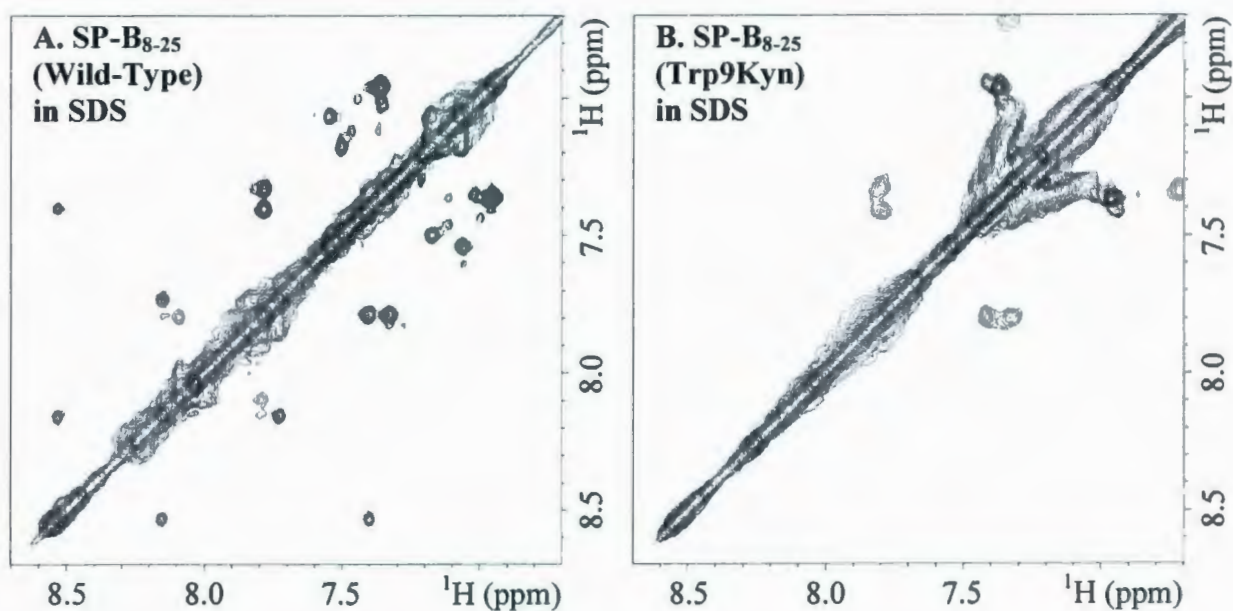


**Figure 7.3** : HN-HN regions of 2D  $^1\text{H}$ - $^1\text{H}$  NOESY spectra of (A) 1 mM SP-B<sub>8-25</sub> (Wild-Type) and (B) 1 mM SP-B<sub>8-25</sub> (Trp9Kyn) in 100 mM SDS at pH 7.0 and temperature 37 °C, acquired using 128 scans and 200 ms mixing time. The base contour level, level increment and number of levels are the same for both spectra.

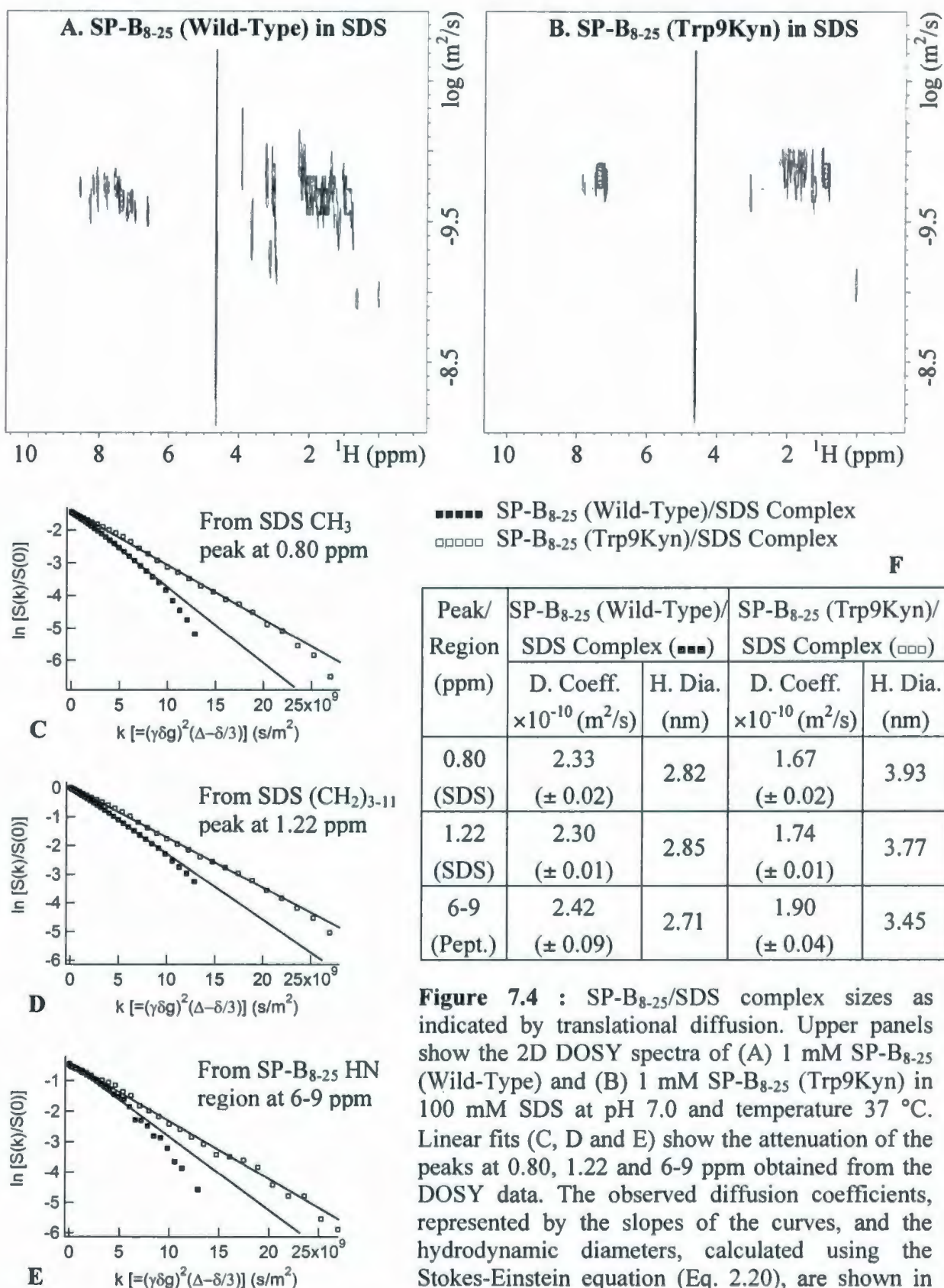
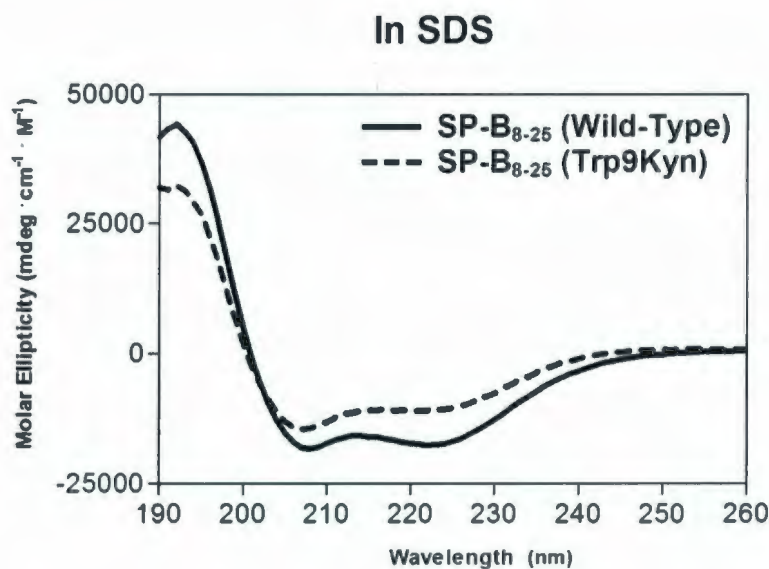


**Figure 7.4** : SP-B<sub>8-25</sub>/SDS complex sizes as indicated by translational diffusion. Upper panels show the 2D DOSY spectra of (A) 1 mM SP-B<sub>8-25</sub> (Wild-Type) and (B) 1 mM SP-B<sub>8-25</sub> (Trp9Kyn) in 100 mM SDS at pH 7.0 and temperature 37 °C. Linear fits (C, D and E) show the attenuation of the peaks at 0.80, 1.22 and 6-9 ppm obtained from the DOSY data. The observed diffusion coefficients, represented by the slopes of the curves, and the hydrodynamic diameters, calculated using the Stokes-Einstein equation (Eq. 2.20), are shown in the table (F).

### 7.3.2 CD Spectra of SP-B<sub>8-25</sub> in SDS

CD spectroscopy provides an alternate measure of the secondary structural content of both versions of the peptide to complement the NMR data. Figure 7.5 shows the CD spectra of SP-B<sub>8-25</sub> (Wild-Type) and SP-B<sub>8-25</sub> (Trp9Kyn) in SDS at pH 7.0 and temperature 37 °C. It is observed that more than half of SP-B<sub>8-25</sub> (Wild-Type) is helical (~ 52%), with the remainder in random coil (~ 18%) and extended (~ 30%) conformation. However, the features for SP-B<sub>8-25</sub> (Trp9Kyn) are substantially different, with reduction of helical content to about one-fourth (~ 27%) and a considerable increase in random coil (36%) along with some increase in extended (~ 37%) conformation.



Secondary Structure (%) in SDS			
Peptide	$\alpha$ -helix	Extended	Random
SP-B <sub>8-25</sub> (Wild-Type)	52	30	18
SP-B <sub>8-25</sub> (Trp9Kyn)	27	37	36

**Figure 7.5** : Far-UV CD spectra of 1 mM SP-B<sub>8-25</sub> (Wild-Type) and 1 mM SP-B<sub>8-25</sub> (Trp9Kyn) in 100 mM SDS at pH 7.0 and temperature 37 °C, acquired using 5 accumulations and a 0.1 mm light path. The molar ellipticity is calculated from the observed ellipticity following the method described in Ref. [213]. The secondary structural contents are calculated from the molar ellipticities following the method described in Ref. [214].

### 7.3.3 NMR Spectra of SP-B<sub>8-25</sub> in DPC

The results for both Wild-Type and Trp9Kyn versions of SP-B<sub>8-25</sub> in DPC micelles, a mimetic for lung surfactant phospholipids with zwitterionic headgroups, were similar to those obtained in the anionic SDS micelles. Figure 7.6 shows the 1D <sup>1</sup>H spectra of SP-B<sub>8-25</sub> in DPC. For SP-B<sub>8-25</sub> (Wild-Type), well-dispersed signals from the backbone and sidechain amide protons (HNs) are seen in the enlarged 6-9 ppm region. The 6-9 ppm region of SP-B<sub>8-25</sub> (Trp9Kyn), on the other hand, looks substantially different. In spite of the signals in 7.1-7.5 ppm region with greater intensity, likely from sidechain HNs, there are much fewer and less intense backbone HN signals present. Again, the dispersion and intensity of backbone HN signals indicate SP-B<sub>8-25</sub> (Wild-Type) is structured but that of SP-B<sub>8-25</sub> (Trp9Kyn) are atypical for a structured peptide.

This interpretation is supported further from the analysis of HN-HN regions of 2D <sup>1</sup>H-<sup>1</sup>H NOESY spectra of SP-B<sub>8-25</sub> (Wild-Type) and SP-B<sub>8-25</sub> (Trp9Kyn) in DPC (Figure 7.7). About eight backbone HN-HN cross peaks and some sidechain HN-HN cross peaks are seen for SP-B<sub>8-25</sub> (Wild-Type). The intense backbone HN-HN correlations indicate an  $\alpha$ -helical folding of the peptide for about 9 amino acids (i.e., 2.5 helical turns). However, for SP-B<sub>8-25</sub> (Trp9Kyn), only two backbone HN-HN cross peaks are seen. This indicates that SP-B<sub>8-25</sub> (Wild-Type) contains a helical region comprised of only about 3 amino acids (i.e. approximately 1 helical turn). The HA-HN regions of 2D <sup>1</sup>H-<sup>1</sup>H TOCSY and 2D <sup>1</sup>H-<sup>1</sup>H NOESY spectra [data not shown] also indicate less structuring of SP-B<sub>8-25</sub> (Trp9Kyn) when compared to SP-B<sub>8-25</sub> (Wild-Type).

Similarly to the study in SDS, differences in the complex sizes are also obtained for the peptides in DPC micelles using diffusion NMR spectroscopy (Figure 7.8). Again, three hydrodynamic diameters are calculated from the translational diffusion coefficients obtained for the signal attenuation of the two sharpest DPC peaks at 0.79 ppm (corresponding to CH<sub>3</sub>) and 1.20 ppm (corresponding to (CH<sub>2</sub>)<sub>3-11</sub>) as well as the SP-B<sub>8-25</sub> HN region (6-9 ppm). The diameters are 4.57, 4.51 and 4.19 nm, respectively, for SP-B<sub>8-25</sub> (Wild-Type)/DPC complex and 3.83, 3.74 and 3.73 nm, respectively, for SP-B<sub>8-25</sub> (Trp9Kyn)/DPC complex. The sizes of

the DPC micelle complexes, containing two different peptide versions, are not as dissimilar as for SDS complexes. Also, in contrast to SDS, the hydrodynamic diameter of the SP-B<sub>8-25</sub> (Trp9Kyn)/DPC complex is smaller than the SP-B<sub>8-25</sub> (Wild-Type)/DPC complex.

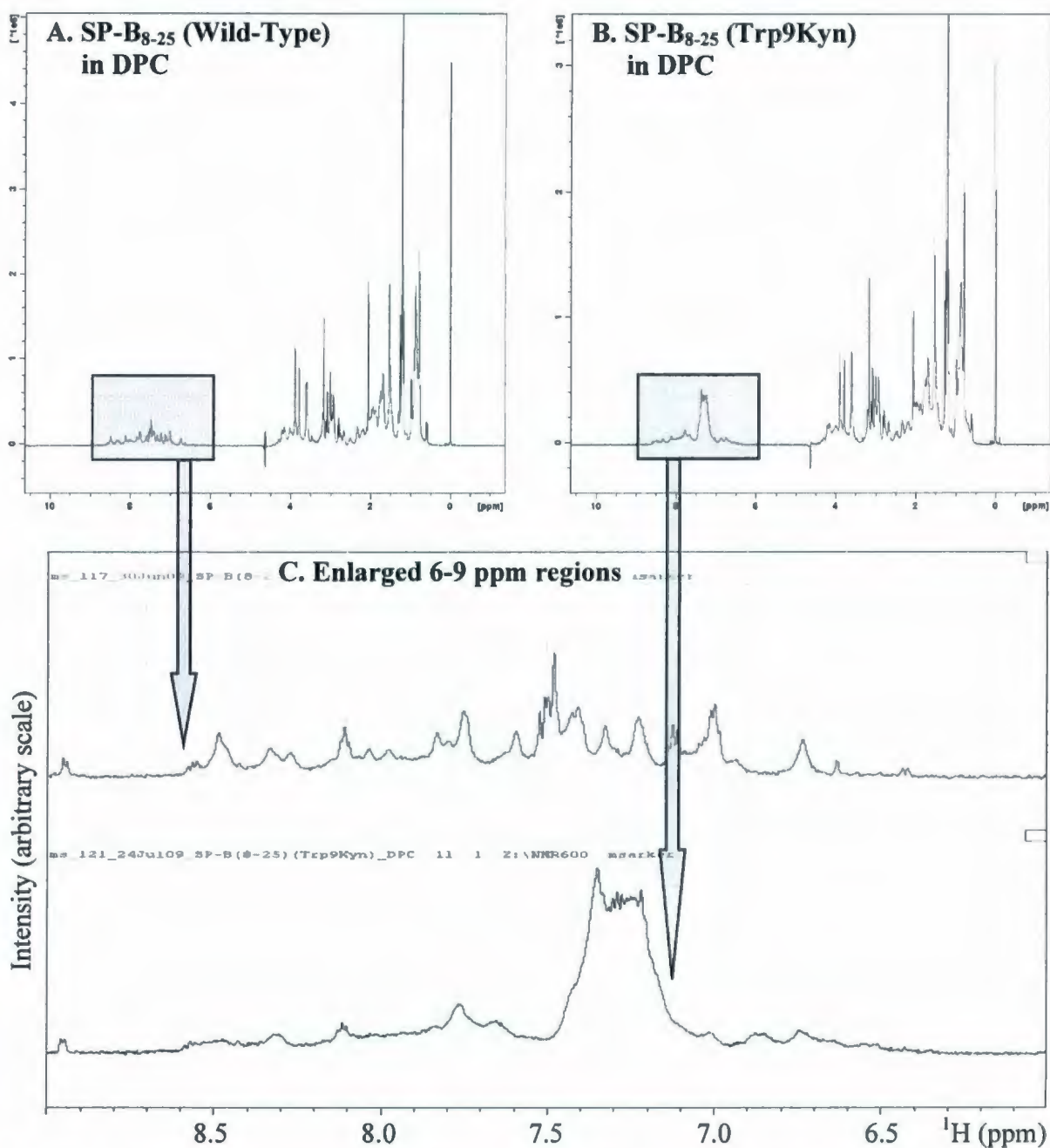


**Figure 7.6** : 1D <sup>1</sup>H spectra of (A) 1 mM SP-B<sub>8-25</sub> (Wild-Type) and (B) 1 mM SP-B<sub>8-25</sub> (Trp9Kyn) in 100 mM DPC at pH 7.0 and temperature 37 °C, acquired using 32 scans. The 6-9 ppm regions of both spectra are enlarged and shown in the bottom panel (C).

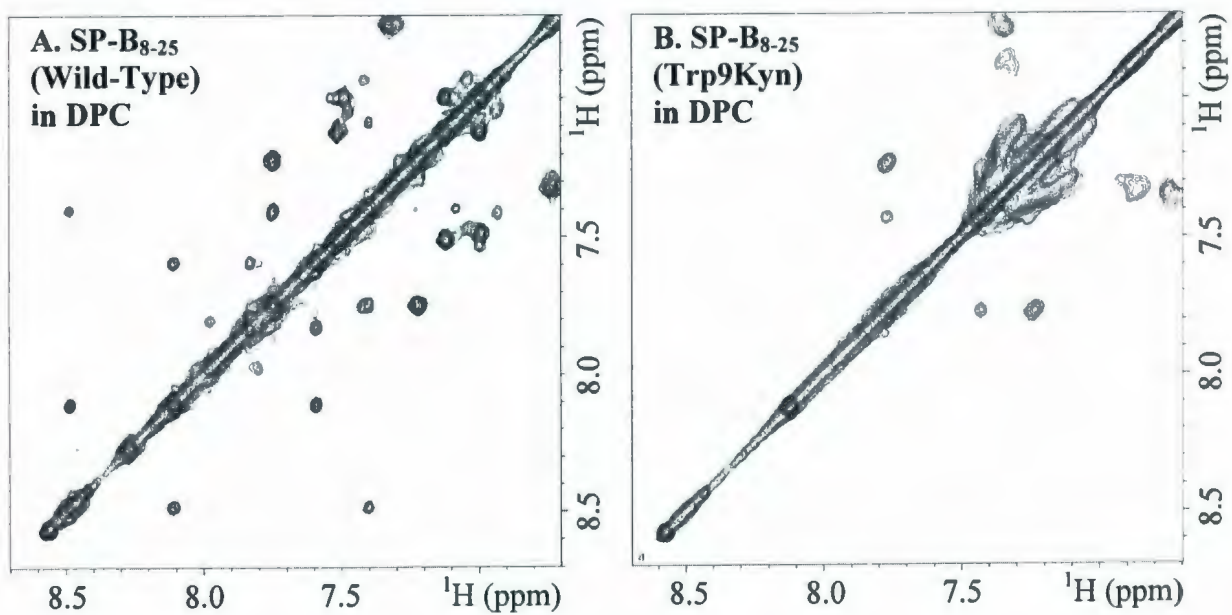


**Figure 7.7 :** HN-HN regions of (A) 2D  $^1\text{H}$ - $^1\text{H}$  NOESY spectra of 1 mM SP-B<sub>8-25</sub> (Wild-Type) and (B) 1 mM SP-B<sub>8-25</sub> (Trp9Kyn) in 100 mM DPC at pH 7.0 and temperature 37 °C, acquired using 128 scans and 200 ms mixing time. The base contour level, level increment and number of levels are the same for both spectra.

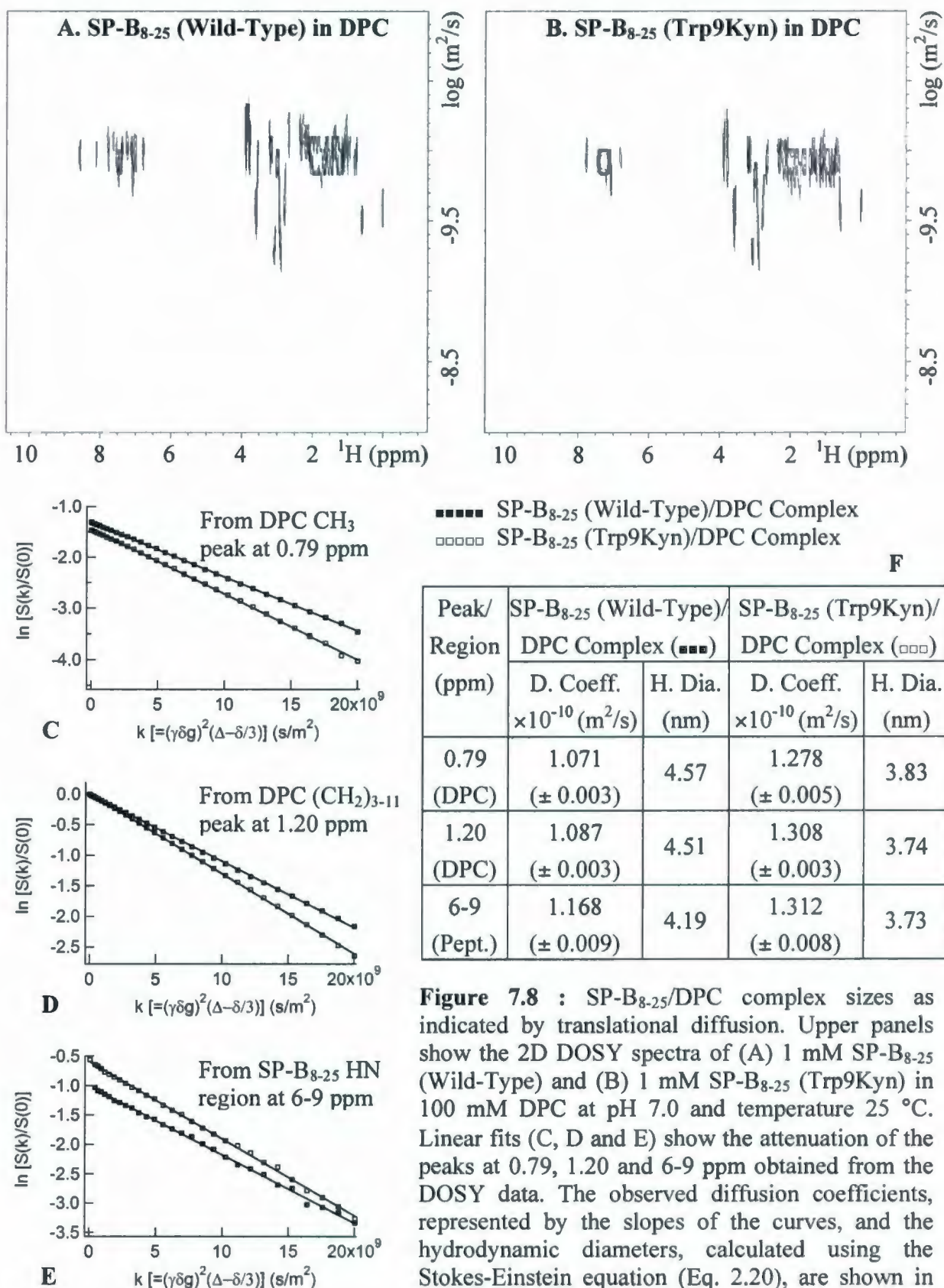
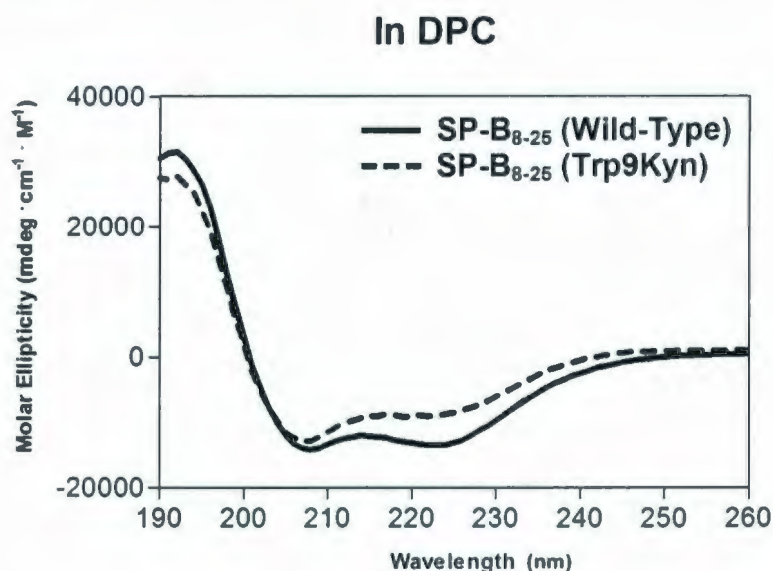


**Figure 7.8** : SP-B<sub>8-25</sub>/DPC complex sizes as indicated by translational diffusion. Upper panels show the 2D DOSY spectra of (A) 1 mM SP-B<sub>8-25</sub> (Wild-Type) and (B) 1 mM SP-B<sub>8-25</sub> (Trp9Kyn) in 100 mM DPC at pH 7.0 and temperature 25 °C. Linear fits (C, D and E) show the attenuation of the peaks at 0.79, 1.20 and 6-9 ppm obtained from the DOSY data. The observed diffusion coefficients, represented by the slopes of the curves, and the hydrodynamic diameters, calculated using the Stokes-Einstein equation (Eq. 2.20), are shown in the table (F).

### 7.3.4 CD Spectra of SP-B<sub>8-25</sub> in DPC

To complement the NMR data and obtain an alternate measure of the secondary structural content, CD spectroscopy was also performed for both versions of SP-B<sub>8-25</sub> in DPC at pH 7.0 and temperature 37 °C (Figure 7.9). The CD data indicate that about two-fifths of SP-B<sub>8-25</sub> (Wild-Type) is helical (~ 38%) with the remainder in random coil (~ 26%) and extended (~ 36%) conformation. However, the features for SP-B<sub>8-25</sub> (Trp9Kyn) are substantially different, with the reduction of helical content to about one-fifth (~ 20%) and a considerable increase in random coil (~ 39%) along with some increase in extended (~ 41%) conformation. Differences in the structures of the two peptide versions in DPC are similar to that observed in SDS.



Secondary Structure (%) in DPC			
Peptide	$\alpha$ -helix	Extended	Random
SP-B <sub>8-25</sub> (Wild-Type)	38	36	26
SP-B <sub>8-25</sub> (Trp9Kyn)	20	41	39

**Figure 7.9** : Far-UV CD spectra of 1 mM SP-B<sub>8-25</sub> (Wild-Type) and 1 mM SP-B<sub>8-25</sub> (Trp9Kyn) in 100 mM DPC at pH 7.0 and temperature 37 °C, acquired using 5 accumulations and a 0.1 mm light path. The molar ellipticity is calculated from the observed ellipticity following the method described in Ref. [213]. The secondary structural contents are calculated from the molar ellipticities following the method described in Ref. [214].

### 7.3.5 NMR Spectra of SP-B<sub>8-25</sub> in HFIP (40%)

In contrast to the micelle systems, 40% HFIP in aqueous solution provides a secondary structure-inducing environment, but without a polar/apolar interface, which can be important in inducing native-like folding of amphipathic helices. For SP-B<sub>8-25</sub> in 40% HFIP (plus 50% H<sub>2</sub>O and 10% D<sub>2</sub>O), likewise in the SDS and DPC micelle systems, the 1D <sup>1</sup>H, 2D <sup>1</sup>H-<sup>1</sup>H TOCSY and 2D <sup>1</sup>H-<sup>1</sup>H NOESY spectra indicate SP-B<sub>8-25</sub> (Wild-Type) is much more structured than SP-B<sub>8-25</sub> (Trp9Kyn) (Figures 7.10 and 7.11). The numbers of intense cross peaks in the HN-HN regions of 2D <sup>1</sup>H-<sup>1</sup>H NOESY spectra indicate an  $\alpha$ -helix at least 8 amino acid long for Wild-Type peptide, but only 3 amino acid long for Trp9Kyn peptide.

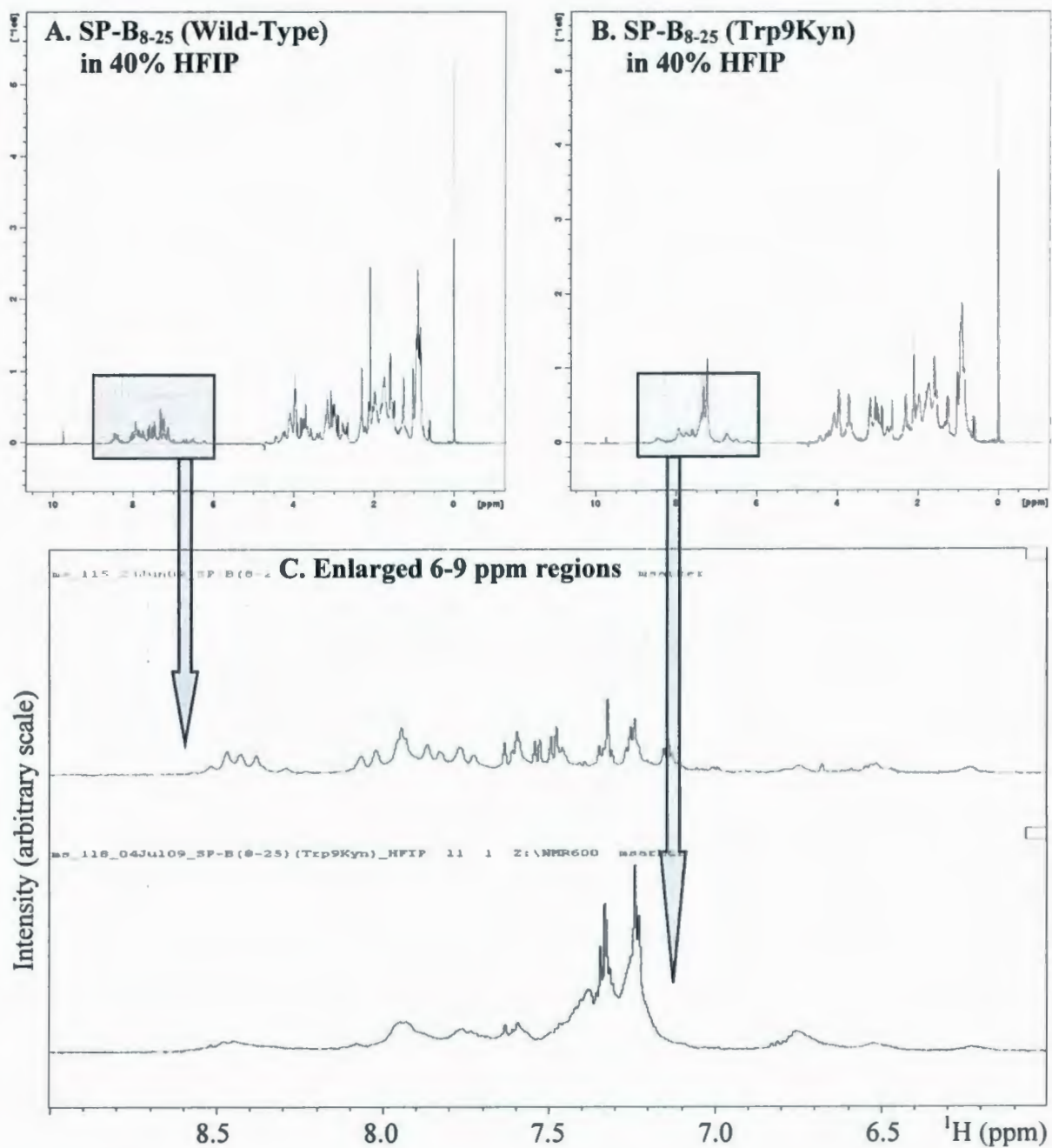


**Figure 7.10** : 1D  $^1\text{H}$  spectra of (A) 1 mM SP-B<sub>8-25</sub> (Wild-Type) and (B) 1 mM SP-B<sub>8-25</sub> (Trp9Kyn) in 40% HFIP (plus 50% H<sub>2</sub>O and 10% D<sub>2</sub>O) at pH 7.0 and temperature 37 °C, acquired using 32 scans. The 6-9 ppm regions of both spectra are enlarged and shown in the bottom panel (C).

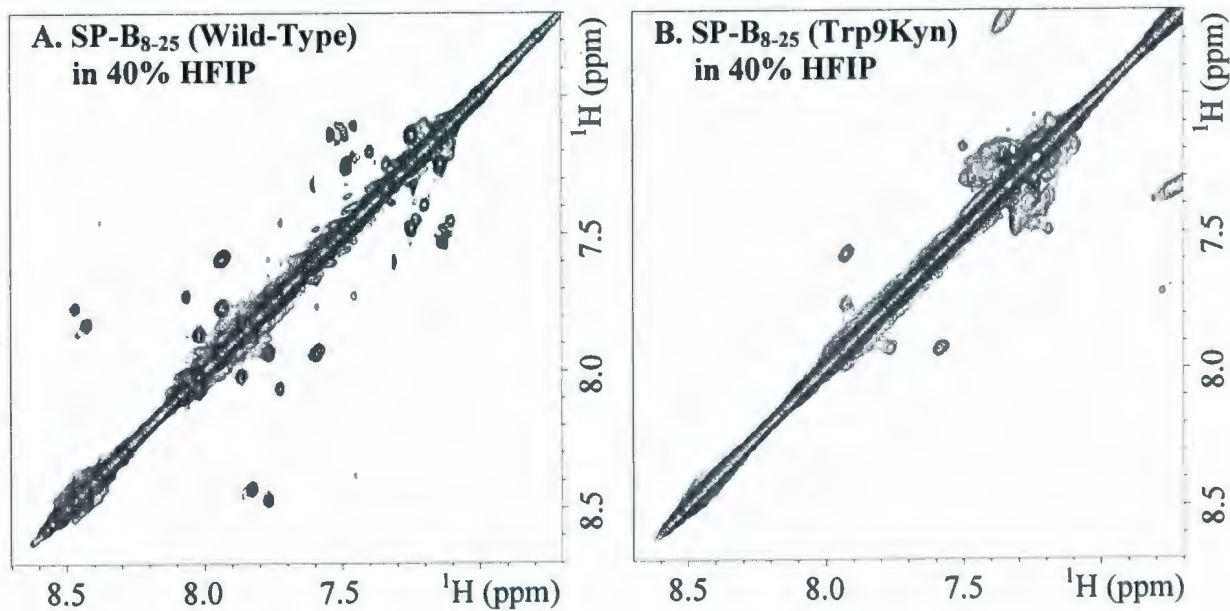
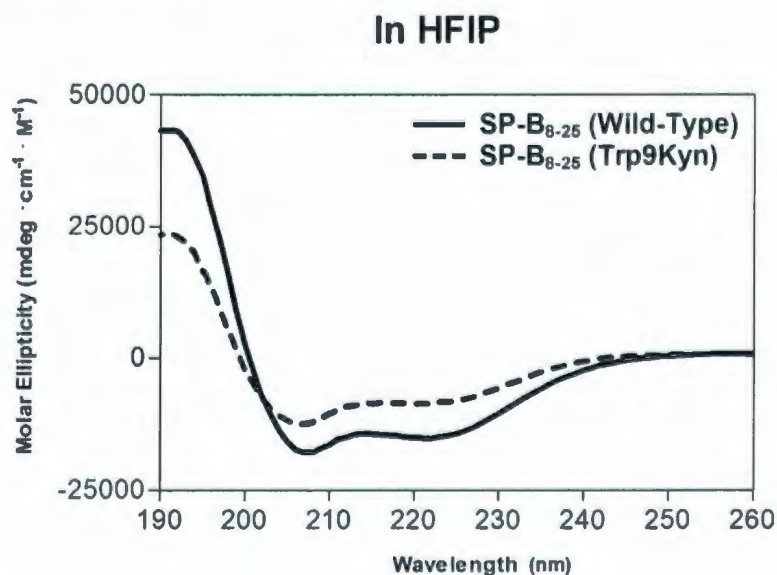


**Figure 7.11** : HN-HN regions of (A) 2D  $^1\text{H}$ - $^1\text{H}$  NOESY spectra of 1 mM SP-B<sub>8-25</sub> (Wild-Type) and (B) 1 mM SP-B<sub>8-25</sub> (Trp9Kyn) in 40% HFIP (plus 50% H<sub>2</sub>O and 10% D<sub>2</sub>O) at pH 7.0 and temperature 37 °C, acquired using 128 scans and 200 ms mixing time. The base contour level, level increment and number of levels are the same for both spectra.

### 7.3.6 CD Spectra of SP-B<sub>8-25</sub> in HFIP (40%)

The interpretation of NMR spectra in 40% HFIP is further supported by the CD spectroscopy of SP-B<sub>8-25</sub> performed at pH 7.0 and temperature 37 °C (Figure 7.12). The secondary structure calculation shows that about two-fifths of SP-B<sub>8-25</sub> (Wild-Type) is helical (~ 41%) with the remainder in random coil (~ 29%) and extended (~ 30%) conformation. However, for SP-B<sub>8-25</sub> (Trp9Kyn), the helical content is reduced to about one-fifth (~ 19%) and the random coil is increased substantially (~ 44%) along with some increase of the extended (~ 37%) conformation. These features are similar to that of the micelle-bound Wild-Type and Trp9Kyn peptides.



<b>Secondary Structure (%) in HFIP</b>			
Peptide	$\alpha$ -helix	Extended	Random
SP-B <sub>8-25</sub> (Wild-Type)	41	30	29
SP-B <sub>8-25</sub> (Trp9Kyn)	19	37	44

**Figure 7.12 :** Far-UV CD spectra of 1 mM SP-B<sub>8-25</sub> (Wild-Type) and 1 mM SP-B<sub>8-25</sub> (Trp9Kyn) in 40% HFIP (plus 50% H<sub>2</sub>O and 10% D<sub>2</sub>O) at pH 7.0 and temperature 37 °C, acquired using 5 accumulations and a 0.1 mm light path. The molar ellipticity is calculated from the observed ellipticity following the method described in Ref. [213]. The secondary structural contents are calculated from the molar ellipticities following the method described in Ref. [214].

### 7.3.7 NMR Spectra of SP-B<sub>8-25</sub> in Water

Unlike in surfactant phospholipid mimetic SDS and DPC micelles, or in structure-inducing organic solvent HFIP, the 1D <sup>1</sup>H, 2D <sup>1</sup>H-<sup>1</sup>H TOCSY and 2D <sup>1</sup>H-<sup>1</sup>H NOESY spectra indicate both version of SP-B<sub>8-25</sub> to be largely unstructured in water alone (90% H<sub>2</sub>O plus 10% D<sub>2</sub>O) (Figures 7.13 and 7.14). There are no cross peaks seen representing backbone HN-HN correlations in the corresponding regions of 2D <sup>1</sup>H-<sup>1</sup>H NOESY. The cross-peaks seen for the Wild-Type are likely from the sidechain HNs. Overall features of the spectra suggest either aggregation or absence of an  $\alpha$ -helical structure for both SP-B<sub>8-25</sub> (Wild-Type) and SP-B<sub>8-25</sub> (Trp9Kyn) in water alone.

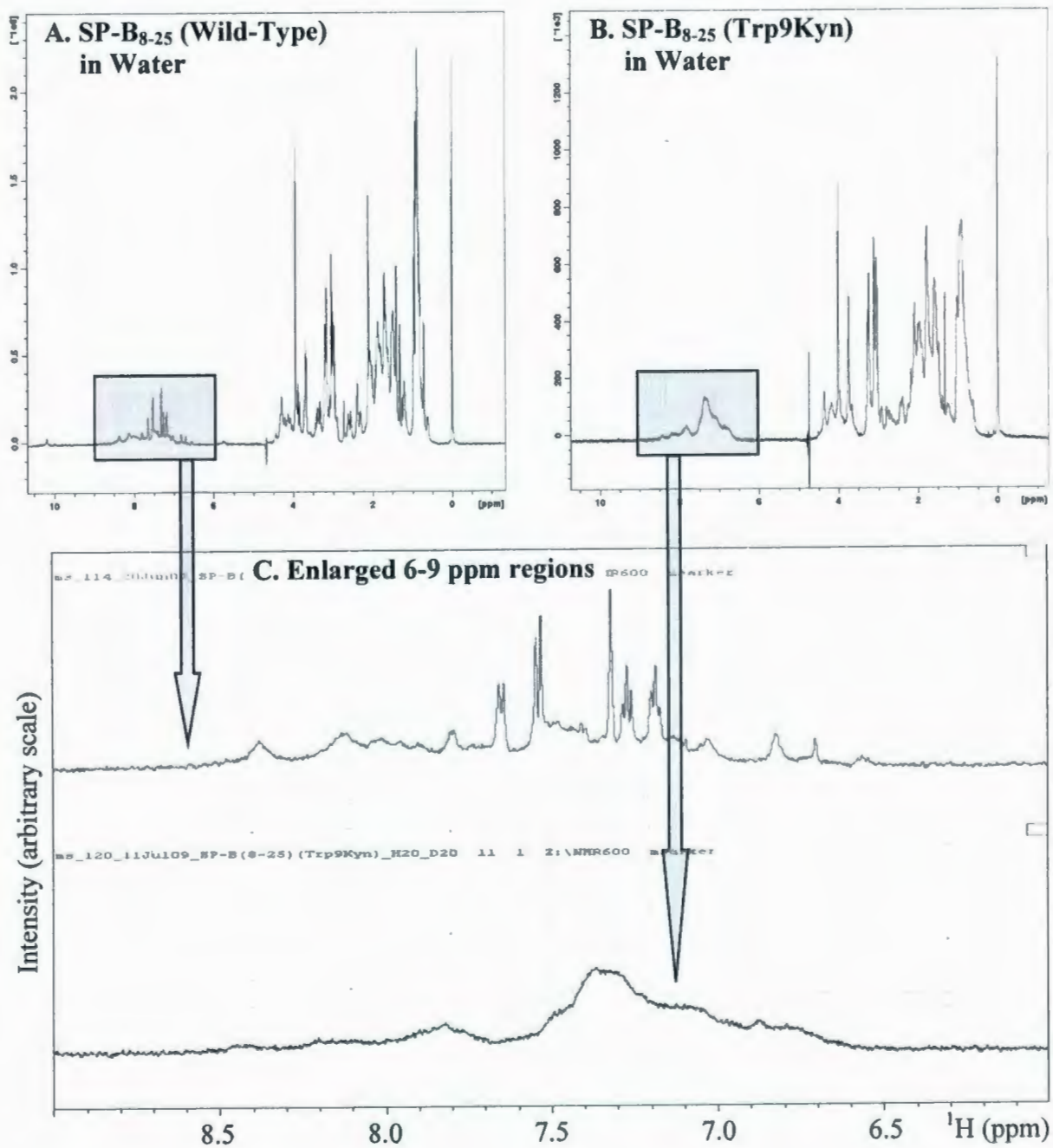


**Figure 7.13 :** 1D <sup>1</sup>H spectra of (A) 1 mM SP-B<sub>8-25</sub> (Wild-Type) and (B) 1 mM SP-B<sub>8-25</sub> (Trp9Kyn) in water (90% H<sub>2</sub>O and 10% D<sub>2</sub>O) at pH 7.0 and temperature 37 °C, acquired using 32 scans. The 6-9 ppm regions of both spectra are enlarged and shown in the bottom panel (C).

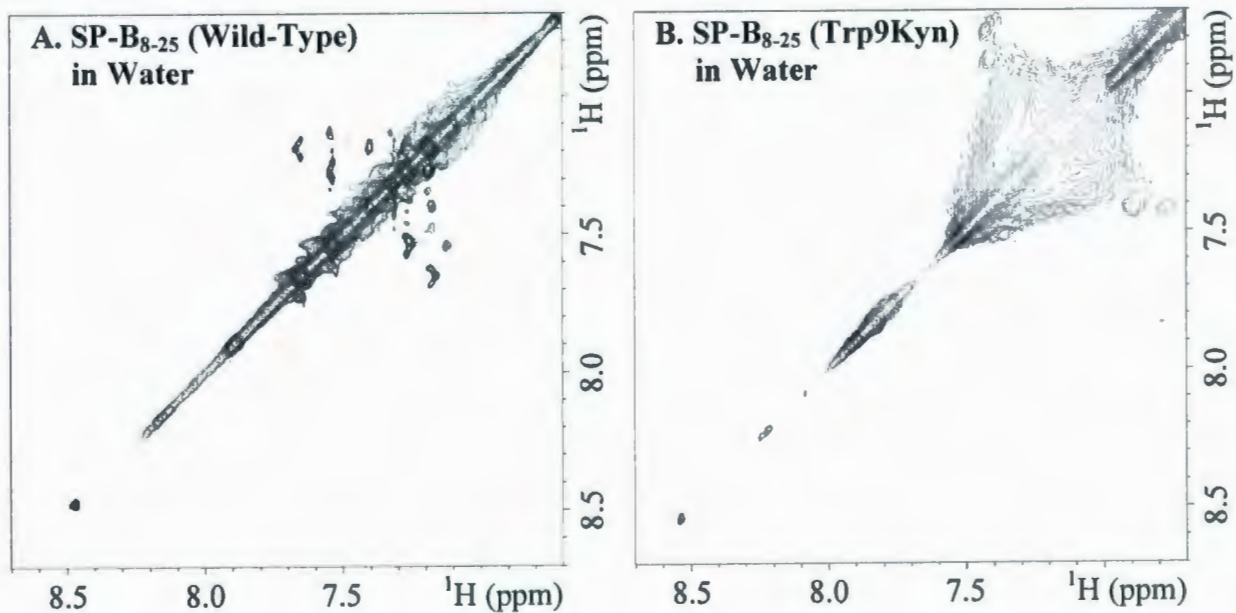
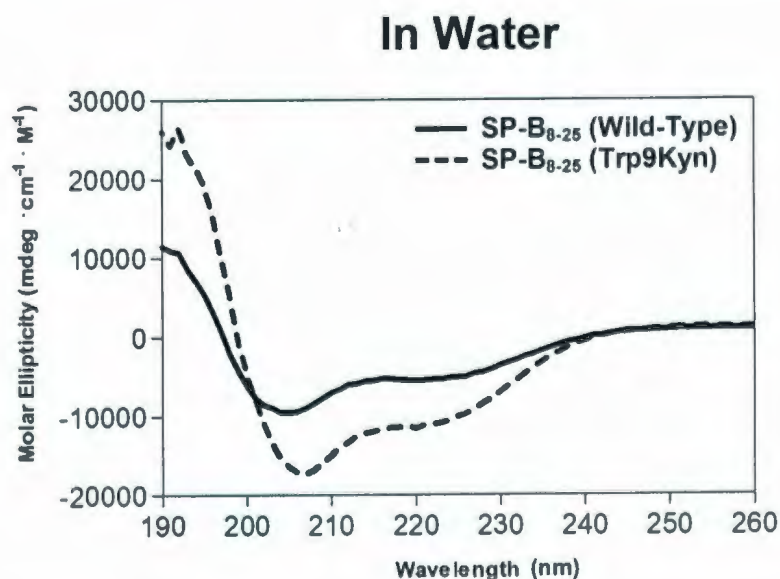


**Figure 7.14** : HN-HN regions of (A) 2D  $^1\text{H}$ - $^1\text{H}$  NOESY spectra of 1 mM SP-B<sub>8-25</sub> (Wild-Type) and (B) 1 mM SP-B<sub>8-25</sub> (Trp9Kyn) in water (90% H<sub>2</sub>O and 10% D<sub>2</sub>O) at pH 7.0 and temperature 37 °C, acquired using 128 scans and 200 ms mixing time. The base contour level, level increment and number of levels are the same for both spectra.

### 7.3.8 CD Spectra of SP-B<sub>8-25</sub> in Water

Complementing the NMR observation, the CD spectra of SP-B<sub>8-25</sub> in water at pH 7.0 and temperature 37 °C indicates no considerable  $\alpha$ -helical secondary structure for the Wild-Type peptide (only ~ 8%) but some helical structure for the Trp9Kyn peptide (~ 33%) (Figure 7.15). The remainders, representing the majority portions of both peptides, are in random coil and extended conformation. These features are substantially different from what are observed for SP-B<sub>8-25</sub> either in detergent micelles or in organic solvent.



Secondary Structure (%) in Water			
Peptide	$\alpha$ -helix	Extended	Random
SP-B <sub>8-25</sub> (Wild-Type)	8	40	52
SP-B <sub>8-25</sub> (Trp9Kyn)	33	24	43

**Figure 7.15** : Far-UV CD spectra of 1 mM SP-B<sub>8-25</sub> (Wild-Type) and 1 mM SP-B<sub>8-25</sub> (Trp9Kyn) in water (90% H<sub>2</sub>O and 10% D<sub>2</sub>O) at pH 7.0 and temperature 37 °C, acquired using 5 accumulations and a 0.1 mm light path. The molar ellipticity is calculated from the observed ellipticity following the method described in Ref. [213]. The secondary structural contents are calculated from the molar ellipticities following the method described in Ref. [214].

## 7.4 Discussion

Inactivation of lung surfactant occurs in potentially fatal respiratory disorders like ARDS [33]. There are multiple biophysical and biochemical alterations of lung surfactant associated with ARDS [215]. However, several studies have confirmed that patients with ARDS show clear evidence of increased oxidative damage to surfactant lipids as well as proteins [179, 205-210]. Oxidative modification of SP-B, an essential component of lung surfactant, appears to be a major contributor to surfactant inactivation [202, 206, 210]. The modifications likely occur through the changes in the chemical structures of the two methionines and the only tryptophan of SP-B [211]. While oxidation of both residues hamper surfactant biophysical activity [211], modification of Trp9 likely produces the most deleterious effect as this amino acid is vital for SP-B function [107, 142].

SP-B<sub>8-25</sub>, an 18 amino acid fragment comprising the N-terminal helical region of SP-B, has been shown to exhibit *in vitro* surface activity [103, 107] as well as to retain partial biological function when included in artificial surfactants [101]. This peptide carries a net charge of +4 (Arg12, Lys16, Arg17 and Lys24) at neutral pH as compared to the net charge of +7 for the full-length SP-B monomer. It also includes the only tryptophan (Trp9) present in the SP-B sequence. The function of SP-B is thought to relate to its positive charges and amphipathic helical structure [83, 106], and thus the retention of these structural features by the fragment SP-B<sub>8-25</sub> is presumably what makes this peptide partially functional.

The structure of SP-B<sub>11-25</sub> in methanol was studied by Kurtz *et al.* and found to be  $\alpha$ -helical for amino acids 13 to 21 [76]. However, this fragment did not include the functionally important Trp9. In my previous structural studies of Mini-B (Chapter 3 and M.Sc. Thesis), a larger peptide comprised of SP-B<sub>8-25</sub> joined to SP-B<sub>63-78</sub> was found to consist of two helices. The N-terminal helix comprises amino acids 10 to 21 in SDS [156] and 11 to 22 in HFIP [110]. The experiments performed for this chapter indicated that SP-B<sub>8-25</sub> (Wild-Type), which corresponds to the N-terminal half of Mini-B, also took on an  $\alpha$ -helical conformation in SDS and DPC micelles, as well as in HFIP, as indicated by NMR

and CD spectra. It is therefore reasonable to consider the corresponding segment of Mini-B (i.e., amino acids 1-18) as a reference structure for SP-B<sub>8-25</sub> (Wild-Type) (Figure 7.16). However, as the other half of Mini-B is missing and interhelix interactions between the two halves were observed for Mini-B in SDS, small differences in the helical structure of SP-B<sub>8-25</sub> (Wild-Type) would not be unexpected.

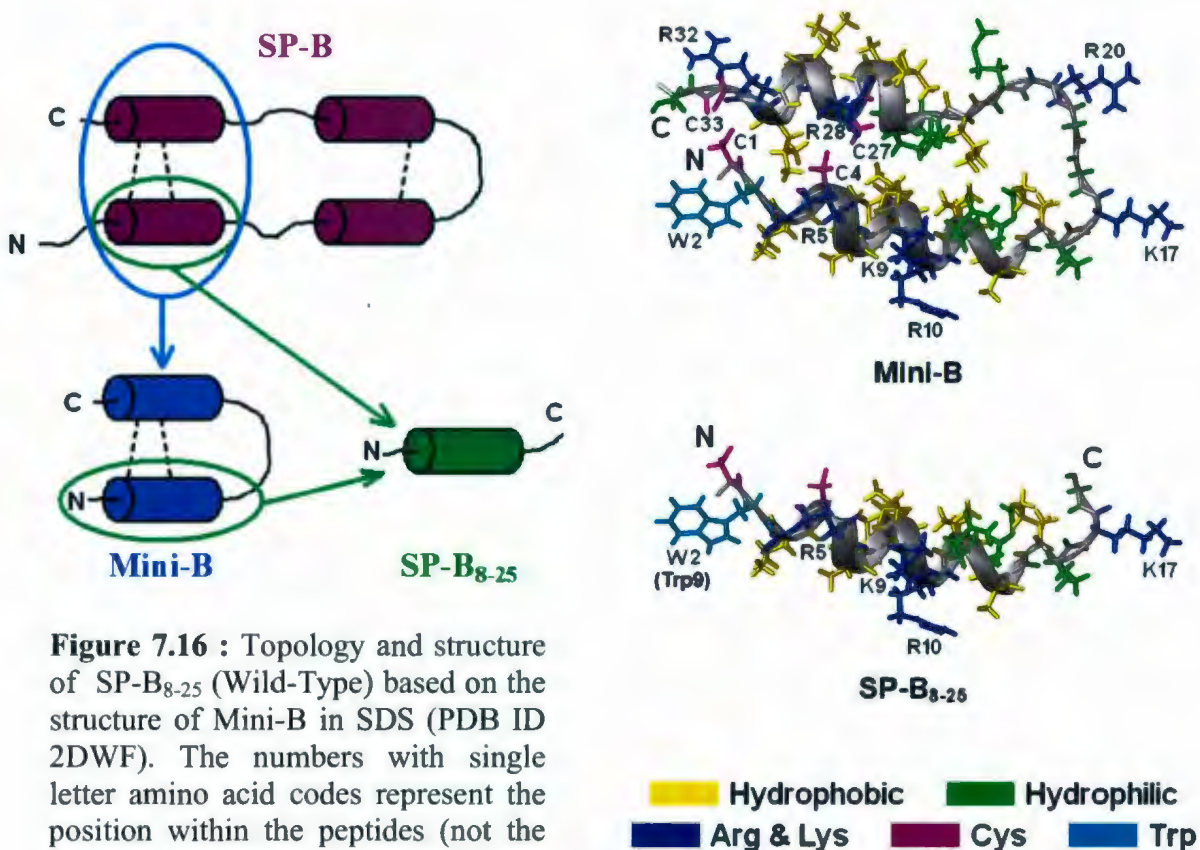


**Figure 7.16 :** Topology and structure of SP-B<sub>8-25</sub> (Wild-Type) based on the structure of Mini-B in SDS (PDB ID 2DWF). The numbers with single letter amino acid codes represent the position within the peptides (not the full-length protein).

The objective of this part of my research was to directly probe the changes in the structure of SP-B<sub>8-25</sub> due to the oxidation of Trp9. Therefore, conformational features of both Wild-Type and Trp-oxidized SP-B<sub>8-25</sub> were studied under four different conditions; in SDS micelles that contain anionic headgroups, in DPC micelles that contain zwitterionic headgroups, in organic solvent HFIP (40%), and in water alone. The choices of detergents were made based on the requirements for mimicking the natural lung surfactant lipid environments. SDS is a mimetic for PGs, the anionic surfactant phospholipids that SP-B is

thought to preferentially bind in surface monolayers of surfactant films [83, 84]. DPC, on the other hand, is a mimetic for DPPC, the most abundant zwitterionic phospholipid generally considered to be of paramount importance in attaining low surface tension in the alveolar air-water interface [24]. HFIP is not a lung lipid mimetic but an organic solvent that induces the helical secondary structure of a peptide. Hence the features of SP-B<sub>8-25</sub> in HFIP would reveal any generic changes in the helical structure due to tryptophan oxidation, even in the absence of an interfacial environment. Although the lipid-associated SP-B and its fragments are unlikely to be properly folded without any intervention of lipids or organic solvents, the features of SP-B<sub>8-25</sub> have still been studied in water alone to unveil any differences owing to the tryptophan oxidation under this condition.

The NMR data reveal that SP-B<sub>8-25</sub> (Wild-Type) adopts an  $\alpha$ -helical conformation comprising 9 to 10 amino acids in both SDS and DPC micelles, as well as in HFIP. The rest of the peptide appears to be random and extended. These structural features are also well supported by the CD data. This structure of SP-B<sub>8-25</sub> (Wild-Type) is not very different from the corresponding segment of Mini-B in SDS, in which the N-terminal helix comprises 12 amino acids. However, the peptide seems to be unstructured and possibly aggregated in water alone. This is not unexpected since about half of SP-B<sub>8-25</sub> (Wild-Type) amino acids are hydrophobic and, therefore, the peptide is presumably insoluble in water.

Assuming it takes on a similar structure alone to its structure within Mini-B, the SP-B<sub>8-25</sub> (Wild-Type) helix is apparently strikingly amphipathic with three positively charged amino acids (Arg12, Lys16 and Arg17) clustering in one face and four non-polar amino acids (Leu10, Leu14, Ile15 and Ile18) grouping at the opposite face. Also, in light of the Mini-B structure, Trp9 is unlikely to be a part of the helix, rather it is located in between the charged and hydrophobic faces. This positioning is very suitable for its sidechain to interact with lipids and anchor the peptide at the lipid/water interface. It is conceivable that the amphipathic helical structure, along with the tryptophan anchor, provide the basis for the partial biological activity of SP-B<sub>8-25</sub> (Wild-Type). Any disruption in the helix could alter the amphipathic nature of the peptide and thus potentially lead to its inactivation.

Indeed, the helical structure of SP-B<sub>8-25</sub> (Wild-Type) is drastically disrupted when tryptophan is replaced by one of its oxidized forms, kynurenine. The helical stretch of two and a half turns (or more) is reduced to less than one turn in both SDS and DPC micelles, as well as in HFIP. This confirms that the oxidative modification of tryptophan makes the SP-B<sub>8-25</sub> helix largely unstructured regardless of whether it is within a micelle environment or in an organic solvent. It is likely that the N-terminus of the helix nearby Trp9 is the most affected part and the oxidation leads to an unwinding of the helix at this end. However, besides this disruption of the helix, there may be additional modifications to the SP-B<sub>8-25</sub> structure due to the replacement of tryptophan by kynurenine.

Trp9 is likely involved in anchoring SP-B<sub>8-25</sub> to the micelles. The oxidation reduces the hydrophobicity of its sidechain and presumably leads to a failure in the anchoring. As a result, the hydrophobic face of the helix near Trp9 may get more exposed to the surrounding water molecules which possibly triggers the partial unfolding. It is reasonable to consider the mechanism of partial unfolding of the SP-B<sub>8-25</sub> (Trp9Kyn) helix to be similar in both SDS and DPC micelles. However, in organic solvent condition too, in the absence of any micelles, the folded SP-B<sub>8-25</sub> (Wild-Type) exhibits similar disruption of the helix owing to the tryptophan replacement by kynurenine. This clearly indicates that tryptophan, not only plays an anchoring role inside the lipids but also contributes to the integrity of the peptide structure, and its oxidation brings about a generic change in the helical structure of SP-B<sub>8-25</sub>. It appears likely that the oxidation causes substantial changes to the quadruple moment and/or the ring current of tryptophan sidechain thus triggering the peptide unstructuring.

The DOSY data correlate with the surface area of the peptide/micelle complex and indicate that SP-B<sub>8-25</sub> (Trp9Kyn)/SDS complex is substantially larger than SP-B<sub>8-25</sub> (Wild-Type)/SDS complex (hydrodynamic diameters are ~ 3.7 and ~ 2.8 nm, respectively). The structure of SP-B<sub>8-25</sub> (Wild-Type), with an intact amphipathic helix, is suitable to strongly interact with both negatively charged headgroups and hydrophobic acyl chains of the SDS micelle. These interactions apparently lead to a compact complex of the peptide and the micelle. Within the complex, SP-B<sub>8-25</sub> (Wild-Type) is likely positioned with its helix parallel

to the surface of the micelle, with its hydrophobic face in contact with the acyl chains of SDS and its positively charged face in contact with the negatively charged headgroups of SDS and surrounding water molecules. When the tryptophan is replaced by kynurenine, a large portion of the helix appears to be unstructured. This likely disrupts the clustering of the positive charges and makes them spread over the peptide surface. The drastic reduction caused thereby to the peptide's amphipathicity would substantially affect the interactions between the peptide and the micelle. Therefore, presumably SP-B<sub>8-25</sub> (Trp9Kyn) is not as compactly bound to the SDS micelle as SP-B<sub>8-25</sub> (Wild-Type) would be. The SDS micelle may be stretched to accommodate the partially unstructured SP-B<sub>8-25</sub> (Trp9Kyn) within it, which would explain the increased size of the complex when tryptophan is replaced by kynurenine.

The DOSY data of SP-B<sub>8-25</sub> in zwitterionic DPC micelles represent a somewhat different scenario. The sizes of the complexes with two versions of the peptide are not as different as in SDS. Also, the difference is opposite to the SDS results, i.e., the SP-B<sub>8-25</sub> (Trp9Kyn)/DPC complex is smaller than the SP-B<sub>8-25</sub> (Wild-Type)/DPC complex (hydrodynamic diameters are ~ 3.7 and ~ 4.5 nm, respectively). There are three plausible explanations for this. First, as DPC headgroups contain both positive and negative charges, the electrostatic component of the peptide/micelle interactions may not be as strong as it is in SDS. As a result, SP-B<sub>8-25</sub> (Wild-Type) is probably not as compactly bound to the DPC micelle as it is with the SDS micelle. When tryptophan is replaced by kynurenine, the helix is disrupted but the overall electrostatic and hydrophobic interactions between the peptide and the DPC micelle do not change much and hence the sizes of the complexes may not be drastically different. Second, the position of the SP-B<sub>8-25</sub> (Wild-Type) in the DPC micelle may not be as deep inside the micelle as it is in the SDS micelle, again owing to the difference in the electrostatic part of the peptide/micelle interactions. Therefore, the disruption in the helix of SP-B<sub>8-25</sub> (Trp9Kyn) may not bring a substantial change in the surface area of the DPC micelle within which the peptide positioning is relatively shallow. This hypothesis is favorably supported by the observation that SP-B<sub>63-78</sub>, the C-terminal half of Mini-B with a similar degree of amphipathicity (due to 3 clustered positive charges), takes a deeper position inside anionic phospholipids-containing bilayers (mimicked by SDS in this

study) than purely zwitterionic bilayers (mimicked by DPC in this study) [162]. Third, because of the loss of amphiphilicity, SP-B<sub>8-25</sub> (Trp9Kyn) may not be able to bind as many DPC molecules in the complex as SP-B<sub>8-25</sub> (Wild-Type) can. Hence, the size of the micelle complex containing the Trp-oxidized peptide is smaller than the complex containing the Wild-Type peptide.

In water alone, contrary to the observations in micelles and organic solvent, the helical content of SP-B<sub>8-25</sub> is increased from 8% to 33% with the replacement of tryptophan by kynurenine as revealed by the CD spectra. However, this is not surprising since kynurenine is less hydrophobic than tryptophan because of the broken indole ring and exposed O and NH<sub>2</sub> groups. Hence the oxidation of tryptophan may partially reduce the insolubility of the peptide in water and induce some helical folding in SP-B<sub>8-25</sub> (Trp9Kyn). However, SP-B<sub>8-25</sub> (Trp9Kyn) is still not so soluble that the backbone HA-HN correlations in the TOCSY or HN-HN correlations in the NOESY can be observed. Thus the partial helical folding does not change much the likely aggregation of the peptide in water alone.

In summary, the findings from this part of my work reveal a substantial disruption in the helical structure of SP-B<sub>8-25</sub> induced by the oxidative modification of tryptophan. This disruption is generic and likely perturbs the amphipathic profile of the peptide. Therefore, tryptophan plays a crucial role in the proper helical folding and lipid interactions of SP-B<sub>8-25</sub> and presumably of the full-length SP-B.

The oxidative modification of tryptophan is a major source of lung surfactant dysfunction as it inactivates an essential component SP-B [202, 206, 210]. This is likely a leading factor in conditions like ARDS. This study indicates, in addition to preventing the protein from anchoring properly to the phospholipids, the oxidation causes a loss of helical structure and amphipathicity of the N-terminus of SP-B. These changes likely drastically affect the interactions between the native protein and surfactant phospholipids thus contributing to the lung surfactant dysfunction.

## *Chapter 8*

# **Conformation of Maxi-B<sub>CT</sub>, the C-Terminal Half of SP-B**

*Note : Maxi-B<sub>CT</sub> was synthesized and purified by Prof. Alan J. Waring and his group (Waring lab, Medicine, UCLA). CD data were acquired and analyzed with help of Prof. David H. Heeley (Heeley lab, Biochemistry, MUN) and Dr. Michael Hayley (Booth lab, Biochemistry, MUN).*

## 8.1 Overview

Despite many efforts, to my knowledge, no lab has yet succeeded in producing recombinant SP-B in the amounts needed for structural studies. Thus, our collaborator Prof. Alan Waring (Medicine, UCLA) has undertaken the challenging task of producing a near-complete version of SP-B, termed Maxi-B, by chemical synthesis. Maxi-B is based on SP-B amino acids 8 to 78. It contains all the helical regions of the SP-B predicted from the sequence alignment with known Saposin proteins and retains the three native-like disulfide bonds (Figure 8.1). Therefore, Maxi-B would be expected to provide significant structural information on full-length SP-B. However, initial attempts to synthesize Maxi-B did not succeed. A new synthesis strategy was planned afterwards which involves first synthesizing the N- and C-terminal halves of Maxi-B separately. Each of these fragments contains two predicted helices (one full and the other near-full) of SP-B. The attempt to synthesize the C-terminal peptide, Maxi-B<sub>CT</sub>, in the Waring lab was indeed successful.

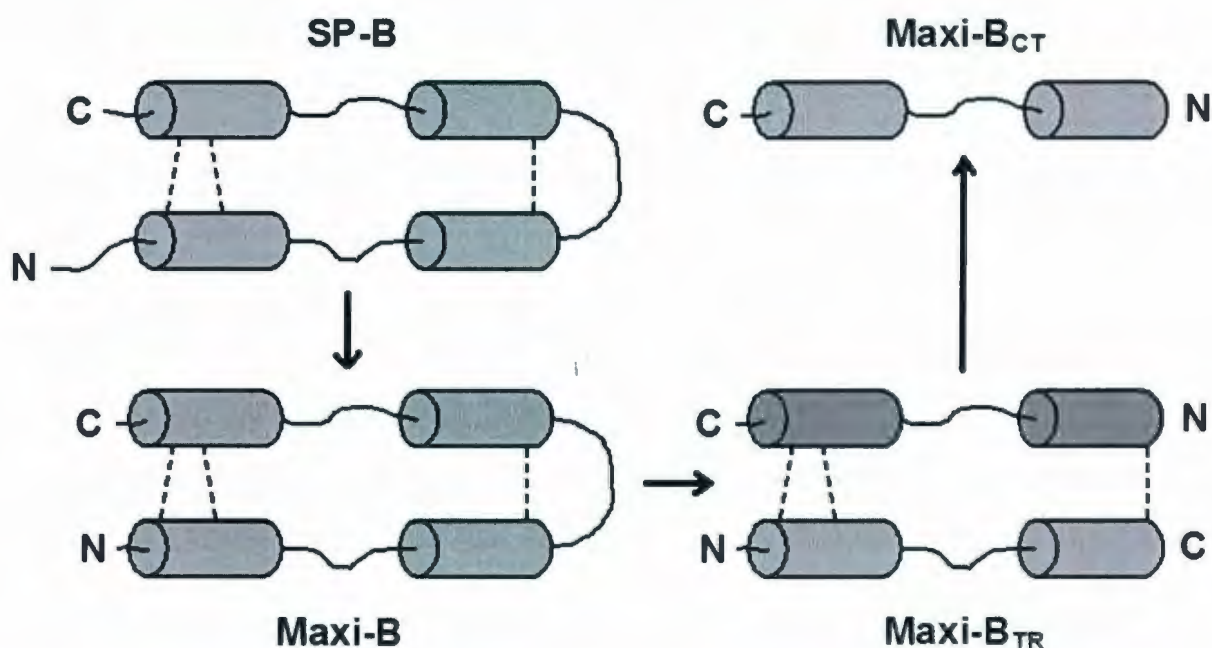


**Figure 8.1 :** Topology of SP-B, Maxi-B, truncated Maxi-B (Maxi-B<sub>TR</sub>) and Maxi-B<sub>CT</sub>, based on known Saposin protein structures. Maxi-B is a proposed synthetic protein based on amino acids 8 to 78 of full-length SP-B. The predicted helical regions are shown as cylinders. The disulfide bonds are shown as dashed lines.

As a step towards the determination of the structure of full-length SP-B, the conformational features of Maxi-B<sub>CT</sub> in organic solvent HFIP and in SDS micelles were studied by solution NMR and CD.

## 8.2 Materials and Methods

### 8.2.1 Peptide Synthesis and Purification

Maxi-B<sub>CT</sub> is a 33 amino acid synthetic peptide based on human SP-B amino acids 46 to 78 with two mutations C48S and E51A (numbers refer to SP-B sequence positions). The two mutations were originally planned for full Maxi-B and have been retained in Maxi-B<sub>CT</sub>. The mutation C48S was proposed to avoid the intermolecular disulfide bond that makes the native SP-B a homodimer. The other mutation E51A was proposed in order to prevent the formation of any intermolecular salt bridge. The primary structure of Maxi-B<sub>CT</sub> is shown below with gray shading on the mutated amino acids :

Cys-Gln-Ser-Leu-Ala-Ala-Arg-Tyr-Ser-Val-Ile-Leu-Leu-Asp-Thr-Leu-Leu-  
Gly-Arg-Met-Leu-Pro-Gln-Leu-Val-Cys-Arg-Leu-Val-Leu-Arg-Cys-Ser

The peptide was produced by the Waring lab using solid-phase chemical synthesis via O-fluorenylmethyloxycarbonyl (Fmoc) chemistry. Fmoc amino acids and coupling agents were purchased from AnaSpec (Fremont, CA). Organic solvents and other reagents used for the synthesis and purification were HPLC grade or better and purchased from Fisher Scientific (Ottawa, ON) and Aldrich Chemical (St. Louis, MO). The peptide was synthesized at a 0.25 mmol scale in an ABI 431A peptide synthesizer configured for FastMoc double-coupling cycles of all residues to optimize yield [143]. A prederivatized N-Fmoc-O-*tert*-butylserine HMP resin (AnaSpec) was used to assemble the peptide during synthesis. Deprotection and cleavage of the peptide from the resin were carried out using a TFA/thioanisole/EDTA/phenol/water mixture (10/0.5/0.25/0.5/0.5 by volume) followed by cold precipitation with *tert*-butylether. The sidechains of the two cysteines in the sequence,

C71 and C77, were kept protected by *tert*-butyl groups to prevent any formation of inter/intra-molecular disulfide bonds. The crude product was purified by preparative reverse-phase HPLC in a Vydac C-18 column using a water/acetonitrile linear gradient with 0.1% trifluoroacetic acid as the ion-pairing agent. The molecular weight of the peptide was confirmed by fast atom bombardment or MALDI-TOF mass spectrometry. The purity of the final product was determined by analytical HPLC and found to be > 95%. The purified peptide was lyophilized and stored at 4 °C.

### 8.2.2 Sample Preparation

First, a stock buffer solution was prepared in H<sub>2</sub>O/D<sub>2</sub>O (90%/10%) with 0.4 mM DSS and 0.2 mM NaN<sub>3</sub>. The final samples were then prepared by dissolving peptide and other contents in the buffer. The sample of Maxi-B<sub>CT</sub> in HFIP contained 1 mM peptide in a buffer adjusted to have 40% HFIP (98% deuterated; Cambridge Isotope, Andover, MA) plus 50% H<sub>2</sub>O and 10% D<sub>2</sub>O. For the sample of Maxi-B<sub>CT</sub> in SDS, 1 mM peptide and 100 mM detergent (98% deuterated; Cambridge Isotope, Andover, MA) were dissolved in the buffer. The pH of the samples was set to 5.0 by use of NaOH and HCl without taking the isotope effects into account. This pH was chosen in order to obtain the NMR spectra in a region where the amide proton/deuteron exchange rate is relatively slow. Only one sample of each composition was prepared and the same sample was used for both NMR and CD experiments.

### 8.2.3 NMR Data Collection and Processing

A set of 1D <sup>1</sup>H, 2D <sup>1</sup>H-<sup>1</sup>H TOCSY, 2D <sup>1</sup>H-<sup>1</sup>H NOESY experiments was performed for each Maxi-B<sub>CT</sub> sample on a Bruker Avance II 14.1 Tesla (600 MHz) spectrometer (Billerica, MA) equipped with z-gradients and an inverse triple resonance TXI probe. The NMR data were collected and processed using the Bruker Topspin 2.0 software. The pulse length (P1) and the transmitter offset (O1) were optimized for each sample before running

the full set of experiments. All NMR experiments were performed at 37 °C using the water-gate water suppression technique [146]. In 1D  $^1\text{H}$  experiments, data were collected with 32 scans and processed using an exponential apodization function with 1 Hz line broadening. The 2D  $^1\text{H}$ - $^1\text{H}$  TOCSY experiments used a 60 ms mixing time and were run with 160 scans. A total of 2048/512 data points were collected in F2/F1 dimensions and the processed spectra had 1024 points in both dimensions. The 2D  $^1\text{H}$ - $^1\text{H}$  NOESY experiments used a 200 ms mixing time and were run with 160 scans. A total of 2048/512 data points were collected in F2/F1 dimensions and the processed spectra had 1024 points in both dimensions. All TOCSY and NOESY spectra were processed using the Qsine apodization function with a sine bell shift of 2.

#### 8.2.4 CD Data Collection and Processing

The CD spectra, in the far-ultraviolet (far-UV) region (from 260 to 190 nm), were recorded for both Maxi-B<sub>CT</sub> samples using a Jasco-810 spectropolarimeter (Easton, MD). The CD data were acquired at 37 °C using a quartz cuvette with 0.1 mm path length. The NMR samples were transferred to the cuvette without making any changes in the sample conditions. The temperature was controlled by a CTC-345 circulating water bath. The scanning speed of the instrument was set at 100 nm/min with normal sensitivity. Five accumulations were collected for each sample in 0.1 nm steps. The Molar ellipticity  $[\theta]$  was calculated using the equation suggested by Heeley *et al.* [213],

$$[\theta] = \theta_{\text{obs}}/(10LC), \quad (8.1)$$

where  $\theta_{\text{obs}}$  is the observed ellipticity, L is the path length of the cell (0.01 cm) and C is the number of amino acids multiplied by the molar concentration of the peptide (0.018 M). The secondary structural content was calculated from the molar ellipticity data using a computer program following the method of Yang *et al.* [214].

## 8.3 Results

### 8.3.1 NMR Spectra of Maxi-B<sub>CT</sub> in HFIP (40%)

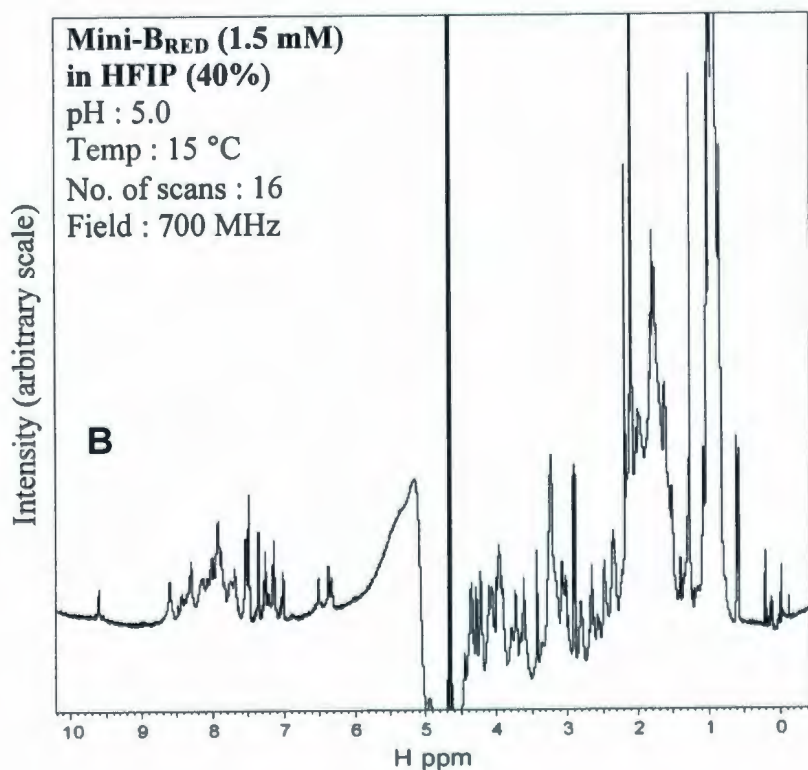
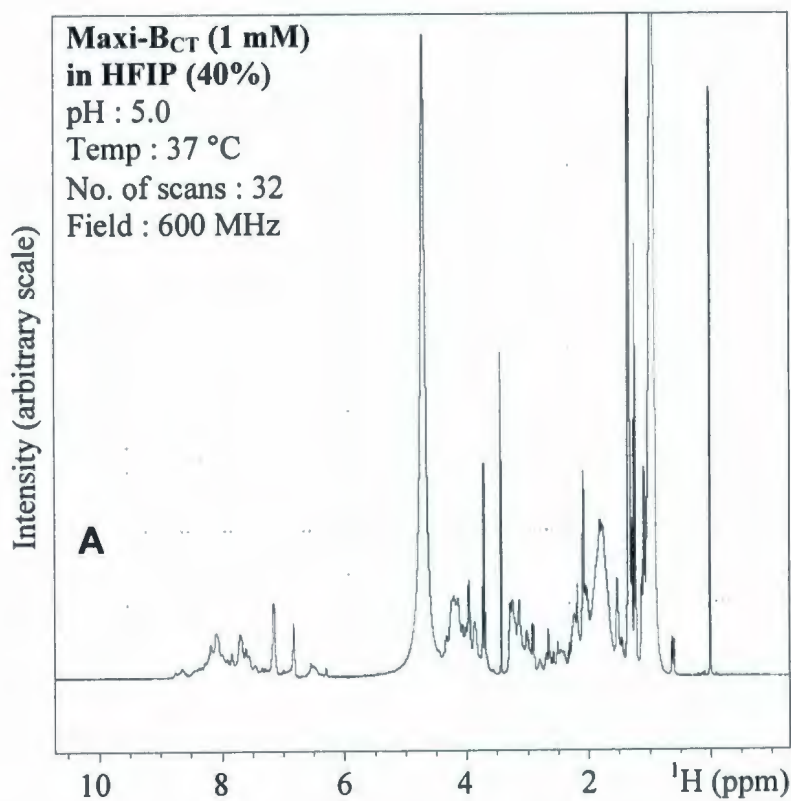
Panel A in Figures 8.2 - 8.4 present the structure characterization of Maxi-B<sub>CT</sub> by NMR and CD. The spectra of Mini-B in 40% HFIP (from My M.Sc. work, Booth lab) provide convenient reference spectra due to the similarity in size and an  $\alpha$ -helical content compared to Maxi-B<sub>CT</sub> and thus are presented in panel B of the figures. Unfortunately, that the Mini-B spectra were acquired at a lower temperature (15 °C) than Maxi-B<sub>CT</sub> (37 °C) sets a limitation on how much information can be gleaned from comparing the two sets of spectra. However, it is still valuable to compare Maxi-B<sub>CT</sub> data to data from a construct whose atomic resolution structure has been determined and for which the exact secondary structure is thus known.

Figure 8.2 shows the 1D <sup>1</sup>H spectra of Maxi-B<sub>CT</sub> acquired on a 600 MHz spectrometer at 37 °C and Mini-B in HFIP acquired on a 700 MHz spectrometer 15 °C. The signals seen in the enlarged 6-9 ppm region of Maxi-B<sub>CT</sub>, corresponding to the backbone and sidechain amide protons (HNs), are more overlapped and less dispersed when compared to Mini-B, even when taking the difference in spectrometer field into consideration. The dispersion of backbone HN signals of Maxi-B<sub>CT</sub> appears to be intermediate between what are typically observed for a random coil and a folded peptide.

The 2D <sup>1</sup>H-<sup>1</sup>H TOCSY spectra provides more insight into the structural features of Maxi-B<sub>CT</sub>. The TOCSY peaks in Figure 8.3 mostly correspond to the HA-HN correlations that result from the through-bond magnetization transfer between alpha and amide protons of the amino acid spin systems. There are 33 amino acids in Maxi-B<sub>CT</sub>, but more than 33 HA-HN crosspeaks are seen including some weak peaks in the panel A of Figure 8.3. The total count of 33-plus peaks and presence of weak peaks suggest some degree of conformational heterogeneity for Maxi-B<sub>CT</sub>. Also, the peaks are mostly grouped in two regions with one

region exhibiting a downfield shift (i.e., higher ppm) in the F2 (HN) dimension. The number of HA-HN crosspeaks present in the down-shifted region is higher when compared to the peaks from the same region of Mini-B shown in the panel B. This comparison of the general appearance of HA-HN crosspeaks likely indicates a decreased  $\alpha$ -helical structure of Maxi-B<sub>CT</sub> in organic solvent environment.

This interpretation is further supported by the examination of HN-HN region of 2D <sup>1</sup>H-<sup>1</sup>H NOESY (Figure 8.4). The downfield shifts of at least 3 backbone HN signals of Maxi-B<sub>CT</sub> are evident when compared to Mini-B. Besides, there are only about 15 intense backbone HN-HN crosspeaks present for Maxi-B<sub>CT</sub> while more than 21 such crosspeaks are observed for Mini-B. These correlations result from short HN-HN distances and indicate an  $\alpha$ -helical folding for about half of Maxi-B<sub>CT</sub> as compared to at least two-thirds of Mini-B.



**Figure 8.2 :** 1D  $^1\text{H}$  spectra of (A) 1 mM Maxi-B<sub>CT</sub> in 40% HFIP (plus 90% H<sub>2</sub>O and 10% D<sub>2</sub>O) at pH 5.0 and temperature 37 °C, acquired using Bruker 600 MHz spectrometer with 32 scans; and for comparison, (B) 1.5 mM Mini-B<sub>RED</sub> in 40% HFIP (plus 90% H<sub>2</sub>O and 10% D<sub>2</sub>O) at pH 5.0 and temperature 15 °C, acquired using Bruker 700 MHz spectrometer with 16 scans. Maxi-B<sub>CT</sub> spectrum was collected using the water-gate water suppression technique and processed by Topspin. Mini-B spectrum was collected using 3-9-19 water suppression technique and processed by NMRPipe. The signal intensities are also not normalized between the two spectra.

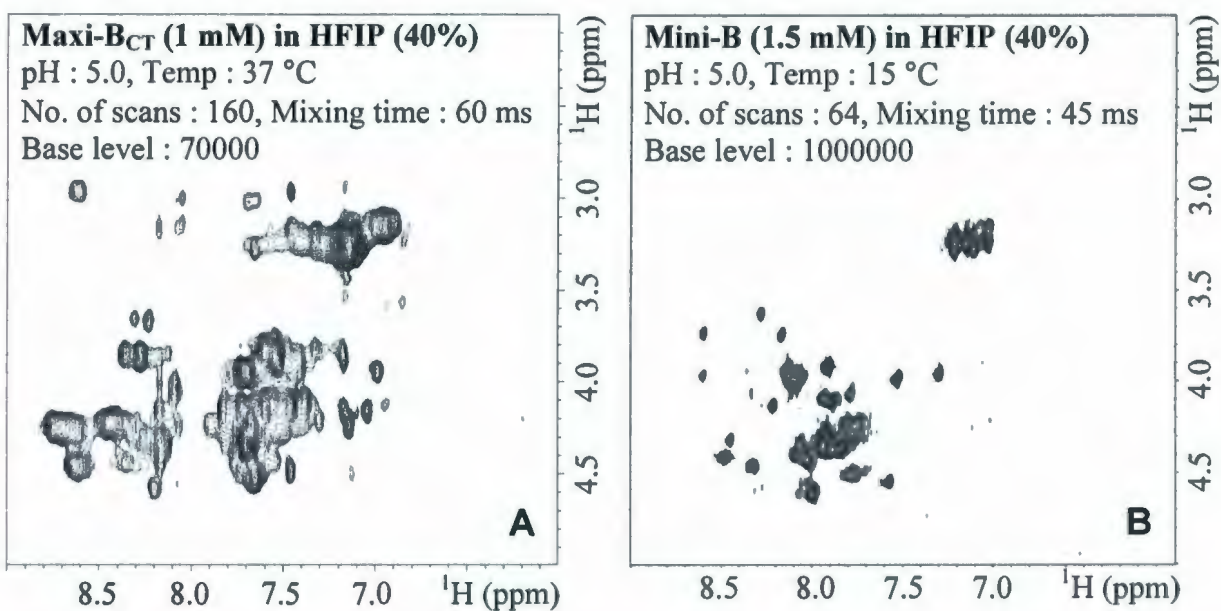


**Figure 8.3** : HA-HN regions of 2D  $^1\text{H}$ - $^1\text{H}$  TOCSY spectra of (A) 1 mM Maxi-B<sub>CT</sub> in 40% HFIP, acquired using Bruker 600 MHz spectrometer and processed by Topspin; and for comparison, (B) 1.5 mM Mini-B<sub>RED</sub> in 40% HFIP, acquired using Bruker 700 MHz spectrometer and processed by NMRPipe. Note, the peptide concentrations, temperatures, numbers of scans, mixing times and base levels are different for the two spectra.

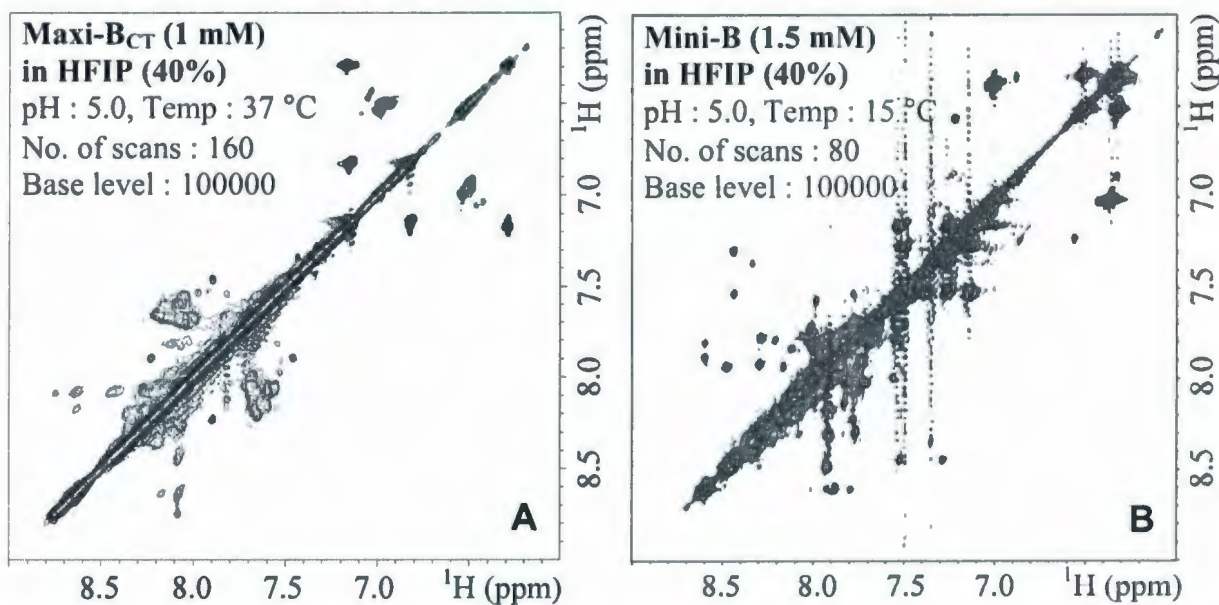


**Figure 8.4** : HN-HN regions of 2D  $^1\text{H}$ - $^1\text{H}$  NOESY spectra of (A) 1 mM Maxi-B<sub>CT</sub> in 40% HFIP, acquired using Bruker 600 MHz spectrometer and processed by Topspin; and for comparison, (B) 1.5 mM Mini-B<sub>RED</sub> in 40% HFIP, acquired using Bruker 700 MHz spectrometer and processed by NMRPipe. Both spectra were acquired using 200 ms mixing time. However, the peptide concentrations, temperatures and numbers of scans are different.

### 8.3.2 NMR Spectra of Maxi-B<sub>CT</sub> in SDS

As for the HFIP studies described in the previous section, the 1D <sup>1</sup>H, HA-HN region of 2D <sup>1</sup>H-<sup>1</sup>H TOCSY, and HN-HN region of 2D <sup>1</sup>H-<sup>1</sup>H NOESY spectra of Maxi-B<sub>CT</sub> are compared to Mini-B in anionic lung lipid mimetic SDS micelles. However, unlike the version of Mini-B used in the HFIP studies, the version of Mini-B used in the SDS micelle studies was oxidized, i.e., it retained the two native-like disulfide bonds. It is known from my previous structural studies (Chapter 3 and [156]) that this version of Mini-B also adopts a well-defined  $\alpha$ -helical conformation in SDS micelles. Comparing the spectra, despite the differences in spectrometer field and temperature at which data were acquired, should therefore provide insight on the extent of the Maxi-B<sub>CT</sub> structuring in lipid mimetic micelle environment.

Figure 8.5 shows the 1D <sup>1</sup>H spectra of Maxi-B<sub>CT</sub> and Mini-B in SDS micelles. The signals seen from the backbone and sidechain amide protons (HNs) in the enlarged 6-9 ppm region are broad and/or overlapped for both peptides but dispersed. This level of line-broadening and overlapping is not unexpected as the peptides are bound to detergent micelles. However, the backbone HNs of Maxi-B<sub>CT</sub> exhibit decreased dispersion, which indicates, in SDS, Maxi-B<sub>CT</sub> is not as structured as Mini-B.

The 2D <sup>1</sup>H-<sup>1</sup>H TOCSY spectra demonstrate more differences in the folding patterns of Maxi-B<sub>CT</sub> in SDS when compared to Mini-B (Figure 8.6). More prominently than in HFIP, a larger group of Maxi-B<sub>CT</sub> HA-HN crosspeaks exhibits a downfield shift (i.e., higher ppm) in the F2 (HN) dimension as shown in the panel A. The number of peaks present in the down-shifted region is also significantly higher when compared to the same region of Mini-B shown in the panel B. Therefore, in SDS micelles, Maxi-B<sub>CT</sub> likely consists of a decreased  $\alpha$ -helical structure than Mini-B. Furthermore, as in HFIP, the apparent count of 33-plus HA-HN crosspeaks and the presence of weak peaks suggest some degree of conformational heterogeneity of Maxi-B<sub>CT</sub> in the micelle environment too.

The examination of backbone HN-HN crosspeaks in the 2D  $^1\text{H}$ - $^1\text{H}$  NOESY spectra further suggests that Maxi-B<sub>CT</sub> is less structured than Mini-B in SDS micelles (Figure 8.7). While there are many backbone HN-HN correlations present for Maxi-B<sub>CT</sub>, in contrast to Mini-B, they are relatively weak and largely obscured by the strong diagonal signals and thus hard to count. However, the downfield shifts for some HN signals are still evident. Furthermore, although it is difficult to draw an inference about the number of Maxi-B<sub>CT</sub> amino acids that belong to the  $\alpha$ -helical structure in SDS micelles, overall the peptide seems to be less structured in the anionic detergent environment when compared to the organic solvent environment.

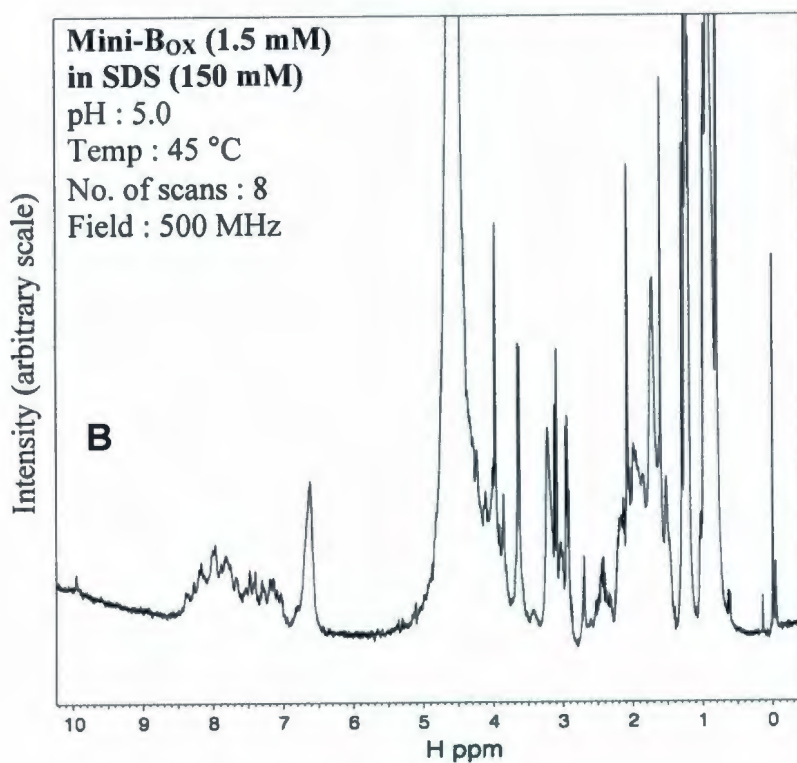
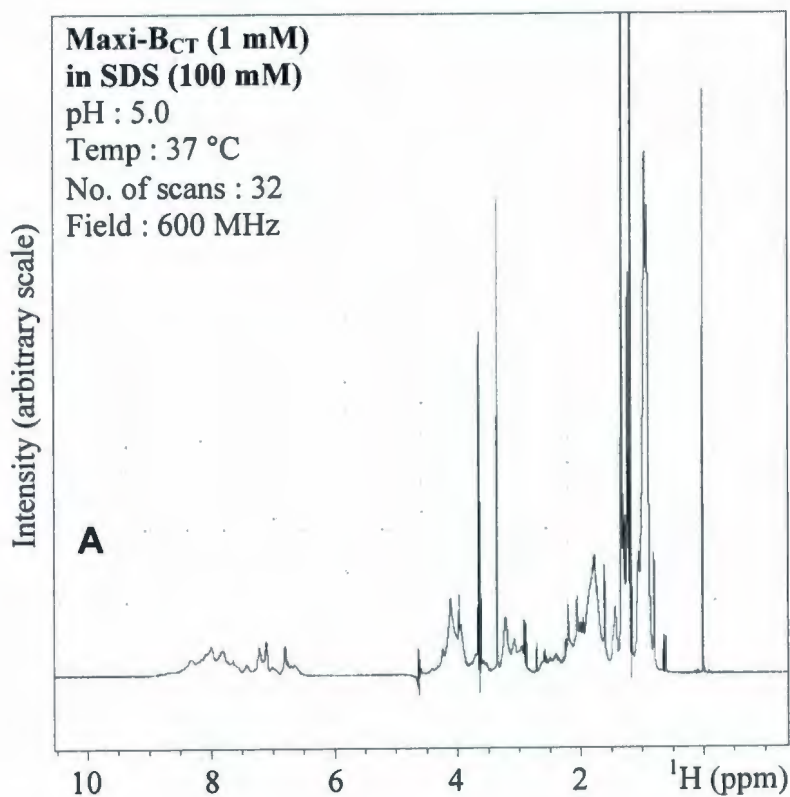


**Figure 8.5 :** 1D  $^1\text{H}$  spectra of (A) 1 mM Maxi-B<sub>CT</sub> in 100 mM SDS at pH 5.0 and temperature 37 °C, acquired using Bruker 600 MHz spectrometer with 32 scans; and for comparison, (B) 1.5 mM Mini-B<sub>OX</sub> in 150 mM SDS at pH 5.0 and temperature 45 °C, acquired using Bruker 500 MHz spectrometer with 8 scans. Maxi-B<sub>CT</sub> spectrum was collected using the water-gate water suppression technique and processed by Topspin. Mini-B spectrum was collected using pre-saturation water suppression technique and processed by NMRPipe. The signal intensities are also not normalized between the two spectra.

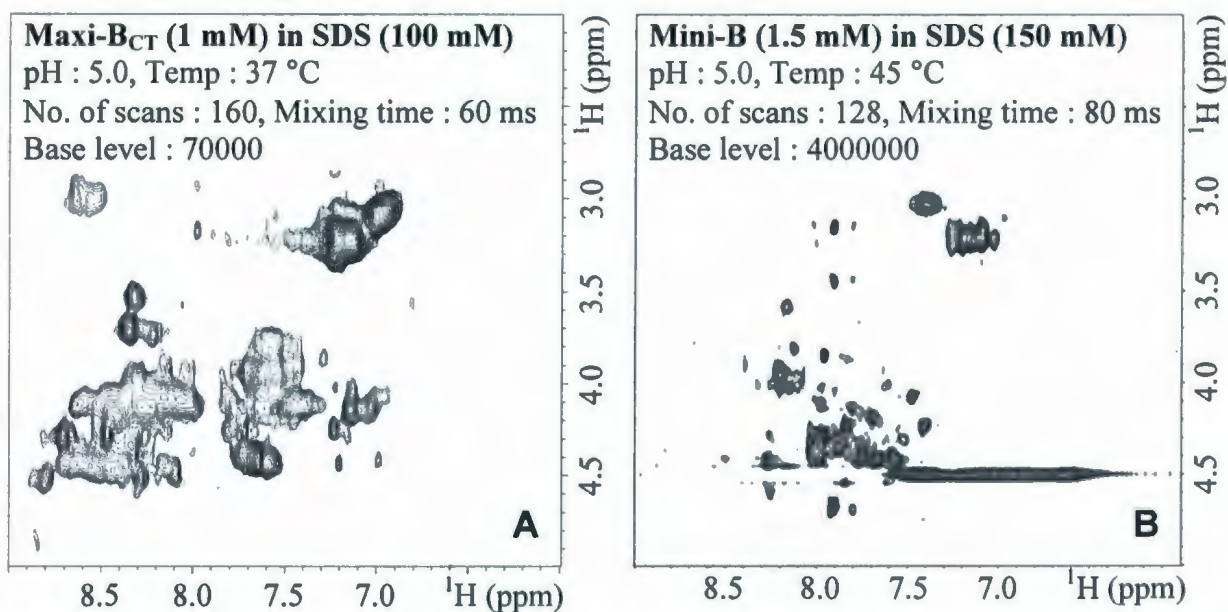


**Figure 8.6 :** HA-HN regions of 2D  $^1\text{H}$ - $^1\text{H}$  TOCSY spectra of (A) 1 mM Maxi-B<sub>CT</sub> in 100 mM SDS, acquired using Bruker 600 MHz spectrometer and processed by Topspin; and for comparison, (B) 1.5 mM Mini-B<sub>OX</sub> in 150 mM SDS, acquired using Bruker 500 MHz spectrometer and processed by NMRPipe. Note, the peptide concentrations, temperatures, numbers of scans, mixing times and base levels are different for the two spectra.

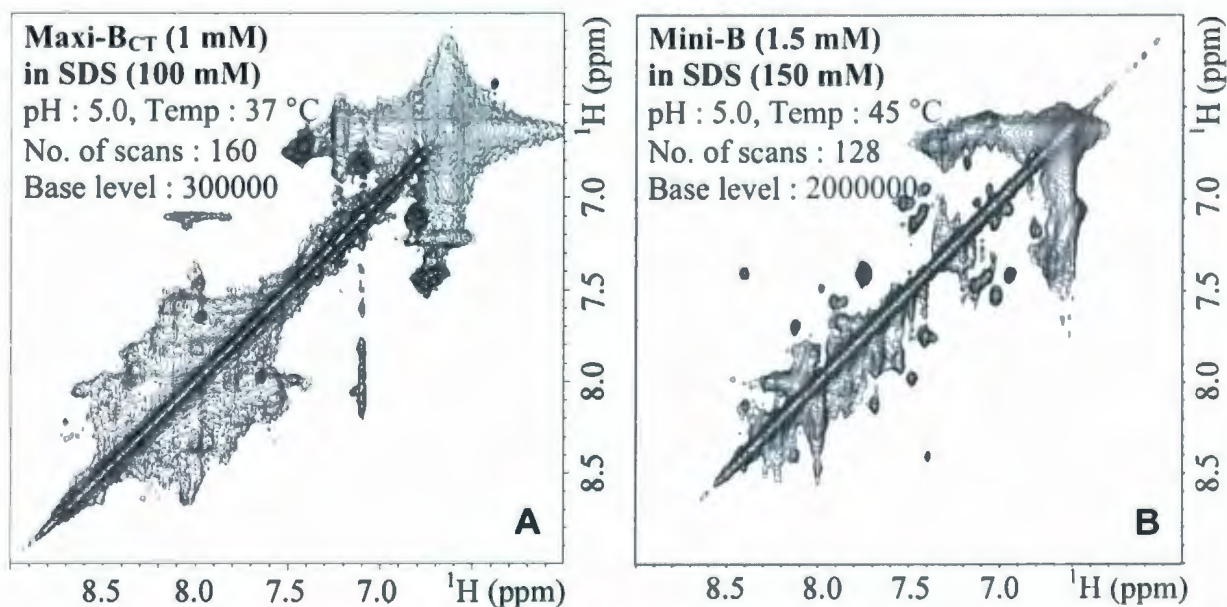


**Figure 8.7 :** HN-HN regions of 2D  $^1\text{H}$ - $^1\text{H}$  NOESY spectra of (A) 1 mM Maxi-B<sub>CT</sub> in 100 mM SDS, acquired using Bruker 600 MHz spectrometer and processed by Topspin; and for comparison, (B) 1.5 mM Mini-B<sub>OX</sub> in 150 mM SDS, acquired using Bruker 500 MHz spectrometer and processed by NMRPipe. Both spectra were acquired using 200 ms mixing time. However, the peptide/detergent concentrations, temperatures, numbers of scans and base levels are different.

### 8.3.3 CD Spectra of Maxi-B<sub>CT</sub> in HFIP (40%) and SDS

To complement the NMR data and obtain an alternate measure of the secondary structural content, circular dichroism spectra were acquired for Maxi-B<sub>CT</sub> in both HFIP and SDS at pH 5.0 and temperature 37 °C (Figure 8.8). Although the computer program used for the secondary structure calculation (following the method described in Ref. [214]) calculated the structure percentages as  $\alpha$ -helix,  $\beta$ -sheet,  $\beta$ -turn and random coil, Maxi-B<sub>CT</sub> is unlikely to contain a  $\beta$ -sheet which requires two or more strands hydrogen-bonded together. It is more plausible that the  $\beta$ -sheet content calculated by the computer program actually represents an extended conformation and hence is reported as such in the table of Figure 8.8. Thus the CD data indicate, in HFIP, about half of Maxi-B<sub>CT</sub> is  $\alpha$ -helical (~ 49%), with the remainder taking extended (~ 18%) and random coil (~ 33%) conformation. However, the features for Maxi-B<sub>CT</sub> in SDS are substantially different, with reduction of  $\alpha$ -helical content to about one-third (~ 35%) and a considerable increase in extended (~ 38%) along with some decrease in random coil (~ 27%) conformation.

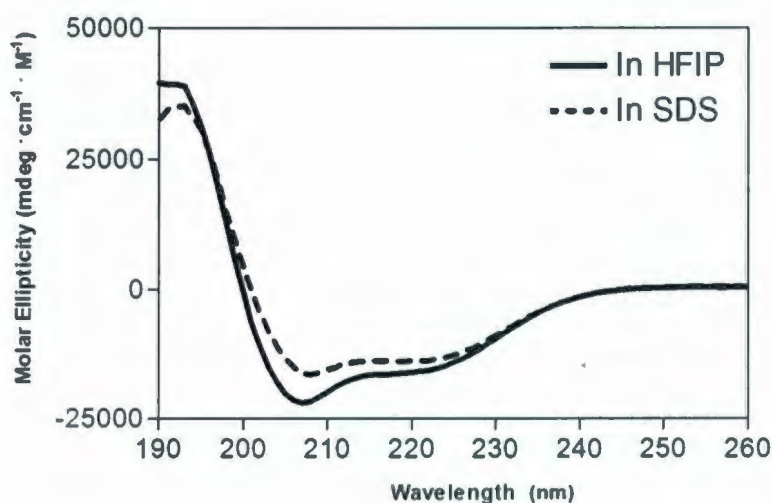


**Figure 8.8** : Far-UV CD spectra of 1 mM Maxi-B<sub>CT</sub> in 40% HFIP and in 100 mM SDS at pH 5.0 and temperature 37 °C, acquired using 5 accumulations and a 0.1 mm light path. The molar ellipticity is calculated from the observed ellipticity following the method described in Ref. [213]. The secondary structural contents, shown in the table, are calculated from the molar ellipticities following the method described in Ref. [214].

Secondary Structure (%)			
Peptide	$\alpha$ -helix	Extended	Random
Maxi-B <sub>CT</sub> in HFIP	49	18	33
Maxi-B <sub>CT</sub> in SDS	35	38	27

## 8.4 Discussion

Knowledge of the high-resolution three-dimensional structure of a protein is an important step in understanding its functional mechanism. The structure of SP-B, an indispensable protein for air-breathing vertebrates, is not known yet which limits our understanding of its crucial contribution(s) to lung surfactant function. Determination of the high-resolution structure of SP-B is one major research goal of the Booth lab (Biochemistry, Memorial University of Newfoundland). However, this is very challenging and attempts to achieve recombinant expression of high levels of  $^{13}\text{C}/^{15}\text{N}$ -labeled protein, required for solution NMR studies have not succeeded yet. As an alternative, the chemical synthesis of a protein based on SP-B amino acids 8 to 78, termed Maxi-B, was proposed by the Waring group (Medicine, UCLA). This synthetic Maxi-B is expected to provide significant structural information on full-length SP-B. However, difficulties were encountered in initial attempts to synthesize Maxi-B in a single step. This was not unexpected, as synthesis of a protein which contains 71 amino acids and 3 internal disulfide bonds is indeed very challenging. An alternate plan was devised, in which the N- and C-terminal halves of Maxi-B would be synthesized separately, and then connected by the three disulfide bonds (termed as truncated Maxi-B (Maxi-B<sub>TR</sub>) in Figure 8.1). The C-terminal fragment, Maxi-B<sub>CT</sub>, was attempted first and successfully synthesized by the Waring group. This part of my work was conducted to obtain the first structural characterization of Maxi-B<sub>CT</sub> in organic solvent and detergent micelles and lay down a foundation for future studies of Maxi-B and/or Full-length SP-B.

Maxi-B would contain all the predicted helical regions of full-length SP-B and retain the three native-like disulfide bonds between C8-C77, C11-C71 and C35-C46. Two mutations, C48S and E51A, were proposed to avoid the intermolecular disulfide bond and salt bridge, respectively. The first seven N-terminal amino acids of SP-B were clipped off in Maxi-B to eliminate the possibility of self-association. The C-terminal amino acid of SP-B, M79, was removed from Maxi-B sequence as it does not belong to the predicted C-terminal helix. Hydrophobic amino acid contents of the two proteins are similar, 52% in SP-B and 54% in Maxi-B. The net charges carried by the proteins at neutral pH are also similar, +8 for

Maxi-B and +7 for SP-B, with the difference resulting from the mutation E51A. All these features render Maxi-B an interesting protein to learn about the structure, properties, lipid/protein interactions and functional mechanism of full-length SP-B.

Maxi-B<sub>CT</sub>, a 33 residue peptide, is based on amino acids 46 to 78 from the C-terminal region of SP-B. Sequence homology with known Saposin proteins predicts this fragment to contain two  $\alpha$ -helical segments, i.e., the C-terminal helix of SP-B, as well as the helix next to it. To obtain the first structural characterization of Maxi-B<sub>CT</sub>, I performed solution NMR and CD studies in organic solvent HFIP and anionic surfactant lipid mimetic SDS micelles. The NMR data are also compared to that of Mini-B, a 34 residue peptide comprised of SP-B amino acids 8 to 25 and 63 to 78. It is known from my previous structural studies (Sarker, M., M.Sc. Thesis and Chapter 3 of this Ph.D. Thesis, Booth lab) that Mini-B adopts a well-defined conformation with two  $\alpha$ -helices in both HFIP and SDS micelles. Thus, the NMR spectra of Mini-B were ideal to compare the extent of Maxi-B<sub>CT</sub> structuring in the same environments.

The NMR data indicate approximately half of Maxi-B<sub>CT</sub> to be  $\alpha$ -helical in organic solvent condition. The helical content of the peptide is reduced in detergent micelles. The NMR data also indicate that the peptide consists of some non-helical content, likely some extended conformation, in HFIP, and an even increased non-helical conformation in SDS micelles. These findings are well supported by the CD data of Maxi-B<sub>CT</sub> that show the structure in HFIP to be 49% helical with 18% extended and 33% random coil, while in SDS, it is 35% helical with 38% extended and 33% random coil. Overall, the peptide is less structured (i.e., less helical) in detergent micelles than in organic solvent.

The relatively decreased helical structuring of Maxi-B<sub>CT</sub> in SDS micelles, when compared to the structuring in HFIP, is likely influenced by the physiochemical properties of the peptide. Maxi-B<sub>CT</sub> consists of four positively charged amino acids and one negatively charged amino acid. Three of the four positively charged amino acids (R64, R72 and R76) are localized in the C-terminal region of the peptide, which correspond to the C-terminal half

of Mini-B (amino acids 63 to 78) that contain an amphipathic  $\alpha$ -helix. The other positively charged amino acid (R52) and the only negatively charged amino acid (D59) make the N-terminal region of Maxi-B<sub>CT</sub> neutral. It is therefore possible that the electrostatic interactions between the positively charged C-terminal region of Maxi-B<sub>CT</sub> and the negatively charged SDS micelle induce an amphipathic helical conformation for this part of the peptide which may be similar to the C-terminal half of Mini-B. However, the N-terminal region of Maxi-B<sub>CT</sub>, because of the lack of a charge bias, may not interact strongly with the SDS micelle and hence may not adopt a well defined helical conformation. These electrostatic interactions, on the other hand, may not be required in inducing the secondary structure of Maxi-B<sub>CT</sub> in HFIP, and thus the peptide presumably adopts a more helical conformation in the organic solvent environment.

Determination of the high-resolution structure of Maxi-B<sub>CT</sub> is not attempted in this study as the main goal is to check the amenability of the peptide to NMR studies and prepare a foundation for study of full Maxi-B. It is not possible to draw a clear inference about whether the peptide consists of a single helical stretch or two distinct helical segments in either of the environments without performing spectral assignments and a high-resolution structure calculation. However, considering the presence of a glycine (G63) and a proline (P67) in the middle region, it seems unlikely that Maxi-B<sub>CT</sub> consists of a single helix spanning this middle region. In light of the NMR data, well supplemented by the CD data, it is possible that, in HFIP, Maxi-B<sub>CT</sub> consists of two helices but in SDS, Maxi-B<sub>CT</sub> has a helical folding mainly at the C-terminus.

Maxi-B<sub>CT</sub> is less helical in both HFIP and SDS micelles when compared to Mini-B. While Mini-B possesses two  $\alpha$ -helices comprising two-thirds of the peptide in both conditions, only half of Maxi-B<sub>CT</sub> is helical in HFIP which reduces to just one-third in SDS micelles. The distribution of seven positively charged amino acids in the two regions, presence of two native-like disulfide bonds and inter-helix interactions likely play crucial roles in the overall helical folding of Mini-B. In contrast, Maxi-B<sub>CT</sub> has no disulfide bonds and has a far less net charge of +3 that is localized in one region only. These properties,

therefore, are apparently essential for the physiologically relevant helical folding of SP-B based peptides.

Although this study finds that Maxi-B<sub>CT</sub> exhibits decreased helical structuring, especially in SDS micelles, the inclusion of Maxi-B<sub>NT</sub>, the other Maxi-B fragment consisting of amino acids 8 to 35 of SP-B, would possibly bring a significant improvement in structuring and induce a more native-like conformation of Maxi-B or Maxi-B<sub>TR</sub>.

In this study, the high resolution structure of Maxi-B<sub>CT</sub> was not attempted, as the main objectives were to gain an insight into the overall conformational features and check the amenability of the proposed Maxi-B/Maxi-B<sub>TR</sub> to future NMR studies. The NMR spectra of Maxi-B<sub>CT</sub> indicate that Maxi-B (or Maxi-B<sub>TR</sub>), if available with sufficient <sup>13</sup>C/<sup>15</sup>N labels, would likely be suitable for a high-resolution structural characterization by solution NMR. The observations from Maxi-B<sub>CT</sub> would also aid in the future investigations of the near-complete or the full-length SP-B.

*Chapter 9*  
**Conclusion**

## 9.1 Summary and Remarks

Lung surfactant is a complex mixture of lipids and proteins that enables normal breathing by reducing the surface tension created at the alveolar air-water interface and additionally provides the first line of defense against inhaled microbes in the lungs. SP-B, a protein component which accounts for not more than  $\sim 1.5\%$  of the total surfactant weight, is absolutely essential for the survival of mammals [37, 38, 216]. Biophysical studies suggest that SP-B facilitates large-scale rearrangements of lipids and stabilizes complex structures required for interfacial adsorption, surfactant film stability and respreading capacity of surfactant materials [82]. To understand the mechanistic basis for this ability and the physiological ramifications of lipid rearrangements, it is important to know the high-resolution structure of SP-B. Unfortunately, the 3D structure of SP-B has not yet been determined since, as is generally the case for membrane and other lipid-associated hydrophobic proteins, the production of an SP-B sample for structural studies has been very challenging and unsuccessful to date. Interestingly, synthetic fragments of SP-B retain substantial biological activity when compared to the full-length protein [109]. Oxidized Mini-B (Mini-B<sub>OX</sub>) tops this list and it likely encompasses the key functional regions of the full-length protein [109]. This Ph.D. research has applied solution NMR methods to Mini-B and two other SP-B-based peptides to reveal at least some of the critical structural features and lipid/protein interactions that presumably underlie the functional mechanisms of SP-B in physiological conditions.

I have determined the high-resolution structure of Mini-B in the presence of micelles composed of the anionic detergent SDS, which provides a reasonable mimetic of SP-B's physiological environment in the lung (Chapter 3). Mini-B consists of two  $\alpha$ -helices connected by an unstructured loop. The helices are packed tightly together and interhelical interactions are stabilized by the two disulfide bonds as well as by several hydrophobic contacts. Mini-B possesses a strikingly amphipathic surface with a large positively charged patch on one face of the peptide and a large hydrophobic patch on the opposite face. The tryptophan side chain extends outward from the peptide in a position to interact with lipids

and anchor Mini-B at the lipid-water interface. Amino acids of Mini-B in the N-terminus and the loop regions appear to exhibit a certain degree of plasticity. All of these distinctive structural features likely contribute to the mechanism by which Mini-B, and presumably SP-B, functions.

The structure of Mini-B in SDS, with its strikingly amphipathic surface and projecting tryptophan anchor, appears very well suited for making strong interactions with surfactant phospholipid analogues. Indeed, Mini-B binds both anionic and zwitterionic micelles composed of SDS, DPC, LMPC, LMPG and mixed LMPC/LMPG and induces substantial rearrangements of the micelle structures (Chapter 4). However, interesting differences are noticed in the overall conformation and dynamics of Mini-B in zwitterionic versus anionic environments. Despite the similarity in structuring of Mini-B in DPC to LMPC and SDS to LMPG, intriguing differences are found in how Mini-B interacts with the smaller SDS/DPC micelles compared to the larger LMPC/LMPG micelles. Thus, subtle differences in the lipid structure can substantially impact Mini-B/lipid interactions. Presumably, in the native lung conditions, SP-B also adopts diverse conformations and forms different types of lipid-associations at various stages of the breathing cycle.

To prepare a foundation for directly probing the interaction between Mini-B and SP-A, I have investigated the conformation and lipid interactions of SP-A in the presence of micelles composed from the same model surfactant lipids (Chapter 5). SP-A's biological roles, in relation to either anti-microbial activities or surfactant biophysical activities, are almost always attributed to its octadecameric structure and preferential interactions with DPPC [17, 53, 56]. However, my investigations unveil that SP-A binds not only to zwitterionic micelles but also to anionic micelles and that the micelle-bound SP-A exists predominantly as smaller oligomers, in sharp contrast to the octadecamers observed when in an aqueous environment, and the form in which SP-A has long been presumed to function. These findings demonstrate the necessity of developing new models to portray how the protein may function as smaller oligomers and interact with different lipid types in the native lung conditions.

Several biophysical studies have indicated an *in vitro* interaction, either direct or indirect, between SP-B and SP-A that may be important in lung surfactant function [59, 62, 170, 171]. I have attempted to directly probe the interaction between Mini-B and SP-A, if any, in the presence of micelles composed of model surfactant lipids LMPC, LMPG and mixed LMPC/LMPG, alongside SDS and DPC (Chapter 6). Mini-B appears to interact with SP-A in all micelle systems, although the degree of the interaction is dependent on the detergent/lipid headgroup. The entire population of Mini-B appears to interact with SP-A when in zwitterionic micelles (at least in DPC) but only a subpopulation of Mini-B interacts with SP-A when in anionic micelles (at least in SDS). Interestingly, in larger LMPC and LMPG micelles, there may occur a Mini-B-induced reduction of the SP-A oligomeric states. In all of these model surfactant lipids, however, the interactions between Mini-B and SP-A are most likely not direct protein-protein interactions but mediated via the micelles.

Next, I have investigated the modifications to SP-B's structure and lipid interactions brought about by tryptophan oxidation using the N-terminal fragment SP-B<sub>8-25</sub> (Chapter 7). Oxidative modification of SP-B, considered to be a major factor in conditions like ARDS, most deleteriously affects the biophysical activity of lung surfactant and can lead to its complete inactivation [202, 206, 210]. Trp9, the only tryptophan present in SP-B sequence, is essential for optimal interface affinity of the protein [140] and is a prime site for oxidative damage [211]. Replacement of tryptophan by one of its oxidized forms, kynurenine, substantially disrupts the helical structure of SP-B<sub>8-25</sub>. This likely perturbs the amphipathic profile of the peptide as well and thereby affects its interactions with the micelles. Thus, in the lung, tryptophan oxidation perhaps causes a loss of the helical structure of native SP-B and interrupts its interactions with surfactant phospholipids, which lead to lung surfactant dysfunction.

Lastly, as a step towards the determination of the structure of full-length SP-B, the overall conformation of Maxi-B<sub>CT</sub>, the C-terminal half of Maxi-B (or SP-B), has been investigated in organic solvent HFIP and SDS micelles (Chapter 8). Although Maxi-B<sub>CT</sub> (33 amino acids) exhibits a decreased helical structuring when compared to Mini-B (34 amino

acids), especially in SDS micelles, the inclusion of Maxi-B<sub>NT</sub>, the N-terminal half of Maxi-B, would possibly bring a significant improvement in the overall structure and induce a more native-like conformation of Maxi-B. The results obtained for Maxi-B<sub>CT</sub> indicate that the synthetic Maxi-B (or the recombinant full-length SP-B), if produced containing an appropriate number of <sup>13</sup>C/<sup>15</sup>N labels, would likely be suitable for high-resolution structural characterization by solution NMR.

SP-B is indispensable for life, but the molecular basis for its activity is not yet understood. The findings of my Ph.D. research contribute to the ongoing endeavor in characterizing SP-B's structure-function relationships and its mechanisms of lipid/protein interactions that are crucial for lung surfactant function. This work also provides a strong foundation for future studies on the conformations and interactions of near-complete or full-length SP-B.

## 9.2 Future Work

What role SP-B exactly plays in lung surfactant function is still a puzzle. A great tool to resolve this puzzle would be the high-resolution structure of full-length SP-B, or at least a near-full SP-B variant (e.g. Maxi-B), in a lipid-bound state. Knowledge of the high-resolution structure of SP-B will facilitate unveiling the mechanisms of its function in the lung and directly probing its interactions with surfactant lipids and other proteins. Production of a synthetic/recombinant sample to conduct the structural studies is the greatest hurdle to overcome in this regard. There are at least three labs currently working on this and hopefully the endeavor will be successful in the near future. In the mean time, further progress can still be achieved by characterizing biologically active fragments of SP-B that are now available.

Mini-B has enormous potential from a therapeutic perspective. In my Ph.D. work, the high-resolution structure of Mini-B has been determined and its interactions with model surfactant lipids and SP-A have been probed. One interesting future study will be to

investigate if tubular myelin can be formed by adding Mini-B, instead of full-length SP-B, with mixtures of DPPC, PG and SP-A in the presence of  $\text{Ca}^{2+}$ .

Recently an extended version of Mini-B, called Super Mini-B, has been synthesized by the Waring group (Medicine, UCLA) which includes the N-terminal seven amino acids of native SP-B that are not part of Mini-B. Super Mini-B shows excellent surfactant activity, even better than Mini-B<sub>OX</sub>, in ventilated rats with ARDS induced by *in vivo* lavage [217]. The first structural characterization using Attenuated Total Reflectance-Fourier Transform Infrared (ATR-FTIR) spectroscopy shows a similar degree of  $\alpha$ -helical conformation of Super Mini-B when compared to Mini-B [217]. This is not unexpected since the first seven amino acids of SP-B represent a putative lipid insertion region of the protein [142] and are unlikely to extend the span of its N-terminal helix. Nevertheless, it may be informative to determine the high resolution structure of Super Mini-B and investigate if it exhibits stronger interactions with model surfactant lipids than Mini-B.

Chemical synthesis of Maxi-B (a near-complete version of SP-B), first in the truncated form as Maxi-B<sub>TR</sub> (Figure 8.1, Page 197), will be attempted soon by the Waring group (Medicine, UCLA). Since it is not feasible to synthesize Maxi-B incorporating  $^{15}\text{N}/^{13}\text{C}$  labels uniformly, I have developed a selective labeling scheme to incorporate an appropriate number of  $^{15}\text{N}$  backbone amide labels at strategic locations along the polypeptide chain of Maxi-B. If successfully synthesized, the first structural characterization of Maxi-B<sub>TR</sub> will be obtained in organic solvent HFIP by the Booth group using solution NMR. Although the absence of some of the native amino acids and the organic solvent environment will limit the structure's ability to explain SP-B's function in physiological conditions, helpful information, such as the span of the helices, distribution of hydrophobic and hydrophilic amino acids along the structure and extent of the positively charged patches on the surface, will be unveiled by this study. Identification of the resonance frequencies of proton spin systems from the HFIP data will also guide future NMR studies of Maxi-B/SP-B in a more physiologically relevant environment such as detergent/lipid micelles or oriented phospholipid bilayers.

Because the synthetic Maxi-B (or Maxi-B<sub>TR</sub>) will carry only a limited number of <sup>15</sup>N-labels, an attempt to determine its high-resolution structure in the presence of detergent/lipid micelles using solution NMR is unlikely to be successful. However, the internal dynamics of different Maxi-B regions and its interactions with model surfactant lipids/proteins can still be probed using solution NMR. In addition, with selected site-specific isotope (<sup>13</sup>C/<sup>15</sup>N/<sup>19</sup>F) labels, solid-state NMR studies can lead to some inferences on the overall tertiary conformation of Maxi-B in lipid environments. One possible option will be to use oriented samples and determine the orientations of the helices in phospholipid bilayers. Another option will be to directly investigate if Maxi-B folds with its two predicted pairs of helices tightly packed as in the closed-type Saposins or further apart as in the open-type Saposins.

Recombinant expression of full-length SP-B in bacteria is currently underway in the Booth Lab. Protocols are being explored to resolve the problems that other labs have encountered in SP-B production. However, given the difficulties in expressing and then purifying a properly folded protein that contains over 50% hydrophobic amino acids and three intrachain and one interchain disulfide bonds, this project still demands formidable efforts to get accomplished. Nevertheless, if successful, it will allow an incorporation of uniform <sup>13</sup>C/<sup>15</sup>N labels in SP-B which will make the protein amenable to the structural studies in the presence of detergent/lipid micelles by solution NMR. The high-resolution three-dimensional structure of full-length SP-B will likely revolutionize the ongoing lung surfactant-related research and contribute significantly in developing a more accurate model for lung surfactant function.

## References

- [1] Notter, R.H. (2000). In: Linfant, C. ed. Lung surfactants: basic science and clinical applications; Lung Biology in Health and Disease; Vol. 143. New York, Marcel Dekker. Page 120. Also, [http://en.wikipedia.org/wiki/Human\\_Lung](http://en.wikipedia.org/wiki/Human_Lung).
- [2] Bastacky, J., Lee, C.Y.C., Goerke, J., Koushafar, D.Y., Kenaga, L., Speed, T.P., Chen, Y., and Clements, J.A. (1995) Alveolar lining layer is thin and continuous: low-temperature scanning electron microscopy of rat lung. *J. Appl. Physiol.* 79(5), 1615-1628.
- [3] Possmayer, F. (1998) Physicochemical aspects of pulmonary surfactant. In: Polin, R.A., Fox, W.W., eds. *Fetal and Neonatal Physiology*; WB Saunders Company. 1259-1275.
- [4] Schürch, S., Bachofen, H., Goerke, J., and Green, F. (1992) Surface properties of rat pulmonary surfactant studied with the captive bubble method: adsorption, hysteresis, stability. *Biochim. Biophys. Acta.* 1103, 127-136.
- [5] Crouch, E., and Wright, J. R. (2001) Surfactant proteins A and D and pulmonary host defense. *Annu. Rev. Physiol.* 63, 521-554.
- [6] von Neergaard, K. (1929) Neue Auffassungen über einen Grundbegriff der Atemmechanik. Die Retraktionskraft der Lunge, abhängig von der Oberflächenspannung in den Alveolem, *Z. Gesamte Exp. Med.* 66, 373-394.
- [7] Pattle, R. (1995) Properties, function and origin of the alveolar lining layer. *Nature* 175, 1125-1126.
- [8] Clements, J. A. (1957) Surface tension of lung extracts. *Proc. Soc. Exp. Biol. Med.* 95, 170-172.
- [9] Johansson, J., and Curstedt, T. (1997) Molecular structures and interactions of pulmonary surfactant components. *Eur. J. Biochem.* 244, 675-693.
- [10] Wright, J.R., and Clements, J.A. (1989) Lung surfactant turnovers and factors that affect turnover. In: Massaro, D. ed. *Lung Cell Biology*; New York: Marcel Dekker Inc. 655-699.
- [11] Schmitz, G., and Muller, G. (1991) Structure and function of lamellar bodies, lipid-protein complexes involved in storage and secretion of cellular lipids. *J. of Lip. Res.* 32, 1539-1570.
- [12] Goerke, J. (1998) Pulmonary surfactant: functions and molecular composition. *Biochim. Biophys. Acta.* 1408, 79-89.
- [13] Massaro, D., Clerch, L., and Massaro, G.D. (1982) Surfactant secretion: evidence that cholinergic stimulation of secretion is indirect. *Am. J. Physiol.* 243, C39-C45.
- [14] Wirtz, H., and Schmidt, M. (1992) Ventilation and secretion of pulmonary surfactant. *Clin. Invest.* 70, 3-13.
- [15] Chander, A., and Fisher, A.B. (1990) Regulation of lung surfactant secretion. *Am. J. Physiol.* 258, L241-L253.
- [16] Lumb, R.H. (1989) Phospholipid transfer proteins in mammalian lung. *Am. J. Physiol.* 257, L190-L194.

- [17] Casals, C., and Garcia-Verdugo, I. (2005) Molecular and functional properties of surfactant protein A. In: Nag, K., and Lenfant, C. eds. *Lung Surfactant Function and Disorder; Lung Biology in Health and Disease*; Vol. 201; Taylor & Francis Group. Pages 59-86.
- [18] Magoon, M.W., Wright, J.R., Baritussio, A., Williams, M.C., Goerke, J., Benson, B.J., Hamilton, R.L., and Clements, J.A. (1983) Subfraction of lung surfactant. Implications for metabolism and surface activity. *Biochim. Biophys. Acta.* 750, 18-31.
- [19] Orgeig, S., Daniels, C.B., and Sullivan, L.C. (2004) The development of the pulmonary surfactant system. In: Harding, R., Pinkerton, K., Plopper, C., eds. *The lung: Development, Aging and the Environment*; London: Academic Press. Chapter 10, 150-167.
- [20] Johansson, J., and Curstedt, T. (1997) Molecular structures and interactions of pulmonary surfactant components. *Eur. J. Biochem.* 244, 675-693.
- [21] Pérez-Gil, J., and Keough, K.M.W. (1998) Interfacial properties of surfactant proteins. *Biochim. Biophys. Acta.* 1408, 203-217.
- [22] Schürch, S., Qanbar, R., Bachofen, H. and Possmayer, F. (1995) The surface-associated surfactant reservoir in the alveolar lining. *Biol. Neonate* 67 (suppl), 61-76.
- [23] Lang, C.J., Daniels, C.B., and Orgeig, S. (2005) New insights into the thermal dynamics of the Surfactant system from warm and cold animals. In: Nag, K., and Lenfant, C. eds. *Lung Surfactant Function and Disorder; Lung Biology in Health and Disease*; Vol. 201. Taylor & Francis Group. Pages 17-57.
- [24] Veldhuizen, R., Nag, K., Orgeig, S., and Possmayer, F. (1998) The role of lipids in pulmonary surfactant. *Biochim. Biophys. Acta.* 1408, 90-108.
- [25] Pérez-Gil, J. (2002) Molecular Interactions in pulmonary surfactant films. *Biol. Neonate.* 81(Suppl 1), 6-15.
- [26] Paul, G.W., Hassett, R.J., and Reiss, O.K. (1977) Formation of Lung Surfactant Films from Intact Lamellar Bodies. *Proceedings of the National Academy of Sciences of the United States of America.* 74(8), 3617-3620.
- [27] Serrano, A.G., and Perez-Gil, J. (2006) Protein-lipid interactions and surface activity in the pulmonary surfactant system. *Chemistry and Physics of Lipids.* 141, 105-118.
- [28] Diemel, R.V., Snel, M.M., Waring, A.J., Walther, F.J., van Golde, L.M., Putz, G., Haagsman, H.P., and Batenburg, J.J. (2002) Multilayer formation upon compression of surfactant monolayers depends on protein concentration as well as lipid composition. An atomic force microscopy study. *J. Biol. Chem.* 277, 21179-21188.
- [29] Palaniyar, N., Nadesalingam, J., and Reid, K.B. (2002) Pulmonary innate immune proteins and receptors that interact with Gram-positive bacterial ligands. *Immunobiology.* 205, 575-594.
- [30] Weaver, T.E., and Conkright, J.J. (2001) Functions of surfactant proteins B and C. *Annual Rev. Physiol.* 63, 555-578.
- [31] Hamvas, A., Cole, F.S., deMello, D.E., Moxley, M., Whitsett, J.A., Colten, H.R., and Noguee, L.M. (1994) Surfactant protein B deficiency: antenatal diagnosis and prospective treatment with surfactant replacement. *J. Pediatr.* 125(3), 356-361.

- [32] Hallman, M., Glumoff, V., and Ramet, M. (2001) Surfactant in respiratory distress syndrome and lung injury. *Comp. Biochem. Physiol., Part A: Mol. Int. Physiol.* 129, 287-294.
- [33] Seeger, W., Gunther, A., Walmrath, H. D., Grimminger, F., and Lasch, H. G. (1993) Alveolar surfactant and adult respiratory distress syndrome. Pathogenetic role and therapeutic prospects, *Clin. Invest.* 71, 177-190.
- [34] Schwartz, R. M., Luby, A. M., Scanlon, J. W., and Kellogg, R. J. (1994) Effect of surfactant on morbidity, mortality, and resource use in newborn infants weighing 500 to 1500 g. *N. Engl. J. Med.* 330, 1476-1480.
- [35] Gunther, A., Ruppert, C., Schmidt, R., Markart, P., Grimminger, F., Walmrath, D., and Seeger, W. (2001) Surfactant alteration and replacement in acute respiratory distress syndrome. *Respir. Res.* 2, 353-364.
- [36] Lewis, J. F., and Veldhuizen, R. (2003) The role of exogenous surfactant in the treatment of acute lung injury. *Annu. Rev. Physiol.* 65, 613-642.
- [37] Noguee, L. M., Garnier, G., Dietz, H. C., Singer, L., Murphy, A. M., deMello, D. E., and Colten, H. R. (1994) A mutation in the surfactant protein B gene responsible for fatal neonatal respiratory disease in multiple kindreds. *J. Clin. Invest.* 93, 1860-1863.
- [38] Clark, J. C., Wert, S. E., Bachurski, C. J., Stahlman, M. T., Stripp, B. R., Weaver, T. E., and Whitsett, J. A. (1995) Targeted disruption of the surfactant protein B gene disrupts surfactant homeostasis, causing respiratory failure in newborn mice. *Proc. Natl. Acad. Sci. U.S.A.* 92, 7794-7798.
- [39] Daniels, C.B., Lopatco, O.V., Oregig, S. (1998) Evolution of surface activity related functions of vertebrate pulmonary surfactant. *Clin. Exp. Pharmacol. Physiol.* 25, 716-721.
- [40] Mohwald, H. (1995) Phospholipid monolayers. In Lipowski, R., and Sackmann, E. eds. *Structure and dynamics of membranes: from cells to vesicles*; Amsterdam, Elsevier. 161-211.
- [41] Piknova, B., Schief, W.R., Vogel, V., Discher, B.M., and Hall, S.B. (2001) Discrepancy between phase behavior of lung surfactant phospholipids and the classical model of surfactant function. *Biophys J.* 81(4), 2172-2180.
- [42] Piknova, B., Schram, V., and Hall, S.B. (2002) Pulmonary surfactant: phase behavior and function. *Curr. Opin. Struct. Biol.* 12(4), 487-494.
- [43] Saad, S.M.I., Policova, Z., Acosta, E.J., Hair, M.L., and Neumann, A.W. (2009) Mixed DPPC/DPPG monolayers at very high film compression. *Langmuir.* 25(18), 10907-10912.
- [44] Grunder, R., Gehr, P., Bachofen, H., Schürch, S., and Siegenthaler, H. (1999) Structures of surfactant films: a scanning force microscopy study. *Eur. Respir. J.* 14(6), 1290-1296.
- [45] Discher, B.M., Maloney, K.M., Schief, W.R., Grainger, D.W., Vogel, V., and Hall, S.B. (1996) Lateral phase separation in interfacial films of pulmonary surfactant. *Biophys. J.* 71(5), 2583-2590.
- [46] Nag, K., Perez-Gil, J., Ruano, M.L., Worthman, L.A., Stewart, J., Casals, C., and Keough K.M.W. (1998) Phase transitions in films of lung surfactant at the air-water interface. *Biophys. J.* 74(6), 2983-2995.

- [47] Zuo, Y., Tadayyon, S., Keating, E., Zhao, L., Veldhuizen, R., Petersen, N., Amrein, M., and Possmayer, F. (2008) Atomic force microscopy studies of functional and dysfunctional pulmonary surfactant films. II. Albumininhibited pulmonary surfactant films and the effect of SP-A. *Biophysical Journal*. 94(9), 3549-3564.
- [48] Yan, W., Piknova, B., and Hall, S.B. (2005) The collapse of monolayers containing pulmonary surfactant phospholipids is kinetically determined. *Biophys. J.* 89(1), 306-314.
- [49] Rose, D., Rendell, J., Lee, D., Nag, K., and Booth, V. (2008) Molecular dynamics simulations of lung surfactant lipid monolayers. *Biophys. Chem.* 138, 67-77.
- [50] Goerke, J., and Gonzales, J. (1981) Temperature dependence of dipalmitoyl phosphatidylcholine monolayer stability. *J. Appl. Physiol.* 51, 1108-1114.
- [51] Notter, R.H., Finkelstein, J.N., and Taubold, R.D. (1983) Comparative adsorption of natural lung surfactant, extracted phospholipids, and artificial phospholipid mixtures to the air-water interface. *Chem. Phys. Lipids.* 33, 67-80.
- [52] Bernardino de la Serna, J., Perez-Gil, J., Simonsen, A.C., and Bagatolli, L.A. (2004) Cholesterol rules: direct observation of the coexistence of two fluid phases in native pulmonary surfactant membranes at physiological temperatures. *J. Biol. Chem.* 279(39), 40715-40722.
- [53] McCormack, F.X. (1998) Structure, processing and properties of surfactant protein A. *Biochimica et Biophysica Acta.* 1408, 109-131.
- [54] Zaltash, S., Palmblad, M., Curstedt, T., Johansson, J., and Persson, B. (2000) Pulmonary surfactant protein B: a structural model and a functional analogue. *Biochimica et Biophysica Acta.* 1466, 179-186.
- [55] Johansson, J., Szyperski, T., Curstedt, T., and Wuthrich, K. (1994) The NMR structure of the pulmonary surfactant-associated polypeptide SP-C in an apolar solvent contains a valyl-rich alpha-helix. *Biochemistry.* 33, 6015-6023.
- [56] Kishore, U., Greenhough, T.J., Waters, P., Shrive, A.K., Ghai, R., Kamran, M.F., Bernal, A.L., Reid, K.B.M., Madan, T., and Chakraborty, T. (2006) Surfactant proteins SP-A and SP-D: Structure, function and receptors. *Molecular Immunology.* 43, 1293-1315.
- [57] Lawson, P.R., and Reid, K.B. (2000) The roles of surfactant proteins A and D in innate immunity. *Immunol. Rev.* 173, 66-78.
- [58] Korfhagen, T.R., Bruno, M.D., Ross, G.F., Huelsman, K.M., Ikegami, M., Jobe, A.H., Wert, S.E., Stripp, B.R., Morris, R.E., Glasser, S.W., Bachurski, C.J., Iwamoto, H.S., and Whitsett, J.A. (1996) Altered surfactant function and structure in SP-A gene targeted mice. *Proc. Natl. Acad. Sci. USA.* 93, 9594-9599.
- [59] Suzuki, Y., Fujita, Y., and Kogishi, K. (1989) Reconstitution of tubular myelin from synthetic lipids and proteins associated with pig pulmonary surfactant. *Am. Rev. Respir. Dis.* 140, 75-81.
- [60] Williams, M.C., Hawgood, S., and Hamilton, R.L. (1991) Changes in lipid structure produced by surfactant proteins SP-A, SP-B, and SP-C. *Am. J. Respir. Cell Mol. Biol.* 5, 41-50.

- [61] Nag, K., Munro, J.G., Hearn, S.A., Rasmusson, J., Petersen, N.O., and Possmayer, F. (1999) Correlated atomic force and transition electron microscopy of nanotubular structures in pulmonary surfactant. *J. Struct. Biol.* 126, 1-15.
- [62] Hawgood, S., Bensen, B.J., Schilling, J., Damm, D., Clements, J.A., and White, R.T. (1987) Nucleotide and amino acid sequences of pulmonary surfactant protein SP 18 and evidence for cooperation between SP 18 and SP 28-36 in surfactant lipid adsorption. *Proc. Natl. Acad. Sci. USA.* 84, 66-70.
- [63] Schurch, S., Possmayer, F., Cheng, S., and Cockshutt, A.M. (1992) Pulmonary SP-A enhances adsorption and appears to induce surface sorting of lipid extract surfactant. *Am. J. Physiol.* 263, L210-L218.
- [64] Robertson, B., Kobayashi, T., Ganzuka, M., Grossmann, G., Li, W.Z., and Suzuki, Y. (1991) Experimental neonatal respiratory failure induced by a monoclonal antibody to the hydrophobic surfactant-associated protein SP-B. *Pediatr. Res.* 30, 239-243.
- [65] Glasser, S.W., Burhans, M.S., Korfhagen, T.R., Na, C.L., Sly, P.D., Ross, G.F., Ikegami, M., and Whitsett, J.A. (2001) Altered stability of pulmonary surfactant in SP-C-deficient mice. *Proc. Natl. Acad. Sci. USA.* 98, 6366-6371.
- [66] Glasser, S.W., Detmer, E.A., Ikegami, M., Na, C.L., Stahlman, M.T., and Whitsett, J.A. (2003) Pneumonitis and emphysema in *sp-C* gene targeted mice. *J. Biol. Chem.* 278, 14291-14298.
- [67] Noguee, L.M., Dunbar, A.E. III, Wert, S.E., Askin, F., Hamvas, A., and Whitsett, J.A. (2001) A mutation in the surfactant protein C gene associated with familial interstitial lung disease. *N. Engl. J. Med.* 344, 573-579.
- [68] Thomas, A.Q., Lane, K., Phillips, J. III, Prince, M., Markin, C., Speer, M., Schwart, D.A., Gaddipati, R., Marney, A., Johnson, J., Roberts, R., Haines, J., Stahlman, M., and Loyd, J.E. (2002) Heterozygosity for a surfactant protein C gene mutation associated with usual interstitial pneumonitis and cellular nonspecific interstitial pneumonitis in one kindred. *Am. J. Respir. Crit. Care Med.* 165, 1322-1328.
- [69] Oosterlaken-Dijksterhuis, M.A., Haagsman, H.P., van Golde, L.M.G., and Demel, R.A. (1991) Characterization of lipid insertion into monomolecular layers mediated by lung surfactant proteins SP-B and SP-C. *Biochemistry* 30, 10965-10971.
- [70] Pérez-Gil, J., Cruz, A, and Plasencia, I. (2005) Structure-function relationships of hydrophobic proteins SP-B and SP-C in pulmonary surfactant. In: Nag, K., and Lenfant, C. eds. *Lung Surfactant Function and Disorder; Lung Biology in Health and Disease*; Vol. 201. Taylor & Francis Group. Pages 125-142.
- [71] Ikegami, M, Whitsett, J.A., Jobe, A., Ross G., Fisher, J., and Korfhagen, T. (2000) Surfactant metabolism in SP-D gene-targeted mice. *AM. J. Physiol. Lung Cell Mol. Physiol.* 279, L468-L476.
- [72] Palaniyar, N., Nadesalingam, J., and Reid, K.B.M. (2005) Receptors and ligands for collectins surfactant proteins A and D. In: Nag, K., and Lenfant, C. eds. *Lung Surfactant*

Function and Disorder; Lung Biology in Health and Disease; Vol. 201. Taylor & Francis Group. Pages 87-123.

[73] Head, J.F., Mealy, T.R., McCormack, F.X., and Seaton, B.A. (2003) Crystal structure of trimeric carbohydrate recognition and neck domains of surfactant protein A. *J. Biol. Chem.* 278, 43254-43260.

[74] Hakansson, K., Lim, N.K., Hoppe, H.J., and Reid, K.B. (1999) Crystal structure of the trimeric alpha-helical coiled-coil and the three lectin domains of human lung surfactant protein D. *Structure Fold. Des.* 7, 255-264.

[75] Shrive, A.K., Tharia, H.A., Strong, P., Kishore, U., Burns, I., Rizkallah, P.J., Reid, K.B.M., and Greenhough. (2003) High-resolution structural insights into ligand binding and immune cell recognition by human lung surfactant protein D. *J. Mol. Biol.* 331, 509-523.

[76] Kurutz, J.W., and Lee, K.Y.C. (2002) NMR structure of lung surfactant peptide SP-B<sub>11-25</sub>. *Biochemistry.* 41, 9627-9636.

[77] Booth, V., Waring, A.J., Walther, F.J., and Keough, K.M.W. (2004) NMR structures of the C-terminal segment of surfactant protein B in detergent micelles and hexafluoro-2-propanol. *Biochemistry.* 43, 15187-15194.

[78] Melton, K.R., Nesslein, L.L., Ikegami, M., Tichelaar, J.W., Clark, J.C., Whitsett, J.A., and Weaver, T.E. (2003) SP-B deficiency causes respiratory failure in adult mice. *Am. J. Physiol.* 285, L543-549.

[79] Pilot-Matias T.J., Kister S.E., Fox J.L., Kropp K., Glasser S.W., and Whitsett J.A. (1989) Structure and organization of the gene encoding human pulmonary surfactant proteolipid SP-B. *DNA.* 8, 75-86.

[80] Hawgood, S. (2004) Surfactant protein B: structure and function. *Biol. Neonate.* 85, 285-289.

[81] Weaver T.E., Whitsett, J.A. (1989) Processing of hydrophobic pulmonary surfactant protein B in rat type II cells. *Am. J. Physiol.* 257, L100-L108.

[82] Hawgood, S., Derrick, M., and Poulain, F. (1998) Structure and properties of surfactant protein B. *Biochim. Biophys. Acta.* 1408, 150-160.

[83] Longo, M.L., Bisagno, A.M., Zasadzinski, J.A., Bruni, R., and Waring, A.J. (1993) A function of lung surfactant protein SP-B. *Science.* 261, 453-456.

[84] Baatz, J.E., Elledge, B., and Whitsett, J.A. (1990) Surfactant protein SP-B induces ordering at the surface of model membrane bilayers. *Biochemistry.* 29, 6714-6720.

[85] Perez-Gil, J., Casals, C., and Marsh, D. (1995) Interactions of hydrophobic lung surfactant proteins SP-B and SP-C with dipalmitoylphosphatidylcholine and dipalmitoylphosphatidylglycerol bilayers studied by electron spin resonance spectroscopy. *Biochem.* 34, 3964-3971.

[86] Lipp, M.M., Lee, K.Y., Zasadzinski, J.A., and Waring, A.J. (1996) Phase and morphology changes in lipid monolayers induced by SP-B protein and its amino-terminal peptide. *Science.* 273, 1196-1199.

- [87] Lipp, M.M., Lee, K.Y.C., Takamoto, D.Y., Zasadzinski, J.A., and Waring, A.J. (1998) Co-existence of buckled and flat monolayers. *Physical Review Letters*. 81, 1650-1653.
- [88] Ding, J., Doudevski, I., Warriner, H.E., Alig, T., Zasadzinski, J.A., Waring, A.J., and Sherman, M.A. (2003) Nanostructure changes in lung surfactant monolayers induced by interactions between palmitoyloleoylphosphatidylglycerol and surfactant protein B. *Langmuir* 19, 1539-1550.
- [89] Beck, D.C., Na, C.L., Whitsett, J.A., and Weaver, T.E. (2000) Ablation of a critical surfactant protein B intramolecular disulfide bond in transgenic mice. *J. Biol. Chem.* 275, 3371-3376.
- [90] John, M., Wendeler, M., Heller, M., Sandhoff, K., and Kessler, H. (2006) Characterization of Human Saposins by NMR Spectroscopy. *Biochemistry*. 45, 5206-5216.
- [91] Ahn, V.E., Leyko, P., Alattia, J.R., Chen, L., and Prive, G.G. (2006) Crystal structures of saposins A and C. *Protein Sci.* 15, 1849-1857.
- [92] Ahn, V.E., Faull, K.F., Whitelegge, J.P., Fluharty, A.L., and Prive, G.G. (2003) Crystal structure of saposin B reveals a dimeric shell for lipid binding. *Proc. Natl. Acad. Sci. USA* 100, 38-43.
- [93] Hawkins, C.A., de Alba, E., and Tjandra, N. (2005) Solution structure of human saposin C in a detergent environment. *J. Mol. Biol.* 346, 1381-1392.
- [94] Liepinsh, E., Andersson, M., Ruysschaert, J.M., and Otting, G. (1997) Saposin fold revealed by the NMR structure of NK-lysin. *Nat. Struct. Biol.* 4, 793-795.
- [95] Hecht, O., Van Nuland, N.A., Schleinkofer, K., Dingley, A.J., Bruhn, H., Leippe, M., and Grotzinger, J. (2004) Solution structure of the pore-forming protein of *Entamoeba histolytica*. *J. Biol. Chem.* 279, 17834-17841.
- [96] Anderson, D.H., Sawaya, M.R., Cascio, D., Ernst, W., Modlin, R., Krensky, A., and Eisenberg, D. (2003) Granulysin crystal structure and a structure-derived lytic mechanism. *J. Mol. Biol.* 325, 355-365.
- [97] Power, J.H., Doyle, I.R., Davidson, K., and Nicholas, T.E. (1999) Ultrastructural and protein analysis of surfactant in the Australian lungfish *Neoceratodus forsteri*: evidence for conservation of composition for 300 million years. *J. Exp. Biol.* 202, 2543-2550.
- [98] Vandenbussche, G., Clercx, A., Clercx, M., Curstedt, T., Johansson, J., Jornvall, H., and Ruysschaert, J.M. (1992) Secondary structure and orientation of the surfactant protein SP-B in a lipid environment. A Fourier transform infrared spectroscopy study. *Biochemistry*. 31, 9169-9176.
- [99] Pastrana-Rios, B., Taneva, S., Keough, K. M., Mautone, A. J., and Mendelsohn, R. (1995) External reflection absorption infrared spectroscopy study of lung surfactant proteins SP-B and SP-C in phospholipid monolayers at the air/water interface. *Biophys. J.* 69, 2531-2540.
- [100] Cruz, A., Casals, C., and Perez-Gil, J. (1995) Conformational flexibility of pulmonary surfactant proteins SP-B and SP-C, studied in aqueous organic solvents. *Biochim. Biophys. Acta.* 1255, 68-76.

- [101] Revak, S.D., Merritt, T.A., Hallman, M., Heldt, G., La Polla, R.J., Hoey, K., Houghten, R.A., and Cochrane, C.G. (1991) The use of synthetic peptides in the formation of biophysically and biologically active pulmonary surfactants. *Pediatr. Res.* 29, 460-465.
- [102] Walther, F.J., Hernandez-Juviel, J.M., Gordon, L.M., Sherman, M.A., and Waring, A.J. (2002) Dimeric surfactant protein B peptide SP-B 1-25 in neonatal and acute respiratory distress syndrome. *Exp. Lung Res.* 28, 623-640.
- [103] Veldhuizen, E.J., Waring, A.J., Walther, F.J., Batenburg, J.J., van Golde, L.M., and Haagsman, H.P. (2000) Dimeric N-terminal segment of human surfactant protein B (dSP-B (1-25)) has enhanced surface properties compared to monomeric SP-B(1-25). *Biophys. J.* 79, 377-384.
- [104] Tanaka, Y., Takei, T., Aiba, T., Masuda, K., Kiuchi, A., and Fujiwara, T. (1986) Development of synthetic lung surfactants. *J. Lipid Res.* 27, 475-485.
- [105] Kang, J.H., Lee, M.K., Kim, K.L., and Hahm, K.S. (1996) The relationships between biophysical activity and the secondary structure of synthetic peptides from the pulmonary surfactant protein SP-B. *Biochem. Mol. Biol. Int.* 40, 617-627.
- [106] Baatz, J.E., Sarin, V., Absolom, D.R., Baxter, C., and Whitsett, J.A. (1991) Effects of surfactant-associated protein SP-B synthetic analogs on the structure and surface activity of model membrane bilayers. *Chem. Phys. Lipids.* 60, 163-178.
- [107] Ryan, M.A., Qi, X., Serrano, A.G., Ikegami, M., Perez-Gil, J., Johansson, J., and Weaver, T.E. (2005) Mapping and analysis of the lytic and fusogenic domains of surfactant protein B. *Biochemistry.* 44, 861-872.
- [108] Wiswell, T.E., Knight, G.R., Finer, N.N., Donn, S.M., Desai, H., Walsh, W.F., Sekar, K.C., Bernstein, G., Keszler, M., Visser, V.E., Merritt, T.A., Mannino, F.L., Mastroianni, L., Marcy, B., Revak, S.D., Tsai, H., and Cochrane, C.G. (2002) A multicenter, randomized, controlled trial comparing Surfaxin (Lucinactant) lavage with standard care for treatment of meconium aspiration syndrome. *Pediatrics.* 109, 1081-1087.
- [109] Waring, A.J., Walther, F.J., Gordon, L.M., Hernandez-Juviel, J.M., Hong, T., Sherman, M.A., Alonso, C., Alig, T., Braun, A., Bacon, D., and Zasadzinski, J.A. (2005) The role of charged amphipathic helices in the structure and function of surfactant protein B. *J. Pept. Res.* 66, 364-374.
- [110] Sarker, M. (2006) NMR Structural Studies of Lung Surfactant Protein B (SP-B) Peptides. M.Sc. Thesis: Department of Physics & Physical Oceanography, Memorial University of Newfoundland.
- [111] Voet, D., Voet, J.G., and Pratt, C.W. (1999) *Fundamentals of Biochemistry.* John Wiley & Sons, Inc. New York, NY.
- [112] Whitford, D. (2005) *Proteins: Structure and Function.* John Wiley & Sons Ltd. West Sussex, England.
- [113] Branden, C., and Tooze, J. (1991) *Introduction to protein Structure.* Garland Pub. Inc.
- [114] Petsko, G.A., and Ringe, D. (2004) *Protein Structure and Function; Primers in Biology.* New Science Press Ltd.

- [115] Blundell, T.L., and Johnson, L.N. (1976) Protein Crystallography. Academic Press.
- [116] Wüthrich, K. (2002) NMR studies of structure and function of biological macromolecules. Nobel Lecture, [http://nobelprize.org/nobel\\_prizes/chemistry/laureates/2002/wutrich-lecture.pdf](http://nobelprize.org/nobel_prizes/chemistry/laureates/2002/wutrich-lecture.pdf).
- [117] Kuchel, P.W., and Ralston, G.B. (2003) Schaum's Outlines Biochemistry, Second Edition. Tata McGraw-Hill Publishing Company Limited, New Delhi.
- [118] Skrisovska, L., Schubert, M., and Allain, F.H. (2010) Recent advances in segmental isotope labeling of proteins: NMR applications to large proteins and glycoproteins. *J. Biomol. NMR.* 46(1), 51-65.
- [119] Rule, G.S., and Hitchens, T.K. (2006) Fundamentals of Protein NMR Spectroscopy. Springer.
- [120] Opella, S.J., and Marassi, F.M. (2004) Structure determination of membrane proteins by NMR spectroscopy. *Chem. Rev.* 104, 3587-3606.
- [121] M. H. (2008) Spin Dynamics Basics of Nuclear Magnetic Resonance. John Wiley & Sons Ltd. West Sussex, England.
- [122] Keeler, J. (2005) Understanding NMR Spectroscopy. John Wiley & Sons Ltd. England.
- [123] Cavanagh, J., Fairbrother, W.J., Palmer III, A.G., Rance, M., and Skelton, N.J. (2007) Protein NMR Spectroscopy Principles and Practice. Second Ed. Elsevier Academic Press.
- [124] Wüthrich, K. (1986) NMR of Proteins and Nucleic Acids. John Wiley & Sons. New York.
- [125] Kay, L. E., Torchia, D. A., and Bax, A. (1989) Backbone dynamics of proteins as studied by <sup>15</sup>N inverse detected heteronuclear NMR spectroscopy: application to staphylococcal nuclease. *Biochemistry*, 28(23), 8972-8979.
- [126] Wishart, D., Bigam, C., Holm, A., Hodges, R., and Sykes, B. (1995) <sup>1</sup>H, <sup>13</sup>C and <sup>15</sup>N random coil NMR chemical shifts of the common amino acids. I. Investigations of nearest-neighbor effects. *J. Biomol. NMR.* 5, 67-81.
- [127] Wishart, D.S., Sykes, B.D., and Richards, F.M. (1991) Relationship between nuclear magnetic resonance chemical shift and protein secondary structure. *J. Mol. Biol.* 222, 311-333.
- [128] Wishart, D.S., and Sykes, B.D. (1993) The <sup>13</sup>C chemical shift index. A simple method for the identification of protein secondary structure using <sup>13</sup>C chemical shift data. *J. Biol. NMR.* 4, 171-175.
- [129] Pochapsky, T.C., and Pochapsky, S.S. (2007) NMR for Physical and Biological Scientists. Taylor & Francis. New York and London.
- [130] Fesik, S.W., and Zuideweg, E.R. (1990) Heteronuclear three-dimensional NMR spectroscopy of isotopically labelled biological macromolecules. *Q. Rev. Biophys.* 23(2), 97-131.
- [131] Clore, G.M., and Gronenborn, A.M. (1991) Applications of three- and four-dimensional heteronuclear NMR spectroscopy to protein structure determination. *Progr. Nucl. Magn. Reson. Spectroscopy* 23, 43-92.

- [132] Griesinger, C., Sorensen, O.W., and Ernst, R.R. (1989) 3-Dimensional Fourier Spectroscopy - Application to High- Resolution NNM. *J. Magnetic Resonance* 84, 14-63.
- [133] LE Kay, L.E., Clore, G.M., Bax, A., and Gronenborn, A.M. (1990) Four-dimensional heteronuclear triple-resonance NMR spectroscopy of interleukin-1 beta in solution. *Science* 249, 411-414.
- [134] Price, W. S. (1997) Pulsed-field gradient nuclear magnetic resonance as a tool for studying translational diffusion: Part 1. Basic Theory. *Concepts Magn. Reson.* 9, 299-336.
- [135] Price, W. S. (1998) Pulsed-field gradient nuclear magnetic resonance as a tool for studying translational diffusion: Part II. Experimental Aspects. *Concepts Magn. Reson.* 10, 197-237.
- [136] Clore, G.M., Brünger, A.T., Karplus, M. and Gronenborn, A.M. (1986) Application of molecular dynamics with interproton distance restraints to three-dimensional protein structure determination: a model study of crambin. *J. Mol. Biol.* 191, 523-551.
- [137] Brünger, A.T. (1992) X-PLOR Version 3.1 : A System for X-ray Crystallography and NMR. Yale University, New Haven.
- [138] Wallin, E., and von Heijne, G. (1998) Genome-wide analysis of integral membrane proteins from eubacterial, archaean, and eukaryotic organisms. *Protein Sci.* 7(4), 1029-1038.
- [139] Gao, F.P., and Cross, T.A. (2006) Recent developments in membrane-protein structural genomics. *Genome Biology* 6, 244.
- [140] Hayter, J.B., and Penfold, J. (1981) Self-consistent structural and dynamic study of concentrated micelle solutions. *J. Chem. Soc., Faraday Trans. 1* 77, 1851-1863.
- [141] Sheu, E.Y., Wu, C.F., Chen, S.H., and Blum, L. (1985) Application of a rescaled mean spherical approximation to strongly interacting ionic micellar solutions. *Phys. Rev. A* 32, 3807-3810.
- [142] Serrano, A., Ryan, M., Weaver, T., and Pe' rez-Gil, J. (2006) Critical Structure-Function Determinants within the N-Terminal Region of Pulmonary Surfactant Protein SP-B. *Biophys. J.* 90, 238-249.
- [143] Fields, C.G., Lloyd, D.H., Macdonald, R.L., Otteson, K.M., and Noble, R.L. (1991) HBTU activation for automated Fmoc solid-phase peptide synthesis. *Pept. Res.* 4, 95-101.
- [144] Guéron, M., Plateau, P., and Decorps, M. (1991) Solvent signal suppression in NMR. *Prog. NMR Spectrosc.* 23, 135-209.
- [145] Grzesiek, S. and Bax, A. (1993) The importance of not saturating water in protein NMR. Application to sensitivity enhancement and NOE measurements. *J. Am. Chem. Soc.* 115, 12593-12594.
- [146] Liu, M., Mao, X.A., Ye, C., Huang, H., Nicholson, J. K., and Lindon, J.C. (1998) Improved WATERGATE pulse sequences for solvent suppression in NMR spectroscopy. *J. Magn. Reson.* 132, 125-129.

- [147] Delaglio, F., Grzesiek, S., Vuister, G. W., Zhu, G., Pfeifer, J., and Bax, A. (1995) NMRPipe: a multidimensional spectral processing system based on UNIX pipes. *J. Biomol. NMR* 6, 277-293.
- [148] Goddard, T.D., and Kneller, D.G. Sparky 3, University of California, San Francisco (<http://www.cgl.ucsf.edu/home/sparky>).
- [149] Brünger, A.T., Adams, P.D., Clore, G.M., DeLano, W.L., Gros, P., Grosse-Kunstleve, R. W., Jiang, J.S., Kuszewski, J., Nilges, M., Pannu, N.S., Read, R.J., Rice, L.M., Simonson, T., and Warren, G.L. (1998) Crystallography & NMR system: A new software suite for macromolecular structure determination. *Acta Crystallogr. D: Biol. Crystallogr.* 54, 905-921.
- [150] Koradi, R., Billeter, M., and Wuthrich, K. (1996) MOLMOL: a program for display and analysis of macromolecular structures. *J. Mol. Graphics* 14, 51-55.
- [151] Wishart, D.S., and Nip, A.M. (1998) Protein chemical shift analysis: a practical guide. *Biochem. Cell Biol.* 76, 153-163.
- [152] Sanner, M.F., Olson, A.J., and Spehner, J.C. (1996) Reduced surface: an efficient way to compute molecular surfaces. *Biopolymers* 38, 305-320.
- [153] Serrano, A.G., Cruz, A., Rodriguez-Capote, K., Possmayer, F., and Perez-Gil, J. (2005) Intrinsic structural and functional determinants within the amino acid sequence of mature pulmonary surfactant protein SP-B. *Biochemistry* 44, 417-430.
- [154] Itri, R., and Amaral, L.Q. (1991) Distance distribution function of sodium dodecyl sulfate micelles by X-ray scattering. *J. Phys. Chem.* 95, 423-427.
- [155] Humphrey, W., Dalke, A., and Schulten, K. (1996) VMD: visual molecular dynamics. *J. Mol. Graphics* 14, 33-38.
- [156] Sarker, M., Waring, A.J., Walther, F.J., Keough, K.M.W., and Booth, V. (2007) Structure of Mini-B, a Functional Fragment of Surfactant Protein B, in Detergent Micelles. *Biochemistry* 46, 11047-11056.
- [157] Morris, K.F., and Johnson, C.S. (1992) Diffusion-ordered two dimensional nuclear magnetic resonance spectroscopy. *J. Am. Chem. Soc.* 114 (8), 3139-3141.
- [158] Tanner, J.E. (1970) Use of the stimulated echo in NMR diffusion studies. *J. Chem. Phys.* 52, 2523-2526.
- [159] Sklenár, V., Piotto, M., Leppik, R., and Saudek, V. (1993) Gradient-tailored water suppression for proton-nitrogen-15 HSQC experiments optimized to retain full sensitivity. *J. Magn. Reson.* 102, 241-245.
- [160] Colafemmina, G., Fiorentino, D., Ceglie, A., Carretti, E., Fratini, E., Dei, L., Baglioni, P., and Palazzo, G. (2007) Structure of SDS Micelles with Propylene Carbonate as Cosolvent: a PGSE-NMR and SAXS Study. *J. Phys. Chem. B* 111(25), 7184-7193.
- [161] Lipfert, J., Columbus, L., Chu, X.V.B., Lesley, S.A., and Doniach, S. (2007) Size and Shape of Detergent Micelles Determined by Small-Angle X-ray Scattering. *J. Phys. Chem. B* 111, 12427-12438.

- [162] Yang, T.C., McDonald, M., Morrow, M.R., and Booth, V. (2009) The effect of a C-terminal peptide of surfactant protein B (SP-B) on oriented lipid bilayers, characterized by solid-state <sup>2</sup>H- and <sup>31</sup>P-NMR. *Biophysical Journal* 96(9), 3762-3771.
- [163] Sueishi, K., and Benson, B.J. (1981) Isolation of a major apolipoprotein of canine and murine pulmonary surfactant. Biochemical and immunochemical characteristics. *Biochim. Biophys. Acta* 665, 442-453.
- [164] Voss, T., Schafer, K.P., Nielsen, P.F., Schafer, A., Maier, C., Hannappel, E., Maaben, J., Lavides, B., Klemm, K., and Przybylski, M. (1992) Primary structure differences of human surfactant-associated proteins isolated from normal and proteinosis lung. *Biochim. Biophys. Acta* 1138, 261-267.
- [165] Hickling, T.P., Malhorta, R., and Sim, R.B. (1998) Human lung surfactant protein A exists in several different oligomeric states: oligomer size distribution varies between patient groups. *Molecular Medicine* 4, 266-275.
- [166] Weaver, T.E. (1988) Pulmonary surfactant-associated proteins. *Gen. Pharmacol.* 19, 361-368.
- [167] Palaniyar, N., Ikegami, M., Korfhagen, T., Whitsett, J., and McCormack, F.X. (2001) Domains of surfactant protein A that affect protein oligomerization, lipid structure and surface tension. *Comp. Biochem. Physiol., Part A: Mol. Integr. Physiol.* 129, 109-127.
- [168] Kuroki, Y., Takahashi, M., and Nishitani, C. (2007) Pulmonary collectins in innate immunity of the lung. *Cell Microbiol.* 9, 1871-1879.
- [169] Wright, J.R. (2005) Immunoregulatory Functions of Surfactant Proteins. *Nature Reviews Immunology* 5, 58-68.
- [170] Nag, K., Munro, J.G., Hearn, S.A., Rasmusson, J., Petersen, N.O., and Possmayer, F. (1999) Correlated atomic force and transmission electron microscopy of nanotubular structures in pulmonary surfactant. *J. Struct. Biol.* 126, 1-15.
- [171] Schurch, S., Possmayer, F., Cheng, S., and Cockshutt, A.M. (1992) Pulmonary SP-A enhances adsorption and appears to induce surface sorting of lipid extract surfactant. *Am. J. Physiol.* 263, L210-L218.
- [172] King, R.J., Carmichael, M.C., and Horowitz, P.M. (1983) Reassembly of lipid-protein complexes of pulmonary surfactant. Proposed mechanism of interaction. *J. Biol. Chem.* 258, 10672-10680.
- [173] Hawgood, S., Benson Jr., B.J., and Hamilton, R.L. (1985) Effects of a surfactant-associated protein and calcium ions on the structure and surface activity of lung surfactant lipids. *Biochemistry* 24, 184-190.
- [174] Cockshutt, A.M., Weitz, J., and Possmayer, F. (1990) Pulmonary surfactant-associated protein A enhances the surface activity of lipid extract surfactant and reverses inhibition by blood proteins *in vitro*. *Biochemistry* 29, 8424-8429.
- [175] Elhalwagi, B.M., Zhang, M., Ikegami, M., Iwamoto, H.S., Morris, R.E., Miller, M.L., Dienger, K., McCormack, F.X. (1999). Normal surfactant pool sizes and inhibition-resistant surfactant from mice that overexpress surfactant protein A. *Am. J. Respir. Cell Mol. Biol.* 21, 380-387.

- [176] Haagsman, H.P., Sargeant, T., Hauschka, P.V., Benson, B.J., and Hawgood, S. (1990) Binding of calcium to SP-A, a surfactant-associated protein. *Biochemistry* 29, 8894-8900.
- [177] Haagsman, H.P., Diemel, R.V. (2001) Surfactant-associated proteins: function and structural variation. *Comp. Biochem.* 129, 91-108.
- [178] Ikegami, M., Korfhagen, T.R., Whitsett, J.A., Bruno, M.D., Wert, S.E., Wada, K., and Jobe, A.H. (1998) Characteristics of surfactant from SP-A-deficient mice. *Am. J. Physiol.* 275, L247-L254.
- [179] Bridges, J.P., Davis, H.W., Damodarasamy, M., Kuroki, Y., Howles, G., Hui, D.Y., and McCormack, F.X. (2000) Pulmonary surfactant proteins A and D are potent endogenous inhibitors of lipid peroxidation and oxidative cellular injury. *J. Biol. Chem.* 275, 38848-38855.
- [180] Sanchez-Barbero, F., Strassner, J., Garcia-Canero, R., Steinhilber, W. and Casals, C. (2005) Role of the degree of oligomerization in the structure and function of human surfactant protein. *A. J. Biol. Chem.* 280, 7659-7670.
- [181] Spissinger, T., Schäfer, K.P., and Voss, T. (1991) Assembly of the surfactant protein SP-A. Deletions in the globular domain interfere with the correct folding of the molecule. *Eur. J. Biochem.* 199(1), 65-71.
- [182] Haagsman, H.P., White, R.T., Schilling, J., Lau, K., Benson, B.J., Golden, J., Hawgood, S., and Clements, J.A. (1989) Studies of the structure of lung surfactant protein SP-A. *American Journal of Physiology* 257, L421-L429.
- [183] Weaver, T.E., and Whitsett, J.A. (1991) Function and regulation of expression of pulmonary surfactant-associated proteins. *Biochem. J.* 273, 249-264.
- [184] King, R.J., Simon, D., and Horowitz, P.M. (1989) Aspects of secondary and quaternary structure of surfactant protein A from canine lung. *Biochimica et Biophysica Acta - Lipids and Lipid Metabolism* 1001(3), 294-301.
- [185] Voss, T., Eistetter, H., Shtifer, K.P. (1988) Macromolecular Organization of Natural and Recombinant Lung Surfactant Protein SP 28-36 Structural Homology with the Complement Factor Clq. *J. Mol. Bio.* 201, 219-227.
- [186] Casals, C. (2001) Role of surfactant protein A (SP-A)/lipid interactions for SP-A functions in the lung. *Pediatr. Pathol. Mol. Med.* 20, 249-268.
- [187] Kuroki, Y., and Akino, T. (1991) Pulmonary surfactant protein A (SP-A) specifically binds dipalmitoylphosphatidylcholine. *J. Biol. Chem.* 266, 3068-3073.
- [188] King, R.J., Phillips, M.C., Horowitz, P.M., and Dang, S.C. (1986) Interaction between the 35 kDa apolipoprotein of pulmonary surfactant and saturated phosphatidylcholines. Effects of temperature. *Biochim. Biophys. Acta.* 879, 1-13.
- [189] Casals, C., Miguel, E., and Perez-Gil, J. (1993) Tryptophan fluorescence study on the interaction of pulmonary surfactant protein A with phospholipid vesicles. *Biochem. J.* 296, 585-593.
- [190] Haagsman, H.P., Hawgood, S., Sargeant, T., Buckley, D., White, R.T., Drickamer, K., and Benson, B.J. (1987) The major lung surfactant protein, SP 28-36, is a calcium-dependent, carbohydrate-binding protein. *J. Biol. Chem.* 262, 13877-13880.

- [191] Cañadas, O., García-Verdugo, I., Keough, K.M.W., and Casals, C. (2008) SP-A permeabilizes lipopolysaccharide membranes by forming aggregates that extract lipids from the membrane. *Biophysical Journal* 95, 3287-3294.
- [192] Rodriguez-Capote, K., Nag, K., Schürch, S., and Possmayer, F. (2001) Surfactant protein interactions with neutral and acidic phospholipid films. *Am. J. Physiol. Lung Cell. Mol. Physiol.* 281, L231-L242.
- [193] Poulain, F.R., Allen, L., Williams, M.C., Hamilton, R.L., and Hawgood, S. (1992) Effects of surfactant apolipoproteins on liposome structure: implications for tubular myelin formation. *Am. J. Physiol. Lung Cell. Mol. Physiol.* 262, L730-L739.
- [194] Poulain, F.R., Nir, S., and Hawgood, S. (1996) Kinetics of phospholipid membrane fusion induced by surfactant apoproteins A and B. *Biochimica et Biophysica Acta* 1278, 169-175.
- [195] Morrow, M.R., Temple, S., Stewart, J., and Keough, K.M.W. (2007) Comparison of DPPC and DPPG environments in pulmonary surfactant models. *Biophysical Journal* 93, 164-175.
- [196] Venkitaraman, A.R., Hall, S.B., Whitsett, J.A., and Notter, R.H. (1990) Enhancement of biophysical activity of lung surfactant extracts and phospholipid-apoprotein mixtures by surfactant protein A. *Chem. Phys. Lipids.* 56, 185-194.
- [197] Taneva, S.G., and Keough, K.M.W. (2000) Adsorption of pulmonary surfactant protein SP-A to monolayers of phospholipids containing hydrophobic surfactant protein SP-B or SP-C: potential differential role for tertiary interaction of lipids, hydrophobic proteins, and SP-A. *Biochemistry* 39, 6083-6093.
- [198] Possmayer F. (2004) Physicochemical aspects of pulmonary surfactant. In: *Fetal and Neonatal Physiology* (3rd Ed.), edited by Polin, R.A., Fox, W.W., and Abman, S.H. Philadelphia: W. B. Saunders Company, 2004, p. 1014-1034.
- [199] Hickman-Davis, J.M., Fang, F.C., Nathan, C., Shepherd, V.L., Voelker, D.R., and Wright, J.R. (2001) Lung surfactant and reactive oxygen-nitrogen species: antimicrobial activity and hostpathogen interactions. *Am. J. Physiol.* 281, L517-523.
- [200] Lang, J.D., McArdle, P.J., O'Reilly, P.J., and Matalon, S. (2002) Oxidant-antioxidant balance in acute lung injury. *Chest* 122, 314S-320S.
- [201] Devendra, G., and Spragg, R. G. (2002) Lung surfactant in subacute pulmonary disease. *Respir. Res.* 3, 19-33.
- [202] Rodriguez-Capote, K., Faulkner, J., Possmayer, F., and Nag, K. (2005) Alteration of alveolar surfactant function by reactive oxygen species. In: Nag, K., and Lenfant, C. eds. *Lung Surfactant Function and Disorder; Lung Biology in Health and Disease; Vol. 201; Taylor & Francis Group.* Pages 425-448.
- [203] Putman, E., van Golde, L.M., and Haagsman, H.P. (1997) Toxic oxidant species and their impact on the pulmonary surfactant system. *Lung.* 175, 75-103.
- [204] Seeger, W., Lepper, H., Wolf, H.R., and Neuhof, H., (1985) Alteration of alveolar surfactant function after exposure to oxidative stress and to oxygenated and native arachidonic acid in vitro. *Biochim. Biophys. Acta.* 835, 58-67.

- [205] Andersson, S., Kheiter, A., and Merritt, T.A. (1999) Oxidative inactivation of surfactants. *Lung*. 177, 179-189.
- [206] Gilliard, N., Heldt, G.P., Loreda, J., Gasser, H., Redl, H., Merritt, T.A., and Spragg, R.G. (1994) Exposure of the hydrophobic components of porcine lung surfactant to oxidant stress alters surface tension properties. *J. Clin. Invest.* 93, 2608-2615.
- [207] Mark, L., and Ingenito, E.P. (1999) Surfactant function and composition after free radical exposure generated by transition metals. *Am. J. Physiol.* 276, L491-500.
- [208] Haddad, I.Y., Zhu, S., Ischiropoulos, H., and Matalon, S. (1996) Nitration of surfactant protein A results in decreased ability to aggregate lipids. *Am. J. Physiol.* 270, L281-288.
- [209] Ingbar, D.H., Bair, R., Jung, P., Heinecke, J., and Haddad, I.Y. (1999) Hyperoxic lung injury increases HOCl-modified lung proteins and NA,K-adenosine triphosphatase nitrotyrosine content. *Chest* 116, 100S.
- [210] Rodriguez-Capote, K., Manzanares, D., Haines, T., and Possmayer, F. (2006) Reactive oxygen species inactivation of surfactant involves structural and functional alterations to surfactant proteins SP-B and SP-C. *Biophys. J.* 90, 2808-2821.
- [211] Manzanares, D., Rodriguez-Capote, K., Liu, S., Haines, T., Ramos, Y., Zhao, L., Doherty-Kirby, A., Lajoie, G., and Possmayer, F. (2007) Modification of tryptophan and methionine residues is implicated in the oxidative inactivation of surfactant protein B. *Biochemistry*. 46, 5604-5615.
- [212] Yau, W.M., Wimley, W.C., Gawrisch, K., and White, S.H. (1998) The preference of tryptophan for membrane interfaces. *Biochemistry* 37, 14713-14718.
- [213] Heeley, D.H., Hong, C. (1994) Isolation and characterization of tropomyosin from fish muscle. *Comparative biochemistry and physiology. Biochemistry and Molecular Biology* 108(1) 95-106.
- [214] Yang, J.T., Wu, C.S., Martinez, H.M. (1989) Calculation of protein conformation from circular dichroism. *Methods Enzymol.* 130, 208-269.
- [215] Hartog, A., Gommers, D., and Lachmann, B. (1995) Role of surfactant in the pathophysiology of the acute respiratory distress syndrome (ARDS). *Monaldi Arch. Chest. Dis.* 50, 372-377.
- [216] Melton, K.R., Nesslein, L.L., Ikegami, M., Tichelaar, J.W., Clark, J.C., Whitsett, J.A., and Weaver, T.E. (2003) SP-B deficiency causes respiratory failure in adult mice. *Am. J. Physiol. Lung Cell. Mol. Physiol.* 285, L543-L549.
- [217] Walther, F.J., Waring, A.J., Hernandez-Juviel, J.M., Gordon, L.M., Wang, Z., Jung, C., Ruchala, P., Clark, A.P., Smith, W.M., Sharma, S., and Notter, R.H. (2010) Critical Structural and Functional Roles for the N-Terminal Insertion Sequence in Surfactant Protein B Analogs. *PLoS one* 5(1), e8672.
- [218] Barhoum, S., and Yethiraj, A. (2009) An NMR study of macromolecular aggregation in a model polymer-surfactant solution. *The Journal of Chemical Physics* 132, 024909.
- [219] Göbl, C., Dulle, M., Hohlweg, W., Grossauer, J., Falsone, S.F., Glatter, O., and Zangger, K. (2009) Influence of phosphocholine alkyl chain length on peptide-micelle interactions and micellar size and shape. *J. Phys. Chem.* 114, 4717-4724.





